Rheology Of Semisolid Alloys Under Rapid Change In Shear Rate

Tze Yong Liu

Department of Engineering Materials

The University of Sheffield, U.K

Submitted for the Doctor of Philosophy

March 2002

Rheology Of Semisolid Alloys Under Rapid Change In Shear Rate

Summary

Industrial thixoforming processes are carried out within a second. Characterisation of the rheological behaviour of the semisolid metal slurry during this short space of time is therefore important.

Rheological experiments were carried out on Sn15%Pb alloy (fraction solid 0.2-0.5) in a HAAKE cylindrical rotational viscometer using ~1kHz data collection rate to obtain the shear stress response to a rapid change in shear rate. Results and conclusions based on them are valid over a limited range of 0 s^{-1}-200 s^{-1}. The slurry undergoes an initial rapid structural breakdown during a jump upwards in shear rate, followed by a more gradual breakdown. The former occurs within a second of the start of the jump. The metal slurry breaks down more rapidly with a higher final shear rate, but is independent of the initial shear rate. The reverse is found with downward jumps in shear rate: recovery times increase with increasing final shear rate. Again, it is independent of the starting shear rate.

The rheological behaviour of aluminium alloys with solid fraction >0.5 at 1 to 100 s^{-1} was studied by rapidly compressing cylindrical slugs against a load cell. The slurry exhibits a near-Newtonian behaviour at the thixoforming temperature, after an appropriate soaking time is employed and a near-spheroidal microstructure develops. Use of image analysis to quantify the spheroidicity indicates that particle shape affects the flow of the slurry, a higher spheroidicity corresponding to a lower load. Using solid-state mechanical deformation to break up the dendrites, produces thixoforming feedstock with lower resistance to flow than magnetohydrodynamic stirring.

Power law index values were obtained for both rapid compression and viscometry experiments. Results from this work have shown the importance of understanding the rheological behaviour of a semisolid slurry in the transient state.

Acknowledgements

I would like to express my deepest gratitude to Dr Helen Atkinson for giving me the chance to work with her and for her continuing support during the course of this work, even when progress was slow at times.

I thank also to Dr D.H. Kirkwood, whose knowledge is as vast as a library, for his helpful advice and suggestions.

To Drs P. Kapranos and P.J. Ward for their help and advice with the experimental work and for their constant support.

I thank all my colleagues in the Thixoforming Group in the University of Sheffield, especially to Dr S.C. Hogg for his patience and understanding and for making 'Oiii' the catch phrase in the department.

I would like to extend my thanks to all the technicians whom have been ever so kind, friendly and helpful to me.

Finally, I like to thank my mother and father, for their love and support, conveyed every weekend over 6900 miles by phone.

And to all, whom I have missed out, since it will probably take up a whole chapter to include all your names.

My deepest thanks to everyone.

TzeYong Liu

Preface

Semisolid processing marks its 30th year of foundation in 2002 after the first discovery in Massachusetts Institute of Technology, USA. The commercialisation of this process has led to an ever-increasing interest in promoting semisolid processing as an alternative route in the manufacturing industry. Many unanswered questions and challenges in semisolid processing still remain, including around the thixotropic behaviour, a intriguing yet complicated phenomenon, of a metal slurry during the forming process. This work aims to address the issue of the rheological behaviour of metal alloy slurries under a rapid change in shear rate, akin to an actual semisolid processing environment. Limitations of the experimental equipment may not allow the answer to every question but hopefully, a better insight can be gained through this work.

This thesis is written in several chapters with figures included within the text, for ease of reading. The figures are numbered sequentially in each Chapter. Chapters 1 to 4 aim to provide the reader with some basic understanding towards semisolid processing, some background on rheology, rheological behaviour and mathematical models of semisolid alloy slurries. Review papers and publications by M.C. Flemings and D.H. Kirkwood (on semisolid processing and rheological behaviour) have been used quite extensively in this thesis whilst mathematical models are mostly drawn from the work of C.J. Quaak and Z. Fan. Publications by H.A. Barnes, D C-H Cheng and R.W. Whorlow are used heavily in fundamental rheology. Chapter 5 describes the experimental work carried out during the course of the author's PhD. The results obtained experimentally are discussed in Chapters 6 and 7 respectively. This is followed by conclusions in Chapter 8 with a brief discussion of future work in Chapter 9. The references are listed according to the author's last name followed by the year of publication.

In the course of this study, the author has written, in collaboration with his supervisor and other workers on the rheological behaviour of semisolid alloy slurries under a rapid change in shear rate [Kir 00, Liu 00a, War 00a and War 00b] and on the rapid compression of aluminium alloys via the Thixoforming route [Liu 00b and Kap 01

CONTENTS PAGE

CHAPTER 4

CHAPTER 5

CHAPTER 6

CHAPTER 7

CHAPTER 8

CHAPTER 9

APPENDICES

CHAPTER 1

Semisolid Processing

Semisolid processing is a novel method of forming complex shape components whist in the semisolid state. This near-net shape method was first introduced in the early 1970s. The key to this process is the internal non-dendritic microstructure (Figure 1.a), which gives the alloys thixotropic properties when in the semisolid state [Spe 72].

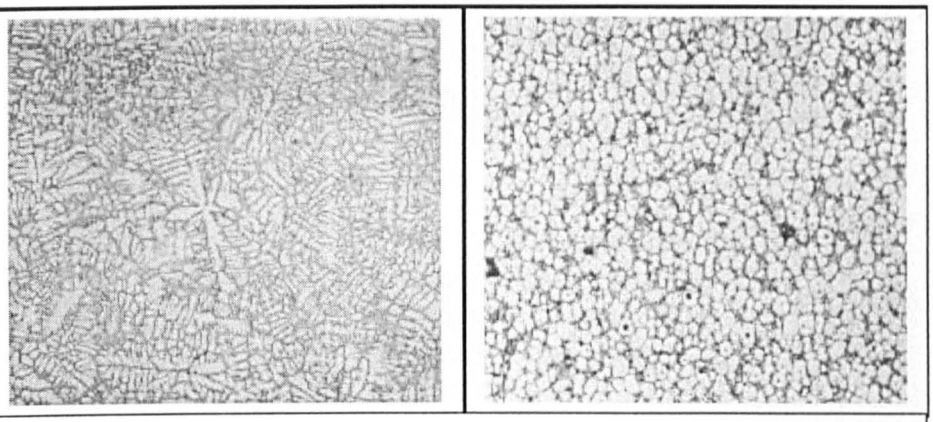

Figure 1.a: Micrograph of a typical (a) dendritic microstructure in an as-cast sample and (b) globular microstructure in a semisolid alloy sample.

In the early stages, researchers obtained alloys with non-dendritic microstructure by cooling a fully liquid alloy to its semisolid state whilst undergoing vigorous agitation by mechanically stirring throughout the cooling operation. Upon reaching its desired solid fraction, the semisolid slurry was then injected into a shaped die. This process was patented in the USA by MIT and was known as rheocasting. Mechanical testing of these rheocast components showed that they possessed better properties than those produced by traditional liquid casting. Furthermore, shaping in the semisolid state meant that the energy required to generate a component is much lower than that of solid forging. The vigorous agitation of metal alloys during solidification leads to the formation of spheroidal particles suspended in the liquid matrix through a process of dendrite shearing and grain growth. Such microstructures exhibit thixotropic behaviour (i.e. a decrease in viscosity under stress, followed by gradual recovery with time when the stress is removed).

When such alloys are heated to their semisolid state, they can be cut and spread like butter (i.e. the semisolid alloy behaves like a viscous liquid) through the application of shear forces but thicken again when allowed to stand (this thickening effect allows the alloy to be handled like a soft solid) (Figure 1.b). This behaviour is largely due to the behaviour of the spheroidal particles that tend to slide past each other under shear with the liquid matrix acting as a lubricant between the particles.

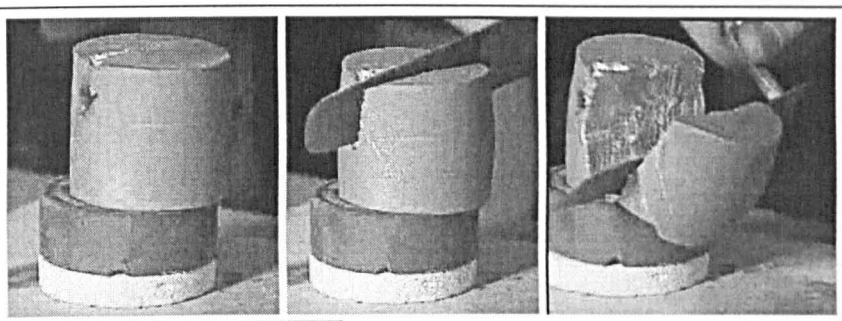

Figure 1.b: A photographic sequence illustrating the thixotropic behaviour of semisolid alloy slugs

Nearly 30 years of work and effort have been invested in the field of semisolid processing and the increase in interest in this field has been marked by six international conferences (Sophia-Antipolis, France 1990 [SSP 1], Cambridge-Massachusetts, USA 1992 [SSP 2], Tokyo, Japan 1994 [SSP 3], Sheffield, UK 1996 [SSP 4], Colorado, USA 1998 [SSP 5], Turin, Italy 2000 [SSP 6]) and an up-coming international conference in Tsukuba, Japan in September 2002. Semisolid processing has managed to rival other manufacturing routes in the field of military, aerospace and most notably automotive components [You 94, You 00, Fan 02]. In Europe, STAMPAL, Florence et Peillon and Alusuisse-Alcan produce suspension parts, engine brackets and fuel rails for automotives. In USA, mechanical parts for mountain bikes and snowmobiles are produced by Formcast [Gar 00] while in Asia, production of electronic components like computer notebook cases and electrical housing components are more widespread [Fan 02]. Figure 1.c shows some of the components produced by STAMPAL for an Alfa Romeo car.

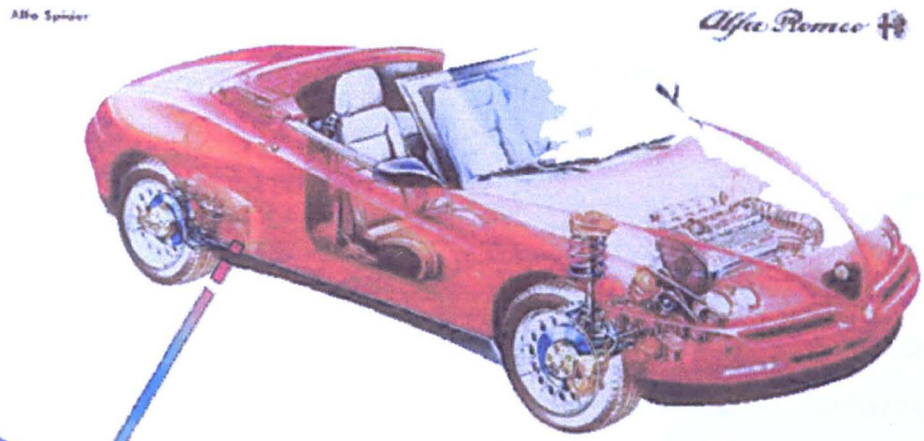

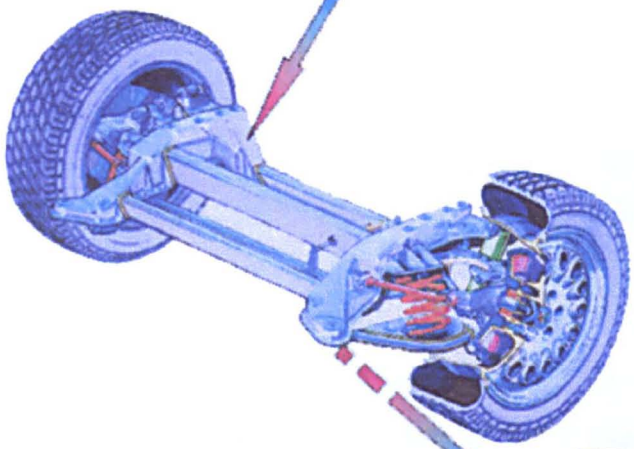

Multilink rear suspension system produced by Thixoforming. (Picture courtesy of Stampal, S.P.A)

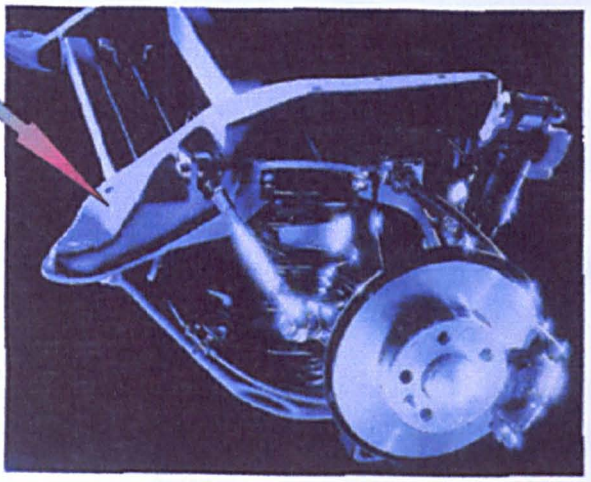

Engine Brackets and Links (Picture courtesy of Alusuisse-Alcan)

Figure 1.c: Examples of automotive components produced by Thixoforming routes.

Research in semisolid processing can be roughly divided into four major groups. They are:

(1) Rheological behaviour of semisolid alloys slurries;

(2) Mathematical modelling;

(3) Alloy Development and

(4) Feedstock production

The rheological behaviour of semisolid alloy slurries is strongly dependent on the microstructure of the semisolid alloy which in turn affects the flow behaviour of the alloy during processing operation. With complete understanding of their rheological behaviour, mathematical modelling can be applied with confidence to understand and predict the actual slurry flow. Knowing how the slurry will flow under shear force, other alloys can be developed for use in semisolid processing.

Several methods exist for producing components by semisolid processing. Two main routes have been identified [Kir 94]: (1) Liquid state processing and (2) Solid state processing. In the liquid state processing, the liquid metal alloy slurries are agitated during solidification. The mechanical stirring route of producing feedstock for semisolid processing in rheocasting has a number of drawbacks, the most obvious is that it is suitable for 'batch' rather than continuous production. Furthermore, contamination of the melt from the stirrer, erosion of the stirrer and gas entrapment [Fle 91, Kir 94] makes this process highly unfeasible in industrial production. Recent stirrers made using reaction bonded silicon nitride may eliminate contamination of the melt [Bra 98] while attempts to increase production rates by increasing the container size result in areas of low shear rate (dead zones). These dead zones cause a decrease in melt homogeneity.

An alternative method to overcome the problems associated with mechanical stirring is the magnetohydrodynamic stirring (MHD) process developed by ITT in the USA. In this technique, rotating electromagnetic fields situated within a continuous casting mould produce continuous billets of solidified non-dendritic feedstock alloys (globular particles of 30-100 μm are feasible) [Qua 96a]. The stirring is deep in the sump of the liquid which has been previously degassed and filtered, eliminating contamination of the melt [Kir 94]. Spray casting of alloys (Osprey process) is

another route for producing non-dendritic feedstock doing away with the need for agitation of liquid metal alloys during solidification. In this process, a stream of liquid metal is atomised by a gas jet and deposited at high speeds in the semisolid state onto a collector (target) thus producing on impact, a fine non-dendritic structure (typical particles sizes of 20μm are feasible).

In solid state processing, feedstocks for semisolid processing are produced by deforming the alloy in its solid state. Two examples of solid state processing are the SIMA (strain-induced, melt-activated) [Ken 88] and the RAP (recrystallisation and partial melting) [Kir 89] processes. Both processes make use of a deformation plus recrystallization route. The microstructure of a material that is sufficiently deformed will change upon partial re-melting from an elongated (along the direction of the deformation) one to one consisting of rounded spheroidal particles in the liquid matrix. In the SIMA process, deformation of the alloys is done above the recrystallization temperature (known as hot-working) whilst the RAP process is done below the recrystallization temperature (warm-working). Typical particle sizes of 30 μm can be achieved for both processes.

Another means of producing spheroidal structure in the feedstock involves heating a dendritic structure to the semisolid temperature range for a period of time sufficient to allow a spherical structure to evolve. This is known as semi-solid thermal transformation, or SSTT.

The feedstock material obtained from the above processes can be shaped into various components either by reheating it into its semisolid state before forging or casting. Thixocasting is where the feedstock is forced into a die cavity as in a diecasting machine and Thixoforging is where the feedstock is forged between two dies (either open or closed heated/non-heated dies). The current term used for all semisolid metal processing involving feedstock material is Thixoforming [Kir 94]. Figure 1.d shows schematically the routes for semisolid metal processing. Thixoforming has an advantage over the rheocasting route as the need for handling liquid metal is removed and the process can be easily automated.

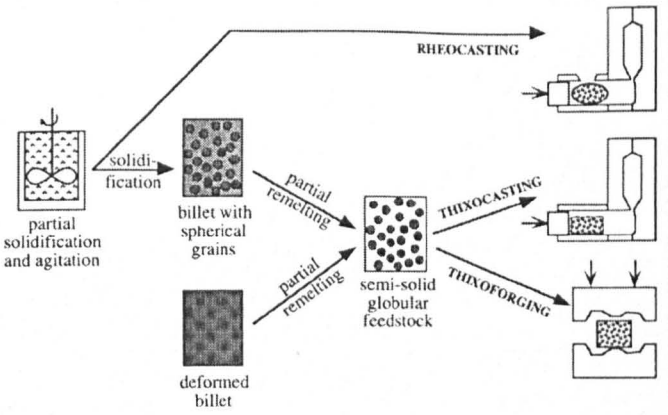

Figure 1.d: Schematic illustration of different routes for semisolid metal processing [Qua 96b].

A process that uses a similar technique to plastic injection moulding was developed by Dow Chemical [Pas 92] and is termed Thixomolding™ (Figure 1e). This involves feeding alloy chips or pellets into a reciprocating screw within a heated barrel. The rotating motion and heating in the barrel cause the alloy to be sheared and partially re-melted. The semisolid alloy is then injected into a die cavity. This process is being used widely for processing magnesium alloys of thin-walled components, mainly for electronics components housing like mobile phone covers.

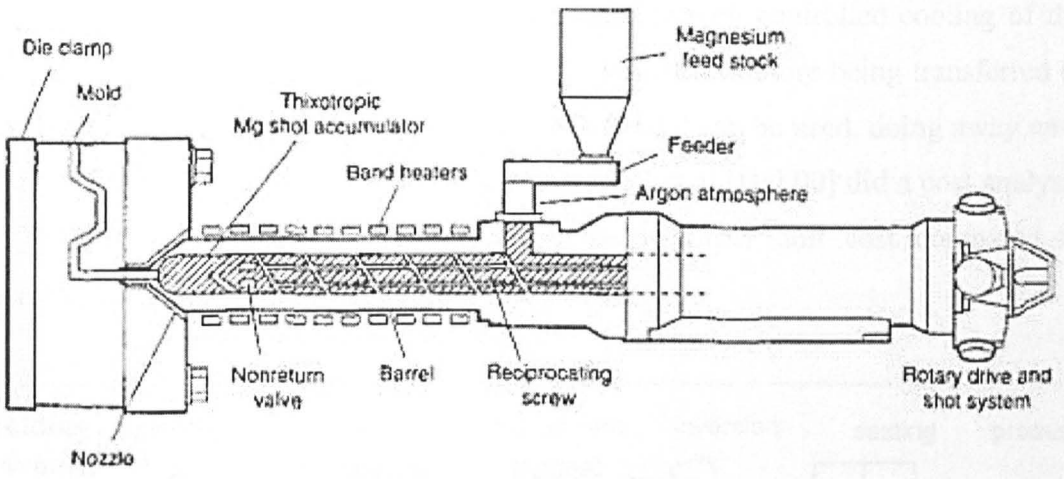

Figure 1e: Schematic diagram of Thixomolder™ used mainly in magnesium.

A similar process to Thixomolding™ is the rheomolding process (Figure 1.f) which uses a single screw process [Pen 94, 00] or a twin screw process [Ji 01]. In this process, liquid metal is fed into a barrel where it is cooled while being mechanically stirred by a rotating screw. The semisolid material is then injected into a die cavity. Such processes have an added advantage in that they are suitable for continuous casting of large quantities of components and doing away with the high price of obtaining feedstock material for semisolid processing. However, these processes can only produce components of limited size.

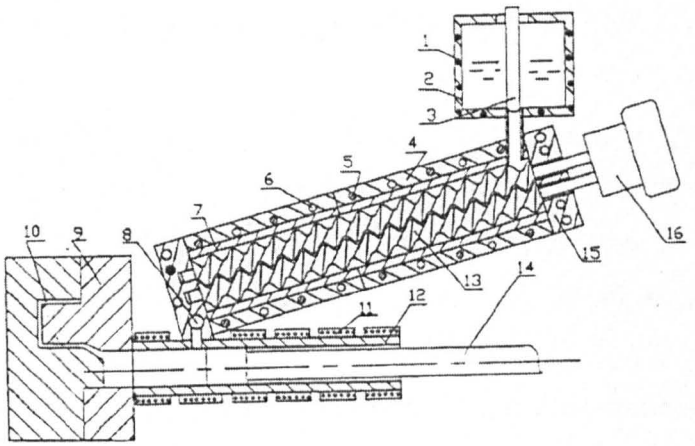

1, Heating elements; 2, crucible; 3, stopping rod; 4, barrel; 5, heating elements; 6, cooling channels; 7, barrel liner; 8, transfer valve; 9, die; 10, mould cavity; 11, heating elements; 12, shot sleeve; 13, twin-screw; 14, piston; 15, end cup; 16, driving system.

Figure 1.f: Schematic diagram of a Rheomolder using a twin screw process [Ji 01]. Liquid metal is used instead of the solid chips used in the Thixomolder™.

Other processes include the shear-cooling roll (SCR) process [Kiu 92, 94], cooling slope process [Hag 00] and the New Rheocasting (NRC) process [Mit 96] patented by UBE Industries Ltd. NRC (Figure 1.g) involves the pouring of the melted alloy slightly above the liquidus into a steel crucible with controlled cooling of the slurry's temperature to achieve spheroidal microstructures before being transferred to a forming machine. In NRC, conventional cast material can be used, doing away with the need for a non-dendritic feedstock material. Hall et al [Hal 00] did a cost analysis of the NRC route and showed that it has a lower per unit cost compared to Thixoforming, due to the lower starting material cost.

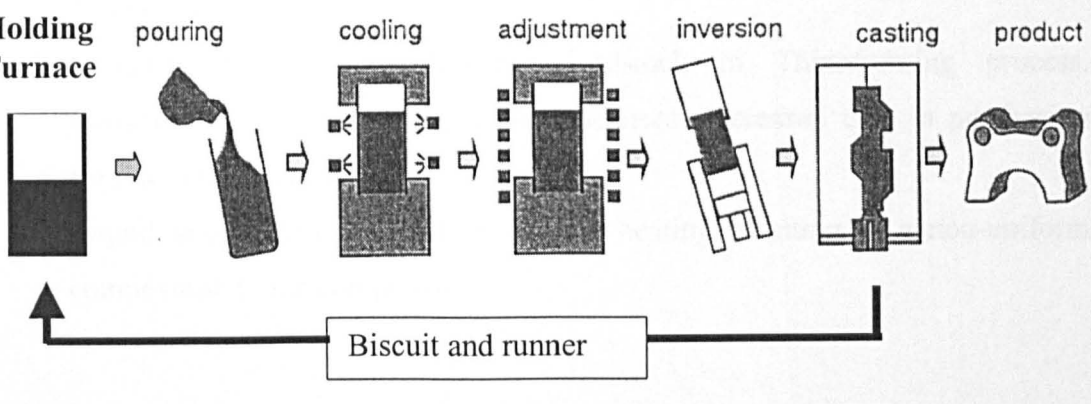

Figure 1.g: Schematic diagram of the New Rheocasting (NRC) process The inversion procedure causes the oxide skin on the exposed surfac to run into the runner and biscuit.

As with any manufacturing process, there are certain advantages and disadvantages in semisolid processing. They are [Fle 91, You 92, Kir 94, Qua 96a]:

Advantages

(1) Enhanced die life due to the lower heat content of semisolid alloys compared to a fully liquid alloy in a die casting process. This helps to reduce die costs.
(2) Lower temperature needed to heat up to semisolid state therefore energy efficiency.
(3) Near-net shape components. Thin-walled sections can be produced.
(4) High integrity components. Little or no porosity and/or solidification shrinkage in comparison with that commonly found in a conventional die casting operation.
(5) Compared to conventional forging, smaller loads are required during the forming process hence longer tool life and reduced tool wear.
(6) The laminar flow behaviour in semisolid alloys allows more intricate parts to be made compared to solid forging.

Disadvantages

(1) Temperature control. Fraction solid and viscosity in the semisolid state are very dependent on temperature. Alloys with a narrow temperature range in the semisolid region require accurate control of the temperature and there should be little variation in the liquid content with temperature at about 50% liquid.
(2) Specialised equipment and staff for the operation process. This increase the overhead cost.
(3) Specially prepared non-dendritic feedstock in Thixoforming process. Conventional feedstock alloy cannot be used. Increased cost in purchasing from a separate supplier.
(4) Liquid segregation due to non-uniform heating resulting in a non-uniform composition in the component.

The potential of thixoforming as a replacement for conventional casting, requires detailed insight into the complete route in this process. Die filling is of particular importance here since the flow behaviour of the alloy slurry is different to that in liquid metal casting. In the latter, the viscosity of the liquid metal is low, making bulk and surface turbulence unavoidable. In this aspect, thixoforming, usually done when the alloy is about 50% solid, has a relatively high viscosity ensuring that laminar flow is present during die filling. In order to have successful die filling, die design must be appropriate for the thixoforming process. Using conventional die design experience from die casting is inappropriate because it can result in incomplete die filling and incorporation of defects. Figure 1.h shows an example of how computer simulation can be used in the design of an appropriate gate design for thixoforming process.

Computer simulations of the die filling process can provide us with valuable information and the necessary parameters for obtaining optimum die fill. In order to achieve this, we must first obtain rheological properties of the semisolid alloy slurry during a rapid change in the strain or shear rate. It is these rheological properties that are concentrated in this work. Using the rheological parameters obtained, an iteration process can begin proving the robustness of CFD packages like Flow-3d® for predicting thixotropic die filling. Lastly, various feedstock routes and alloys can be used to produce defect free components in the evaluation of the completed model.

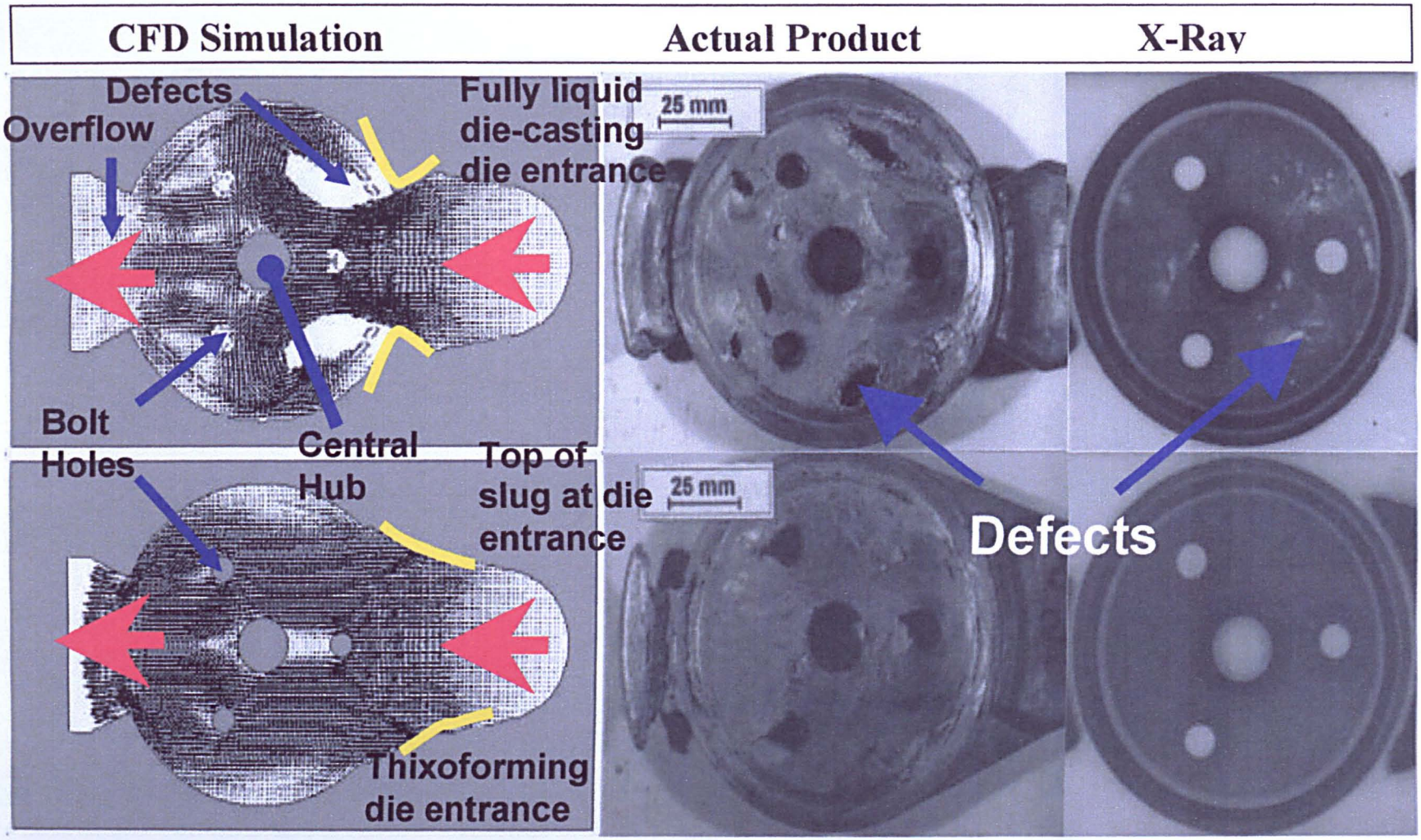

Figure 1.h: The top row shows the results using a conventional fully liquid die casting entrance (yellow lines). Note the holes in the component near the entrance on the right, both in the CFD prediction and in the actual product. The lower row shows much improved flow pattern and product that can be obtained by tailoring the entrance design (yellow lines) to the features of the thixoforming process.

CHAPTER 2

2.1 Background to Rheology

In 1678, Robert Hooke developed his 'Theory of Elasticity'. The Hooke's Law states that, for relatively small deformations of an object, the displacement or size of the deformation is directly proportional to the deforming force or load. Under these conditions, the object returns to its original shape and size upon the removal of the load. Imagine a spring being stretched by a load attached to it. If the load is now taken away, the spring reverts back to its original length. Robert Hooke identified this a The Theory of Elasticity for Solids. Mathematically, Hooke's Law states that the applied force, F, equals a constant k times the displacement or change in length x (i.e. $F = kx$) where k (the modulus of rigidity) is dependent on the material's elasticity, dimension and shape. Hooke's Law may also be expressed diagrammatically in terms of stress and strain (Figure 2.1A). The force results in an instantaneous deformation where the deformed state (with no further deformation) persists as long as the stress is applied.

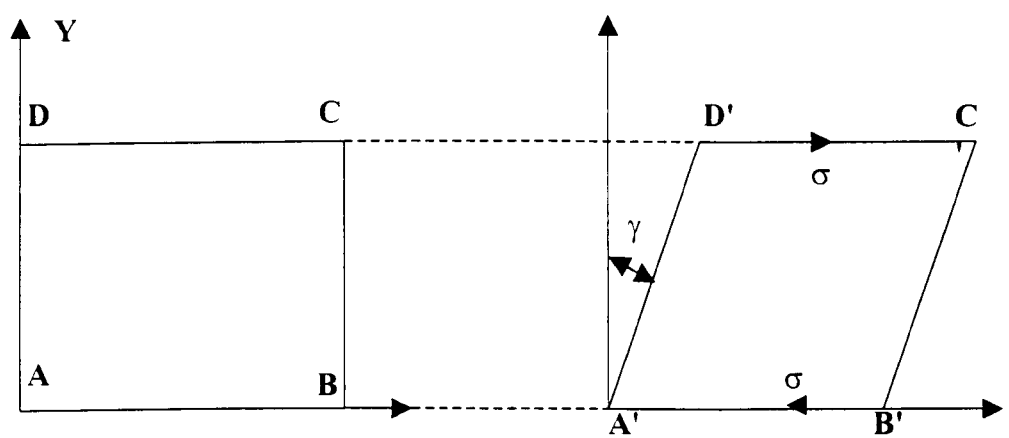

Figure 2.1A: The deformation of a Hookean Solid under the application of a force expressed in terms of shear stress,σ, and strain,γ, where σ= kγ. k is the modulus of rigidity

In 1687, Issac Newton considered the deformation and flow of liquids as opposed to Hooke who considered the behaviour of elastic solids, and stated the following hypothesis: 'That the resistance which arises from the *lack of slipperiness* of the parts of a liquid, other things being equal, is proportional to the velocity with which the parts of the liquid are separated from one another'. The lack of slipperiness is now known more widely as the viscosity. (i.e. it is a measure of 'resistance to flow'). Mathematically, Newton's Law of Viscosity for Liquids states that the force per unit area (or shear stress) required to produce a motion is proportional to the velocity gradient (or shear rate) and the constant of proportionality, η, is also known as the coefficient of viscosity. Newton's Law of Viscosity can be expressed diagrammatically in terms of shear stress and shear rate (Figure 2.1B). The shear stress on a liquid results in flow and this flow persists as long as the stress is applied.

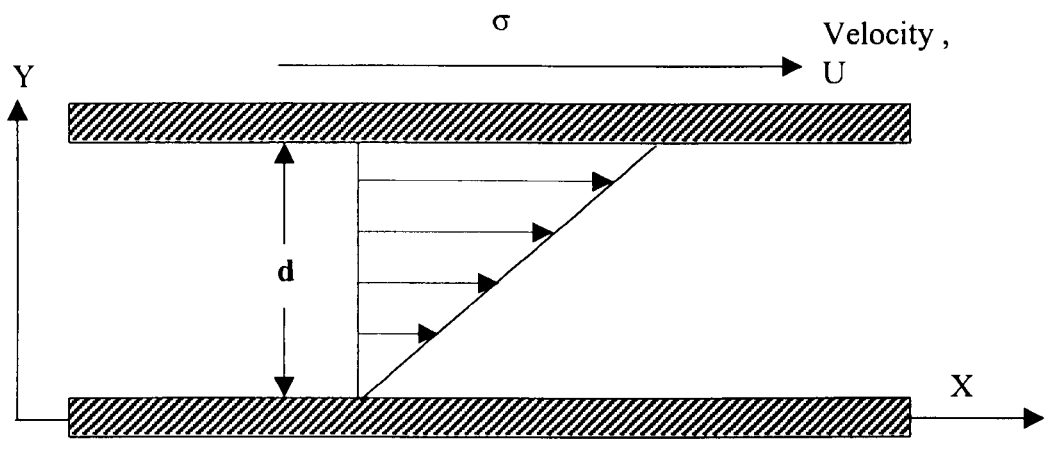

Figure 2.1B: Two parallel planes with their intervening space filled with sheared liquid. The upper plane moves relative to the velocity gradient that is proportional to the applied force or shear. The constant of proportionality,η, is called the coefficient of viscosity denoted as $\sigma = \eta(U/d)$ where U/d (or $\dot{\gamma}$) is the shear rate.

Hooke's Law of Elasticity and Newton's Law of Viscosity are the two extremes in describing the behaviour of solids and viscous liquids respectively. These are known as linear laws, which assume a direct proportionality between the stresses, strain and shear rate. However, the applicability of such linear laws is very limited if one considers the wide range of material behaviour. Most materials fall between these two extremes, where they may exhibit elasticity and viscosity in varying degrees. Such behaviour is described as non-linear behaviour. Non-linearity can be also accompanied by elastic effects. Substances that store some of their mechanical energy as elastic energy when the imposed stress is removed are termed viscoelastic materials.

A common example of non-linearity is known as shear thinning. Shear thinning is defined as the reduction of viscosity with increasing rate of shear under steady flow. This is sometimes called the 'toothpaste effect'. Toothpaste in a tube sits unmoving but is easily squeezed out when a pressure is applied to it. Its viscosity changes occur almost instantaneously. Shear thinning that does not occur instantaneously can be found in non-drip household paint. The paint, when stirred, reduces its viscosity and so can be easily applied to a wall. Upon standing, the paint recovers its viscosity and does not drip. Such shear thinning behaviour combined with the recovery of viscosity over time upon standing is termed thixotropy. Thixotropic materials do not store the energy elastically and show no elastic recovery when the stress is removed. The opposite of shear thinning is shear thickening (or dilatant) behaviour where the viscosity increases with increase in stress or shear rate. Such behaviour has a high degree of Brownian motion. Brownian motion is the kinetic energy of a molecule, thermally agitated, that is transferred to the particle causing the particles to move in a vibratory motion. Theoretically, all suspended particles are in Brownian motion except at absolute zero. However, it is not possible to observe Brownian motion for large particles since the amount of displacement would be too small to detect (When the particle is large, the number of bombarding molecules is likewise large and the impacts are uniformly distributed over the particle surface so that the net result when the particle is pushed in any direction is about zero, hence Brownian motion is only observed for very small particles.). In shear thickening, the particles are thought to settle into a position of minimum voids in the suspended medium through this motion. Since the particles are settling into the voids, a sudden

shear force will be met with strong resistance by the material. This is attributed to the sudden expansion of the voids in the material. Hence the resistance causes a stiffening action in the material.

An example of shear thickening is quicksand where the more one struggles in it, i.e. increasing the stress, the faster one sinks. If shear thickening is accompanied by recovery with time, we term this non-thixotropy or rheopexy. The typical responses to shear rate change of substances showing viscoelasticity, thixotropy and rheopexy are shown in Figure 2.1C.

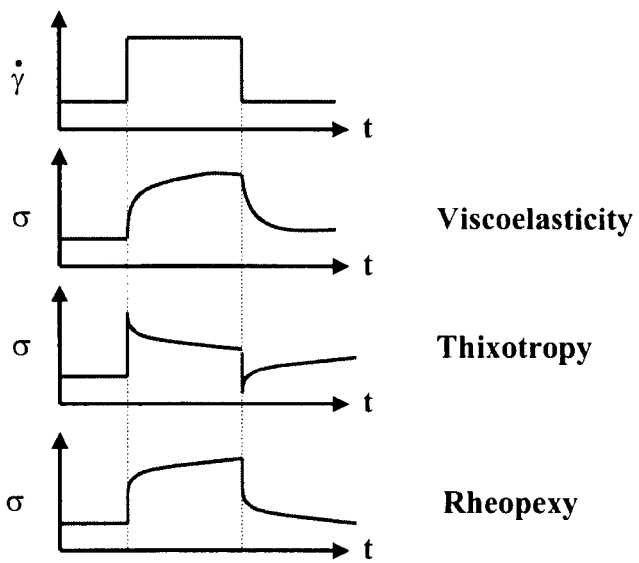

Figure 2.1C: Typical shear stress versus time response after a shear rate jump for non-linear behaviour

It can be seen that shear thinning and shear thickening behaviours do not follow the behaviour of either Hooke's Law of Elasticity or Newton's Law of Viscosity. Such behaviour is now more widely termed Non-Newtonian. In Non-Newtonian material, the viscosity, η, is sometimes termed the apparent viscosity [Old 56, Fer 91] under equilibrium conditions and it is affected by variables such as shear rate, time, temperature and pressure. Non-Newtonian behaviour can be found in almost all types of material and it is this behaviour, especially thixotropy in semisolid alloys, which has caused much interest in the field of semisolid processing. In order to understand thixotropic behaviour, it is necessary to relate the material's viscosity to the shear rate, time and temperature.

2.2 Effects of Viscosity

In the previous section, it was stated that the viscosity is the measurement of the resistance to the flow of a liquid. The table below (**Table 2.2A**) gives some examples of viscosity values in some familiar materials at room temperature and atmospheric pressure.

Liquid	Approximate viscosity (Pas)
Glass	10^{40}
Molten glass (500 °C)	10^{12}
Bitumen	10^{8}
Molten polymers	10^{3}
Golden Syrup	10^{2}
Liquid honey	10^{1}
Glycerol	10^{0}
Olive oil	10^{-1}
Bicycle oil	10^{-2}
Water	10^{-3}
Air	10^{-5}

Table 2.2A: Approximate viscosity values of some materials at room temperature and pressure taken from Barnes et al [Bar 89a]

Most of the materials shown above exhibit Newtonian behaviour under constant temperature and pressure (i.e. the viscosity, η, is independent of the shear rate). Materials that show Newtonian behaviour should have the following characteristics:

(i) The shear stress,σ, is the only stress generated under simple shear flow;

(ii) The viscosity does not vary with shear rate;

(iii) The viscosity is constant with time of shearing and the viscosity falls to zero when shearing is stopped and it does not change from its initial measured value upon application of any subsequent shearing.

2.2.1 Effect of shear rate on viscosity

The table below shows the approximate magnitude of shear rates of some materials used in industry. (Data taken from Barnes et al, [Bar 89a])

Table 2.2.1A

Situation	Typical range of shear rates (s^{-1})	Application
Sedimentation of fine powders in suspending liquid	10^{-6} to 10^{-4}	Medicines, paints
Levelling due to surface tension	10^{-2} to 10^{-1}	Paints, printing inks
Draining under gravity	10^{-1} to 10^{1}	Painting and coating
Semi-solid forming	10^{-1} to 10^{4}	Manufacturing, Casting
Extruders	10^{0} to 10^{2}	Polymers
Chewing and swallowing	10^{1} to 10^{2}	Foods
Dip coating	10^{1} to 10^{2}	Paints, confectionery
Mixing and stirring	10^{1} to 10^{3}	Manufacturing liquids
Pipe flow	10^{0} to 10^{3}	Pumping, Blood flow
Spraying and brushing	10^{3} to 10^{4}	Spray-drying, fuel atomisation
Rubbing	10^{4} to 10^{5}	Application of creams and lotions to the skin
Milling pigments in fluid bases	10^{3} to 10^{5}	Paints, printing inks
High speed coating	10^{5} to 10^{6}	Paper
Lubrication	10^{3} to 10^{7}	Gasoline engines

From Table 2.2.1A, it can be seen that the enormous range of shear rates (around 13 orders of magnitude) corresponding to the viscosity of the material plays a very important role in applications in industry and our everyday use.

It is common to represent the behaviour of flowing materials by plotting a shear stress against shear rate graph (i.e. plotting flow curves). Figure 2.2.1A shows

the behaviour of several non-Newtonian materials. In Figure 2.2.1A(**a**), the flow curve of a Newtonian fluid is shown. This is represented by a straight line through the origin, of slope, η, (i.e. the viscosity). Figure 2.2.1A can also be represented by a plot of viscosity against shear rate graph as shown in Figure 2.2.1B. For a Newtonian fluid, it is clear that η is just a constant of proportionality between shear stress and shear rate.

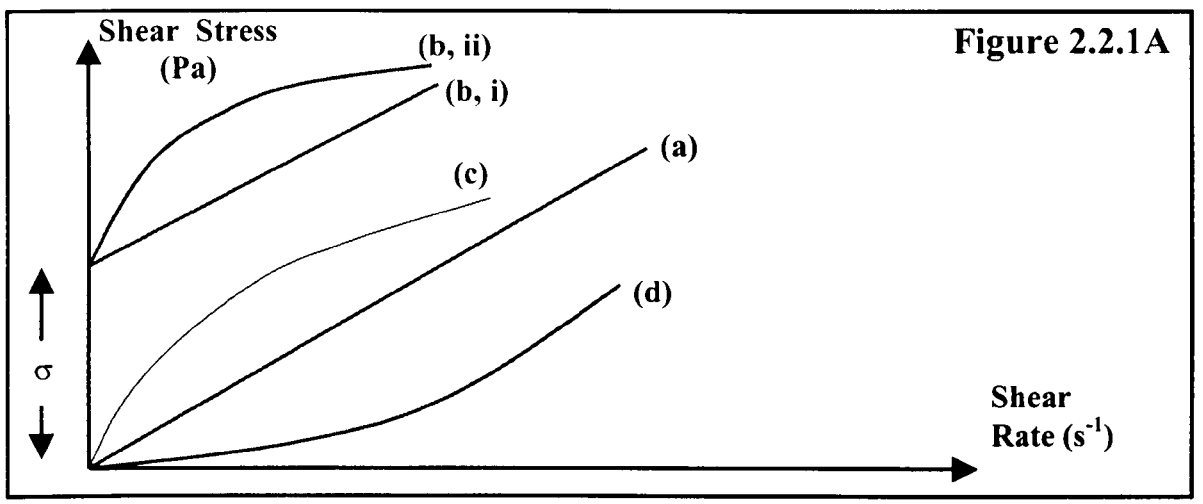

Figure 2.2.1A

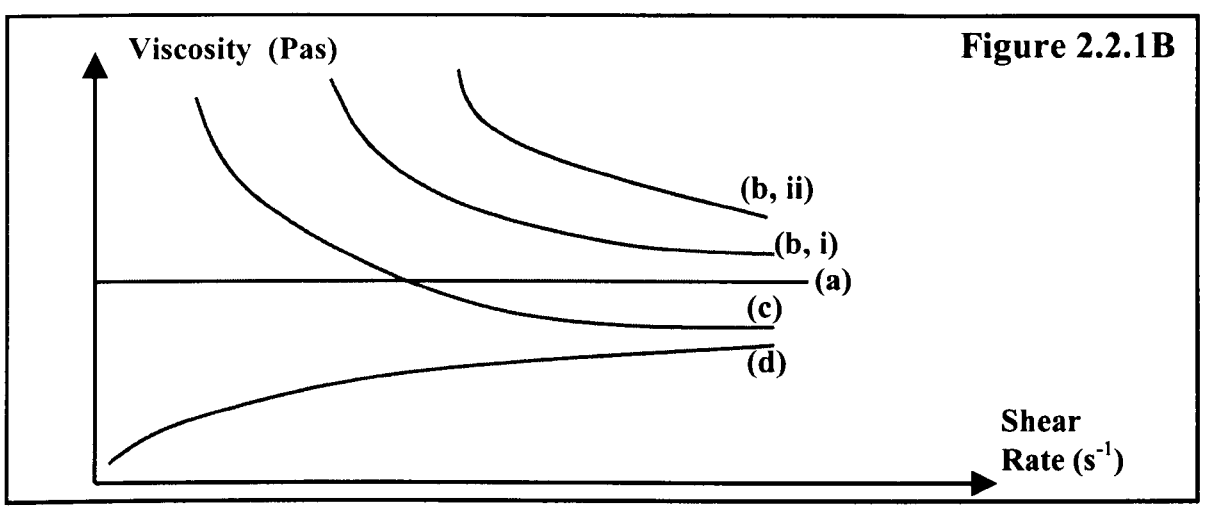

Figure 2.2.1B

Figure 2.2.1A(**b**), (**c**) and (**d**) are representative of non-Newtonian fluid flow. Figure 2.2.1A(**b, i**) represents a material which behaves as an elastic solid until it exceeds a critical stress (known as the yield stress, σ_y) and the material starts to flow thereafter. The rate of flow after the yield stress would then depend on the material properties and the characteristic of the instrument used. Figure 2.2.1A(**b, i**) is known as the Bingham model. It is disputable as to whether a Bingham material flows like a Newtonian fluid after exceeding its yield stress. It was pointed out by R.W. Whorlow [Who 92] that most material's flow curves are not linear except over a very limited

range of shear rates. **Figure 2.2.1A**(b,ii) shows a variation of the Bingham model known as the Herschel-Bulkley model where the material behaves in a non-Newtonian way after exceeding its yield stress.

Another dispute that arises from the Bingham model is the presence of the yield stress itself in a material. Barnes and Walters [Bar 85] did several experiments investigating the concept of a yield stress. They found that the value of the yield stress in their material is dependent on the shear rate range used (Figure 2.21C). From Figure 2.2.1C, the yield stress value (taken from the y-intercept of the flow curves graphs) differs at different shear rate ranges. In fact, from Figure 2.2.1C, they showed that using the lowest applicable shear rate from their apparatus, yield stress has disappeared.

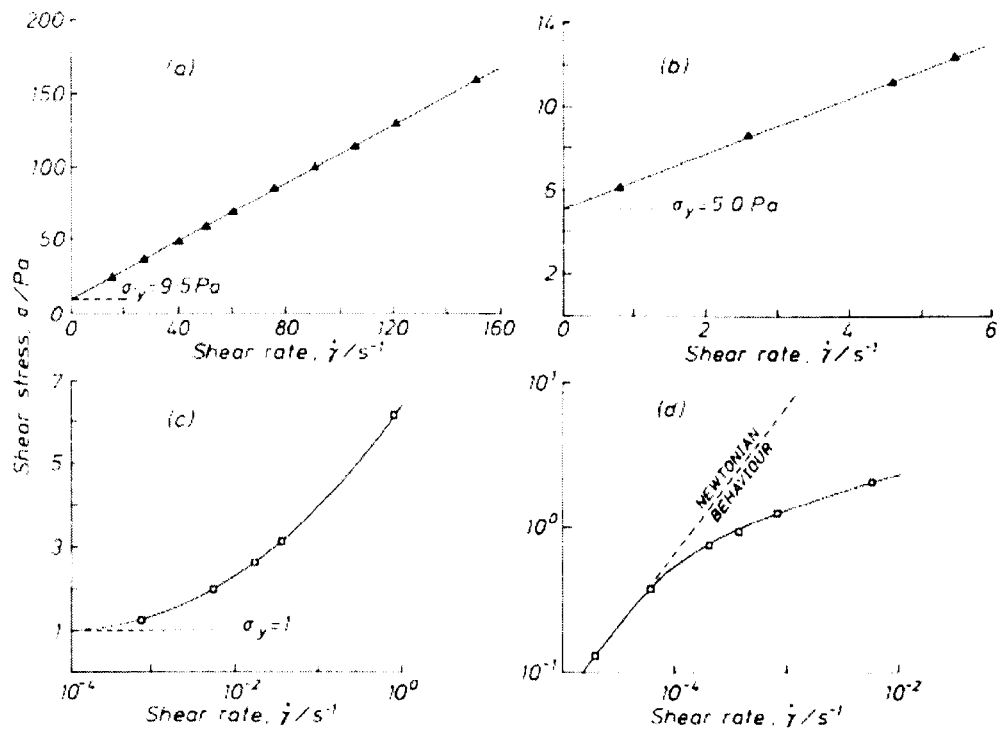

Figure 2.21C: Flow curves for a synthetic latex (taken from Barnes and Walters, [Bar 85]):
(a) and (b) showed a Bingham plot over two ranges of shear rate with two different intercepts;
(c) A semi-logarithmic plot of data obtained at much lower shear rates, showing another intercept;
(d) Logarithmic plot of data at the lowest obtainable shear rates, showing no yield stress behaviour

Barnes et al [Bar 85, 89a] deduced that the presence of a yield stress as reported by other workers is probably due to the limitations of their experimental apparatus in measuring shear stresses at very low shear rates. As declared by Deborah in the fifth chapter of the book of Judges in the Old Testament, "The mountains flowed before the Lord....", (everything flows if you wait long enough, even the mountains !). Such deduction is perhaps true if a material does actually flow but at a very slow rate because of its very high viscosity (i.e. its resistance to flow). It may take several years to even notice a slight displacement.

However, Cheng [Che 85] disagrees with Barnes et al. He finds that there are certain materials where the stress goes thorough a minimum before starting to rise at very low shear rates. It is perhaps fitting and appropriate of Whorlow [Who 92] to state that the applicability of a yield stress is dependent on the type of applications required of the material. For example, whether a material (e.g. clay) will retain its shape (i.e. before it exceeds its yield value) under the action of gravity until it is fired, or a toothpaste that will retain its shape on the bristles before brushing commence may give one certain guidance into its applicability.

Figure 2.2.1A(**c**) and (**d**) represent power law fluids (sometimes known as Ostwald de Waele fluids). The equation of such fluid may be written as $\sigma = k \dot{\gamma}^{n}$ where n represents the slope of the curve. From the equation, it is generally assumed that at very low shear rates, $\dot{\gamma}$, $n \rightarrow 1$, that is the material becomes a Newtonian fluid. For $n < 1$, we have a shear thinning fluid (i.e. the viscosity decreases as the shear rate increases, (Figure 2.2.1B(**c**)). A typical flow curve of a shear thinning material over a range of shear rates is shown in Figure 2.2.1D. Two regions, the upper band and the lower band corresponding to the very high and very low shear rates respectively have been identified. In these two regions, the viscosities are assumed to be constant.

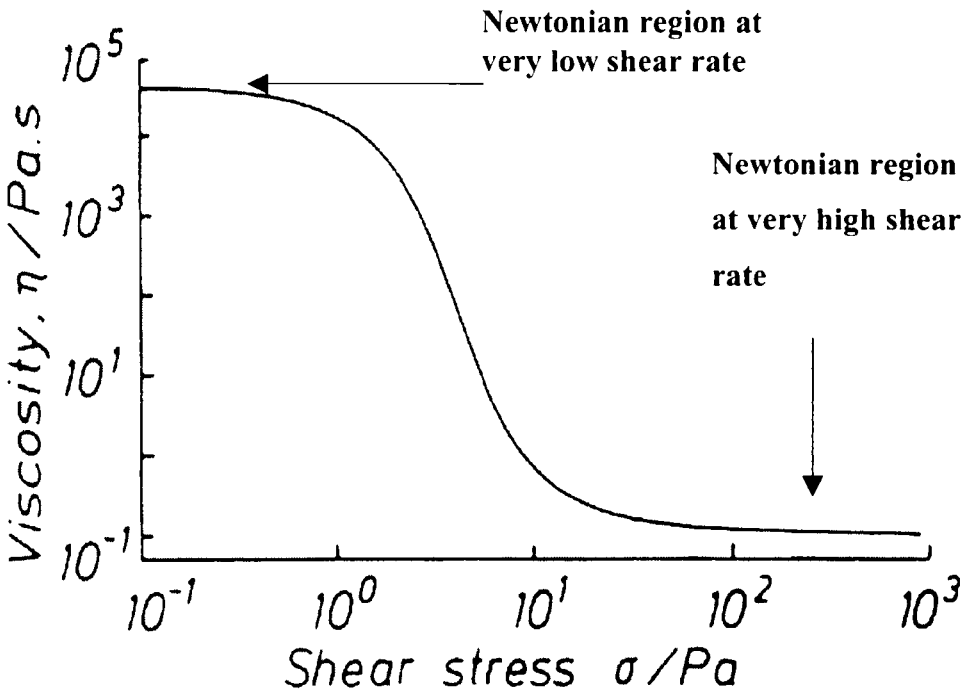

Figure 2.2.1D: A typical shear thinning material showing the two Newtonian regions; (a) and (b) at very low and very high shear rates respectively

In **Figure 2.2.1B(d)**, we have a shear thickening fluid where its viscosity increases with increasing shear rate. In this case, $n > 1$. Shear thickening materials are not very common and as pointed out by Whorlow and Barnes, most shear thickening materials have a shear thinning region at the very low shear rates but show the shear thickening behaviour with an increase in the shear rates. Many mathematical models exist [Fer 91, Who 92] to describe steady state flow curves as described previously. Various workers have proposed models independently. Table 2.2.1B below shows a list of some of the more general mathematical models (including those discussed previously).

Table 2.2.1B

Author(s) model	Year	Mathematical Model
Issac Newton	1687	$\sigma = \eta \dot{\gamma}$
E.C. Bingham	1919	$\sigma = \sigma_y + \eta_p \dot{\gamma}$ where η_p is the plastic viscosity, a constant
Ostwald de Waele	1924	$\eta = k \dot{\gamma}^{n}$ where k and n are constants
Herschel-Bulkley	1926	$\sigma = \sigma y + k\dot{\gamma}^{n}$ where k and n are constants
Ellis	1927	$\dot{\gamma} = k_1 \sigma + k_2 \sigma^{N}$ where k_1, k_2, N (N>1) are all constants
Casson [Cas 59]	1959	$\sigma^{1/2} = \sigma_y^{1/2} + k \dot{\gamma}^{1/2}$ where k is a constant
Cross [Cro 65]	1965	$\eta = \eta_\infty + [(\eta_o - \eta_\infty) / (1 + k\dot{\gamma}^{n})]$ where k and n are constants
Parzonka and Vocadlo [Par 68]	1968	$\sigma = (\sigma_y^{1/n} + k \dot{\gamma})^{n}$ where k and n are constants
Carreau [Car 72]	1972	$\eta - \eta_\infty = (\eta_o - \eta_\infty) / [1 + (k \dot{\gamma})^2]^s$ where k and s (s = 1- n / 2) are constants

The Cross Model is perhaps one of the most widely used models. Its derivation is based on the formation and rupture of structural linkages in a suspension system (see Appendix 1). The Cross Model has been used to fit experimental data on various solutions by other workers. Figure 2.21E shows some results taken from Barnes [Bar 89a].

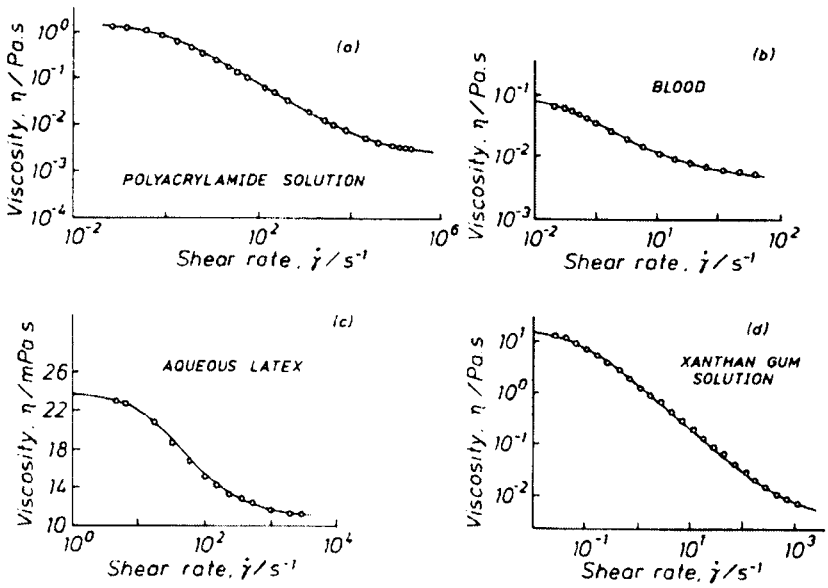

Figure 2.21E: Some examples of the applicability of the Cross model (from Table 3) [Bar 89a]:

(a) 0.4% aqueous solution of polyacrylamide,

(b) Blood of human,

(c) Aqueous dispersion of polymer latex spheres and

(d) Aqueous solution of Xanthan gum.

From the Cross Model, at least two other viscosity models can be derived if we make certain assumptions. They are the power law model (Ostwald de Waele) and the Sisko Model [Sis 58]. The derived equations however, only apply over limited parts of a shear thinning flow curve. Figure 2.21F illustrates how the power law model fits only the central region whilst the Sisko model fits in the mid to high shear rate range.

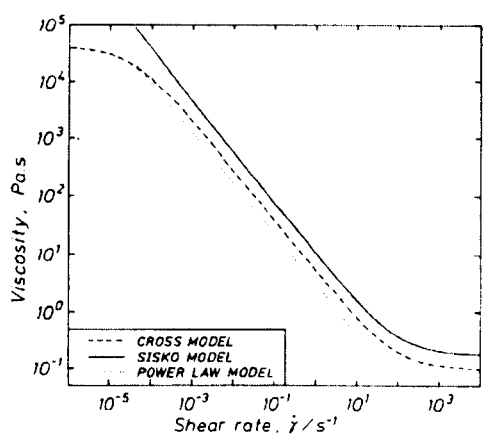

Figure 2.21F: Typical curves obtained using the Cross, Power-law and Sisko models. Curves from the power-law model and the Sisko model have been shifted for clarity [Bar 89a].

So far, discussions have been based on non-Newtonian fluids that do not include any time, temperature and pressure effects. The following sections describe these effects in relation to the viscosity.

2.2.2 Effect of Pressure on Viscosity

The viscosity of liquids increases exponentially with isotropic pressure except for water (below 30°C) where the viscosity first decreases before increasing exponentially. Changes in viscosity are quite small if the difference from the atmospheric pressure is about 1 bar. Hence, for laboratory experiments and most practical purposes (except operations like drilling mud at elevated pressure, i.e. >20 MPa), the pressure effects are usually ignored.

2.2.3 Effect of Temperature on Viscosity

Viscosity is highly dependent on the temperature. For a Newtonian fluid, a graph of log η against 1/T is found to be linear and it is usual to write it as:

$$\eta = A \exp(E_v / kT) \quad \text{---------- (2.2.3a)}$$

where A is the material's constant, E_v the activation energy for viscous flow, k the Boltzman's constant and T the temperature.

From Equation 2.2.3a, the viscosity of a Newtonian liquid decreases with increase in temperature. The greater the viscosity, the stronger is its temperature dependence. Figure 2.2.3A shows the trend for a series of lubricating oils. It is thus important to maintain a constant temperature in the material throughout the experiment. Other factors include changes in the material's temperature due to the act of shearing the material, where heat generated may reduce the viscosity, and heat conduction to the surface of the viscometer from the material. Therefore the dimensions of the viscometer are critical.

Temperature affects the microstructural behaviour of a material and thus in turn affects the viscosity. In polymeric materials, the intermolecular forces and the amount of free volume are both dependent on the temperature. In suspensions of material (e.g. coal slurries, paints, etc.), the particle radius and particle distances for diffusion processes are both affected by the temperature.

For semisolid metal slurries, the fraction solid (dependent on the temperature) is one of the most important factors affecting the viscosity.

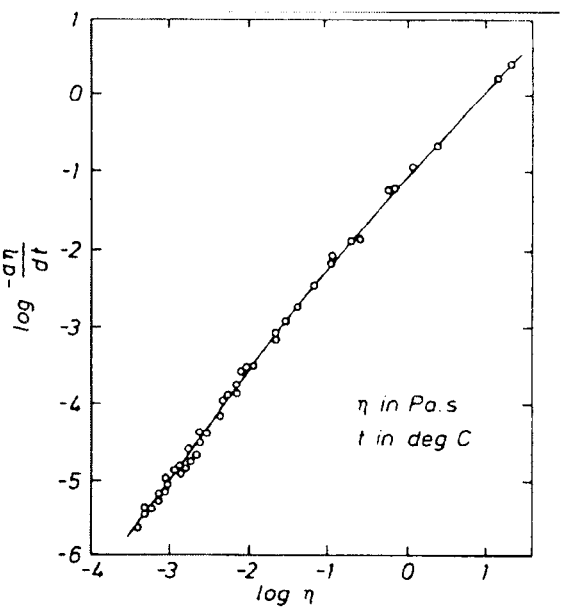

Figure 2.2.3A: Logarithmic plot of viscosity/temperature derivative versus logarithm of viscosity for a series of lubricating oils [Bar 89a].

2.2.4 Effect of Time on Viscosity

In Section 2.2.1, it was mentioned that shear thinning fluids that recover their initial viscosity after the applied stress is removed over time, are known as thixotropic. Peterfi coined the term 'thixotropy' in 1927 to describe the phenomenon of sol-gel transformation where the sols were liquefied during shaking but solidified again after a period of time when the shaking stops. The change of this state (from sols to gel back to sols again) in this process is repeatable with no change in the whole system at any time. Thixotropy is now defined, according to the British Standards Institution as the 'decrease in viscosity under stress, followed by gradual recovery when the stress is removed [Mew 79, Che 87]. The effect is time dependent'. Figures Figure 2.2.4A, 2.2.4B and 2.2.4C show the typical characteristics of thixotropic behaviour.

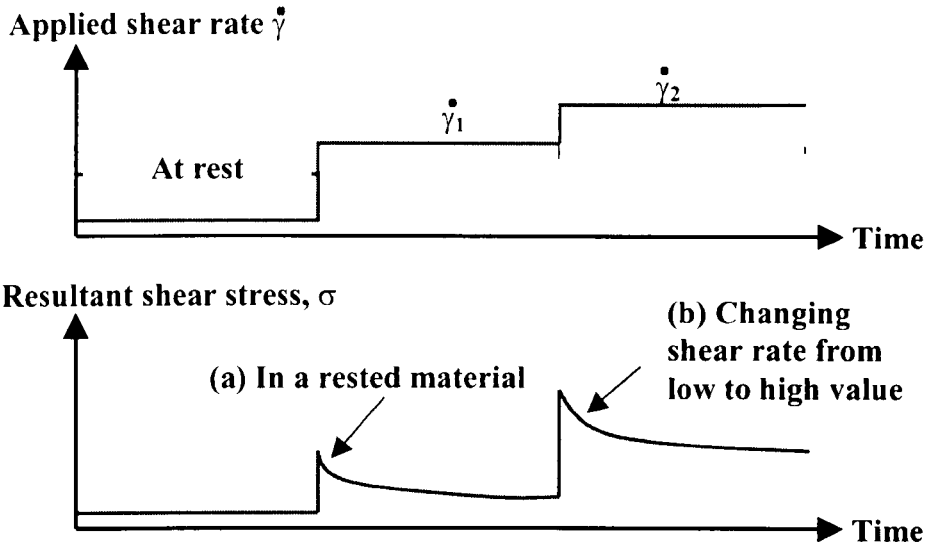

Figure 2.2.4A: Resulting shear stress behaviour of a thixotropic material: (a) in a rested material where a shear stress us suddenly applied and (b) changing the shear rate from an initial low value to a higher value

For a thixotropic material at rest, increasing the shear rate imposed on the material will decrease its viscosity until it reaches an equilibrium value over time under the constant shear rate or when the shear rate is changed from a low value to a high value (Figure 2.2.4A). When the material is rested for different lengths of time, the peak viscosity encountered will increase with increasing rest time before it recovers back to the equilibrium viscosity of the shear rate specified (Figure 2.2.4B(**a**)). The same applies when the material is sheared from a higher shear rate to a low shear rate (Figure 2.2.4B(**b**)). The time of recovery (or time to breakdown) depends on the amount of rest time or the final shear rate specified.

Figure 2.2.4B(a): Thixotropic behaviour showing shear stress (or viscosity) decrease

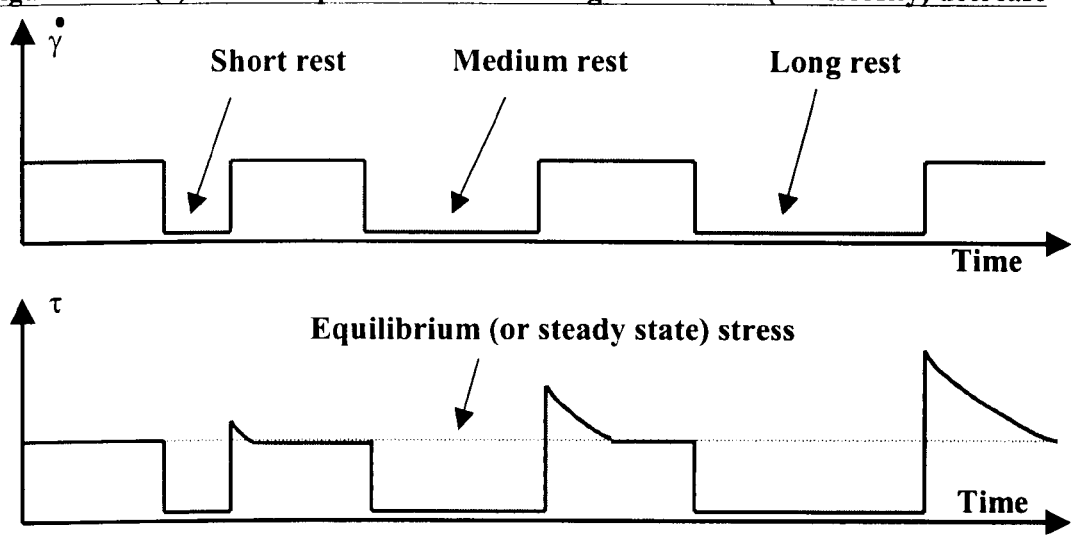

Figure 2.2.4B(b): Thixotropic material showing shear stress (or viscosity) recovery

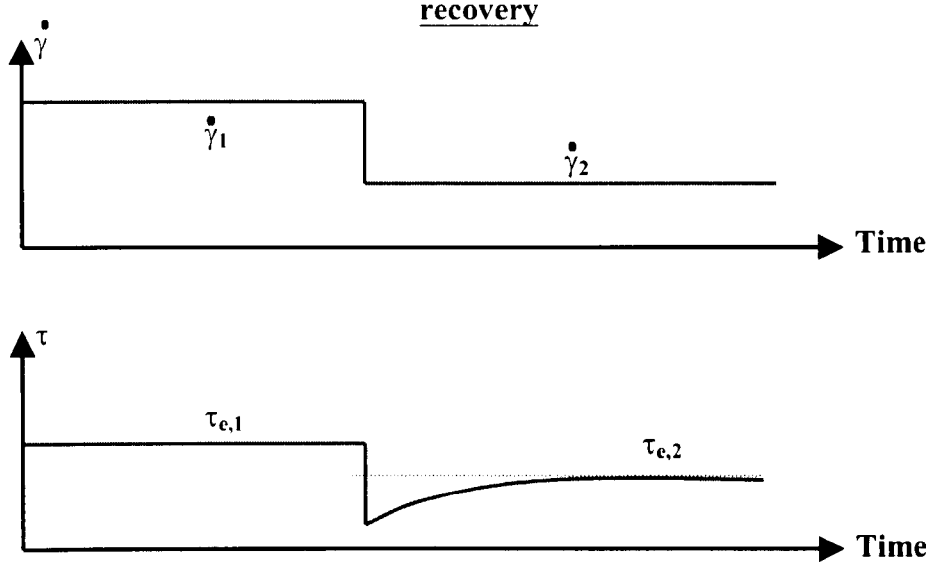

A hysteresis loop under cyclic shearing can be obtained by linearly increasing the shear rate from zero to a maximum value and returning it back to zero at the same rate. After repeat cyclic shearing, an equilibrium loop will be obtained. The area under this hysteresis loop indicates the degree of thixotropy in the material (Figure 2.2.4C).

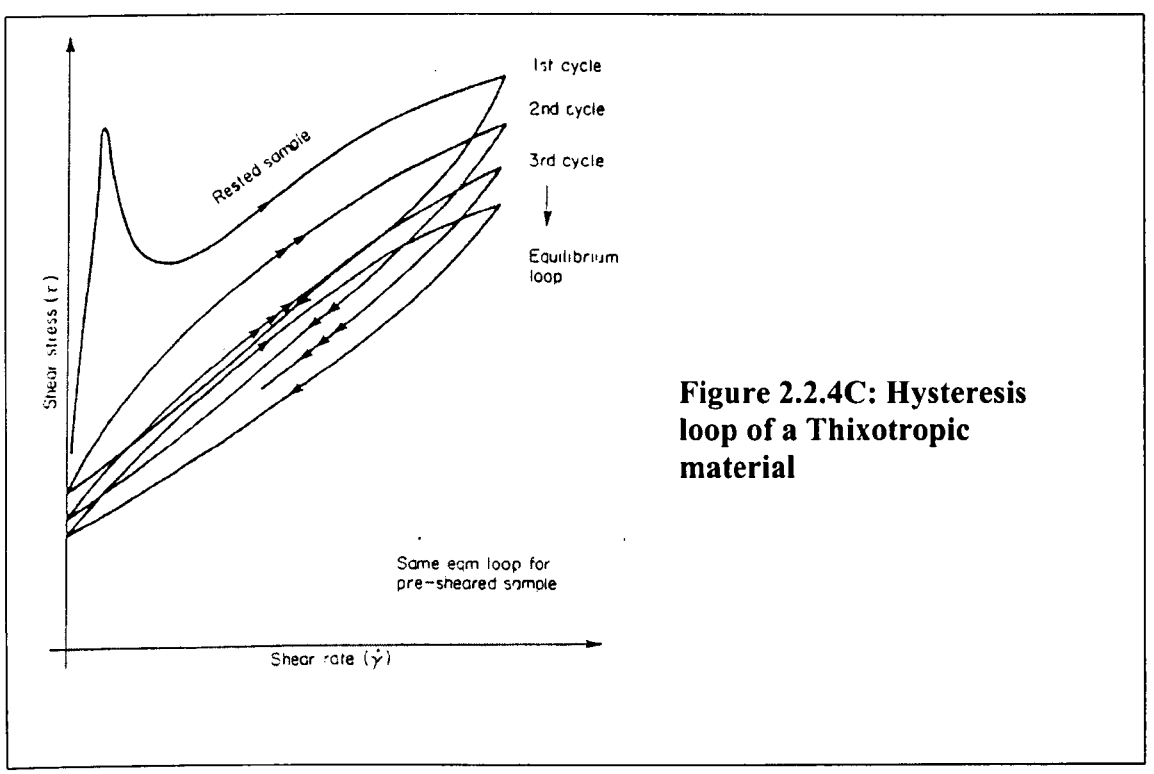

Figure 2.2.4C: Hysteresis loop of a Thixotropic material

The above section describes the flow stress behaviour under shear rate and time. In a microscopic view, it is usual to relate thixotropy with the molecular or particle structure. A simple way of relating these two behaviours is shown in Figure 2.2.4D for a flocculated suspension. At rest, the microstructure can be considered as a series of large flocs. If shear rate is being applied now, increasing the shear rate progressively, the floc size will decrease with time and with even higher shear rate, the floc will be completely disintegrated, consisting of just its constituent primary particles. Another scenario would be where the shear rate is changed from a low shear rate to a high shear rate. The floc size will start to break up as it experiences higher shear rate until it reaches an equilibrium size with time appropriate to the higher shear rate. If the shear rate is changed from a high value to a low value, the reduced movement in the particles will cause collisions and flocculation until the size of the floc structure is appropriate to the shear rate. This is the nature of recovery.

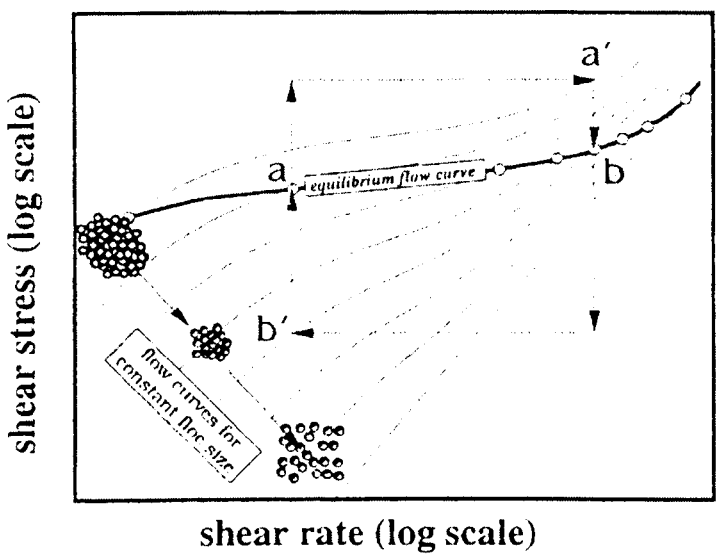

Figure 2.2.4D: Flow curves of a flocculated suspension. Point 'a' shows the microstructures at rest as a series of large flocs. If shear rate is increased from *a* to *a'*, the flocs begins to break up as the shear rate reaches point *a'*, this breaking up continues until it reaches the equilibrium size appropriate to the higher shear rate, point *b*. Vice versa, if the shear rate is now changed from *b* to *b'*, the individual particles begin to collide and flocculate until it reaches the equilibrium size appropriate to the new lower shear rate, point *a* [Bar 97].

Variation of structure with time is the basis of the time dependent nature of thixotropy. Many materials showing thixotropic behaviour can be categorised according to the physical and chemical nature of their internal structure as mentioned

in the previous paragraph. Table 2.2.4A shows some examples of thixotropic materials relating the behaviour of break up and recovery of the structure.

Table 2.2.4A. Examples of thixotropic materials relating structural break up and recovery

Materials	Structural build-up at rest	Structural breakdown under shear
Colloidal dispersion and suspensions of solids: 1) Paints 2) Coatings 3) Inks 4) Clay slurries 5) Cosmetics 6) Agricultural chemicals	Flocculation under inter-particle forces	Break-up of flocs (deflocculation)
Emulsions	Flocculation of droplets	Deflocculation
Foamed systems: 1) Mousses	Flocculation of bubbles	Defloccualtion Coalescence
Crystalline systems: 1) Waxy crude/fuel oils 2) Waxes 3) Butter/Margarine 4) Chocolate	Interlocking of growing crystals	Break-up of long needles
Polymeric systems: 1) Solutions/melts 2) Starch /gums 3) Sauces	Agglomeration of macromolecules Entanglement	De-agglomeration Disentanglement
Fibrous suspensions: 1) Tomato ketchup 2) Fruit pulps 3) Fermentation broths 4) Sewage sludges	Agglomeration of fibrous particles Entanglement	De-agglomeration Disentanglement
Semi-solid metallic systems	Agglomeration of particles	De-agglomeration

Inter-particle forces can be used to describe the behaviour of certain thixotropic material's internal structure (e.g. clay slurries). Inter-particle forces are described by their potential energy giving rise to 2 kinds of behaviour: (1) The Born Repulsion, (2) Van de Waals Attraction. The degree of attraction between the particles due to their potential energy determines the resistance to flow (i.e. viscosity). Breaking up of the particles is time dependent. Brownian motion is another cause of particle interactions. Under shear forces, random Brownian motion causes collisions between particles resulting in agglomeration. The smaller the particle the bigger is the Brownian motion. Therefore larger agglomerates result in higher viscosity. (The Brownian force required to orientate the larger particles into favourable structure takes a longer time). In metallic system, the collision of particles causes welds between the particles forming agglomerates resulting in an increase in the viscosity. The introduction of shear stress breaks up the welds thus decreasing the viscosity. The particles are now in constant motion with the direction of the flow field hence particle to particle welding occurs less often than when the material is at rest or at a lower shear rate.

Several mathematical models have been proposed to describe thixotropic behaviour [Mew 79, Che 97, Bar 97]. It should be noted that none of the models proposed account for all the factors discussed in the preceding sections (i.e. pressure, time, temperature, Brownian movement and particle interactions). Mathematical models are validated through experimental results with certain assumptions made. Although the models do not provide a complete understanding of the kinetics of thixotropic behaviour, they are usually sufficient enough for most practical uses. The most common thixotropic model considers two types of equations, the equation of state and the rate equation. The following gives a brief discussion of some of the models proposed by various workers.

The Moore model was first proposed in 1959 [Moo 59]. It relates the flow unit concentration, shape and size distribution and its internal constitution to a single structural parameter term, λ. The viscosity is evaluated in terms of λ and the rate equation using λ is proposed for its time dependent behaviour. Moore's equation is given as:

$$\eta = \eta_\infty + c\lambda \qquad (2.2.4a)$$

where η_∞ is the limiting viscosity at infinitely high shear rate and c is a material constant.

Moore then assumed that for a fully built up structure, $\lambda = 1$, therefore:

$$c = \eta_o - \eta_\infty \qquad (2.2.4b)$$

where η_o is the limiting viscosity at very low shear rate; and for a fully broken down structure, $\lambda = 0$, hence :

$$\eta = \eta_\infty \qquad (2.2.4c)$$

Equation 2.2.4a can be written as:

$$\sigma = (\eta_\infty + c\lambda) \dot{\gamma} \qquad (2.2.4d)$$

Equation 2.2.4d is known as the state equation, relating the state of the structure to its viscosity and shear rate.

In order to describe the net rate of change of the structure, i.e. rate of structural breakdown or buildup, Moore proposed a rate equation:

$$d\lambda / dt = a(1-\lambda) - b \dot{\gamma} \lambda \qquad (2.2.4e)$$

From Equation 2.2.4e, $-b\dot{\gamma}\lambda$ is the breakdown rate while $a(1-\lambda)$ is the build-up which is independent of the shear rate. a is a constant in the recovery process unaffected by shear rate but promoted by only Brownian motion. b is the constant during the breakdown process where the shear rate is a more significant influence than the Brownian motion.

Moore also proposed an equation for the equilibrium flow curve. Combining the equation of state and the rate equation, the equilibrium flow is given as:

$$\frac{\eta - \eta_\infty}{\eta_o - \eta_\infty} = \frac{1}{1 + \frac{b}{a}\dot{\gamma}} \qquad (2.2.4f)$$

It can be seen that the Moore's model (Equation 2.2.4f) is very similar to the Cross Model (c.f. Table 2.2.1B). The difference is that Cross assumed the breakdown rate to be a power law function of the shear rate. Hence in Cross's model, the rate equation is given as:

$$d\lambda /dt = a (1 - \lambda) - b \lambda \dot{\gamma}^m \qquad (2.2.4g)$$

and the equation of state as:

$$\sigma = (\eta_\infty + c\lambda) \dot{\gamma}^{m} \qquad (2.2.4h)$$

where m is the power law exponent and reported by Cross to have an even number for its numerator while an odd number for its denominator. The Cross equation for equilibrium flow is that given in Table 2.2.1B.

Another model that uses the Moore's model as its basis is due to Worral and Tuliani [Wor 64]. In this model, the authors used the same rate equation as Moore but introduced the Bingham yield stress into the equation of state:

$$\sigma = \sigma_y + (\eta_\infty + c\,\lambda) \dot{\gamma} \qquad (2.2.4i)$$

and the equilibrium flow can be written as:

$$\sigma_e = \sigma_y + (\eta_\infty + \frac{c}{1 + \frac{b}{a}\dot{\gamma}})\dot{\gamma} \qquad (2.2.4j)$$

Other possibilities deriving from the Moore's model can be obtained. An example is given by Cheng [Che 87] where he combined a modification of the Worral and Tuliani's equation of state (by using a power law exponent) with the Cross rate equation giving a model of:

$$\sigma_e = \left(\sigma_o + \frac{\sigma_1}{1 + \frac{b}{a}\dot{\gamma}^{m}} \right) + \left(\eta_\infty + \frac{c}{1 + \frac{b}{a}\dot{\gamma}^{m}} \right)\dot{\gamma} \qquad (2.2.4k)$$

More recently, Barraco-Serra et al [Bar 00] proposed a thixotropic model for carbopol gels. The rate equation is the same as Moore whilst the equation of state is similar, but instead of a single parameter the authors used two structural parameters, λ_1 and λ_2:

$$\eta = \eta_\infty + c\,(\lambda_1 + \lambda_2) \qquad (2.2.4L)$$

and the thixotropic model relating the shear stress, τ, with an exponential decay with time, t, of the material is given as:

$$\tau = \tau_e + (\tau_o - \tau_e)\{[a\exp(-k_1 t) + (1-a)\exp(-k_2 t)]\} \qquad (2.2.4m)$$

where subscripts e and o represents the equilibrium viscosities at its limiting shear rates (c.f. Cross Model, Table 2.2.1B). 'a' is the structural parameter while k_1 and k_2 are the material's relaxation times.

The work of Mewis and Schryers [Mew 96] used the viscosity as a direct measure of the structure without the use of a structural parameter. They proposed that the rate of change of viscosity rather than the rate of change of the structure be related to the viscosity difference between the steady state and the current values of viscosity (i.e. not the structural difference). This was given as:

$$d\eta / dt = k [\eta_s (\dot{\gamma} - \eta)]^n \qquad (2.2.4n)$$

Upon integration,

$$\eta = \eta_{\infty,e} - [\eta_{\infty,e} - \eta_{o,e}] [(\eta - 1) kt (\eta_{\infty,e} - \eta_{o,e})^{n-1} + 1]^{1/(1-n)} \qquad (2.2.4o)$$

Mewis and Schryers made the assumption that $\eta_{o,e} = \eta_{\infty,i}$ (i.e. the viscosity at the end of the initial steady state period is the same as that at the beginning of the new shear rate test). This is a Newtonian assumption where the system is assumed to be essentially Newtonian between the two conditions. However, this is only true for certain systems and at very high shear rates. A probable reason is that at low shear rates, coalescence or agglomeration are more pronounced than at high shear rates (i.e. the shear force generated at high shear rate reduces the chances of welding and thus agglomeration of the particles.). Like Mewis and Schryers, workers like Kristensen et al [Kri 96] have also done away with the use of a structural parameter. They modelled the thixotropic breakdown behaviour as:

$$(\eta - \eta_\infty)^{1-m} = [(m-1)kt + 1] (\eta_o - \eta_\infty)^{1-m} \qquad (2.2.4p)$$

where η_o and η_∞ are the viscosity values representing fully structured and fully de-structured states at time t under any particular shear rate. m and k are material constants.

2.3 Rheological Measurements

Several techniques are used to investigate the rheological behaviour of materials. The most common type of technique is by using viscometers. In this class, viscometers are split into 2 general groups. The first group is the rotational viscometers. The main advantage of a rotational viscometer is its ability to achieve a simple shearing flow with an approximately uniform shear rate generated throughout the sample. The majority of rotational instruments are based on the relative rotation about a common axis:

(a) For two concentric cylinders: If the outer cylinder rotates and torque is measured on the inner cylinder, it is called the Couette system. If the inner cylinder rotates and the torque is measured from it while the outer cylinder stays stationary, this system is called the Searle system.

(b)A plate whose surface lies in a plane throughout the apex of a cone

(c)A double cone plate or **(d)** two parallel plates in relative rotation about an axis perpendicular to the plates.

Figure 2.3A below shows the arrangement of the above systems. The limitations of the rotational viscometers are that (1) very high shear rates cannot be achieved and (2) viscous heating of the sample due to shearing may occur.

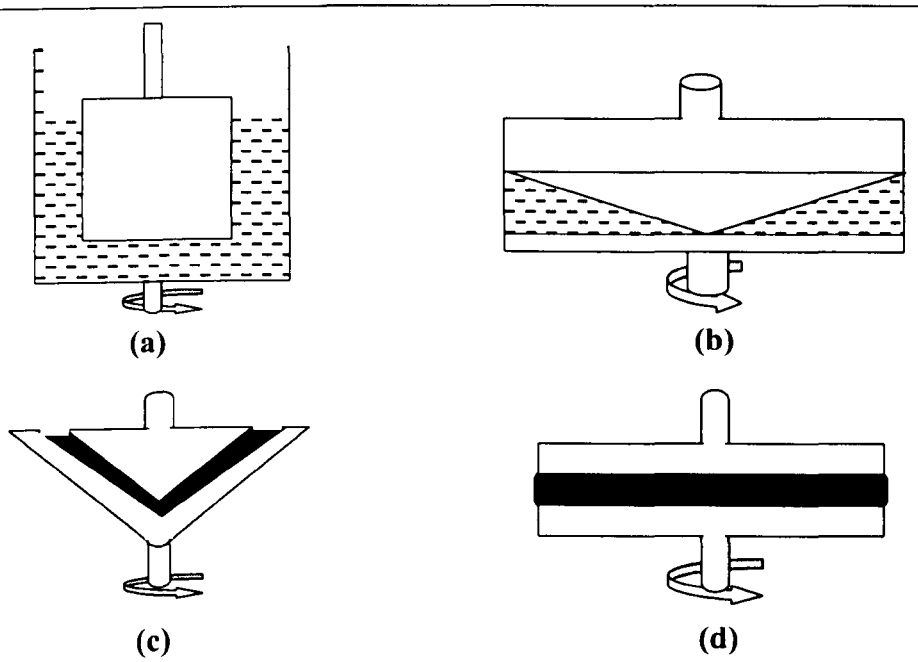

Figure 2.3A: Common types of rotational viscometer. (a) Concentric cylinders viscometer; (b) Cone and Plate viscometer; (c) Cone and Cone viscometer; (d) Parallel Plate viscometer

In the second group, we have the tube and slit viscometers (Figure 2.3B (**a**), (**b**)). Both of these viscometers measure the rate of flow due to a known pressure difference. For a slit viscometer, fluid flow is between two parallel stationary walls. This has the advantage of being a 2-dimensional geometry in comparison with the tube viscometers, which have a 3-dimensional geometry. The tube and slit viscometers are more accurate in measuring Newtonian, elastic and viscoelastic fluids and for very viscous material at very high shear rates. In fact, most calibration of oils (e.g. Silicone Oil) for calibrating various viscometers is done using the U-tube viscometer. Flow regions at the entrance and exit when employing such viscometers are important considerations as effects like die-swell or jet thrust affect the flow curves and behaviour in the fluid.

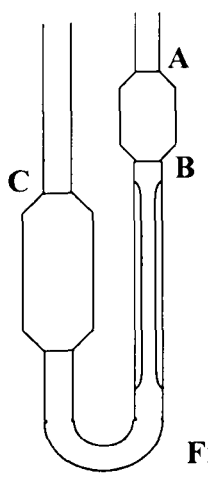

Test liquid is filled to level at mark C at the require conditions (i.e. temperature). The liquid is then brough up to a level above mark A. Upon removal of pressur source, the time taken for the liquid to fall from mark to mark B is approximately the kinematic viscosity, ν, o the fluid where:

$$\nu = \eta / \rho$$

ρ is the density of the fluid.
η is the coefficient of the viscosity or sometimes known as the dynamic viscosity.

Figure 2.3B(a): Schematic diagram of a U-tube viscometer [Who 92].

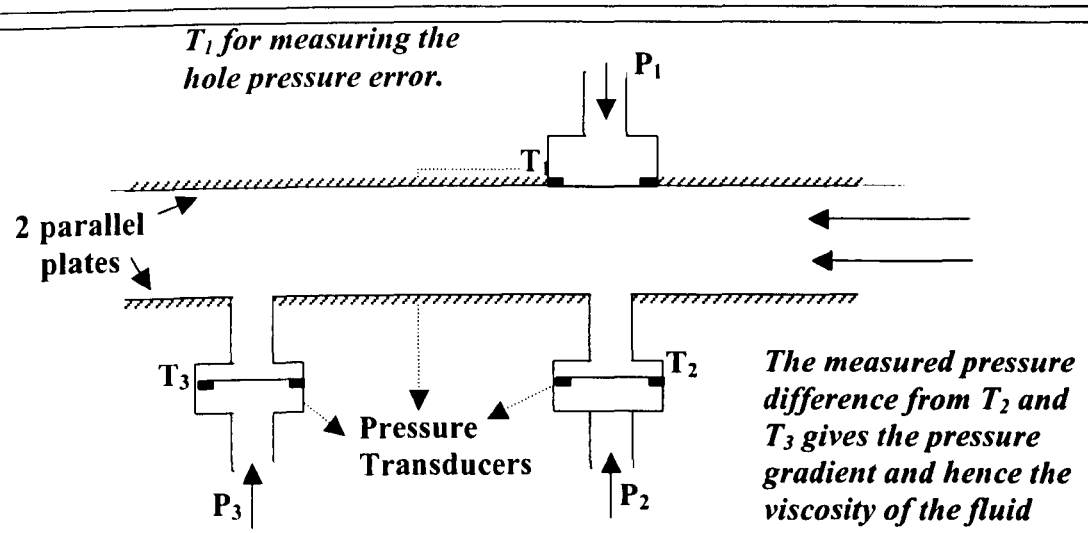

Figure 2.3B(b): Schematic diagram of a slit viscometer [Who 92].

Other types of rheological measurements include mechanical testing (e.g. tensile, bending and compression) where the normal stresses of the fluid are calculated, dynamic (oscillation) testing, flow visualisation methods and wave propagation techniques. It is outside the scope of this thesis to describe these techniques. A detailed study given by Whorlow [Who 92] can be found. In this thesis, two types of rheological testing are used to determine the rheological properties of semisolid slurries. The first testing involves the use of a Searle-type rotational viscometer while the second type involves the use of rapid compression testing. The experimental procedures and the limitations of the equipments will be described in Chapter 5. We shall now turn to the origin of semisolid slurries, their rheological behaviour and the various mathematical models proposed by other workers.

CHAPTER 3

Solidification Processes

It was mentioned in the introduction that semisolid processing is the process of forming alloys in the semisolid state. In the semisolid region (mushy region), the alloys consist of solid spheroidal particles suspended in a liquid metal matrix. In this section, a brief introduction to solidification, the morphology of the primary phases formed during solidification and the evolution of this phase to that found in semisolid processing is given. For a more complete understanding of solidification processes, the reader should refer to Kurz [Kur 92] and Flemings [Fle 74].

3.1 General Solidification

Solidification is one of the most common steps in the materials processing of metal alloys. It is a complex process where phenomena such as crystallisation, ripening, inclusions and interdendritic flow occur. The microstructure and properties of solidified alloys are strongly dependent on the alloy composition and the solidification conditions. Alloys consist of a matrix metal (e.g. iron, aluminium, copper or tin) to which other elements (solutes) are added. These alloying elements are normally soluble in the liquid and solid metal but usually in different concentrations. Commercial alloys are usually modelled as binary alloys of the major alloying elements using a binary phase diagram.

Figure 3.1A shows part of a binary phase diagram. The top curve is called the liquidus line. At temperatures above this curve, the base metal and its alloying elements are completely soluble as a liquid phase. The bottom curve is called the solidus line. At temperatures below this line, the two components are present as a single solid crystalline phase (i.e. solid solution). The ratio, k, between the solidus and liquidus composition at a fixed temperature is called the equilibrium partition coefficient.

Figure 3.1A shows a case where the liquidus and solidus temperature falls with increasing alloying concentrations (i.e. k<1).

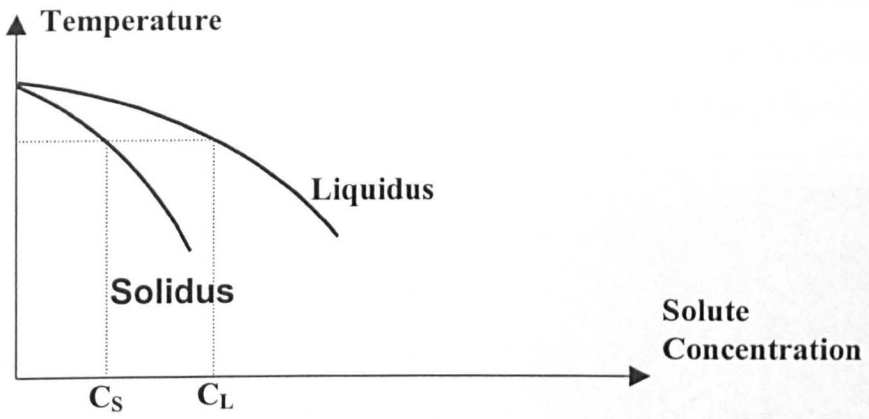

Figure 3.1A. A typical binary alloy phase diagram. Equilibrium partition coefficient is the ration between the solidus and liquidus composition at a fixed temperature.

The microstructure of alloys after solidification can be divided roughly into four types (Figure 3.1B). The α phase formed in the 'α + L' region (or the semi-solid region) in the phase diagram is called the primary phase particles (Figure3.1B, 'Region 3'). Semisolid processing is carried out in Region 3 and it is in this region that the work conducted here is done.

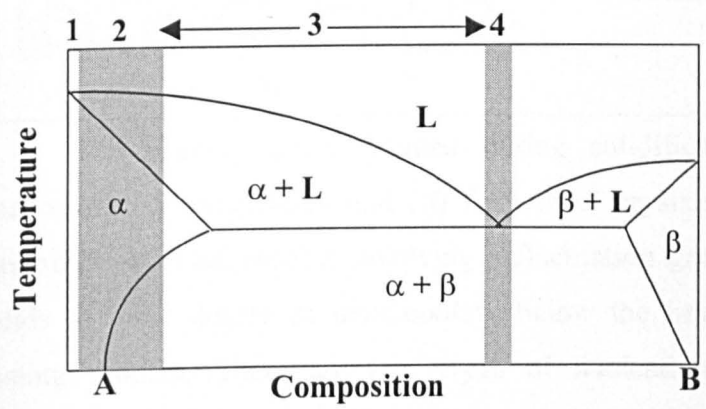

Figure 3.1B. Phase diagram of a binary alloy AB, with principal alloy types as a function of composition. (1) pure metals; (2) solid-solution alloys; (3) hypoeutectic alloys; (4) eutectic alloys. [Kur 92]

Most metal alloys of commercial importance solidify dendritically either with a columnar (Figure 3.1C) or equiaxed structure (Figure 3.1D). These tree-like shapes

are observed in the regions of constitutional supercooling or when solidification occurs during growth from the melt with a negative temperature gradient in the direction of growth. In the case of very dilute alloys where the equilibrium freezing range of the alloy (or the temperature difference between the liquidus and solidus lines) are very small, the metal alloy takes on a cellular structure, Figure 3.1E.

C

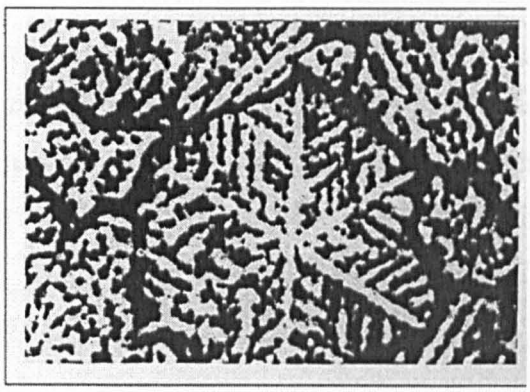

D

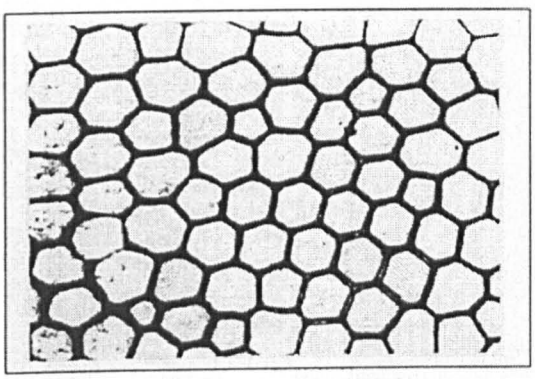

E

Solidification of metal alloys into various structures:
Figure 3.1C: Columnar dendrites
Figure 3.1D: Equiaxed dendrites
Figure 3.1E: Cellular structure

The primary phase formed during solidification comprises of 2 basic phenomena: (i) Nucleation and (ii) Growth of crystals from melt. Nucleation is a thermally activated process involving a fluctuation growth in the size of cluster of solids at some degree of undercooling below the liquidus temperature during the casting process. There are two types of nucleation: (a) Homogenous and (b) Heterogeneous nucleation.

Homogenous nucleation is the occurrence of nucleation that transforms an initially homogenous system (consisting only of atoms in the liquid state) into a heterogeneous system (solid crystal plus liquid), without the involvement of any impurity atoms or other surface sites in contact with the liquid melt. In practice, this is observed in very pure samples and is of little interest in normal casting processes, especially when a large undercooling of the melt is required to promote nucleation.

When a melt contains solid particles, or is in contact with foreign impurities such as inclusions, oxide films or the crucible walls, crystallisation from the impurity bodies occurs (usually at a few degrees or less undercooling temperature). This is called heterogeneous nucleation and is common in the commercial casting of metal alloys.

Growth of crystals from alloy melts may occur in a constrained manner (e.g. from a mould or chill wall) where the crystal growth is opposite to the heat flow (giving rise to directional or columnar dendrites) or in an unconstrained manner (growth within the liquid) where the crystal growth is in the same direction as the heat flow (giving rise to equiaxed dendrites). Both growth conditions are shown schematically in Figure 3.1F.

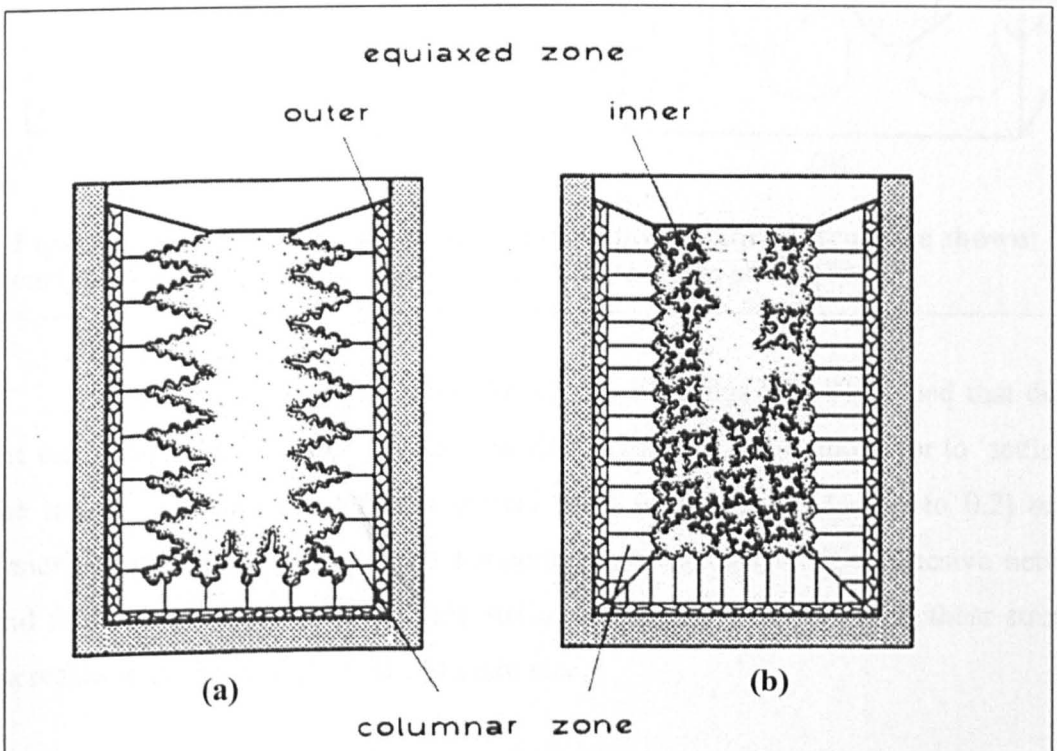

Figure 3.1F:Growth of crystals from alloy melts in:(a) Constrained manner, giving rise to columnar dendrites and (b) unconstrained manner, giving rise to equiaxed dendrites. [Kur 92]

In both equiaxed and columnar structures, the dendrites evolve greatly during solidification as a result of ripening due to surface energy, shown schematically in Figure 3.1G [Fle 91]. The structure becomes gradually coarser during solidification as a result of the remelting of dendrite arms of smaller radius.

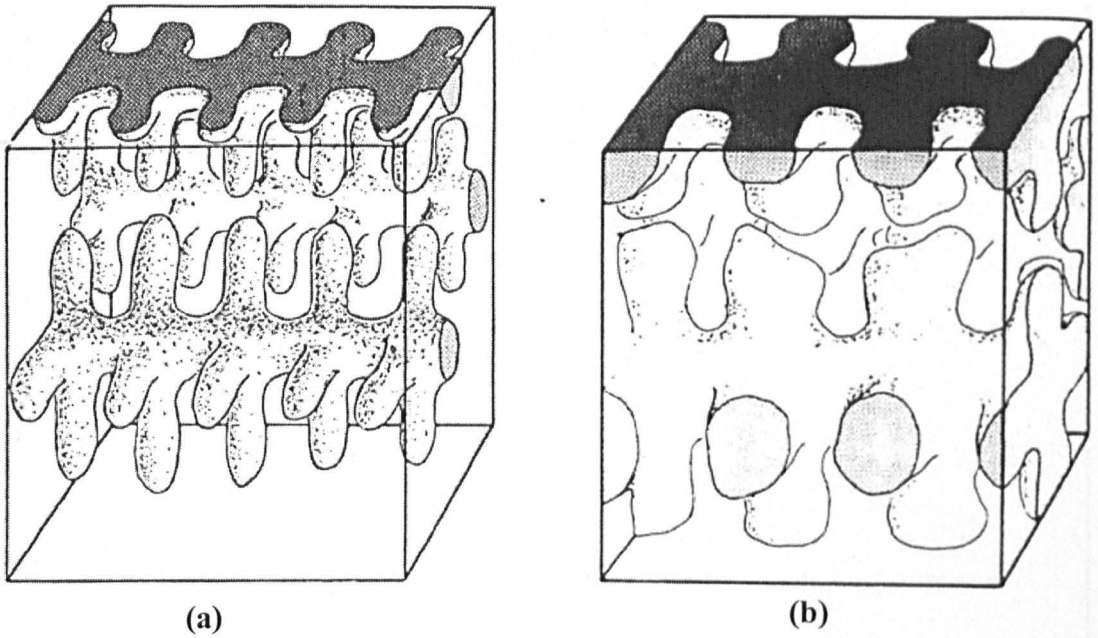

Figure 3.1G: Schematic illustration of ripening. Dendrite structure shown: (a) early in solidification and (b) at about 50% fraction solid. [Fle 91]

In his review paper on semisolid alloys, Flemings [Fle 91] stated that during the early stages of solidification, the dendritic grains are free to move (or to 'settle') in the liquid melt until it reaches a critical local solid fraction (~ 0.1 to 0.2) or the dendritic coherency point. At this temperature, the grains form a cohesive network and the melt starts to develop some strength from the network. This shear strength increases with increasing strain and grain size.

3.1.1 Solidification under shear

Spencer et al [Spe 72] carried out similar tests to those done previously by Metz and Flemings [Met 70] except that his sample was sheared during solidification. He obtained similar results where measurable strength began to develop at a fraction solid of about 0.2. (Figure 3.1H). Using a Couette viscometer, at a given strain rate, Spencer found that the stress increases initially with displacement to a maximum value after which it falls to a low value before increasing again with increasing fraction solid. He also found that at fraction solid up to about 0.9, the grains are

primarily deformed by grain boundary sliding with some dendrite distortion (Figure 3.1I).

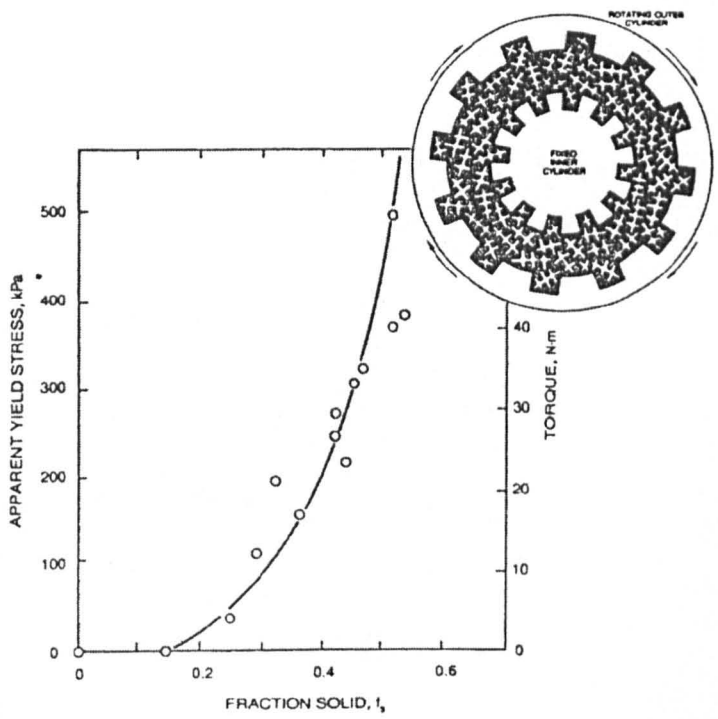

Figure 3.1H: Isothermal shear strength of semisolid dendritic Sn15%Pb alloy [Spe 72]

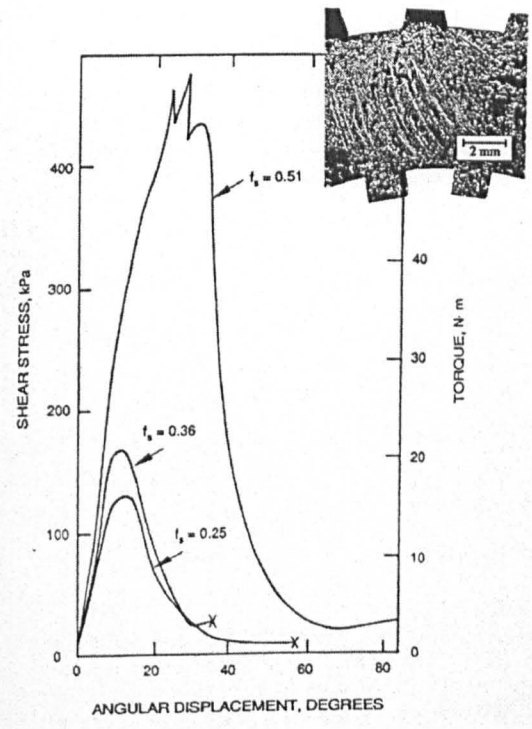

Figure 3.1I: Isothermal shear test results of semisolid Sn15%Pb alloy. Photograph at upper right shows actual specimen macrostructure [Spe 72].

The increase of stress with initial strain is probably because strain increases the number of contacts (or 'welds') between the particles. At sufficiently high strain, continuous fissures open, so the stress falls to a low level. The fissures become filled with liquid except at very high fractions solid [Fle 91]]. During the course of solidification, the liquid phase becomes more enriched and the composition of the liquid moves towards the eutectic composition and the remaining liquid solidifies in the eutectic morphology towards the end of the solidification. A more detailed study into solidification under shear will be discussed later in this chapter (see Section 3.3)

3.2 Determination of Fraction Solid

Usually, solidification occurs under non-equilibrium conditions but it can be assumed that at the liquid-solid interface, with negligible undercooling in front of the dendrite tips or between the dendrite arms, equilibrium is considered to be present [Fle 74, 91]. Figure 3.2A(a) describe a simple model of solidification. For a given temperature distribution (Figure 3.2A,b), the liquid composition at any location within the solid-liquid region (or the mushy region) is defined by the liquidus line of the alloy system (Figure 3.2A,c).

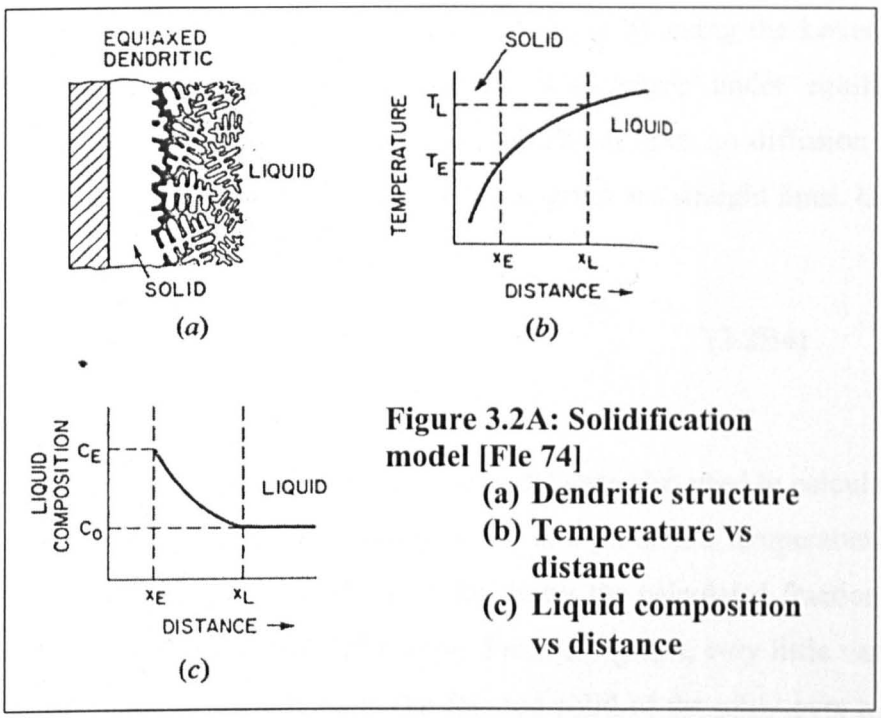

Figure 3.2A: Solidification model [Fle 74]
(a) Dendritic structure
(b) Temperature vs distance
(c) Liquid composition vs distance

Assuming (1) no solid diffusion or ripening effect, (2) Complete composition uniformity of the liquid remaining at any instant, and (3) Fluid flow adequate only to feed solidification shrinkage, the composition of the liquid that forms as a function of the fraction liquid, F_L, is given by the Scheil Equation of:

$$C_L = C_O (F_L)^{k-1} \qquad (3.2A1)$$

where C_L is the liquid composition

k is the equilibrium partition coefficient (as before)

C_O is the initial alloy composition

Since temperature, T, in the mushy region and C_L are related by the equilibrium liquidus line, Equation 3.2A1 can also be written as:

$$F_L = [(T_M\text{-}T)/(T_M\text{-}T_L)]^{(-1/1-k)} \qquad (3.2B2)$$

where T_M and T_L are the melting point of the pure solvent and the liquidus temperature of the alloy of the initial composition, C_O, respectively.

It is common in most literature to state the fraction solidified (f_S) during solidification process. Hence, from Equation 3.2B2, f_S is simply given as:

$$F_S = 1 - F_L \qquad (3.2B3)$$

Another method of calculating the fraction solid is by using the Lever Rule. This method assumes complete diffusion in the solid phase under equilibrium solidification (as opposed to the Scheil Equation which assumes no diffusion in the solid phase) and that the liquidus lines in the phase diagram are straight lines. Using a mass balance method at the specific temperature, T,

$$F_S = \frac{1}{1-k}\left(\frac{T_L - T}{T_M - T}\right) \qquad (3.2B4)$$

Computation methods using thermodynamic data are also used to calculate the various fractions solid of a given alloy composition at a particular temperature. One such software package is MTDATA. Figure 3.2B shows the calculated fraction solid using the above 3 methods for a Sn15%Pb alloy. From the graph, very little variation exists between the different predictions in the fraction solid of the alloy over a range of temperatures (i.e. fraction solid). However, the predictions of the fraction solid during solidification do differ at high cooling rates (~ 5 Ks^{-1})[Fle 91]. At these high cooling rates, 'dendrite tip undercooling' as a result of effects of tip curvatures and solute rejection has a significant effect on the predicted fraction solid. Tzimas and Zavaliangos [Tzi 00a] conducted an evaluation into the accuracy of using thermodynamic data. The authors concluded that such a technique can be used to establish accurately the evolution of the solid content during melting and also allows for the evaluation of the sensitivity of the volume fraction of solid to any slight temperature variations.

Figure 3.2B: Calculation of fraction solid vs. temperature for Sn15%Pb

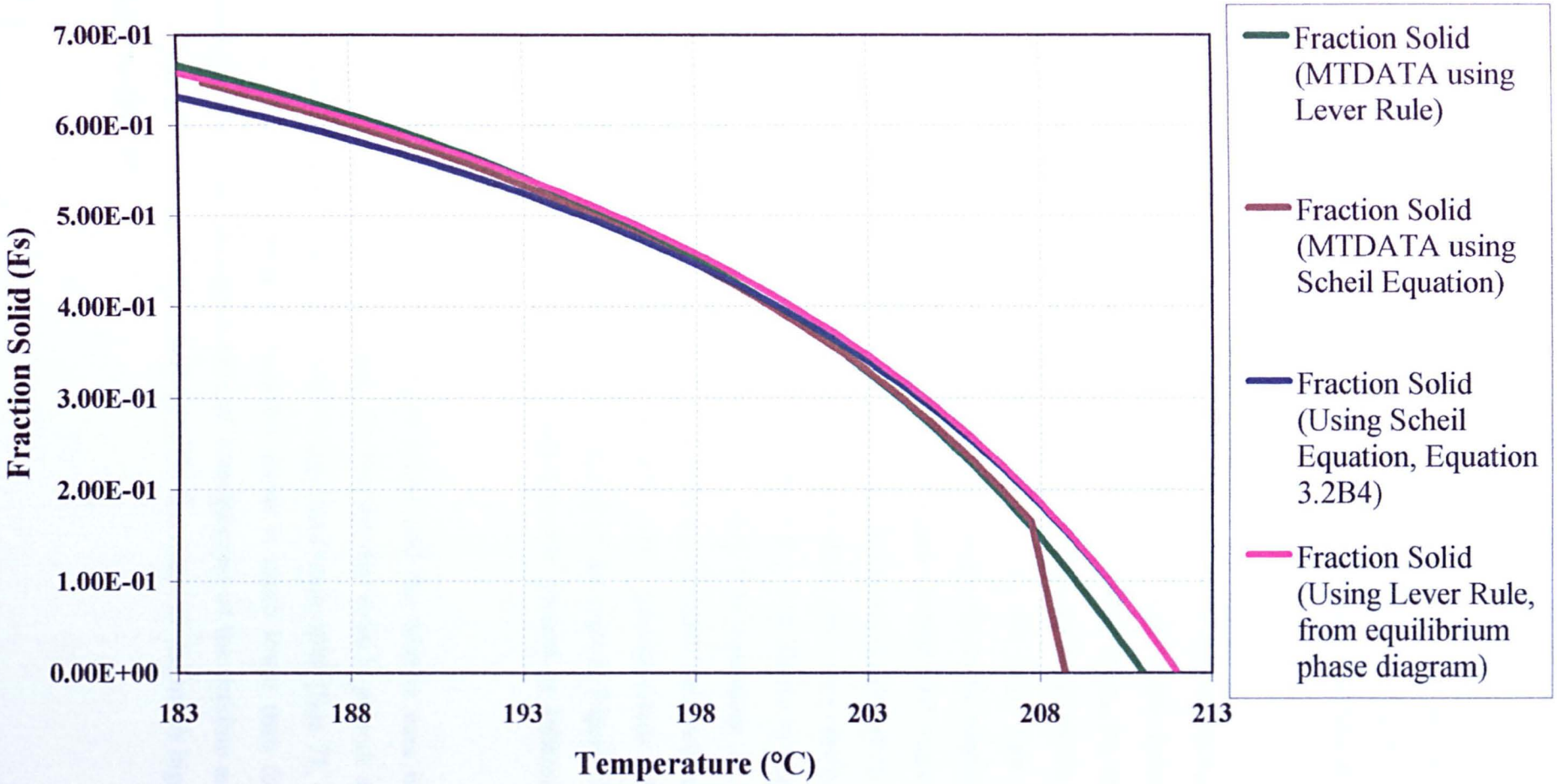

3.3 Solidification under vigorous agitation

When a solidifying alloy is stirred, the morphology of the crystal structure is changed from a columnar dendritic structure to a finer equiaxed grain structure. In order to achieve a finer equiaxed grain structure, methods like mechanical or electromagnetic agitation can be used.

In 1971, during the course of his doctoral thesis in measuring the maximum stresses needed to overcome the strength of an almost solid Sn15%Pb alloy, Spencer [Spe 71] discovered the basis for semisolid processing. Instead of shearing the alloy after partial solidification to the required faction solid, he began the shear above the liquidus line of the alloy composition whilst slowly cooling the alloy into the solidification range (to the same fraction solid) before measuring the stress needed to overcome the strength of the alloy. The results he obtained showed that vigorous agitation of a metal alloy postpones the formation of a continuous solid network in the alloy to a much higher fraction solid. The shear stress increased only very slowly as temperature was decreased below the liquidus (up to about $f_S = 0.4$), shown in Figure 3.3A. The stress measured at any specific fraction solid (corresponding to the temperature) was orders of magnitude less than that when the samples were cooled to the given temperature before shearing commences. The microstructure of a continuously cooled alloy slurry under agitation is shown in the inset of Figure3.3A. Instead of a skeletal dendritic structure, the grains are now present as spheroidal grains.

The material is behaving as a liquid-like slurry and the relative ease with which shearing can be performed results from the fact that the solid is present as a suspension of small rounded grains which tend to slide past each other [Spe 71, 72, Fle 74, 91]. The resistance to shear for rounded grains is much lower than for a dendritic structure. With their tree-like structures, entanglement of the dendrite arms or branches impedes ease of flow. This is likely to be the cause of the much higher measured stresses observed.

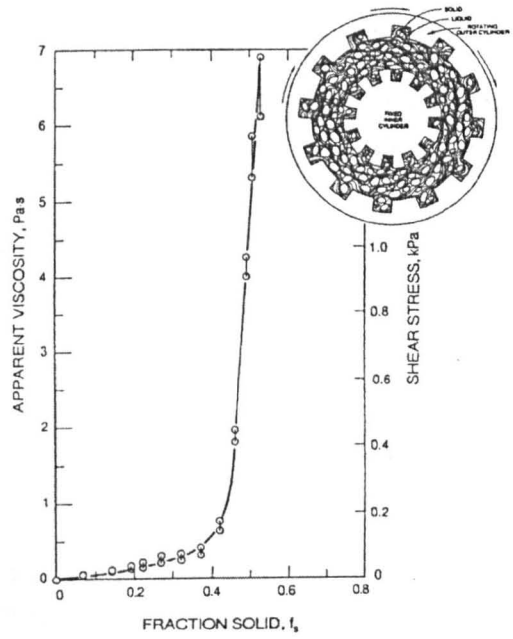

Figure 3.3A: Shear stress and viscosity behaviour of Sn15%Pb alloy continuously cooled under vigorous agitation. Schematic diagram (insert) shows the particle shape. [Fle 91]

During solidification, single dendrite grain crystals are formed. Upon agitation, the shear forces imposed cause the fragmentation of the secondary dendrite arms. Experimental work by Spencer [Spe 72] showed dendritic fragmentation in the annular space between the cylinders of his Couette Viscometer (see inset in Figure 3.1I). Flemings [Fle 91] has listed a number of possible mechanism whereby fragmentation of dendrites can occur:

(1) Dendrite arms break off at the roots due to the imposed shear forces

(2) Dendrite arms re-melt off at their roots as a result of ripening. The fluid flow assists the remelting in several ways:

   a. Accelerated diffusion of solute in the liquid

   b. Produces stresses at the dendrite root thus aiding remelting

   c. Introduces localised high solute content in the solid at the dendrite root thus lowering the melting point

(3) Dendrite arms bend under flow stresses and the plastic strain is accommodated by dislocations.

The evolution of a dendritic structure to a spheroidal structure can be shown schematically as in Figure 3.3B.

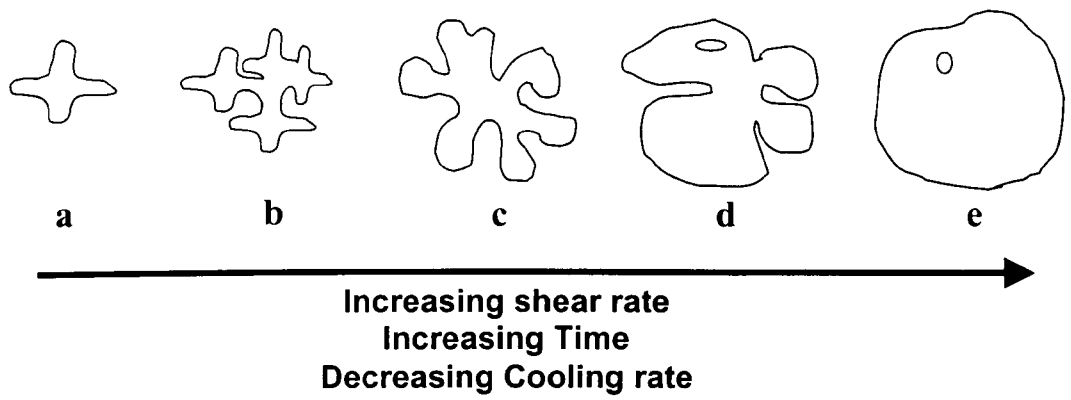

Figure 3.3B
Schematic illustration of evolution of structure during solidification with vigorous agitation: (a) Initial dendritic fragment (b) dendritic growth (c) rosette (d) spheroid [Fle 91]

With continuing shear and time during solidification, the dendrite changes from an equiaxed structure to that of a rosette-like shape structure. This is a result of ripening, shear and abrasion with other grains [Fle 91, Kir 94, Kok 99]. Spheroidisation of the rosette-like structure proceeds through coarsening with isothermal holding, usually with a small amount of entrapped liquid within the spheroids. The amount of this entrapped liquid depends on the former secondary arm spacing.

3.4 Agglomeration of particles

During stirring of semi-solid slurries, the spheroidal particles often collide into each other. Such collisions may result in clustering of the particles, forming aggregates. Aggregation of solid suspensions occurs with both interacting and non-interacting particles. To differentiate between these types, agglomeration will be referred to the aggregation of interacting particles while flocculation will be used for the aggregation of non-interacting particles. For semisolid particles, agglomerates form when two or more particles collide. If the particles stay in contact (i.e. along the grain boundary) long enough, a bond (or 'weld') will form. Under favourable orientation, a 'neck' will form from the bond. Agglomeration can occur between individual particles, between particles and agglomerates and between agglomerates. Given enough time, grain boundary migration or grain rotation to a more favourable orientation, leads to the agglomerates forming a single large grain. This grain will now undergo spheroidisation. Between the agglomerates in a cluster, a certain amount of liquid is entrapped (Figure 3.4A, [Qua 96a]).

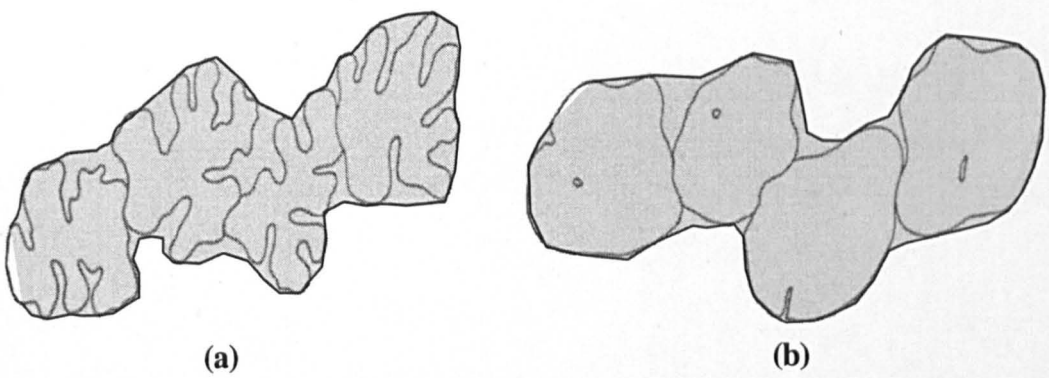

Figure 3.4A: Agglomerates formed by collision and (partial) coalescence: (a) rosettes and (b) globules. An estimate of the effective fraction solid is shaded which takes into account the amount of liquid entrapped within the particles

These fractions of liquid entrapped between the agglomerates do not contribute to fluid flow but move together with the agglomerates as a whole. Hence, the effective fraction solid is somewhat larger than the actual fraction of solid as calculated from the phase diagram. B. Niroumand et al [Nir 00] showed this effect by doing a series of serial sections on Aluminium Copper (Al-Cu) alloy.

However, there is another process occurring during stirring. De-agglomeration is the reverse process of agglomeration. It is the breaking down of an agglomerate into smaller agglomerates or constituent particles hence reducing the particle size and impeding coarsening mechanisms. Both agglomeration and de-agglomeration are competing processes. Hence, there will be a dynamic equilibrium between these two processes. The average size of a cluster or agglomerate therefore depends largely on the fraction solidified, the initial primary particle size, the shear rate and the duration of shearing [Jab 92].

3.4.1 Coarsening of particles

Coarsening is a process in which the particles become larger and fewer. This is due to competitive growth driven along by the high surface energies of these incoherent particles. The smaller of particles have higher free energies per atom than the larger ones, because of their higher ratios of surface to volume. The concentration of solute in the liquid is higher near the smaller particles than the larger ones. This sets up a diffusion flux causing the small particles to dissolve and disappear eventually whilst the larger particles grow larger.

Coarsening can be described by a power law equation in terms of a characteristic microstructural dimension versus the coarsening. For example, the average particle size D after a coarsening time, t, is given by the following equation:

$$D^n - D^n_o = kt \qquad (3.4.1A)$$

where D_o is the initial average grain size,

n is the coarsening exponent

k is the rate constant for coarsening (this is dependent on shear rate and fraction solid [San 94a, Ann 95]).

Experimental values for 'n' are in the range of ~2.3 to 4 [Doh 84, Mol 87, Kat 91, Aka 91, Ann 95]. More recently, Liu and Liu [Liu 98] have predicted the coarsening exponent using Monte-Carlo simulation to be 3. This was the value used in the classical coarsening approach.

However, there are certain discrepancies to the effect of fraction solid on coarsening rates. Standard coarsening theory for spherical particles in a solid or liquid matrix [Voo 84, Jay 89, Cha 86, Dav 80] predicts an acceleration of coarsening with increasing fraction solid and this is supported by experimental results [Kan 82, Har 88, Whi 99]. Other experimental work [Ann 95, Yan 92] shows the opposite effect. One mechanism has been given for this difference by Annavarpu et al [Ann 95]. The authors noted that at higher fraction solid, there are larger amounts of solute to move across the solid-liquid interface at lower temperature (as a result of higher concentration of solute in the liquid that has to be transferred), hence reducing the coarsening rate (Standard theory). Annavarpu et al [Ann 95] noted that this effect is more than compensated for by the decrease in the diffusion distance due to the closer spaced particles at higher fraction solid.

The coarsening of the spheroids with time in agitated semisolid slurries is caused by diffusion controlled Ostwald Ripening (OR) and Coalescence Ripening (CR).

3.4.2 Ostwald Ripening (OR)

Ostwald ripening is the process of coarsening of spherical particles by bulk diffusion. As a result, smaller particles (with large curvature) disappear while larger particles with small curvature grow. OR can be enhanced by stirring due to accelerated solute diffusion. OR is described by the LSW theory of Lifshitz and Slyosov [Lif 61] and Wagner [Wag 61] in the limit of infinite particle separation in a surrounding matrix with no convection. In the semisolid state, this theory is only valid when the fraction of the coarsening phase is approaching zero and under isothermal conditions. In this case, the coarsening index, n, in Equation 3.4.1A is equal to 3.

3.4.3 Coalescence Ripening (CR)

CR occurs when two or more particles collide and become interconnected by forming solid necks on the grain boundary. The particles spheroidize by material transport in the neck region [Tak 84, Wan 90c, 92a]. These workers have shown that

in the presence of stirring where liquid convection and grain rotation would occur, grain sizes increase as stirring time increases.

However, experimental work by Yang and Tsao [Yan 92] showed that grain sizes only increase after exceeding a critical stirring time. In their work on Al-Si alloy, they found this critical time to be 600 seconds. Below this the grain sizes decrease initially before increasing again. The authors proposed that below the critical time, dendritic fragmentation is occurring resulting in smaller grain size with stirring time after which (above the critical stirring time) coarsening would be the dominant mechanism.

Both OR and CR are thought to operate independently and additively [Tak 84, Wan 90c, San 94a] and can be discriminated by the broader particle size distribution predicted after coarsening by coalescence ripening (Figure 3.4.3A).

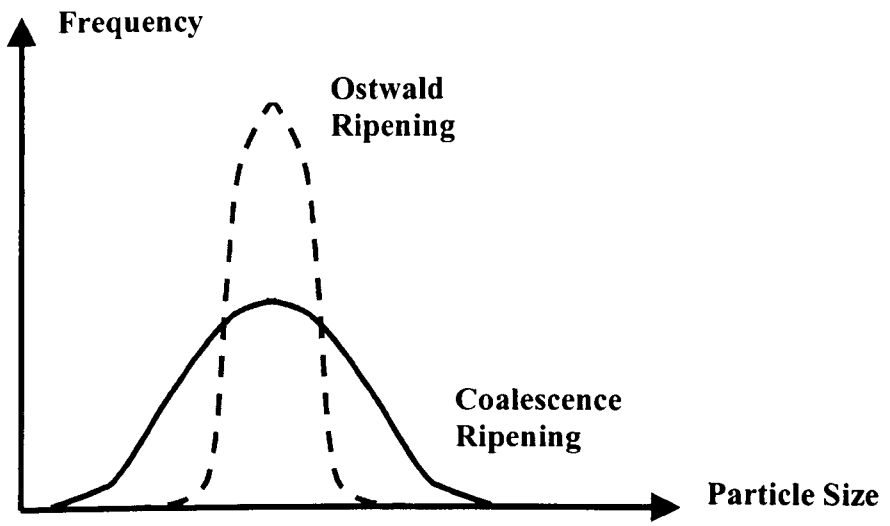

Figure 3.4.3A Particle size distribution calculated on the basis of Coalescence Ripening and Ostwald Ripening [Tak 84].

CHAPTER 4
Rheology of Semisolid Alloys

In the previous chapter, a brief discussion of the formation of spheroidal microstructures was given. It is this microstructure that forms the basis of semisolid processing. The rheological behaviour of semisolid alloys has been investigated extensively by various workers. Extracting the rheological parameters from these investigations has led to many proposed mathematical models to quantify the behaviour of semisolid alloys. P.A. Joly [Jol 74, 76] was the first to do an extensive investigation into the rheological properties of a semisolid Sn15%Pb alloy following the initial discovery by Spencer et al [Spe 72]. Other investigations by various workers have confirmed the general behaviour discovered by Joly or have extended the studies to other alloys that are of commercial importance. However, certain discrepancies still exist in understanding the rheological behaviour of a semisolid alloy slurry. A slurry is defined as a liquid continuum having in suspension a large number of small solid particles which have formed by solidification from the liquidus state [Lop 92]. In this chapter, discussion will be based on (1) rheological results and (2) mathematical models.

4.1 Rheological Behaviour

Investigations of the rheological behaviour of semisolid alloys can be divided into four parts:

(1) Viscosity measurements during continuous cooling
(2) Steady state viscosity measurements over time under isothermal shearing
(3) Thixotropic behaviour
(4) Transient behaviour under changing shear rate

(1), (2) and (3) have been extensively investigated by various workers over the past 30 years. They are usually known as the steady state behaviour. The fourth part (i.e. the transient behaviour) is the current challenge in the rheology of semisolid alloys slurries. This transient behaviour is used to characterise the structural evolution kinetics (i.e. agglomeration and de-agglomeration processes). Furthermore, injection into a die in semisolid processing in industry occurs in about a second, so the

behaviour of semisolid alloy slurries during this transient period is important. Nevertheless, certain rheological parameters extracted from steady state experiments provide an understanding of the flow behaviour of such alloys.

One important point to note is that the rheological behaviour is different for a partially solidified semisolid material and a partially re-melted semisolid material. Modigell et al [Mod 00] have shown that a partially re-melted material tends to have finer grain particles (therefore stronger particle bonds) than a partially solidified material so a higher viscosity is observed at a given fraction solid. Tzimas and Zavaliangos [Tzi 00a] conducted a modified quenching experiment to explain the microstructures arising from partially solidified and partially re-melted alloys. Partially re-melted alloys are usually tested by parallel plate compression while partially solidified alloys are studied in rotating viscometry experiments. An evaluation by Modigell of the different techniques showed that a direct relation between these two techniques could not be quantitatively made although, qualitatively, their behaviours are similar (Figure 4.1A). In the following sections, the rheological behaviour observed in semisolid alloy slurries using a rotational viscometer is discussed.

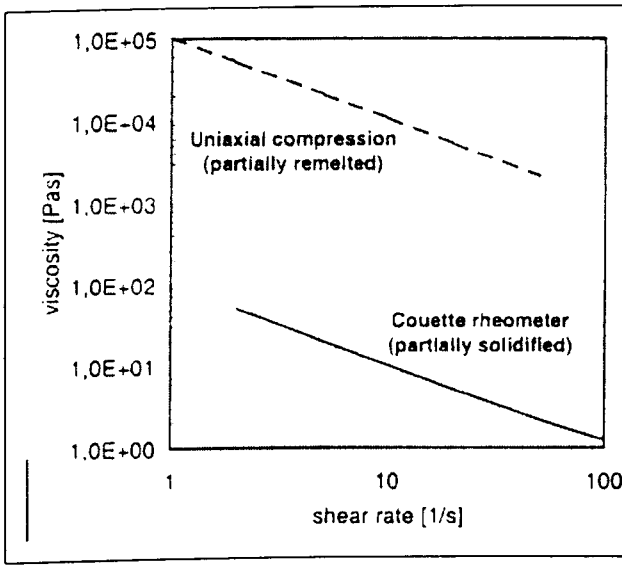

Figure 4.1A. Partially solidified and partially re-melted semisolid slurries showing similar behaviour. [Mod 00]

4.1.1 Effect of viscosity during continuous cooling

As a first measure of the rheological behaviour of semisolid materials, the apparent viscosity during continuous cooling into the solidification zone is measured. The effect of shear rate and cooling rate on the viscosities can thus be studied. Figure

4.1.1A and 4.1.1B show a typical response in such an experiment. Figure 4.1.1A shows a typical response of an unstirred alloy during solidification. The viscosity increases sharply upon reaching a fraction solid of 0.2 [Met 70, Spe 72]. This behaviour was also shown by the work of Guochai et al [Guo 92] on various aluminium alloys. However, if the alloy is continuously stirred during the solidification process, the viscosity increases sharply after a fraction solid of ~0.35 (see Figure 4.1.1B). This difference is due to the spheroidal microstructures formed using the latter technique.

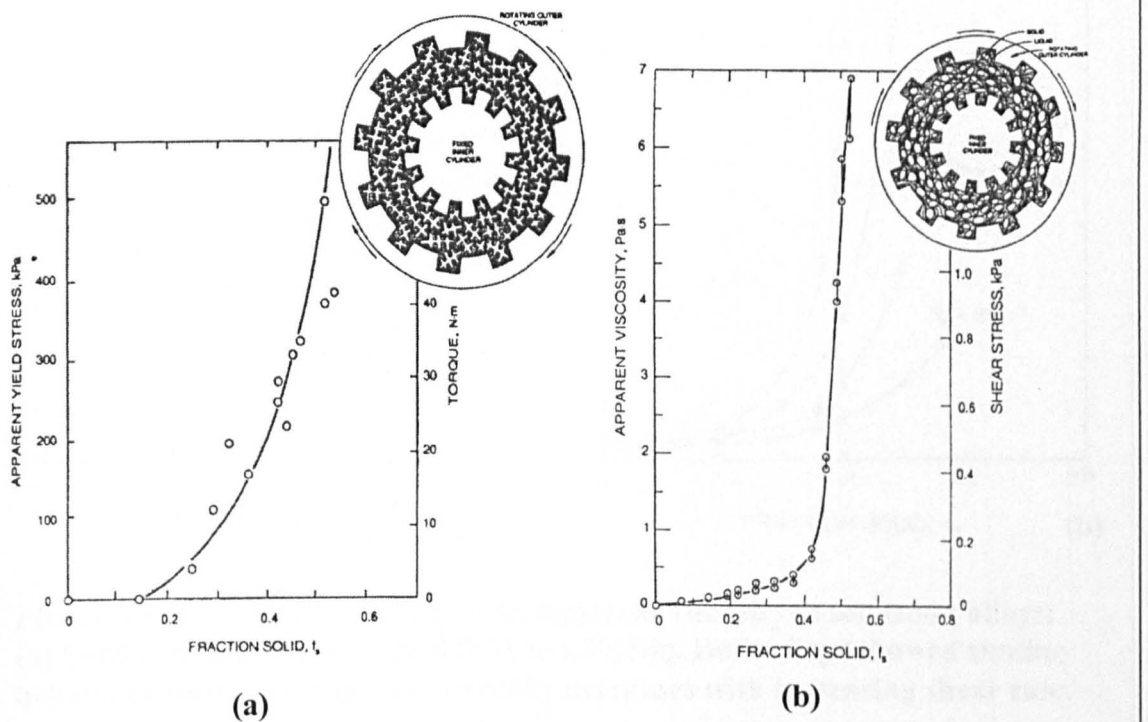

Figure 4.1.1A and Figure 4.1.1B show the behaviour for (a) a dendritic alloy and (b) spheroidal alloy. Spheroids retard the sharp increase in stresses to a fraction solid of 0.35

The point at which the viscosity increases sharply is known as the coherency point. Flemings [Fle 91] remarked that this coherency point shifts to higher fraction solids when the grains are smaller or when the stirring rate is higher. The sharp increase in viscosity is due to the alloy achieving its maximum packing fraction with decreasing temperature as the alloy goes through the solidification process. Figure

4.1.1C [Fle 91] shows that with increasing shear rate, the viscosity is lower at a given fraction solid.

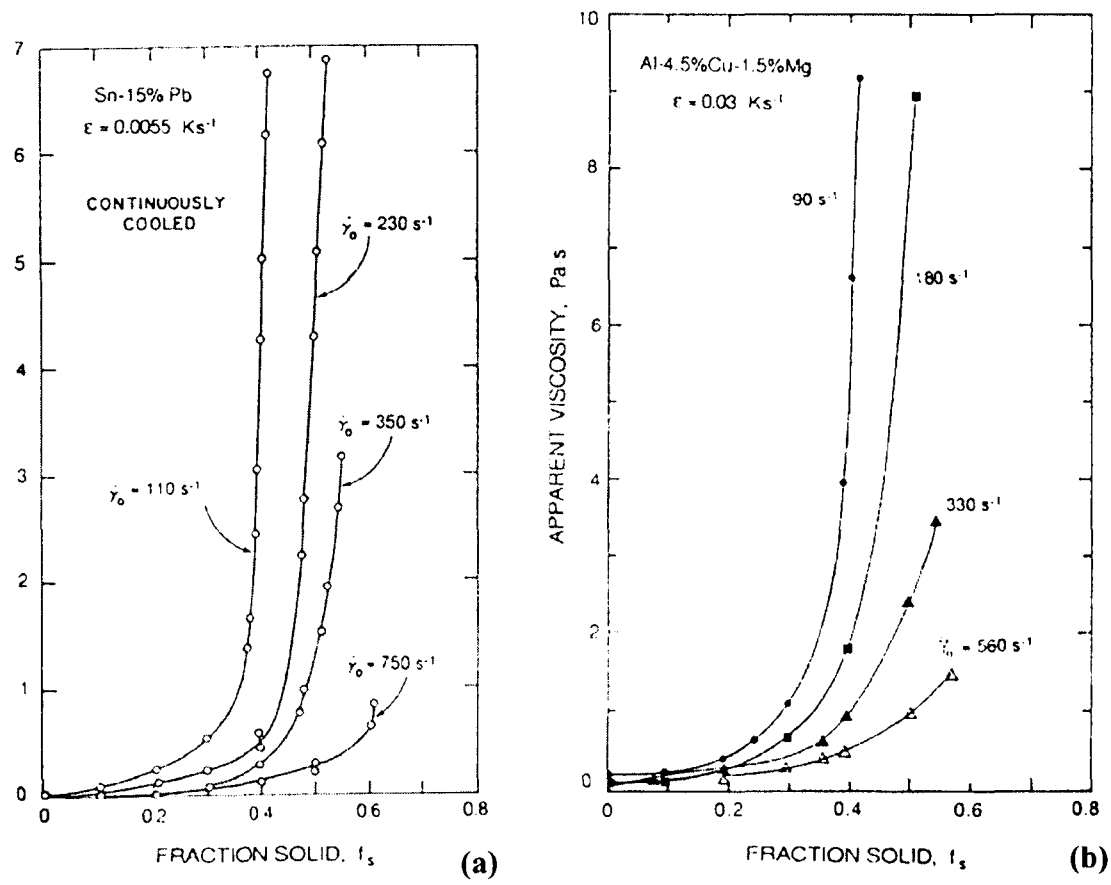

Figure 4.1.1C: Effect of shear rate on apparent viscosity of semisolid alloys; (a) Sn15%Pb alloy and (b) Al-4.5%Cu-1.5%Mg. Both alloys showed similar behaviour where the apparent viscosity decreases with increasing shear rate.

Such experiments also showed that with lower cooling rates and higher shear rates during cooling, the viscosity decreases (Figure 4.1.1D). Both higher shear rate and lower cooling rate result in more spheroidal particles, so the particles are able to move more easily past one another resulting in the lower viscosity recorded [Fle 91].

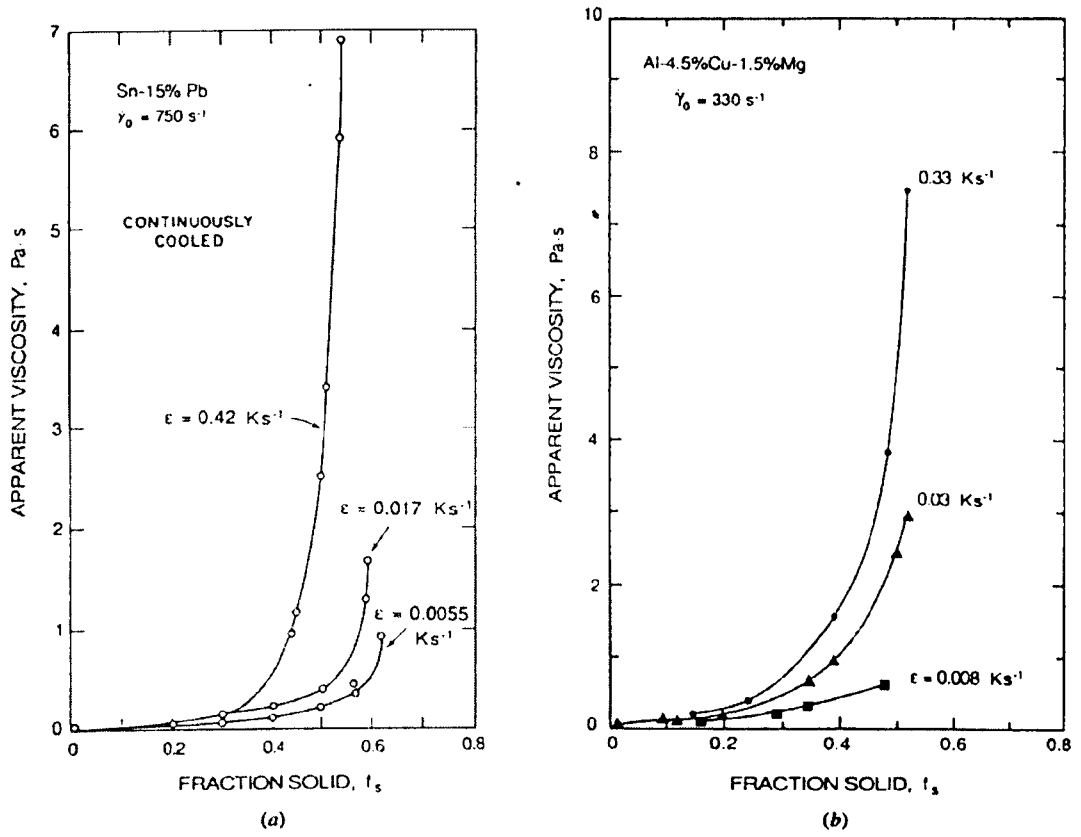

Figure 4.1.1D. Effect of cooling rate on apparent viscosity of semisolid alloys: (a) Sn-15%Pb and (b) Al-4.5%Cu-1.5%Mg. Both alloys showed a decreasing apparent viscosity with decreasing cooling rates. [Fle 91]

Experiments have been done by various workers on different alloy systems. They are:

(1) Sn15%Pb [Jol 74, 76, Wan 90a, 90b, Tur 91, Mod 99]

(2) Al-4.5%Cu1.5%Mg [Kat 91, 92b]

(3) Al-6.5%Si [Moo 90, 91, Ito 92], Al-7%Si0.3Mg [Lou 92, Bra 01],

(4) Al-0.35%Si0.2%Mg [Hor 92, Qua 94, 96a, 96b, Yan 97]

(5) Magnesium alloys [Gho 94]

(6) Al-18%Si [Hor 92, Qua 94, 96a], Al-25%Si [Fle 92]

Joly and Mehrabian [Jol 76] found that the size of the solid particles decreases with increasing cooling rate and increasing shear rate although this was observable only at the low cooling rates (**Figure 4.1.1E**). Photomicrographs of the structure showed that there is less entrapped liquid (hence decrease in the effective fraction solid) with increasing shear rate.

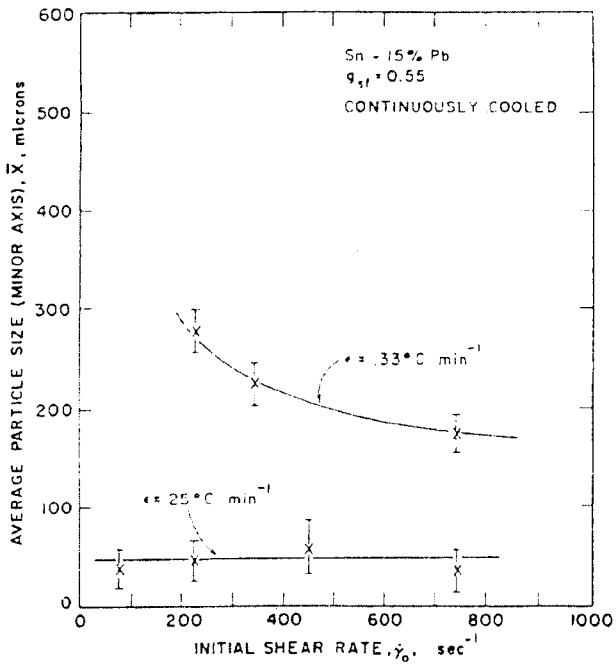

Figure 4.1.1E. Decrease in particle size with increasing shear rate (more apparent at low cooling rates) for Sn-15%Pb alloy.[Jol 76]

The work of Ramati et al [Ram 78] supported the results by Joly and Mehrabian [Jol 76]. The only discrepancy found was that the authors observed a decrease in the size distribution of the primary solid particles with increasing cooling rate, contrary to Joly and Mehrabian's observation of decreasing size distribution with decreasing cooling rate. However, the cooling rates employed by Joly and Mehhrabian are much lower than that of Ramati et al (Joly: 0.005 to 0.55 °C/min, Ramati: 5.57 °C/min). Both Joly and Ramati observed that the effect of shear rate on particle size and distribution is more pronounced at low cooling rates. This may therefore explain the difference in the results obtained between them. Wang Nan [Wan 90b] proposed that the decrease of particle size is due to the inhibition of agglomeration of the solid particles caused by increasing shear rates and decreasing cooling rates. This proposal was supported by Hirai [Hir 93], Yang [Yan 92] and Quaak [Qua 96b], where Ostwald ripening and coarsening of the particles are affected by the shear rates and cooling rates. Experimental results by Jabrane [Jab 92] showed that the number of particles per agglomerate decreases with time and shear rate supporting the work of Kattamis et al [Kat 91, 92b] who attribute the decrease of particle size to the long residence time in the semisolid region where structural breakdown of the agglomerate particles is more complete.

Continuous cooling experiments provide one with the understanding of semisolid alloy slurries during solidification. It is however not adequate enough to fully describe the rheological behaviour of semisolid slurries [Kir 94, Sue 96]

4.1.2 Steady state viscosity under isothermal shearing

In this type of experiment, the semisolid slurry is sheared and held isothermally at the specified shear rate and fraction solid until an effective steady state viscosity is reached. At this state, shear rate is either increased or decreased and the steady state viscosity at the new shear rate is recorded again. In the first part, workers have showed a decrease of viscosity with time [Lou 92, Moon 91, Kat 91,92a, 92b, Gho 94]. Furthermore, experiments with increasing isothermal holding times have shown that the particles become more spheroidal [Jol 76, Qua 94, 96a, 96b, Hel 96, Ryo 96, Yan 97]. After attaining its steady state viscosity, following Van Wazer's proposal for shear thinning experiments, increasing the shear rate demonstrates a shear thinning (or pseudoplastic) behaviour where the apparent viscosity decreases with increasing shear rate [Jol 74, 76] (Figure 4.1.2A).

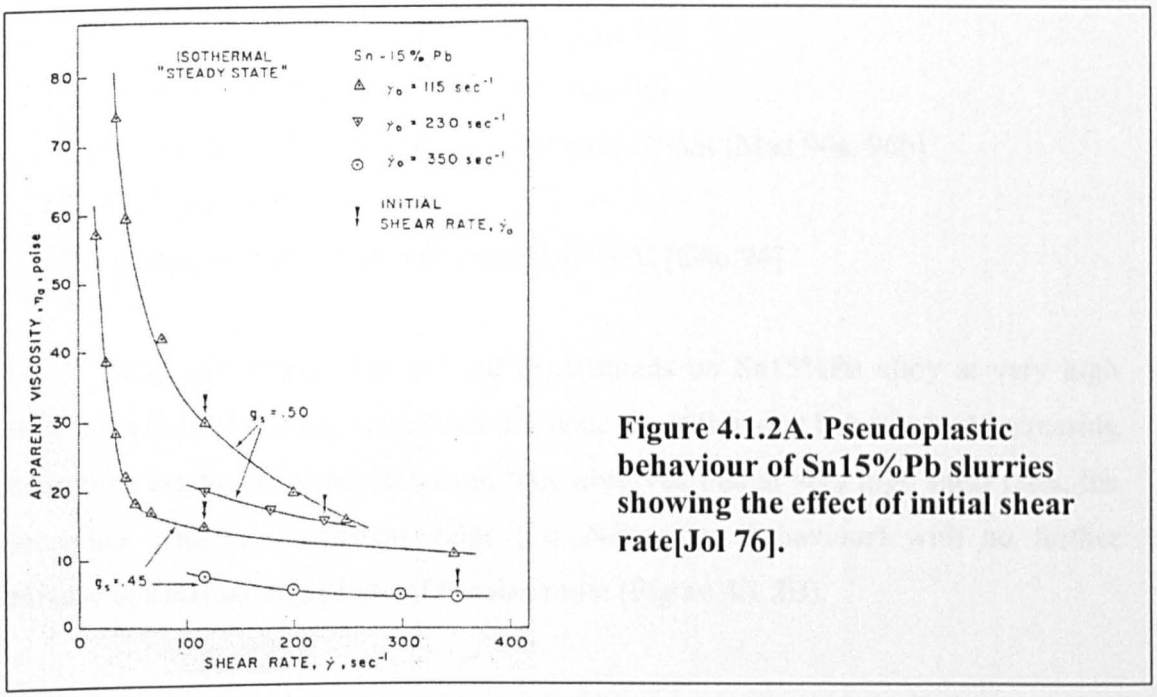

Figure 4.1.2A. Pseudoplastic behaviour of Sn15%Pb slurries showing the effect of initial shear rate[Jol 76].

This behaviour is reversible so that on returning back to the original shear rate, the same viscosity value is recorded as before [Kir 94, Sal 96]. Joly [Jol 74] described this behaviour as the breaking up of the agglomerates's particle bonds (hence a smaller agglomerate size) with increasing shear rates. This reduction in size leads to a release of the entrapped liquid in the agglomerates thus lowering the viscosity. This was subsequently supported by the work of Wang Nan [Wan 90a], Y.Ito [Ito 92] and Y.S. Yang [Yan 97]. Ito showed particle agglomeration by serial sectioning their test material. Metallographic examination showed agglomeration of some particles and isolated individual particles and that higher shear rates lead to a lower amount of entrapped liquid (i.e. reduction in agglomerate size due to higher shear rate).

Generally, it is now accepted that the steady state viscosity at any given shear rate is the result of a dynamic equilibrium between the agglomeration and de-agglomeration process [Kir94, Kat 92a, Sué 96, 00, Yan 97]. In general, steady state shear thinning behaviour has been confirmed by other workers:

(1) Sn15%Pb [Wan 90a, Tur 91, Mcl 92, 97, Wan 92b, Pen 94, Mod 98, 99]
(2) Al-4.5%Cu1.5%Mg [Kat 92a, 92b], Al-38%Zn [Wan 90a]
(3) Al-6.5%Si [Moo 91, Ito 92], Al-7%Si0.3%Mg [Lou 92], Al-16.5%Si5%Cu0.5%Mg [Hen 92, 93]
(4) Al-50%Si, Al-40%Si and Al-30%Si [Die 96]
(5) A356 [Hor 92, Qua 94, 96a, Bra 98, Azz 00]
(6) A356 with 18%Si [Hor 92, Qua 94] with 20%Si [Mad 96a, 96b]
(7) A357 [Fig 00]
(10) Magnesium alloys with 9%Al and 4.5%Al [Gho 94]

Turng and Wang [Tur 91] did experiments on Sn15%Pb alloy at very high shear rates (>1000 s^{-1}) and found that the same shear thinning behaviour at increasing shear rates can be observed. However, they observed that at very high shear rates, the viscosities tend to a constant value (i.e. Newtonian behaviour) with no further increase or decrease regardless of the shear rate (Figure 4.1.2B).

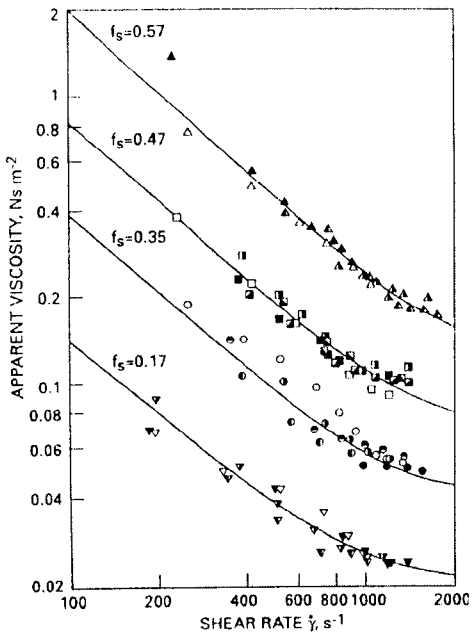

Figure 4.1.2B.
Apparent viscosity trends showing clustering of data (i.e. values do not differ greatly, viscosity assumed constant) at very high shear rates (> 1000 s^{-1}) [Tur 91].

Turng and Wang [Tur 91] suggested that at this limiting case of very high shear rates, no agglomerates exist in the material and each particle becomes an individual entity by itself, thereby leading to a constant viscosity as recorded. The approach to a Newtonian behaviour was also observed in the work by Moon et al [Moo 91]. Not only does the apparent viscosity depend on the shear rate employed, it is also very much dependent on the initial shear rate used to achieve its steady state (or iso-structure) structure before the shear rate jump [Lou 92, Qua 94, 96a]. A higher initial shear rate shows a lower viscosity compared to one done on a lower initial shear rate after a shear rate jump to the same final shear rate (Figure 4.1.2C, Qua 94).

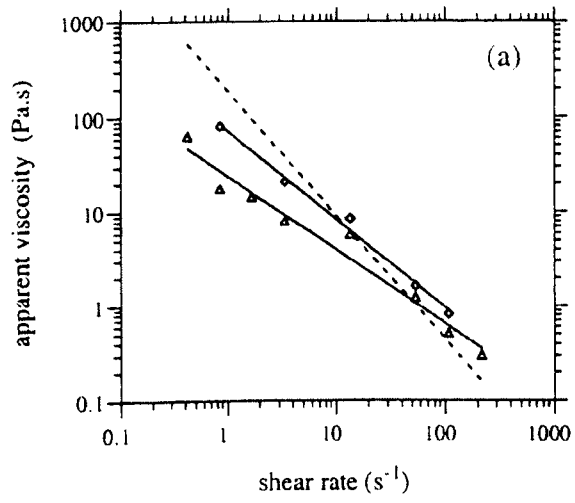

Figure 4.1.2C.
Apparent iso-structure viscosity as a function of shear rate of 13 s^{-1} and 108 s^{-1} (denoted by ◇ and △ respectively).

This behaviour can be explained by the fact that at the high initial shear rate, the degree of de-agglomeration is higher than that at the low shear rate, hence lower apparent viscosity after a shear rate jump [Kir 94]. More recently, Azz [Azz 00] related the effect of reduced shear thinning effect at high initial shear rate compared to low initial shear rate before a shear rate jump to the degree of the required state of agglomeration. At the initially higher shear rate, the material is already in an advanced state of de-agglomeration hence the rate of de-agglomeration (i.e. the rate of breaking down the agglomerates or inter-particle bonds) is much slower than when the material is sheared initially at a low shear rate. Kattamis et al [Kat 92a, 92b] and Yang [Yan 97] observed that the average particle size decreases with increasing initial shear rate. This evidence seemed to support the theory explained above. Turng [Tur 91] however found that the steady state viscosity values tend to cluster together regardless of the initial shear rate or the number of isothermal holding stages employed in the very high shear rate region.

4.1.3 Effects of rest times

Work has also been done to investigate the effect of rest time before a shear rate jump [Moo 91, Lou 92, Hen 92, Mad 96b, Yan 97]. Experimental results showed that with increasing rest times, the peak viscosity recorded at the onset of a shear rate jump increases. This increase of peak viscosity is due to the formation of agglomerates where inter-agglomerate bonds are reformed in the absence of shear [Moo 91, Lou 92, Mad 96a]. These workers have also observed the effect of reinforcing particles where increasing Silicon Carbide (SiC_p) content in an aluminium alloy decreases the peak viscosity. This effect has been thought to be due to the silicon carbide particles preventing bond formation between the primary aluminium particles.

4.1.4 Thixotropic Effects

Thixotropic effects in semisolid materials can be observed during an abrupt change in shear rate. The new structure in the material does not occur instantaneously (as would be expected from a Newtonian material, c.f. Chapter 2). This time lag before the material attains a steady state viscosity is dependent on the shear rate, fraction solid and rest time. Workers have done experiments to observe this time lag or, the 'relaxation' time of a slurry after a step change to a higher shear rate and the 'restoration' time after a step change to a lower shear rate. This time describes the time needed for a slurry to attain a steady state viscosity after a change in shear rate either from rest or from an initial shear rate where steady state has been reached [Hor 92, Qua 94, 96a, 96b, Kum 94a, 94b, Pen 96, Mad 96a, Mod 98, 99]. Generally, these workers have shown that the 'relaxation' time is much faster than the 'restoration' time. Horsten [Hor 92] and Quaak [Qua 94 and 96a, 96b] observed that during a shear rate increase, the 'relaxation' time is independent of the magnitude of the jump while in a shear rate decrease, the 'restoration' time increases with increasing magnitude of change. Modigell and Koke [Mod 99] observed that the rate at which the 'relaxation' occurs decreases with shear rate while Moon concluded that this breakdown rate is dependent on the peak viscosity. Recent experiments by Ward et al [War 00a] have observed that the 'relaxation' time is strongly dependent on the rest time (which in turn affects the peak viscosity) but not strongly on the final shear rate. Quaak [Qua 96a, 96b) concluded that there are in fact two different periods of time in which agglomeration or de-agglomeration take place during a step change from an initial shear rate. The first 'relaxation' or 'restoration' occurs rapidly while the second time occurs more gradually. Quaak noted that the first 'relaxation' or restoration' time increases with increasing initial shear rate and decreases with increasing final rate. He was not able to fully describe the effects of the first 'relaxation' or 'restoration' time as the data collection rate (~9 Hz) was not fast enough to capture the fast transient effects. However, Quaak did observe that the 'relaxation' or 'restoration' time seemed quite independent of the shear rate jump magnitude or direction.

Another method of observing the thixotropic effects is by using the hysteresis loop method (see Figure 2.2.4C) [Jol 76, Mod 99]. Joly have identified six parameters affecting the thixotropy of a semisolid Sn15%Pb alloy. The parameters are:

(i) The fraction solid of the alloy. With increasing fraction solid, the area of the hysteresis loop increases indicating a higher degree of thixotropy. Such behaviour should be related to the higher degree of agglomeration at higher fraction solid and hence a high degree of thixotropy during the hysteresis experiments. This behaviour was also shown by Modigell and Koke [Mod 99].

(ii) Initial shear rate during solidification into the semisolid region. This determines the mechanical history of the alloy. It was observed that increasing the initial shear rate decreases the thixotropy. Like (i), this can be attributed to the fewer agglomerates in the structure at higher shear rate (see also Section 4.1.1).

(iii) The down time (or the rate of decrease in shear rate) spent in decreasing the shear rate of the semisolid slurry from its initial value to zero prior to hysteresis loop measurements. Results showed that the degree of thixotropy increases with increasing downtime. This effect was reported to be the same as the amount of rest time (i.e. increasing rest time, increases the thixotropy). The longer the semisolid alloy was left unstirred, the higher is the effect of agglomeration and coarsening taking place (see Section 3.4). However, it is disputable in the author's view that increasing the downtime leads to a higher degree of thixotropy. Agglomeration and coarsening processes take place due to particle to particle interactions. Shortening the downtime indicates a shorter time in which such interactions can take place. In other words, particle interactions cause the formation of welds (see Chapter 3.4) between the particles. The break up of these welds is the cause of time lag seen in shear thinning and thixotropic materials during a step change to a higher shear rate whilst the time lag in the formation of these welds is seen during a step decrease. This point could also be viewed on the other hand where a faster down time prevents the structure achieving its desired state in relation to the final shear rate, thus the structure is still in the higher agglomerated state.

(iv) The up-time (or the rate of increase) spent in increasing the shear rate from zero to its maximum. The degree of thixotropy in this case, decreases with increasing up time.

(v) The maximum final shear rate specified. Results obtained showed an increase in thixotropy with increasing maximum final shear rate. Since the time needed to reach the maximum shear rate and back to its initial starting point increases, it seemed reasonable to conclude that more particle interactions would occur leading to a higher degree of thixotropy.

One interesting result observed by Joly and Mehrabian [Jol 76] was that no thixotropic effect was observed for a fraction solid below 0.3 and below 2 minutes of rest time. Although no explanation was given for this behaviour, it is felt that at this low fraction solid, the material consists of widely spaced particles separated by the liquid matrix. The rest time needed for particle interaction is evidently longer. Thus Joly and Mehrabian observed thixotropic behaviour after a rest time exceeding 5 minutes.

Although the hysteresis loop method allows one to understand the effect of shear rate, time and fraction solid on thixotropy in semisolid slurries, it is not well suited to understanding the kinetics of agglomeration and de-agglomeration of the particles (which governs the thixotropic behaviour of the slurry) during a rapid change in shear rate [Kir 94, Sué 96].

Other workers have associated a yield stress value with thixotropic behaviour in semisolid slurries. Peng et al [Pen 96] observed an apparent yield stress below a critical shear rate that increases with increasing fraction solid while Modigell and Koke [Mod 99] showed that the yield stress is a function of the rest time and fraction solid. As proposed by Sannes et al [San 94b], particle interactions and neck formation between the particles are responsible for the existence of a yield stress and this yield stress is dependent on fraction solid, structure and particle morphology. It should be noted that the experiments done by Sannes are by reheating the semisolid alloy where the structure is gradually broken down when grain boundaries melt. The yield stress in this case would be higher than those reported by Peng and Modigell.

4.1.5 Transient Behaviour during a Rapid Shear Rate Jump

It was mentioned in Section 4.1 that industrial semisolid processing occurs in a matter of seconds. The preceding sections (4.1.1 to 4.1.4) describe work on the steady state viscosity behaviour at longer times that do not reflect the actual kinetics of a slurry during processing. Therefore, the effects on viscosity during a rapid change in shear rate in a short space of time are needed to understand this behaviour in a thixotropic material. Such transient experiments are usually carried out by 'instantaneously' varying the shear rate after the slurry has attained its steady state structure. During these shear rate jumps, the 'iso-structure' viscosities or stresses are recorded [Tur 91, Hor 92, Kum 93, 94b, Pen 96, Qua 96a, 96b, Mad 96a, Mod 99, Fig 00, Azz 00, Kir 00]. Most of the workers observed that during the onset of the jump, the structure remains the same as the previous steady state structure before decreasing or increasing with increasing or decreasing shear rates respectively to a steady state structure corresponding to the final shear rate. Turng and Wang [Tur 91] and Peng et al [Pen 96] observed an overshoot in the measured stress during a rapid increase in shear rate. They found that this overshoot or undershoot (in the case of a decrease in shear rate) is proportional to the change in the shear rate. Therefore, according to Newton's Law of Viscosity, the viscosity (hence the structure) is constant during this transient change before showing a pseudoplastic behaviour. Peng et al observed that the overshoot or undershoot increases or decreases respectively with increasing fraction solid. Horsten et al [Hor 92] and Quaak [Qua 96a, 96b] observed that at this transient period, structure evolution has not yet developed hence the structure corresponds to that of the previous shear rate. With increasing time at the new shear rate, agglomeration or de-agglomeration followed by coarsening takes place (Figure 4.1.5a) [Qua 96a, 96b].

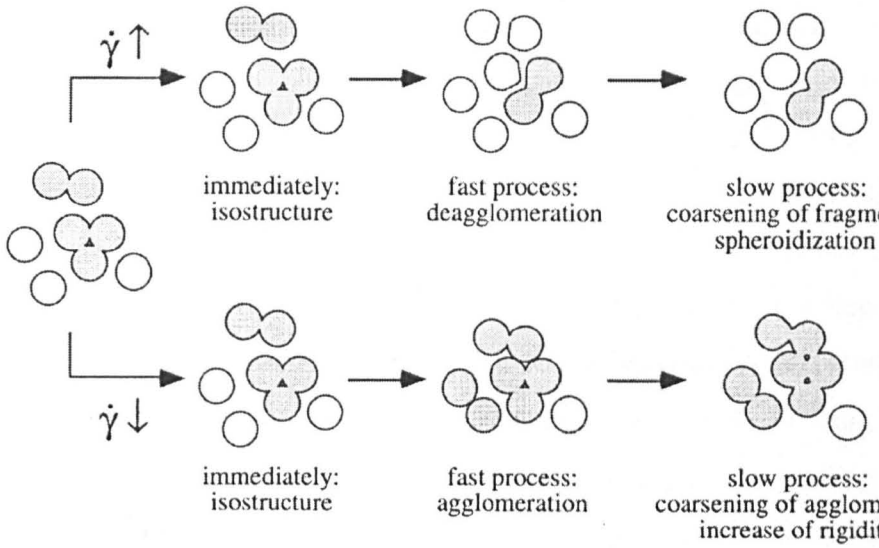

Figure 4.1.5a. Qualitative model describing the structure evolution after shear rate jumps. A fast and a slow process are present for any jump magnitude [Qua96a].

The work of Kumar et al [Kum 94b] and Modigell and Koke [Mod 99] however showed that a shear thickening effect was observed during this transient period. Their results showed an increasing viscosity with shear rate (i.e. shear thickening) followed by a decreasing (shear thinning) behaviour as opposed to the constant structure observed by the other workers. These discrepancies have not yet been adequately accounted for. However, it should be noted that Kumar et al [Kum 94a] conditioned their Sn15%Pb slurry at a very high initial shear rate (~ 764 s^{-1}) before conducting their shear rate jump experiments at a different initial shear rate (300 to 340, 385, 436 and 495 s^{-1}, note that the initial shear rate of 300 s^{-1} is actually below the conditioning shear rate of 764 s^{-1}). This may indicate that the structure is not in the constant structure state corresponding to the initial conditioning shear rate (i.e.764 s^{-1}).

It was discussed in the previous sections that the initial shear rate determines the particle size and this in turn affects the rheological behaviour of the slurry. The work of Modigell and Koke [Mod 99] was done at much lower initial shear rate (113 s^{-1}). Like Kumar et al [Kum 94b], the authors showed shear thickening behaviour during step changes in shear rates. They have attributed this behaviour to the presence of an apparent yield stress and have successfully confirmed their work with a mathematical model. The shear thickening behaviour observed by Kumar and Modigell could be related to the early work by Wang et al [Wan 90a] who found that

the effect of shear thinning behaviour only occurs above a critical shear rate (50 s^{-1} in their results) in the initial conditioning of the alloy slurry during solidification. They proposed that below this initial shear rate (<50s^{-1}), the slurry flow could not effectively break down the dendritic solids in the early stages of solidification and these solids will in fact further develop into well grown network structures hence giving an increase in viscosity (shear thickening effect) during a step change in shear rate. However, one should be reminded that theoretically, all dendrites should be broken down leading to spheroidal particles given enough time at the steady state condition.

Although the above results showed opposite behaviour, Barnes [Bar 89b] indicates that a suspension can present several behaviours depending on the shear rate: shear thinning followed by shear thickening and shear thinning again as shear rate increases. Barnes defined a critical shear rate (10 s^{-1} in his results) at which the transition from shear thinning to shear thickening behaviour occurs. This effect has only been reported once in semisolid alloy slurries [Mcl 97]. It becomes quite clear then that the understanding of the transient behaviour in semisolid slurry still requires much further work.

So far, discussions of the rheological behaviour have been based on rotating viscometry experiments. As stated in the beginning of this chapter, rapid compression testing is another method to relate the rheological behaviour of semisolid slurries. Rapid compression testing is usually done to investigate slurries at a higher fraction solid. The following sections will deal with the rheological results obtained by various workers using compression testing.

4.1.6 Compression Testing

Laxmanan and Flemings [Lax 80] have perhaps done one of the most comprehensive experiments on Sn15%Pb alloy using parallel plate compression testing. A small cylindrical slug produced by the 'Rheocast' method (c.f. introduction) was heated up to various temperatures (hence different fraction solids) before load was applied and the strain consequently measured. These authors compared the

compressing pressure between dendritic and non-dendritic (or globular) semisolid alloys and found that the non-dendritic semisolid alloys require about 2 orders of magnitude less pressure in the compression experiments. The authors showed that the viscosity decreases with increasing shear rate at a given fraction solid (i.e. pseudoplastic material). Their experimental results were fitted to a power law equation (Figure 4.1.6a).

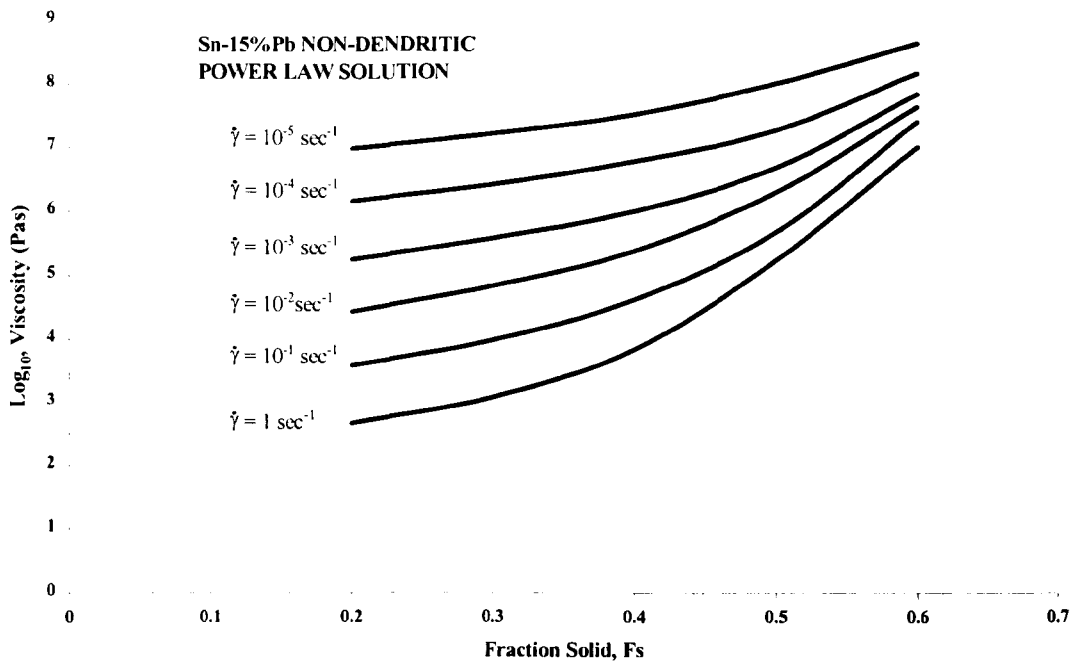

Figure 4.1.6a. Calculated viscosity versus fraction solid at different shear rates using power-law equation (Table 2.2.1b) for partially remelted Sn15%Pb alloys [Lax 80].

Laxmanan and Flemings [Lax 80] obtained rheological results at very low shear rates using the compression methods. The authors have also shown that at such low shear rates (~0.025 s^{-1} to 0.2 s^{-1}), shear thinning behaviour is present in non-dendritic semisolid alloys although at the very low shear rates, it can be seen that the viscosities are almost constant (i.e. Newtonian behaviour). It was mentioned in Chapter 2 (Figure 2.2.1D) that a typical pseudoplastic (or shear thinning) material has two Newtonian regions, at the very low and very high shear rates, The viscosities at very low and very high shear rates in semisolid Sn15%Pb alloys obtained by Laxmaman and Flemings [Lax 80] and Turng and Wang [Tur 91] (c.f. Section 4.1.2) respectively, can allow non-dendritic semisolid alloys to be described by the Cross equation mentioned in Chapter 2.

The work of Laxmanan and Flemings [Lax 80] was supported by M.Suéry et al [Sué 82]. The authors found that the deformation is almost homogenous for non-dendritic and very fine dendritic Sn15%Pb alloys compared to the as-cast dendritic alloys. Suéry explained that coarsening in the very fine dendritic structures causes the structures to resemble that of a non-dendritic alloy hence the similar deformation behaviour whilst the as-cast dendritic alloys structures were more interconnected through their dendrite arms initially causing a higher deformation stress before breaking down with increasing strain. Both Laxmanan and Flemings and Suéry et al found that the shear thinning behaviour in semisolid Sn15%Pb alloy is controlled by the fraction solid of the alloy. Suéry also pointed out that this behaviour is largely dependent on the structure of the primary solid phase.

Seconde et al [Sec 84] looked into the effect of microstructure at different holding times and solidification routes before compression. The authors found that with increasing holding time, the primary particles coarsen and becomes more spheroidal. This increase in spherodicity corresponds to the low stress needed to deform the specimen. Seconde et al conducted experiments on the effect of cooling rate with dendritic Sn15%Pb alloys and found that increasing the cooling rate decreases the stress encountered (Figure 4.1.6b).

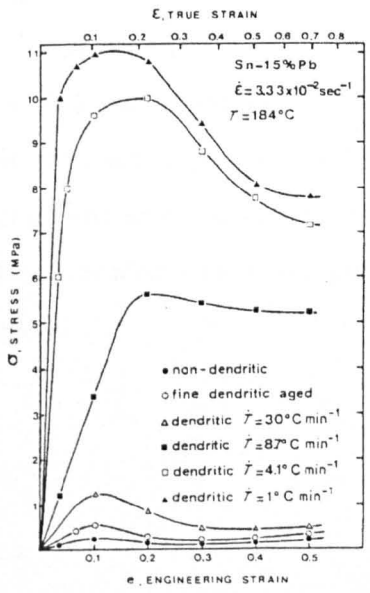

Figure 4.1.6b. Stress versus strain curve for dendritic and non-dendritic Sn15%Pb alloy [Sec 84].

In fact, at the highest cooling rate, the stress-strain curve of the dendritic structure is almost the same as for the non-dendritic specimens This is due to the interlocking structures of the particles which decrease with increasing cooling rates

(producing a much finer dendritic structure). Examination of the micrographs also showed large amounts of liquid segregation for the dendritic alloys while practically no liquid segregation occurred in the non-dendritic and very fine dendritic alloys. It is believed that the liquid film acts as a lubricant for the particles to slide past each other easily hence the lower stress needed to deform a non-dendritic and very fine dendritic alloy.

Loue et al [Lou 92] conducted compression testing on Al6%Si0.3%Mg and Al7%Si0.3%Mg alloys. The authors found a critical deformation rate at which when exceeded, a maximum stress is recorded before decreasing rapidly to a near constant value. Furthermore, the specimen cracked during the deformation. Microstructural examinations however showed no liquid segregation or particle deformation. The authors proposed that at this very high deformation rate, the liquid film which acts as a lubrication medium for the solid particles to slide past each other was not able to accommodate the high deformation rate, resulting in the cracking of the specimen. On the other hand, if the deformation rate is below the critical value, the authors found homogenous deformation during the compression experiments. Loue et al next carried out experiments under different strain rate jumps up and down. Their results showed similar behaviour to that previously reported by Turng and Wang [Tur 91] using a rotating viscometer. Figure 4.1.6c showed a comparison between the work of Turng and Loue [Lou 92] for a sudden change in shear rate and/or strain rate. Loue et al reported that a sudden increase in strain rate resulted in an increase in shear stress after which the shear stress decreases to the previous value it had before the strain rate jump. The same behaviour was observed during a strain rate jump to a lower value (the shear stress decreases initially before increasing to a value it had before the jump down).

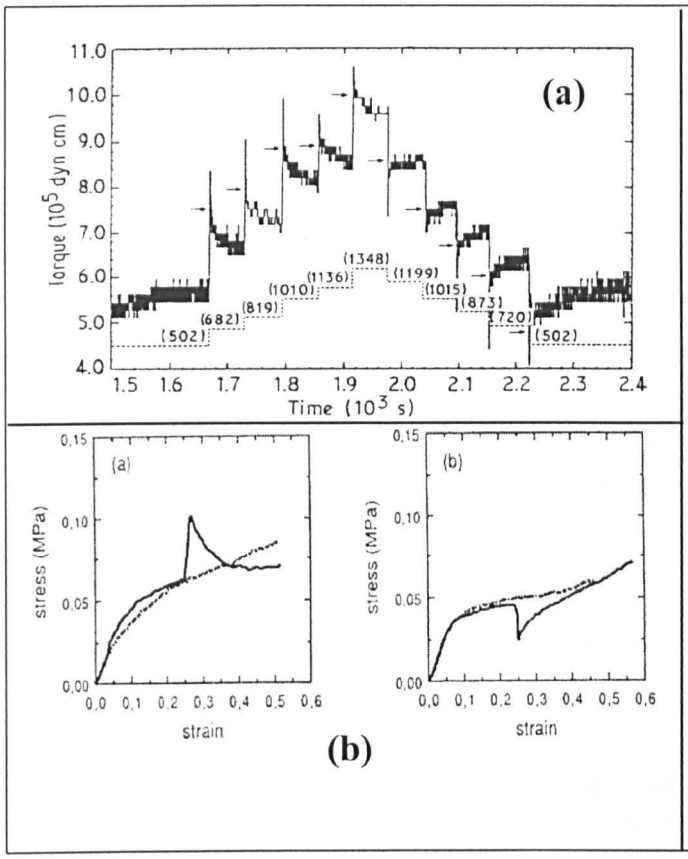

Figure 4.1.6c.
Comparison of shear rate jumps up and down between (a)Turng and Wang [Tur 91] in Sn15%Pb alloy, and (b)Loue [Lou 92] on AlSiMg0.3 alloy.

- **(a) is done on a rotational viscometer while**
- **(b) is carried out using parallel plate compression.**

Both works showed similar behaviour in the slurries where an increase in strain rate corresponds to a overshoot in shear stress while a decrease in strain rate shows an undershoot in the shear stress.

Loue et al proposed that this behaviour during the transient change can be explained by relating the material's flow behaviour to the change in shear rate. Following the work of Laxmanan and Flemings, Loue et al looked at the effect of viscosities with increasing shear rates. Generally, viscosity decreases with increasing shear rates. Comparing experimental results for partially remelted and partially solidified semisolid alloys the authors observed that both exhibit the same shear thinning behaviour during deformation. However, the authors did mention that they could not quantitatively compare partially remelted and partially solidified alloys due to the difference in particle sizes obtained. The work of Loue et al was repeated and supported by L.Salvo [Sal 94] and Han et al [Han 98] showing similar behaviour for Al7%Si3%Cu alloys and wrought alloys respectively.

The work of Ngyuen et al [Ngy 92] showed the effect of temperature and holding time (at the specific temperature hence fraction solid) before deformation on metal matrix composite alloys. The authors observed that with increasing temperature, the stresses during the deformation decrease and at the very high temperature, the stresses are almost constant (Figure 4.1.6d).

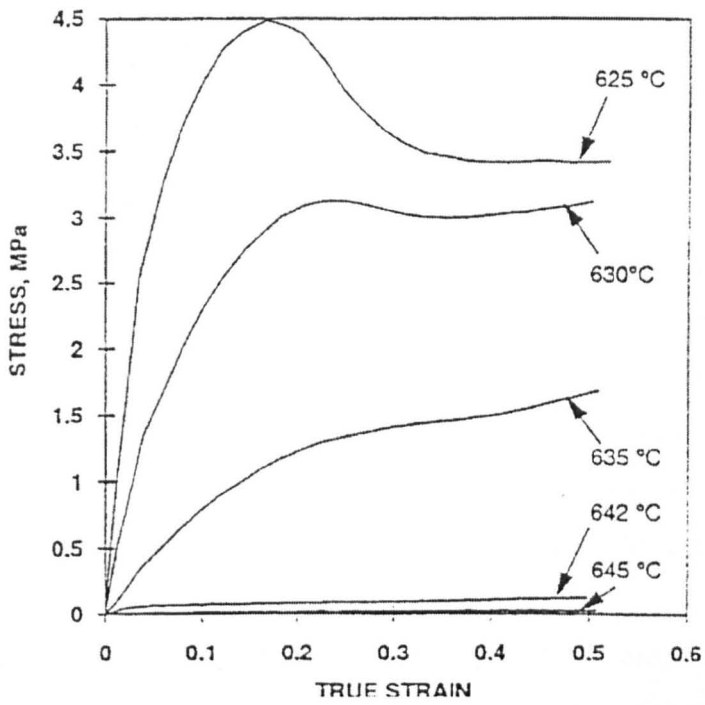

Figure 4.1.6d. Influence of temperature on the stress-strain curve for as-cast composites deformed in compression at constant strain rate [Ngy 92].

Ngyuen at al explained that at the high temperature, the high amount of liquid aids the deformation (or sliding) of the particles without any deformation to the solid particles or liquid phase segregation from the specimen. For low temperatures, the stress reaches a maximum before decreasing. This behaviour is attributed to the little amount of liquid present in the specimen. The amount of liquid is not large enough to accommodate the large amount of solid particles. Microstructural evidence showed deformation of the solid phase particles and cracking in the specimen. The authors next looked at the influence of the holding time at a specified temperature before deformation. With increasing holding time, the stress decreases. The authors proposed that at the short holding time, globularisation of the solid phase particles was not yet fully completed hence a high stress value was recorded which reaches a maximum before decreasing with increasing deformation.

S.M. Nabulsi et al [Nab 96] investigated the shear strength of AlSi alloys using horizontal compression testing. By correlating the shear stress encountered with the shear strength of a semisolid alloy, the authors found that the shear stress increases initially before decreasing to a low value. They proposed that this behaviour is due to the interaction of the inter-dendritic liquid phase and/or the rosette like solid particles where interlocking may occur resulting in the increase in shear stress. With increasing shear deformation, the sliding or rolling motion of the particles over one another in the liquid phase takes place resulting in the decrease of the shear stress recorded. The authors suggested that at 60% fraction solid, the maximum packing fraction (c.f. Chapter 4.1.1) is reached where the material can no longer accommodate the imposed stress through flow. This will also cause fracture in the specimen.

J.Valer et al [Val 98] investigated the rheological behaviour of Al-Ge alloys under strain increase and decrease. The authors observed similar behaviour to that reported by Loue et al [Lou 92] i.e. that during a step change in strain rate, the stress increases rapidly but decreases thereafter to reach the value it would have had before the step change. Valer et al [Val 98] attribute this behaviour to the de-agglomeration of the particles. The authors proposed that before a step change in the strain rate, the particles are partially agglomerated hence the transient state during the step change remains as before after which de-agglomeration of the particles takes place resulting in the decrease of the shear stress. Conversely, during a step change to a lower strain rate, the shear stress decreases initially before increasing to reach a value close to that before the strain rate change. This is due to agglomeration process of the particles at the final lower strain rate (Figure 4.1.6e).

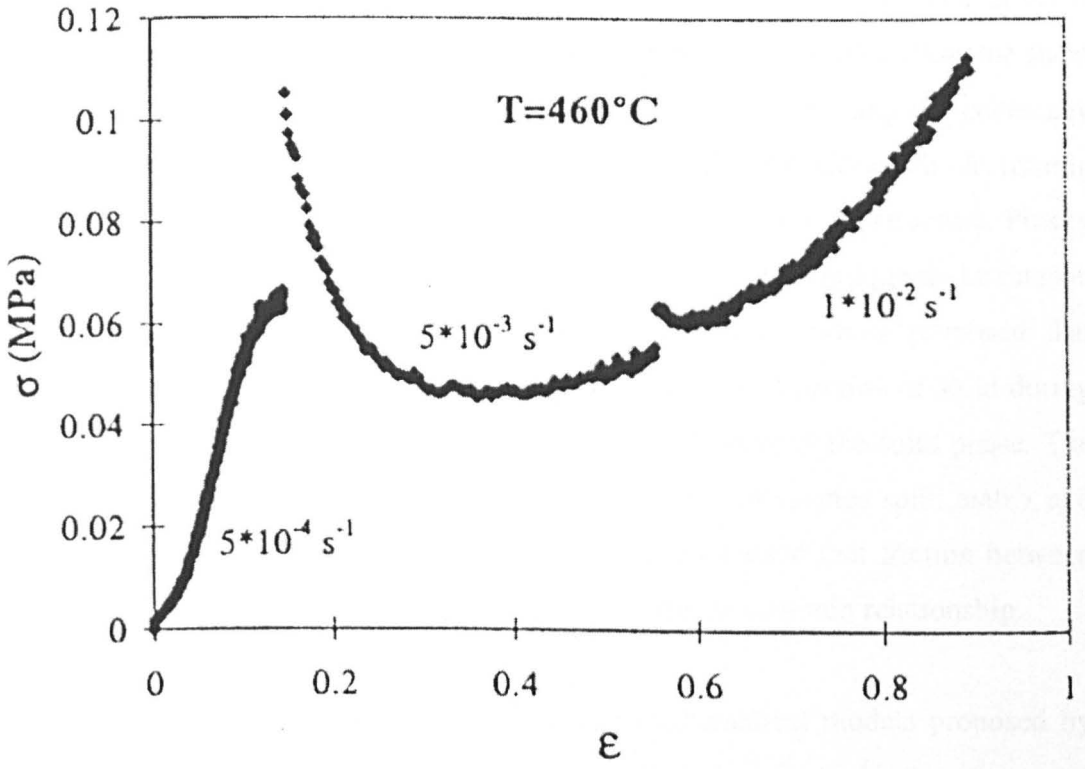

Figure 4.1.6e. Influence of strain rate on the stress-strain curve deformed in compression. A change in the strain rate is followed by an increase in the shear stress before the stress decreases to a value corresponding to the shear rate.

Using the vertical compression method, Kapranos et al [Kap 98] investigated the rheological behaviour of A357 alloys under different temperatures by measuring the force encountered during the compression test. The authors recorded peak stress at the lower temperature. However, no peak stress was recorded at the high temperature. This temperature was identified with the thixoforming temperature (i.e. the temperature at which a material is thixoformable). Following the work of Laxmanan and Flemings [Lax 80], the authors obtained similar behaviour where the viscosity decreases rapidly initially at the onset of compression with increasing shear rate before approaching a near constant value as the material starts to fill the die.

M.Ferrante et al [Fer 98] investigated the rheological properties of Al4%Cu alloys in terms of fraction solid and the initial microstructure condition. The authors found that with increasing fraction solid, the shear stress increases. The authors found that at a fraction solid of 0.82, the shear stress increases rapidly and attributed this to the coherency point as proposed by Flemings [Fle 91]. Ferrante et al also showed that a globular structure has almost a constant stress with increasing fraction solid under

compression up till a fraction solid of 0.82 before a marked increase in shear stress is encountered. Comparing the results with that for a dendritic semisolid alloy, the shear stress is continually increasing before increasing rapidly after passing the coherency point. The authors also showed the rapid decrease in viscosity with decreasing fraction solid for a globular microstructure compared to a dendritic structure. Pinsky et al [Pin 84] conducted similar experiments using the same technique as Laxmanan and Flemings [Lax 80] and obtained similar results. The authors proposed that deformation occurred in two stages. The first stage is the compaction of solid during which liquid is squeezed out without any significant flowing of the solid phase. The second stage is where there is a homogeneous flow in the compacted solid matrix and the remaining liquid at constant stress. Pinksy et al concluded that friction between the specimen and the compression plates may affect the stress-strain relationship.

In Section 4.2, discussion of the various mathematical models proposed by several authors will be presented. Mathematical modelling is an important area of research since it enables the description of the flow behaviour of semisolid alloy slurries during the die-filling behaviour [Lev 90, Kir 94, Ale 00]. Although several mathematical models have been proposed and used, it is still unclear which model is appropriate to use industrially. However, it should be noted that the behaviour of semisolid alloy slurries consists of varying degrees of thixotropy and pseudoplasticity hence a full understanding of the rheological behaviour of semisolid alloys is still needed. Section 4.2 will give a brief discussion to the current understanding of the mathematical models used to describe semisolid alloy slurries during a shear rate or strain rate jump. It is out of the scope of this thesis to go into the programming aspect of the models.

4.2 Mathematical Models

Mathematical models have been proposed over the years to describe the rheological behaviour of semisolid alloys. However, these models are used to describe the rheological behaviour for a particular alloy at specific conditions (e.g. a range of shear rates or fraction solid and temperatures). Furthermore, these models contain parameters that are obtained by curve fitting to the experimental results. This is mainly due to the complicated behaviour of the semisolid alloy condition (whether it is partially solidified or partially re-melted) and the difference in experimental conditions in the various test methods.

Joly and Mehrabian [Jol 76] were the first to propose mathematical models to describe the results from their continuous cooling and isothermal holding experiments. A linear relationship was found when plotting the viscosity against the volume fraction solid for the continuous cooling experiments. Thomas [Tho 65] proposed an equation:

$$\eta_a = 1 + 2.5 f_s + 10.05 f_s^2 + A \exp B f_s \qquad [4.2.a]$$

and that at fraction solid, f_s, greater than 0.25, Equation 4.2.a can be simply reduced to:

$$\eta_a = A \exp B f_s \qquad [4.2.b]$$

Thomas proposed that at fraction solid greater than 0.25, the last term of Equation 4.2.a becomes more significant in its contribution to the apparent viscosity, η_a due to the rearrangement of the particles under shear.

To describe the shear thinning behaviour of semisolid Sn15%Pb alloy with increasing shear rate, Joly [Jol 74, 76] used the classical power law where the viscosity is described by:

$$\eta_a = k\dot{\gamma}^m \qquad \text{where m = n-1} \qquad [4.2.c]$$

where η_a is the apparent viscosity,

$\dot{\gamma}$ the shear rate,

k and ,m* are material constants (both fraction solid dependent)

* The value of m is negative to indicate a shear thinning material while a positive n value describes a shear thickening (or dilatant) material.

Wang Nan et al [Wan 90a] considered the energy dissipation of the solid phase under shear flow and proposed the following rheological equation for Sn15%Pb alloy:

$$\eta = \eta_o \left[1 + C_1 \left(\frac{\overline{\Delta\sigma} f_s^{\,2} \dot{\gamma}^{n-1}}{\overline{R_o} \dot{\gamma}_c^{\,n}} \right) + C_2 \left\{ \frac{\left(\frac{f_s}{f_s^*} \right)^{1/3}}{1 - \left(\frac{f_s}{f_s^*} \right)^{1/3}} \right\} \right] \qquad [4.2.d]$$

where η_o is the viscosity of pure liquid,

f_s^* is the maximum fraction solid where flow cannot proceed below a yielding stress,

$\dot{\gamma}_c$ is the critical shear rate for solids with a mean size, $\overline{R}_o$,

C_1, C_2, $\overline{\sigma}$ and n are the material constants, determined experimentally.

Wang Nan et al proposed that at high fraction solid, the forming of chain-like solids causes the solid's structure to become insensitive to shear rate variation, hence the slurry could be described as a Bingham fluid. From Equation 4.2.d, the authors proposed the rheological equation of the Bingham fluid as:

$$\tau = A + B\dot{\gamma}^{n} \qquad [4.2.e]$$

where $A = C_1 \dfrac{\eta_O . \overline{\Delta\sigma} . {f_s}^2}{\overline{R_O}}$ [4.2.f]

and $$B = \eta_O \left[1 + C_2 \left\{ \frac{\left(\dfrac{f_s}{f_s^*} \right)^{1/3}}{1 - \left(\dfrac{f_s}{f_s^*} \right)^{1/3}} \right\} \right] \qquad [4.2.g]$$

'A' stands for the shear yielding stress of the fluid while 'B' stands for the viscosity when the shear rate approaches infinity.

Turng and Wang [Tur 91] proposed a mathematical model to describe the shear thinning behaviour and the 'near' Newtonian behaviour at the very high shear rates region for a Sn15%Pb alloy as:

$$\eta = \eta_\infty (f_s) \left[1 + \left(\frac{\dot{\gamma}_c (f_s)}{\dot{\gamma}} \right)^a \right]^{n/a} \qquad [4.2.h]$$

where η_∞ is the viscosity at the very high shear rates,

$\dot{\gamma}_c$ (= τ_c/η_∞) is the critical shear rate where the viscosity reaches a constant value, dependent on the fraction solid, f_s

'n' and 'a' are the parameters determined by fitting the experimental data.

The authors found that the parameters η_∞, $\dot{\gamma}_c$ and τ_c dependent on the fraction solid can be described exponentially as Equation 4.2.b. By adding an additional empirical factor to Equation 4.2.h, Turng and Wang were able to fit their experimental results for their continuous cooling experiments. However, the authors mentioned that the fits are more of an average trend where the effect of cooling rates was not taken into account.

Kattamis and Piccone [Kat 91, 92a, 92b] considered the microstructural effects (i.e. particle shape and size) to relate the effect on the viscosity of Al4.5%Cu1.5%Mg alloys. They proposed a mathematical model where:

$$\eta = \eta_L \left[1 + \left\{ \frac{k f_s \left(\frac{S_v}{S_{vo}} \right) \left(\frac{\bar{d}}{d_o} \right)}{k - f_s} \right\} + 2.033 \times 10^4 f_s (\dot{\gamma})^{-0.722} \right] \qquad [4.2.i]$$

where η_L is the viscosity of liquid,

k is a constant (= 0.5016 for best fit to their results),

$\bar{d}$ is the effective average diameter of the particle and

S_v is the interface area per unit volume of the particle,

Subscripts o refer to the values at the initial isothermal conditions.

The authors concluded that the particle size and particle surface area decrease with increasing shear rate and isothermal holding time respectively.

W.R.Loue [Lou 92] followed the model proposed by Kattamis and Piccone and obtained good experimental fit to their experiments on Al7%Si0.3%Mg alloys. Hirai et al [Hir 93] studied the effect of chemical composition on the apparent viscosity of aluminium alloys and proposed the following equation:

$$\eta = \eta_L \left[1 + \frac{p}{2} \left(\frac{1}{f_s} - \frac{1}{f_{cr}} \right) \right] \qquad [4.2.j]$$

where η_L is the liquid viscosity of the alloy

P (= $\alpha \rho_m C^{1/3} \dot{\gamma}^{-4/3}$) is the geometrical shape factor of the suspended crystal dependent on the solidification rate and shear rate,

ρ_m is the density of the alloy,

f_{cr} (= 0.72- $\beta C^{1/3} \dot{\gamma}^{-1/3}$) and f_s are the critical fraction solid and fraction solid respectively,

β and α are constants determined experimentally and found to increase with a higher concentration of alloy resulting in an increase in viscosity.

The authors proposed that at higher concentration of the alloy, the geometrical shape parameter of the suspended primary crystal increases and an increase in the quantity of liquid entrapped between the primary crystals results in an increase in the viscosity.

Mada and Ajersch [Mad 96a, 96b] put forward a model that includes the thixotropic effects. Using the structural parameter model from the Cross equation (c.f. Chapter 2), the authors relate the structural parameter, λ, to a kinetic rate factor, k, by:

$$\frac{\lambda - \lambda_e}{\lambda_o - \lambda_e} = \exp(-kt) \qquad [4.2.k]$$

where λ_e refers to the steady state structure and λ_o the initial or peak structure.

Since the structure of the material is directly related to the viscosity at any time with respect to the shear rate, the viscosity evolution after a shear rate jump can be related by:

$$\frac{\eta - \eta_e}{\eta_o - \eta_e} = \exp(-kt) \qquad [4.2.l]$$

As stated above, the kinetic factor k, is a function of shear rate, therefore k is given by:

$$k = m\dot{\gamma}_f^{\,n} \qquad [4.2.m]$$

where $\dot{\gamma}_f$ is the final shear rate after the jump,

m and n are constants determined experimentally.

The work of Mada and Ajersch was later extended to Aluminium-Silicon composite alloys by Moon et al [Moo 91]. Moon et al agreed that the model proposed by Mada et al seemed to be a solid framework for exploring the structure factors in a thixotropic material. However, the authors did point out that the assumptions to the degree of bonding or agglomeration (where λ is assumed to be 1 at the initial shear rate before the jump) should be looked at in more detail.

Kumar et al [Kum 93, 94a, 94b, 94c] proposed mathematical models to describe the kinetics of the agglomeration evolution of semisolid alloys under shear during transient period when the shear rate is changing. Similar to the work of Mada and Ajersch, the model assumes one internal structural parameter (known as the degree of agglomeration). This parameter varies between 0 (for no agglomeration) and 1 (fully connected or agglomerated particles). The authors described two sets of equations to relate the evolution of the internal structures with respect to the viscosity. The first set describes the flow equation by considering the energy dissipation in the slurry with respect to the shear rate. Similar to the work of Wang et al [Wan 90a], Kumar et al proposed the following equation in terms of apparent viscosity:

$$\eta = A(\lambda)\left\{\frac{\left(\frac{f_{eff}}{f_{\max}}\right)^{1/3}}{1-\left(\frac{f_{eff}}{f_{\max}}\right)^{1/3}}\right\}\eta_L + (n+1)C(T)\lambda f_s {\eta_L}^{n+1}\dot{\gamma}^{n-1} \qquad [4.2.n]$$

where n = 4 following the proposal given by Frost and Ashby [Fro 83] for hot deformation of aluminium,

$A(\lambda)$ (= $\alpha\lambda+\beta$) is the hydrodynamic coefficient dependent on particle size, morphology and geometric arrangement,

f_{max} the maximum packing fraction (given as 0.64);

f_{eff} (= $f_s(1+0.1\lambda)$ the effective fraction solid which includes entrapped liquid.

η_L is the liquid viscosity;

C(T) is a temperature dependent power law coefficient.

C(T), α and β are fitted from the experimental results.

The second set of equations proposed by Kumar et al relates the evolution of viscosity with respect to the structural parameter,λ. This parameter is governed by the agglomeration and de-agglomeration processes. As discussed in Chapter 4.1, both processes occur independently even though both processes can occur simultaneously. Kumar et al proposed that agglomeration is caused by random collisions while de-agglomeration results from the breakdown of particle-particle welds caused by the shear stress imposed on the agglomerate. Hence, the evolution of viscosity with the

internal structure is the difference between the agglomeration and de-agglomeration process. This is given as:

$$\frac{d\lambda}{dt} = \underbrace{H(T)(1-\lambda)}_{(agglomeration)} - \underbrace{R(T)\lambda\dot{\gamma}^{n}}_{(de\text{-}agglomeration)} \qquad [4.2.o]$$

where H(T) and R(T) are constants determined experimentally.

By integrating equation 4.2.o, an expression in terms of viscosity can be obtained:

$$\frac{\eta-\eta_{\infty}}{\eta_{o}-\eta_{\infty}} = \exp\left[-\left(H+T\dot{\gamma}^{n}\right)(t)\right] \qquad [4.2.p]$$

Equation 4.2.p describes an exponential function of the evolution of the degree of agglomeration after an instantaneous shear rate jump. Kumar [Kum 94c] fitted his model to Sn15%Pb alloys and Al7%Si0.6%Mg alloys. Although the model was able to describe both sets of experiments quite accurately, it is not clear in the author's thesis [Kum 94c] what the 'undisclosed factor' was for the results on the aluminium alloys.

Quaak [Qua 96a, 96b] further elaborated the work of Mada and Ajersch (Equation 4.2.l) by proposing that the evolution of viscosity after a shear rate jump of A356 and A356/SiC alloys can be described by a double exponential expression of:

$$\frac{\eta-\eta_{\infty}}{\eta_{o}-\eta_{\infty}} = \alpha\exp\left(-t/\lambda_{1}\right) + (1-\alpha)\exp\left(-t/\lambda_{2}\right) \qquad [4.2.q]$$

where α is the structural parameter between 0 and 1

λ_1 and λ_2 are the breakdown times depending on the initial and final shear rates and fraction solids.

Quaak mentioned that there is a fast breakdown/build-up time during the shear rate jump followed by a slower breakdown/build-up time with increasing time. The assumptions made by Quaak are that during a rapid increase/decrease in shear rate, the outer globules either break more easily (i.e. de-agglomeration from shear rate increase) or formed agglomerates (i.e. agglomeration from shear rate decrease).

With increasing shear, the agglomerates are broken up more with time at the higher stirring speed, while on the other hand, with decreasing shear rate, the agglomerates form stronger welds between each other with increasing time at the lower shear rate, hence giving an increase in the shear stress.

More recently, Journeau et al [Jou 00] proposed a model by relating the particle sizes to the viscosity,η, for continuously cooled semisolid alloy using a modified Arrhenius relationship:

$$\eta = e^{2.5C\Phi} \qquad [4.2.r]$$

where Φ is the solid volume fraction

$$C = \frac{\frac{4}{3}\sum D^3_{\max}(i)}{\sum V(i)}$$

D_{max} is the particle largest segment length

V is the particle volume

[i] is the particle number

The value 2.5 is the value used in Einstein equation for spheres in suspension (i.e. equation 4.2.r).

By comparing the results from Spencer et al [Spe 72] and Joly [Jol 74, 76], the authors found that the value of C=6 was able to fit the experimental viscosity data obtained. However, the model did not take into account the effect of shear rate hence this model should be used only as a first approximation to the effect of viscosity in semisolid alloys.

More recently, Fan [Fan 02] proposed mathematical models based on the formation and disruption of agglomerates in semisolid slurries. By considering the effective fraction solid (i.e. taking into consideration liquid entrapment between agglomerates) and the effect of particle size under external flow conditions, the authors put forward a series of mathematical models and obtained good agreement with the experimental results from Joly [Jol 74, 76].

For steady state viscosity on semisolid slurries, the time evolution of the structural parameter, n(t), based on agglomeration and de-agglomeration process is given as:

$$\frac{1}{n(t)} = \frac{1}{n_e} + \left(\frac{1}{n_o} - \frac{1}{n_e}\right)\exp^{-\lambda t} \qquad [4.2s]$$

where n_e is the average agglomerate size at time $t = \infty$ (i.e. at steady state)

n_o is the average agglomerate size a $t = 0$

and λ describes the particle morphology based on the agglomeration and de-agglomeration rates.

The authors proposed that the viscosity of a semisolid slurry is a direct function of the viscosity of the liquid matrix and its effective solid fraction (ϕ_{eff}) given by:

$$\eta = \eta_O \left(1 - \phi_{eff}\right)^{-5/2} \qquad [4.2t]$$

$$\phi_{eff} = \left(1 + \frac{n-1}{n} A\right)\phi \qquad [4.2u]$$

where A is a parameter related to the packing mode.

Using the concept of agglomeration and de-agglomeration process for thixotropic behaviour, the authors considered the characteristic agglomeration time (t_A) and de-agglomeration time (t_D) to describe the transient state behaviour of semisolid slurries:

$$t_D = \frac{2\pi d^3 (n_e - n_o)}{6n_o\left(\alpha_2 \phi n_o + 2\alpha_1 \phi^2\right)K_a - \pi d^3 n_o (n_o - 1)K_d} \qquad [4.2v]$$

$$t_A = \frac{2\pi d^3 (n_e - n_o)}{6\left(\alpha_2 \phi n_e^2 + 2\alpha_1 \phi^2 n_e\right)K_a - \pi d^3 n_e (n_e - 1)K_d} \qquad [4.2w]$$

where K_a and K_d are the average agglomeration rate and de-agglomeration rate respectively, α_1 and α_2 are model parameters and d is the particle size.

There exists certain dispute as to what type of model is appropriate in describing the rheological behaviour of semisolid alloy slurries. Most notably is the use of a yield stress. Peng et al [Pen 96] and Modigell et al [Mod 99] proposed the use of a yield stress in their mathematical models. Both authors used the model proposed by Herschel-Bulkley where:

$$\tau = \tau_a + k\dot{\gamma}^n \qquad [4.2.x]$$

where τ_a is the apparent yield stress
k and n are material constant determined experimentally
(τ_a, k and n are all fraction solid dependent.)

Mathematical models used for partially re-melted alloys are generally the same as those used for partially solidified alloys except that the models are usually defined in terms of shear stress and strain rate [Lax 80, Wah 00, Fin 00]. Most experiments on partially re-melted alloys are carried out using compression methods. However, it should be noted that the stress-strain rate in these experiments is highly inhomogeneous due to the presence of friction. Laxmanan and Flemings [Lax 80] have shown that it is possible to obtain viscosity from the force-displacement curves for Sn15%Pb alloys using solutions derived from the viscous power law model. P.Kapranos et al [Kap 98, 01] have done experiments supporting the work of Laxmanan and Flemings on aluminium alloys. It should be noted though that there is debate as to whether steady state is achieved during the test. However, the compression test does allow the prediction of die-filling behaviour of semisolid alloys as employed in the industry.

Other models used to describe the rheological behaviour of semisolid alloys have been carried out using either Computational Fluid Dynamics (CFD) packages or Finite Element (FEM) analysis. An example where CFD packages are used to simulate the flow behaviour of partially re-melted alloys under compression testing was done by P.Ward et al [War 00a and 00b]. Mathematical models used in computer packages consist of the basic models discussed earlier. The models most frequently used are the Carreau model (an extension to the Cross model, Table 2.21B) or a modification to the Bingham model. Finite element analysis provides another method to predict the die-filling behaviour of semisolid alloy slurries. Elaborating on both CFD and FEM packages is outside the scope of this research work.

CHAPTER 5

Experimental Procedures

This chapter describes the experimental procedures used throughout the research. Two types of experiments were conducted: (1) Viscometry Experiments and (2) Rapid Compression Experiments. As with any kind of experiments, sources of errors have to be accounted for and the accuracies of each experiment will be discussed.

5.1a Viscometry Experiments

For the viscometry experiments, a rotating viscometer consisting of coaxial cylinders is used. The viscometer used is of the Searle type, i.e. a rotating inner cylinder (or a stirrer) in an outer stationary cylindrical cup. The test specimen fills the annulus gap between the inner and outer cylinders. The rotating action from the stirrer is achieved by a direct current motor and the torque imposed by the specimen is measured from a torque transducer. A coaxial rotating viscometer is used because the shear field in the annulus gap can be considered as a one-dimensional flow problem [Who 92] and where shear rate variation is minimal [Appendix 2].

Figure 5.1a shows a schematic diagram of the viscometer used. The viscometer consists of a stainless steel outer and inner cylinder placed in an electric furnace. The cylinders are grooved on their surfaces to ensure no segregation of solid phase particles. **Table 5.1a** shows the physical dimensions of the viscometer. Inert gas is passed into the cylinders to protect the specimen from oxidation.

For this work, the inert gases used to prevent oxidation of the SnPb alloy are argon or nitrogen. It was observed that a liquid flux is needed when using nitrogen gas to prevent oxidation of the alloy specimen. The flux is placed on top of the specimen. Due to its very low viscosity, the flux does not affect any subsequent measurements on the SnPb alloy. Argon gas though as effective, is considered too expensive compared to using the nitrogen gas and the liquid flux.

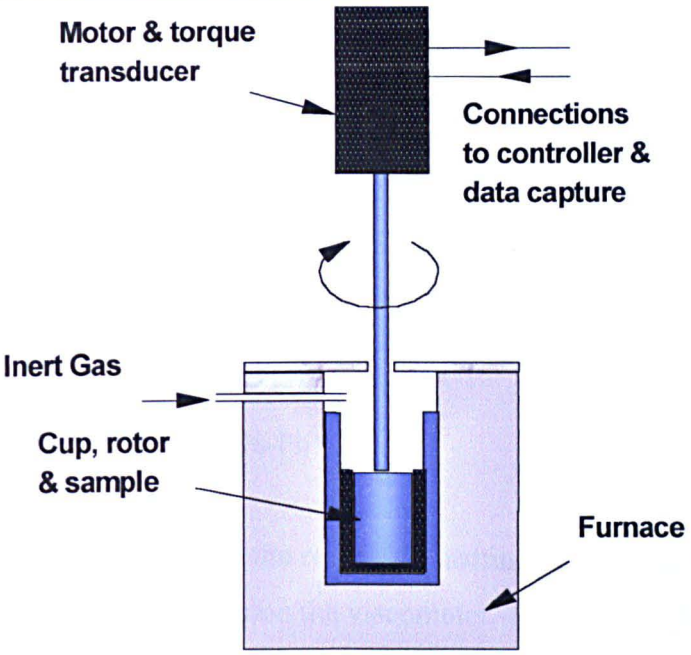

Figure 5.1a. Schematic diagram of the rotating viscometer.

Table 5.1a

Measuring Head (Haake M5)	
Maximum Torque	4.9 Ncm
Maximum Speed	500 rpm
Minimum Speed	0.05 rpm
Sensor System (SV2P)	
Inner Cylinder (Stirrer)	
Radius R_1 (mm)	10.1
Height L (mm)	19.6
Outer Cylinder (Cup)	
Radius R_2 (mm)	11.55
Radii Ratio (R_2/R_1)	1.14
Gap Width (mm)	1.45
Temperature Range (°C)	Room temperature to 250

5.1b Material Used

Due to the limitations of the viscometer (maximum temperature ~ 250 °C, Table 5.1a), the specimens used are of low temperature nature. The specimens tested are:

(i) Air
(ii) 1 Pas Silicone Oil
(iii) Tin - Lead alloy (Sn-Pb)

Air is used to validate the recording instruments. It was found later that it also produces valuable information on the viscometer. This will be discussed later.

The 1 Pas Silicone Oil is used to calibrate the viscometer. The accuracy of the silicone oil was checked by the manufacturer using a long capillary viscometer prior to sale. Accuracy is in the order of ± 0.17%.

Sn-Pb alloy are first cast by melting 99.9 % pure tin with lead to produce the desired proportions. During the casting process, the materials are stirred to ensure homogeneity and nitrogen gas is passed over the melt to reduce possible oxidation. After casting into the mould, the specimen is cut to an appropriate size for use in the viscometer. The compositions of the Sn-Pb alloys are checked by using chemical composition analysis. All Sn-Pb alloys are obtained with a composition of Sn15%Pb (± 0.5 weight %). This composition is used in order to do a qualitative comparison with the works from other workers.

5.1c Software used

The viscometer is a Haake ME500 viscometer with a M5 measuring head. A control unit (Haake Rotovisco RV20) controls the motor head and provides signal output of the shear rate and shear stress to a 486 computer. Haake software (Rotovisco Version 2.2) allows the choice of the shear rate and run time for the experiment. Shear stresses measured via a torque transducer, are recorded and plotted in the computer.

The software allows different graphs to be plotted simultaneously (i.e. viscosity versus shear rate, time and shear stress). However, the initial data collection rate of the software (~100 Hz) was too slow for the purpose of this research, i.e. to observe the transient behaviour of a thixotropic semisolid slurry during a rapid change in shear rate. A faster data card (Strawberry Tree Inc., [Str 89]) is therefore used. A schematic diagram of the program used in the data card is shown in Appendix 3. This data card allows up to 1 kHz of capture rate. Results from the data card are captured in terms of analogue signal from the control unit (RV20, which gives an output of ± 10 V for both the shear stress and shear rate, [Hak 91]). The analogue signal can be converted to the appropriate shear rate and shear stress by:

(1) Shear rate, D:

$D = M \,.\, \%D \;\; (s^{-1})$

where M is the shear rate factor (= 3.9 for the SV2P system) and %D is the present shear rate set.

(2) Shear stress, τ:

$\tau = A \,.\, \%\tau$ (Pa)

where A is the shear stress factor (= 37.6 for the SV2P system) and $\%\tau$ is the shear stress value on display.

5.1d Experimental Procedures

Several types of experiments were carried out on the viscometer. In the air experiments, the viscometer was subjected to various shear rate changes. The initial shear rate range was from 0 to 100 s^{-1} while the final shear rate range was from 10 to 200 s^{-1}. For the experiments on silicone oil (viscosity 1 Pas), the experimental procedures followed that of the air experiments. Three main types of experiments were carried out with the Sn15%Pb alloy.

5.1d(i) Continuous cooling experiments.

In this experiment, the stirrer is first aligned in the outer cylinder cup. After alignment, the Sn15%Pb alloy is melted at 240 °C and left for a few minutes so that gravity brings the stirrer slowly into the melt ensuring that no air bubbles are entrapped in the bottom part of the viscometer. The temperature is then decreased at a rate of 1°C/min while stirring the melt. Several different shear rates were employed to give a comparison of the effect of stirring rate on the torque and/or viscosity

behaviour of the alloy under continuous cooling. With decreasing temperature, the torque imposed by the alloy on the stirrer increases as the primary phase solidifies. Finally, stirring is interrupted as the maximum available torque from the viscometer is reached.

5.1d(ii) Isothermal holding experiments

In the isothermal holding experiments, the procedure follows that of the continuous cooling experiments except that temperature is set at a specific value (corresponding to a particular fraction solid) in the semisolid region. After reaching the specific temperature stirring is continued at that temperature until a constant stress or viscosity is achieved. This viscosity is known as the steady state viscosity and is related to the steady state structure of the alloy. The experiment is conducted again at a different shear rate (or stirring rate). The range of fraction solid is in the range of 0.2 to 0.5. This experiment also allows the 'conditioning' of the alloy slurry so that the slurry's structure is constant prior to a shear rate change (i.e. step change experiments).

Experiments on the effect of rest times, whereby coarsening and agglomeration processes can take place, are also investigated by relating the measured peak stress encountered after stopping the stirring of the alloy slurries for different rest times at the specific fraction solid.

5.1d(iii) Step change experiments

In the step change experiments, the alloy slurry is first held at an initial shear rate where viscosity or shear stress is constant before an abrupt increase or decrease in shear rate. The temperature corresponding to the fraction solid is held constant throughout the experiments. The viscosity measured immediately after the change in shear rate is known as the iso-structure viscosity. This experiment allows the investigation of the transient behaviour of semisolid alloy slurries during a rapid change in shear rate. It also allows the investigation of the shear thinning and thixotropic response of the semisolid alloy slurries under different shear rates.

5.2 Rapid Compression Experiments

Rapid compression experiments are done on a vertical forging press. Heating is controlled by a Taylor-made Induction heating system that allows accurate control of the temperature. The frequency can be varied from 800 Hz to 10kHz, with a maximum of 100 kW.

Rapid compression experiments are conducted for higher temperature alloys and at higher fraction solids than can be achieved by using the rotating viscometer. Figure 5.2a shows a schematic diagram of the vertical forging press.

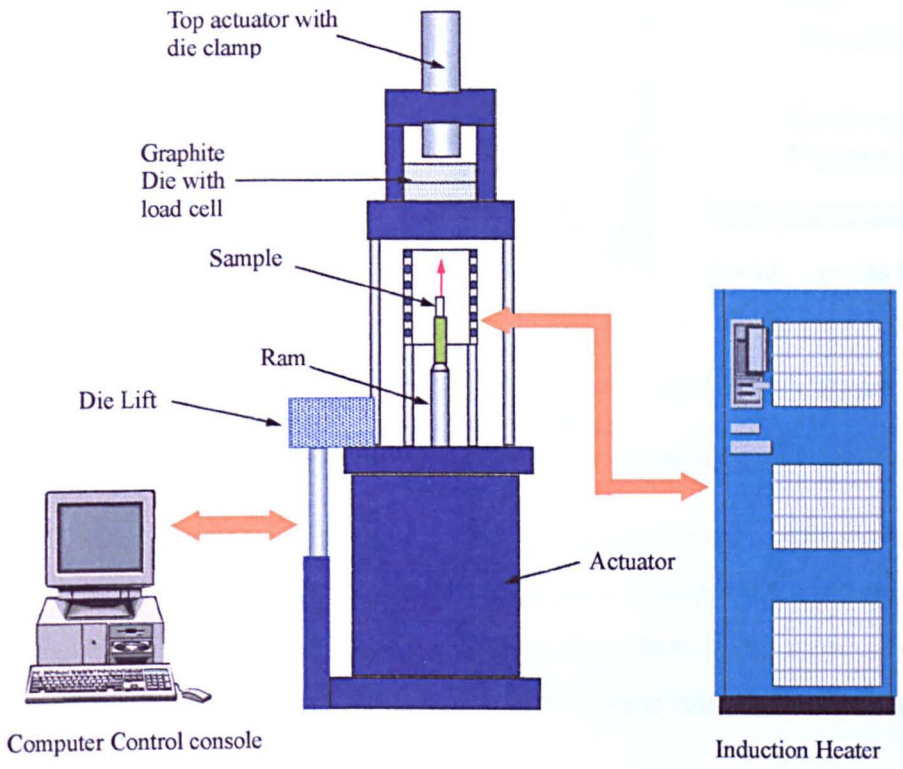

Figure 5.2a: Schematic diagram of the vertical forging press (i.e. Thixoforming press) used in Sheffield University for the rapid compression experiments.

The specimen or slug (dimensions: 42mm high, 36 mm diameter,ϕ) is placed on a ceramic pedestal and heated up to its desired temperature (or fraction solid). Upon reaching the desired temperature, the slug can either be held at that temperature for a period of time (providing the material does not slump) or be forged immediately

into a heated or non-heated metallic (or non-metallic) die. Compression load is recorded as a function of time onto a computer via the load cell located on top of the die (see Figure 5.2b)

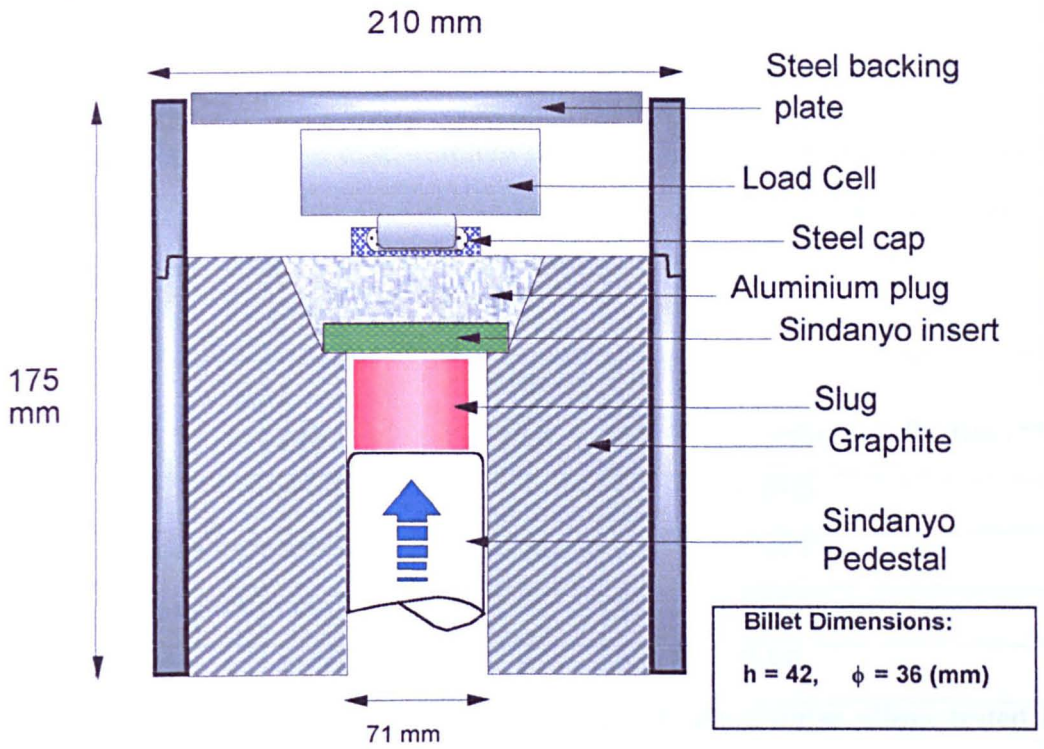

Figure 5.2b. Schematic diagram of the load cell used in the thixoforming machine to record the load versus time signals.

Shear rate can be estimated analytically following the work of Laxmanan and Flemings [Lax 80]. Results obtained from the rapid compression experiments using the Laxmanan and Flemings approach will be discussed later. It should be pointed out that such an experiment does not produce a constant shear rate but one that increases continuously.

Despite this, the tests can provide useful information about the behaviour of semisolid alloys when relating the results obtained with those from the viscometry experiments.

5.2b Material Used

Two main types of alloys were used in the rapid compression experiments. They are:

(i) Aluminium alloys

(ii) Sn15%Pb alloys

Various compositions of aluminium alloys have been used. Table 5.2b shows the composition of the aluminium alloys tested and their feedstock (raw material) production routes.

Manufacturer	Alloy	Composition (%)*			Production Routes (**)
		Si	*Cu*	*Mg*	
Alusuisse	A356	7.0	-	0.3	MHD
NorthWest Aluminium	A319	6.0	3.0	3.0	SSTT
NorthWest Aluminium	A357	7.0	-	0.6	SSTT
Sheffield	A357	7.0	-	0.6	RAP

Table 5.2b. Compositions and production routes of aluminium alloys tested in the rapid compression testing.

* *Si = Silicon, Cu= Copper, Mg = Magnesium*

** *Descriptions of the various production routes were introduced in Chapter 1.*

5.2c Software Used

The forging press is controlled by a computer equipped with a Servotest DCS 2000 digital control system. The data collection acquisition rate can be up to 2kHz. The software allows a number of parameters to be specified by the operator. They are: the speed of transfer of the slug into the die, the velocity profile of the ram during the slug's injection into the die, the magnitude of the final load applied and the time duration of its application (i.e. holding time). Analogue signals obtained from the load cell are collected by the computer controller and can be easily transferred into Microsoft Windows Excel software for analysis.

5.2d Experimental procedures

Experiments were carried out under different conditions. They are:

(1) Varying temperatures (hence fraction solid). The specimens are heated to different temperatures before the compression experiments. The force signal is then related to the displacement of the pedestal. The fraction solid is usually above 0.5 in the rapid compression experiments

(2) Varying the holding time. Specimens are held for a range of time (0 to 5 minutes) at the specified temperature before compression. Care should be taken in ensuring that the specimen is able to support its own weight without slumping.

(3) Varying the ram speed (the injection speed at which the compression experiments are done). Several speeds were employed. They range from 150 mm/s to 1000 mm/s. In this experiment, both the temperatures and soak times are held constant.

(4) Isothermal experiments. The specimen is heated up to a specific temperature in the induction heater on the thixoforming rig and held for different holding times (0 to 5 hours). The slug is then quenched rapidly in water and the microstructure is examined to investigate the coarsening process.

(5) Temperature uniformity was checked by the use of two thermocouples, one at the edge and another placed in the centre of the specimen.

5.2e Metallographic Examination

Slugs from the compression testing and viscometry experiments are sectioned into the appropriate shape for grinding and polishing. These specimens are then cold mounted (for Sn15%Pb alloys) or hot mounted (for aluminium alloys).

Grinding was done in sequence from 240 grains down to 1200 grains. However, it was noted that during the grinding of Sn15%Pb alloys, fresh grinding paper should not be used as it tends to scratch the sample's surface. Soap water is sprayed before grinding commenced on Sn15%Pb alloys.

Polishing for aluminium alloys was done in three stages:

(1) Stage 1: 6 μm diamond paste with extender. Time: 5 to 10 minutes.

(2) Stage 2: 3μm diamond paste with extender. Time: 5 to 10 minutes

(3) Stage 3: Silco for 4 minutes and *water only* for 1 minute.

(4) Stage 4: Etching using hydrochloric acid to bring out the features of the microstructures under the microscope (for aluminium alloys only).

The polishing procedures for Sn15%Pb alloy follow those for the aluminium alloys except that, at each stage, the sample is 'cleaned' by fast etching using 0.5% Nital. The reason is that lead tends to smear during the polishing stages and the etchant helps to remove the smear. Finally, on the third stage, the time was reduced to 1 minute as the Silco particles will scratch the soft surfaces of Sn15%Pb alloys. Etching using 0.5% Nital was done after the polishing stages for about 30 seconds to bring out the microstructures.

Samples for both alloys are cleaned at each stage (during grinding and polishing) to remove any remaining grit. An Image Analyser has been used to capture the polished microstructures and values of the particle areas and perimeters obtained. The spheroidicity of the particles are measured according to the formula proposed by T.Witulski et al [Wit 98]:

$$FormFactor, FF = \frac{4\pi(Area)}{(Perimeter)^2} \qquad [5.3a]$$

where a value of 1 indicates a spherical particle.

5.3 Sources of Errors

5.3a Errors in Rotational Viscometer

Several common error sources were considered in the viscometry experiments:

(1) Inertia effects

During shear rate jumps, inertia effects from the stirrer system were taken into account. Figure 5.3.a1 shows the effect of inertia from the stirrer system. Shear rate jumps in air and 1 Pas Newtonian oil produce a similar shear stress versus time curve pattern. By subtracting these two curves, it can be seen that the peak produced in the Newtonian oil has disappeared (green curve). This shows the expected behaviour of a Newtonian fluid, i.e. shear stress increases with increasing shear rate.

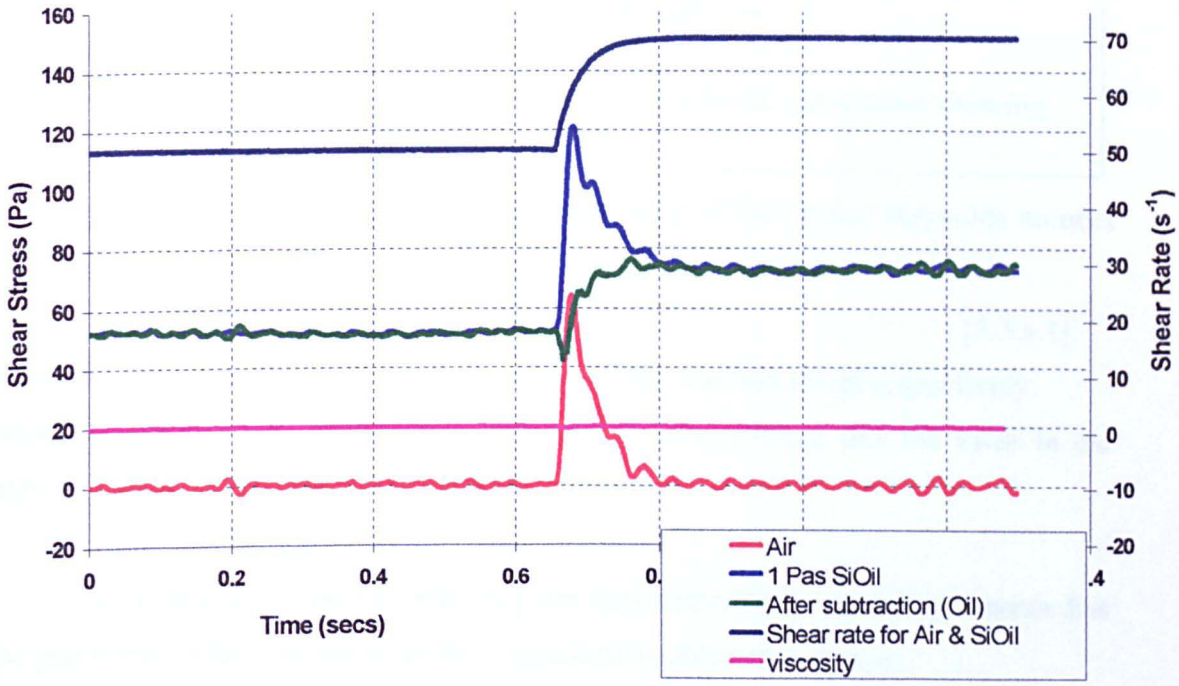

Figure 5.3.a.1. Graph showing the effect of inertia. This effect can be eliminated by subtracting the result for the SiOil with that from the experiment carried out in air.

(2) Taylor Vortices

The flow pattern in a fluid depends also on the geometry of the system. In the viscometer where the inner cylinder rotates, the fast-moving fluid near the rotating inner cylinder tries to move outwards.

Since it cannot do so (due to its constraints between the cylinders), it circulates outwards locally (Figure 5.3a.2) forming 'Taylor Vortices'. With increasing speed of rotation, the flow becomes turbulent. Taylor vortices cause an increase in applied torque at a given rate of rotation.

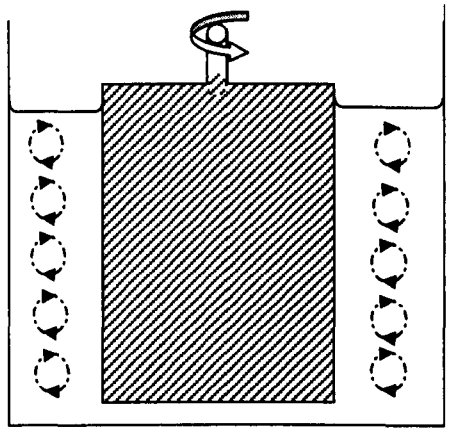

Figure 5.3.a.2. Secondary flow pattern in a Searle viscometer showing Taylor vortices. [Who 92]

According to Taylor, such vortices will occur if the critical Reynolds number (Re_{cr}) of the fluid is:

$$Re_{cr} > 41.3\,[R_o/(R_o-R_i)]^{1/2} \qquad [5.3.a.1]$$

where R_o and R_i are the outer and inner radius of the cup and stirrer respectively. Using the values of R_o and R_i from Table 5.1.A, it was found that the value in the right hand side of equation 5.3.a.1 is 116.

According to Whorlow [Who 92], the Reynolds number in the viscometer has the gap width of the viscometer as the characteristic dimension, hence:

$$Re = \frac{\Omega \rho R_i (R_o - R_i)}{\eta} \qquad [5.3.a.2]$$

where Ω is the rotational speed;

η is the viscosity of the fluid and

ρ the density of the fluid

For a semisolid Sn15%Pb alloy of fraction solid 0.36, the estimated semisolid density is given as 7500 kg/m^3 [Jol 74] and viscosity as 0.087 Pas at a shear rate of 200 s^{-1} [Mcl 93].

The critical Reynolds number was found to be about 34. Since this value is smaller than the value of 116 found from equation 5.3.a.1, it was concluded that no Taylor vortices occur and the flow was within the laminar steady shear regime (i.e. no turbulence flow was expected).

(3) End and Edge effects

The end effect is the torque acting on the bottom surface of the stirrer. Below the stirrer, the sample is sheared at a lower shear rate and this may give rise to higher torque values at the bottom surface. Edge effect is the torque originating from turbulence at the edges of the stirrer where a high Reynolds number could be present. Since it was concluded in the preceding paragraph that turbulent flow was not expected, edge effects from the stirrer were not expected. A most common method of measuring end effects [Who 92] is by measuring the torque of the fluid sample at a given rotation speed using various filling heights in the gap and extrapolating the torque/height curve to zero height (where no material is in the gap). To overcome the end effects, several techniques have been proposed [Who 92]: (1) Fixed guard cylinders at either end of the cylinder on which the torque is measured and (2) By designing the base of the cylinder such that an air bubble is trapped beneath it. This method is adopted by the viscometer used in this research. Although the above two methods may eliminate end effects to a certain extent, there still is uncertainty in the accuracy of the measurements obtained [Who 92]. It should be noted that the high viscosity of the Sn15%Pb alloy tested allows the contribution of any end or edge effects to be minimal with respect to the general behaviour of semisolid slurries.

(4) Wall Slip

A comprehensive review of wall slip is given by Barnes [Bar 95] on various particle suspensions. Wall slip is considered to be the migration of solid particles away from the cylinder wall during shear. It can occur for a number of reasons, usually when the presence of the wall changes the properties of the sample close to the wall.

In the case of a suspension, a local reduction in the concentration of particles might be produced [Qua 96a]. Wall slip can be overcome by using a grooved surface. This was shown by the work of Mclelland [Mcl 93], Henderson [Hen 93] and Koke [Kok 00]. Koke et al showed that a smooth cylinder wall gives a much lower stress value than a grooved surface. The author attributes this behaviour to wall slippage and particle segregation. However, using grooved cylinders induces an uncertainty in the value of the gap width used in the calculations of the shear rate, shear stress and viscosity [Who 92, Bar 95]. Most workers however, assume that the material in the grooves does not flow hence gap width is usually taken from the top of the groove ridge. Microstructural examination by Mclelland [Mcl 93] and Quaak [Qua 96a] showed no particle segregation from the grooved wall. Figure 5.3.a.3 shows a micrograph of a Sn15%Pb alloy (fs=0.4) taken from the current work. No particle segregation from the grooved wall can be seen from the microstructure.

(5) Temperature Uniformity

Temperature variations could be a significant source of error. It was pointed out in Chapter Two that the viscosity follows an exponential relation and in semisolid slurries, the fraction solid and thus the viscosity is strongly dependent on temperature.

Temperature variations may occur from temperature control deviations or viscous heating from the sheared material. Temperature measurements using thermocouples on the inner stirrer and outer cup were compared to the temperature controller. Measurements were found to have an accuracy within 1 °C of the actual slurry temperature under any fixed temperature. During shearing of the material, possible increase in the temperature of the slurry may occur (hence a decrease in fraction solid and shear stress) due to frictional forces between the solid particles. A thin thermocouple was inserted in the slurry (without impeding the stirrer motion) during steady shearing and shear rate ramped up and down to detect any increase in temperature. The temperature variation was within 0.5 °C. Using the Scheil equation to calculate the fraction solid within this variation, it was found that the fraction solid varies by ± 0.01.

Figure 5.3.a.3: Sn15%Pb alloy microstructure showing no particle segregation in the viscometer.

5.3b Errors in Rapid Compression Experiments

In the rapid compression experiments, temperature control from the Taylor-made induction heating system was found to be sufficiently accurate and consistent to within 1 °C.

(1) Temperature uniformity

Two thermocouples were placed on the edge and centre of the specimen during the heating. The temperature in the slug between these two positions was found to vary by about 1 °C. However, no measurements were made during the forming operation into the die cavity. Temperature loss is expected to occur but it is not considered to be significant since the speed of operation is very fast. Furthermore, there is low thermal conductivity from using a ceramic (sindanyo) pedestal and ceramic die inserts in the thixoforming machine.

(2) System compliances

Due to the die design in the thixoforming press machine, it was noted that there is an additional displacement during the forming process. As shown in Figure 5.2b, there is a deliberate gap between the steel backing plate and the load cell. This is to ensure that when the die is clamped, the load cell does not record any additional force from the clamp. As a result, during the rapid compression testing, this gap would result in an additional displacement. This displacement would be accentuated when applying the Laxmanan and Flemings's method [Lax 80] to obtain the related viscosity from the compression results.

(3) Velocity inaccuracy

The ram velocity varies during the test as it is calculated from the time and displacement of the ram and not measured directly. Figure 5.3b shows a plot of the actual velocity plotted against time. It can be seen that the velocity is not constant during the experiment. However this variation is small during the compression, denoted between the two red dotted lines in Figure 5.3b is the start and towards the end of the experiment, therefore the nominal velocity is usually used.

Figure 5.3b: Variation of actual ram velocity (nominal velocity specified at 500 mm/s) during rapid compression testing

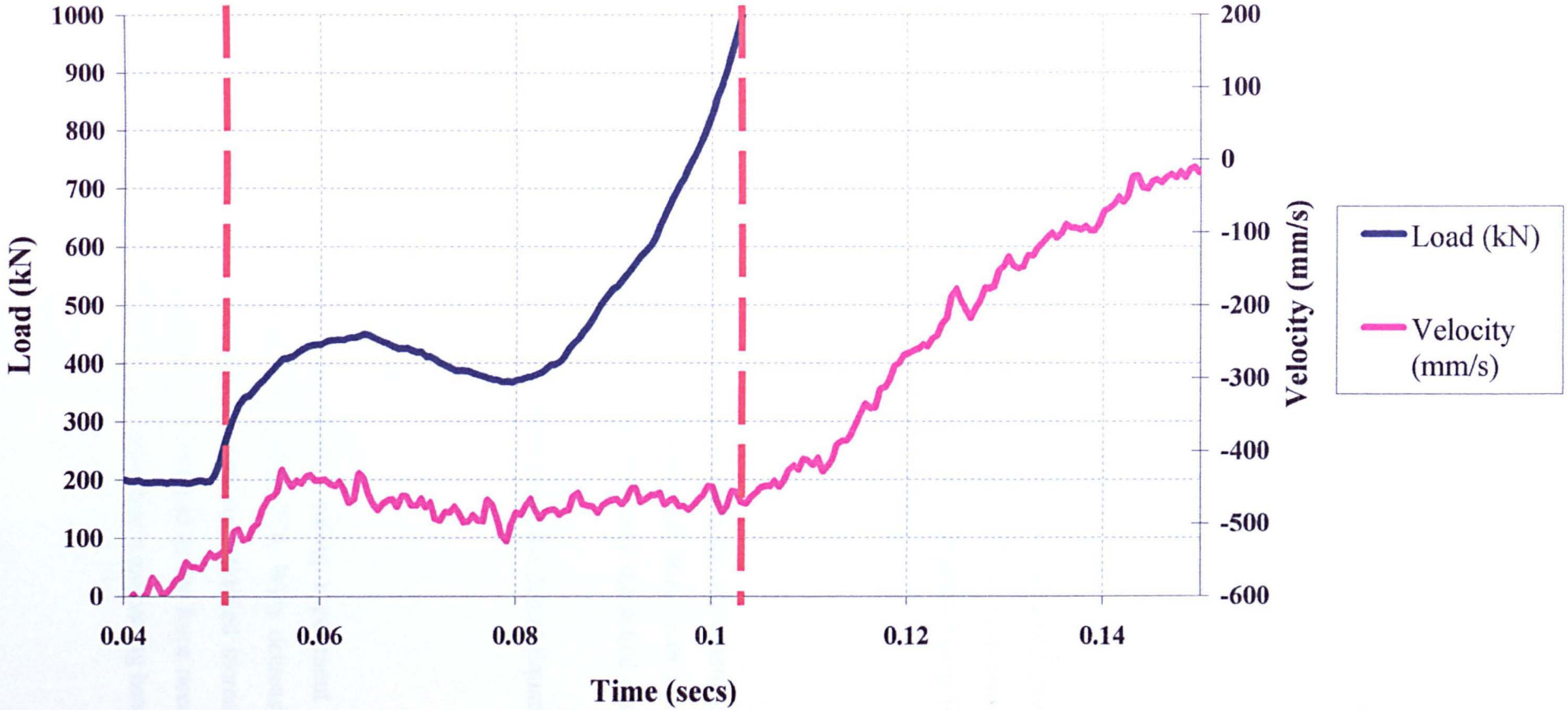

Chapter 6

Results

In this chapter, results of the viscometry experiments on semisolid Sn15%Pb alloys are given, beginning with the effect on viscosity of increasing shear rate and the steady state apparent viscosity at different shear rates and fraction solids. This is followed by results on step change experiments showing the thixotropic response of the semisolid Sn15%Pb alloy slurries under different conditions. A qualitative comparison of the results obtained with other workers will be given in the next Chapter.

The second part of the chapter gives the results of the rapid compression experiments on aluminium alloys and Sn15%Pb alloys under different thixoforming conditions. Results on isothermal holding experiments in the induction heater will also be presented.

6.1 Viscometry Experiments on Sn15%Pb alloys

It was mentioned in Section 5.3 that inertia effects from the viscometer can be accounted for by a simple subtraction method. Hence, all shear rate jumps presented in this chapter have the inertia taken off, showing only the actual slurry behaviour.

Fraction solid of the Sn15%Pb alloy is determined using the Scheil Equation (see Figure 3.2b)

6.1.1 Viscosity behaviour during continuous cooling

Figure 6.1.1a shows the results of a continuous cooling experiment on Sn15%Pb alloy cooled from its melting temperature (220 °C). With decreasing temperature as the alloys is cooled (1 °C/minute), the fraction solidified increases hence increasing its viscosity. Finally the experiment is stopped as the force needed to stir the slurry reaches the maximum allowed by the viscometer's measuring head.

Figure 6.1.1a: Continuous cooling experiments on SN15%Pb alloys under different shear rates (cooling rate=1°C/min)

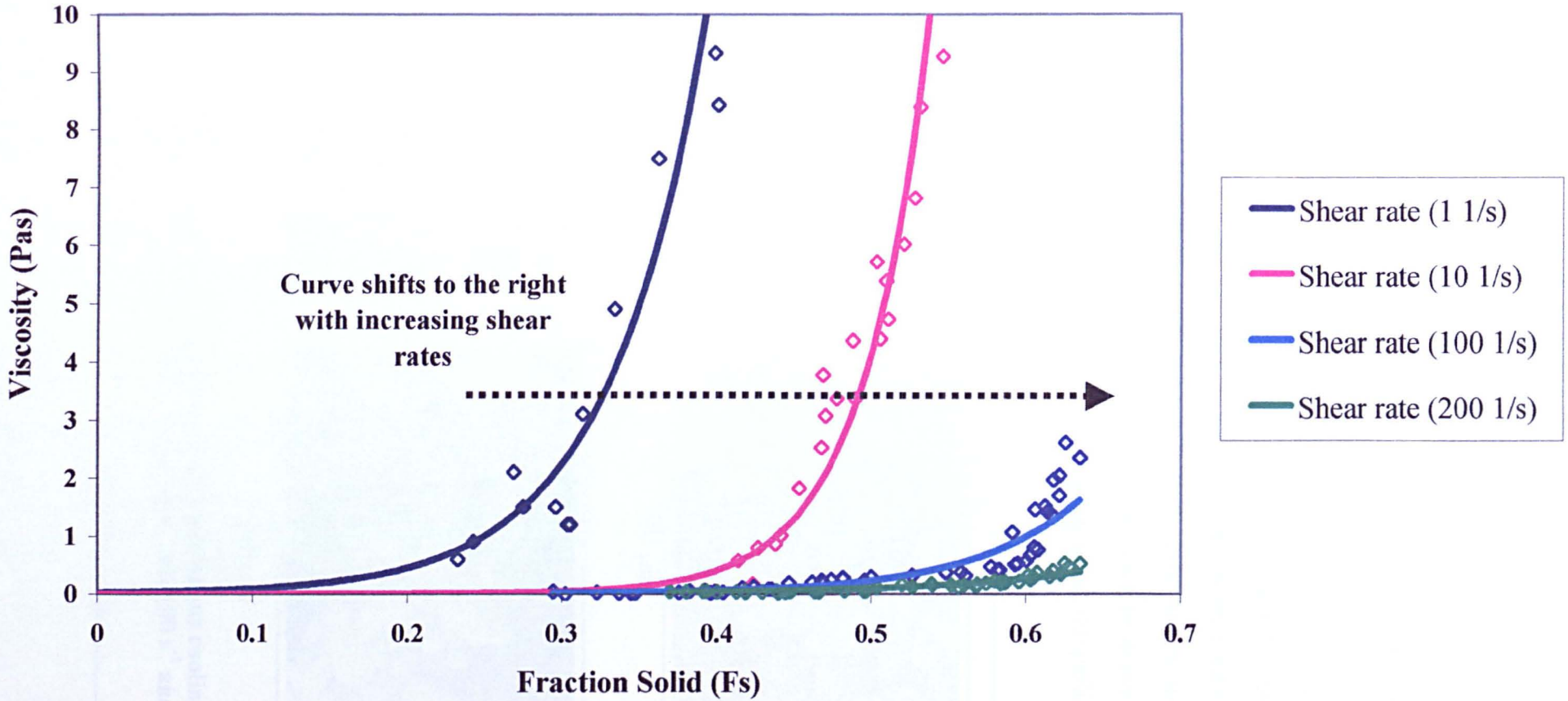

Figure 6.1.1a also shows the viscosity behaviour when the slurry is stirred at different rates. The higher the shear rate, the lower the viscosity encountered and the higher the fraction solidified which can be reached before the experiment is stopped (i.e. curve shifts to the right, shown as dotted arrow, towards a higher fraction solid).

The results showed similar viscosity behaviour compared with other workers [Section 4.1] where the viscosity decreases with increasing shear rate and decreasing cooling rate. It is not possible to vary the cooling rate with the viscometer used here. However, the experiment has shown that shear rate has a significant influence on the viscosity and is affected by the primary particles. Figures 6.1.1b to 6.1.1e shows the microstructures at the various shear rates. With increasing shear rates, the particles become smaller and more spheroidal.

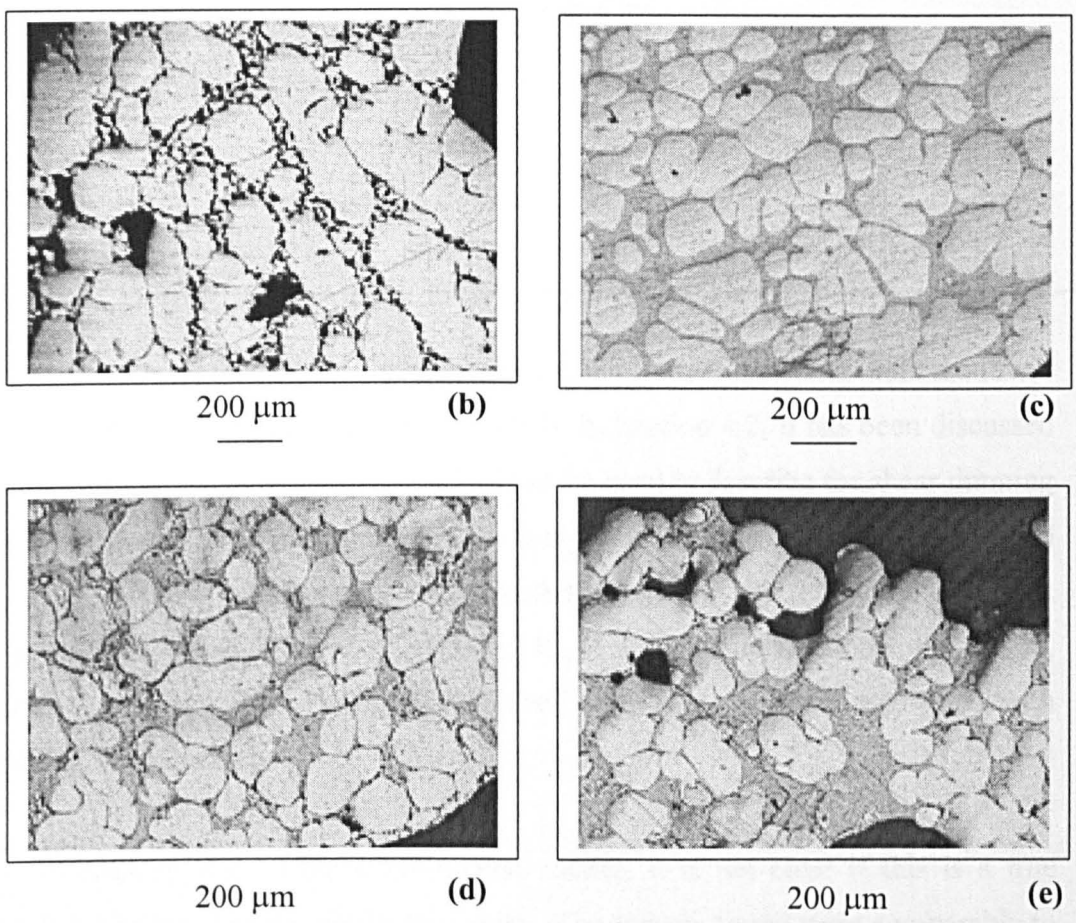

Figure 6.1.1. Microstructures of Sn15%Pb alloy under continuous cooling experiment under various shear rates at: (b) 1 s^{-1}, (c) 10 s^{-1}, (d) 100 s^{-1} and (e) 200 s^{-1}.

6.1.2 Viscosity behaviour from isothermal experiments

The main purpose of the isothermal experiments is to obtain the apparent steady state viscosity at a fixed fraction solid and shear rate. Figure 6.1.2a shows the apparent steady state viscosity decreasing with increasing shear rate for solid fractions of 0.2, 0.36, 0.4 and 0.5 (corresponding to 205, 200, 198 and 195 °C).

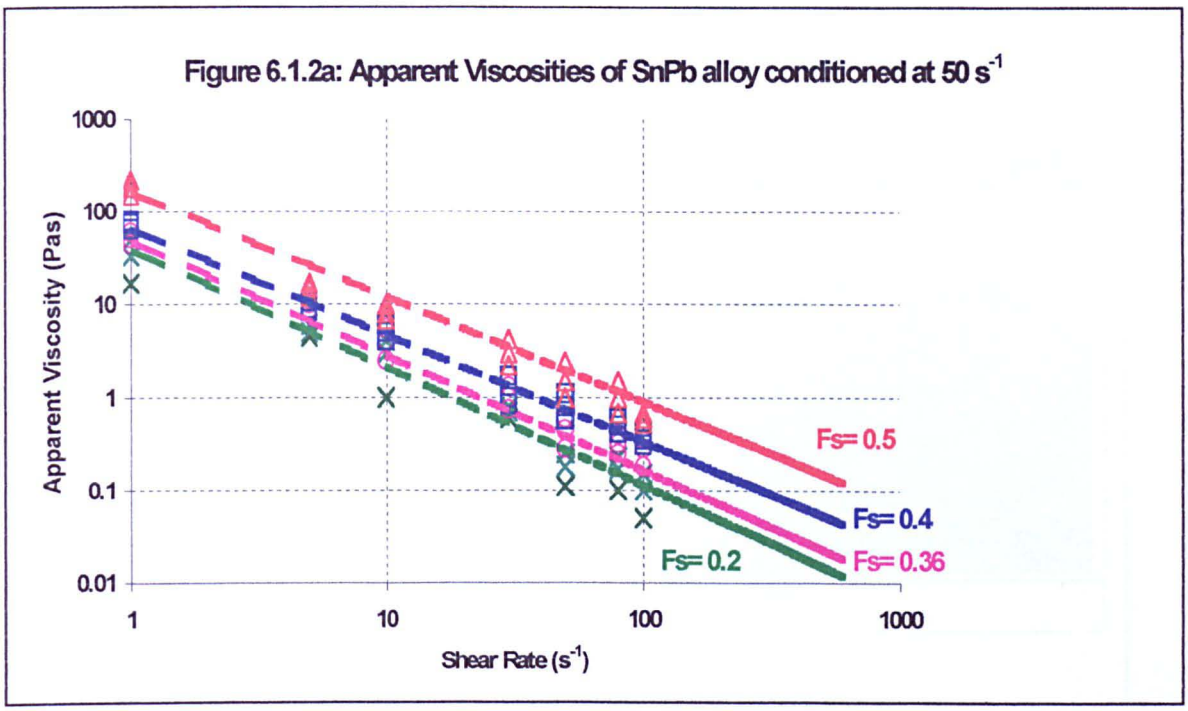

Figure 6.1.2a also shows that the viscosities at any given shear rate are lower at lower fraction solid (as would be expected). In Section 4.2, it has been discussed that a power law equation [equation 4.2.c] can be used to describe the shear thinning behaviour based on the apparent viscosity and shear rate of the Sn15%Pb alloy. In Figure 6.1.2a, the results have been fitted with the equation and the power law index 'n' values were found to be –1.27, -1.24, -1.15, -1.13 for solid fractions of 0.2, 0.36, 0.4 and 0.5 respectively. The indices seemed to indicate a decreasing value with increasing solid fractions.

However, due to the experimental scatter, it is not clear if this is a true indication of a trend in the power law index. The indices found were comparable to the work of A.McLelland [Mcl 93] who found the power law indices to lie between –1.2 and –1.4 for Sn15%Pb alloy at the same fraction solid of 0.36.

Figures 6.1.2b to 6.1.2e show the various microstructures of Sn15%Pb alloys at Fs=0.2, 0.36, 0.4 and 0.5 respectively. With increasing fraction solid, the solid particles agglomerate and coarsened.

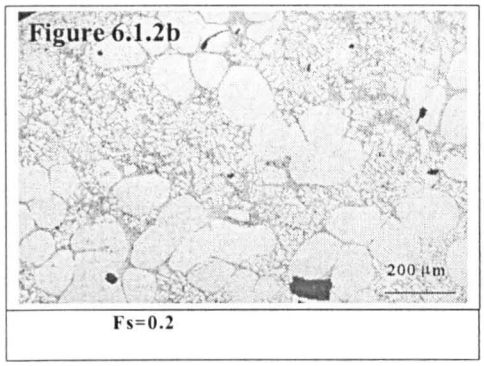

Fs=0.2

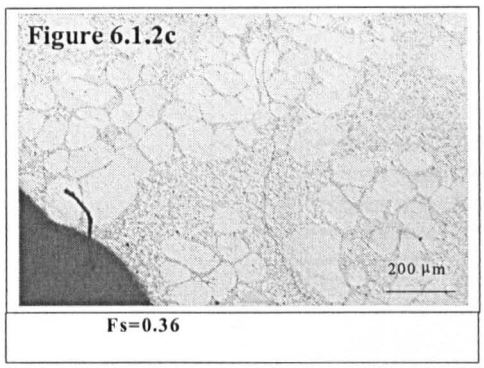

Fs=0.36

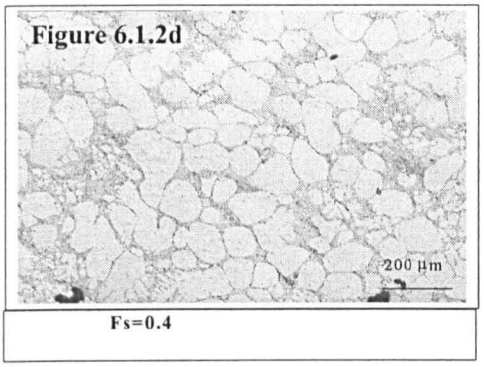

Fs=0.4

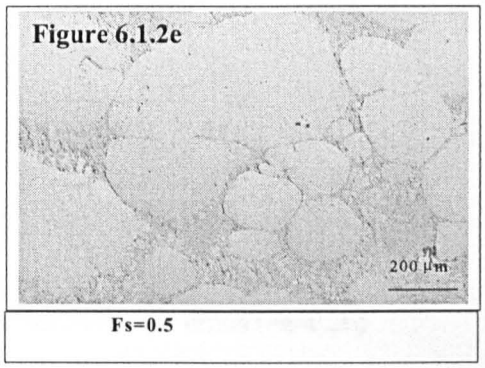

Fs=0.5

Figures 6.1.2b, 6.1.2c, 6.1.2d and 6.1.2e show the microstructures of Sn15%Pb alloys with different fractions solid. Particle sizes increase with increasing fraction solid.

6.1.3 Effect of rest times prior to an increase in shear rate.

In these experiments, Sn15%Pb alloy slurries are left to rest (at zero shear rate) after achieving the conditioned state at the specific fraction solid. All experiments are conditioned at 30 s^{-1} unless otherwise stated. Figures 6.13a to 6.13c (Fs=0.2, 0.36 and 0.5 respectively) show the effect of rest time on the peak stress encountered after a change in shear rate (from 0 s^{-1} to 100 s^{-1}). All the figures showed an increase in the peak stress with increasing rest times. The figures also showed that with increasing rest times, the decay in shear stress as the material breaks down upon the imposition of a shear rate is much steeper.

Figure 6.13a: : Shear rate jumps after different rest times (Fs=0.2)

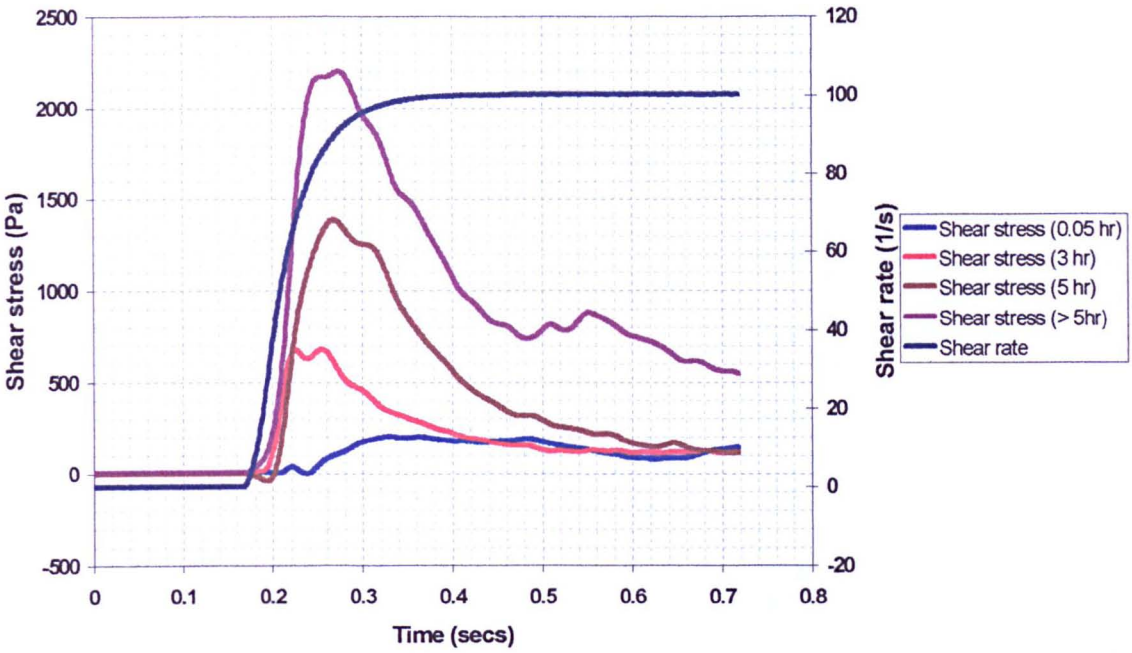

Figure 6.1.3b: Shear rate jumps after different rest times (Fs=0.36)

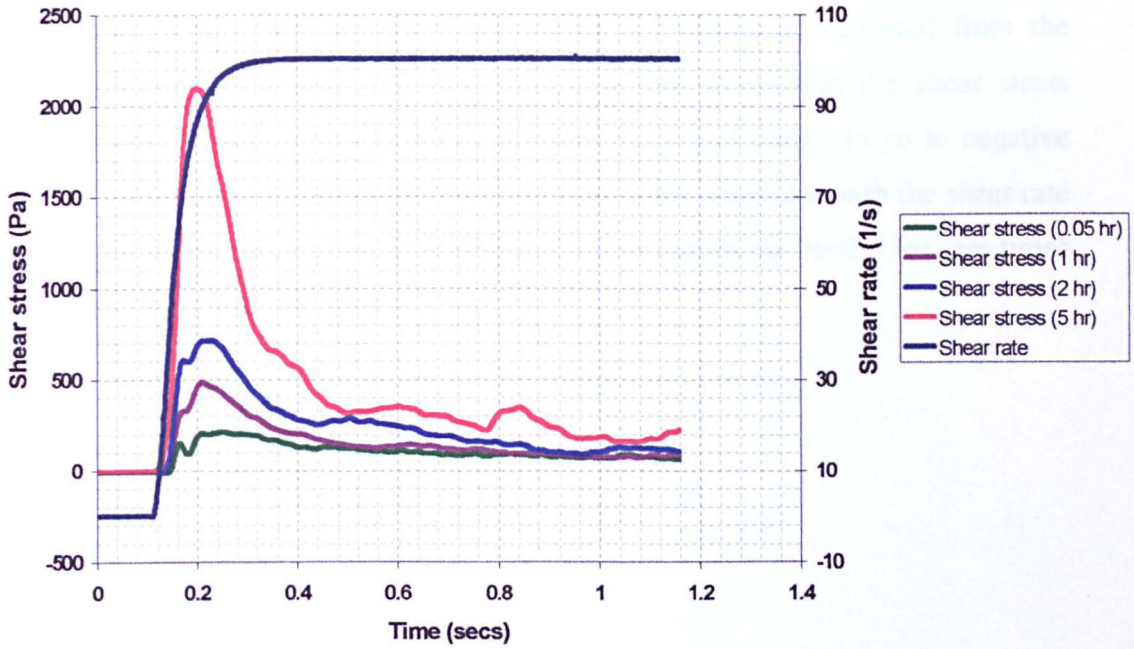

Figure 6.1.3c: Shear rate jumps after different rest times (Fs= 0.5)

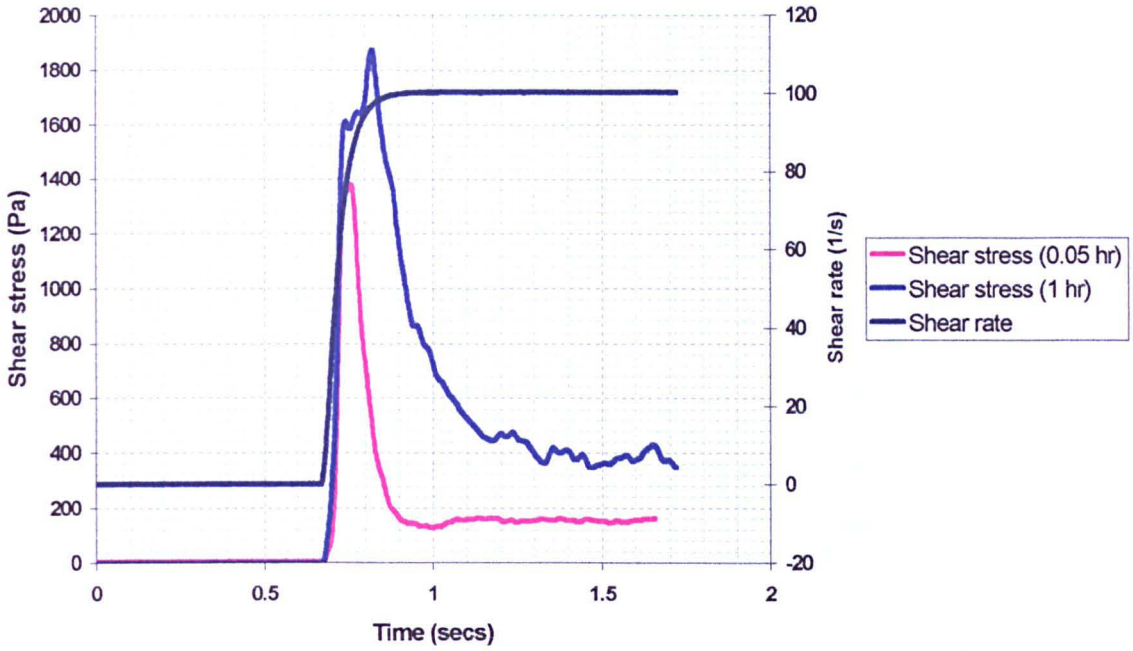

It was not possible to obtain results on Fs=0.5 at longer rest times as the material became very well-structured hence exceeding the maximum available torque on the viscometer. Figure 6.1.3d shows the results as collected from the datacard (Fs=0.5, Rest time = 2 hrs). Figure 6.1.3d shows that the shear stress recorded went through a cut-off effect, causing the signal output to go to negative values before recovering to a positive value. This effect coincides with the shear rate being cut off at the same time. Therefore, no other results on Fs=0.5 for rest times longer than 2 hrs were collected.

Figure 6.1.3d: Shear rate jumps after 2 hrs of rest time

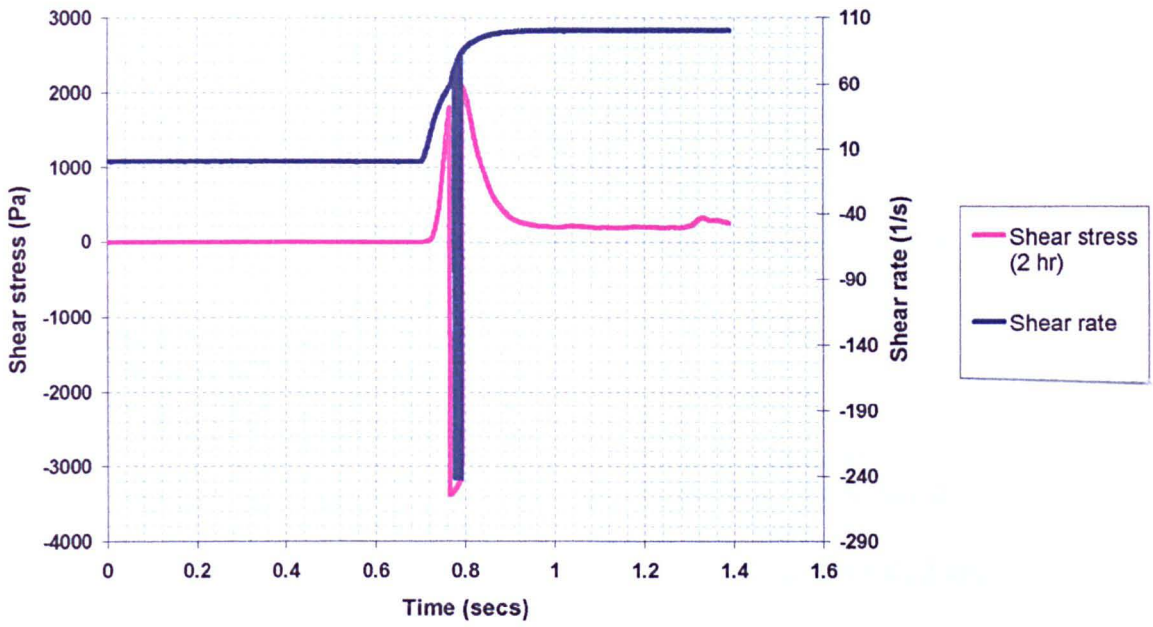

Given enough time, the curves converge to about the same value regardless of the amount of rest time each curve was given initially for a fixed fraction solid. This will be shown later (Figure 6.1.3k). This behaviour can be attributed to the material achieving its steady state value corresponding to the shear rate at that fraction solid. The sample is quenched at the end of the test and the microstructures corresponding to the different rest times at the various fraction solid are shown in Figures 6.1.3e and 6.1.3f.

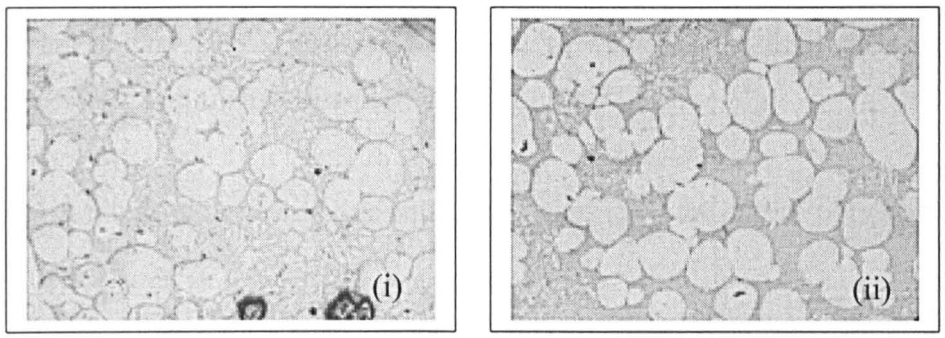

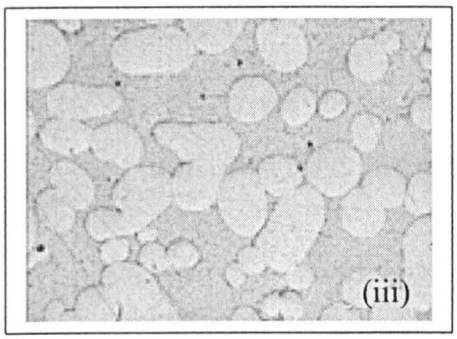

200 μm

(e) Microstructures of Sn15%Pb alloy (Fs=0.36) at various rest times:
(i) 0 hrs; (ii) 1 hr and (iii) 2 hrs

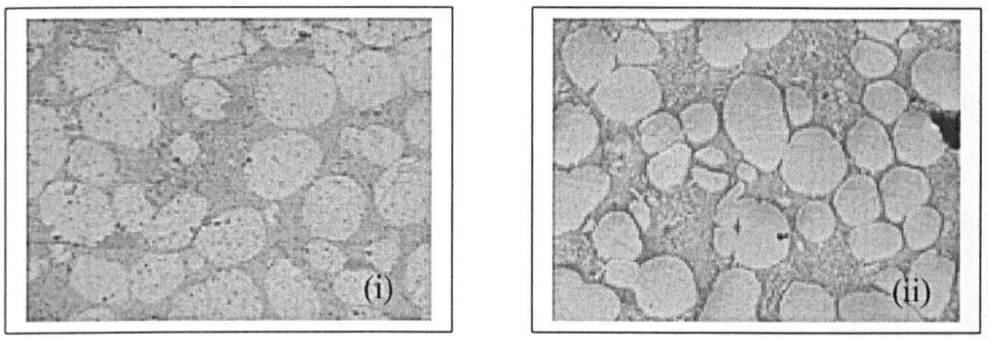

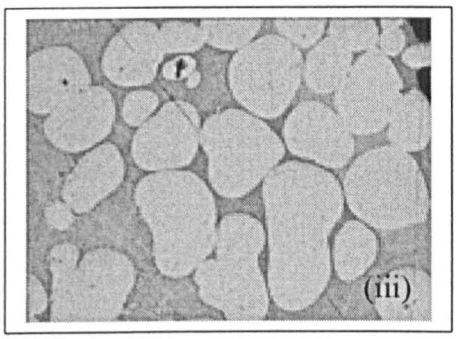

200 μm

(f) Microstructures of Sn15%Pb alloy (Fs=0.5) at various rest times:
(i) 0 hrs; (ii) 1 hr and (iii) 2 hrs

Figure 6.1.3 Microstructures of Sn15%Pb alloys at different rest times for (e) Fs=0.36 and (f) Fs=0.5

Figures 6.1.3g to 6.1.3j show an attempt to fit the descending portion of the shear stress curve (after shear rate changes to ~90% of the final specified 100 s^{-1}) after different rest times at fraction solid 0.36.

A single exponential rate equation is used to fit the curves obtained:

$$\frac{\sigma - \sigma_{s.s}}{\sigma_o - \sigma_{s.s}} = \frac{\eta - \eta_{s.s}}{\eta_o - \eta_{s.s}} = e^{-t/\tau} \qquad [6.1.3]$$

where σ_o, $\sigma_{s.s}$ and σ are the initial, steady state and instantaneous shear stresses respectively, η_o,$\eta_{s.s}$ and η are the corresponding viscosities and τ is the breakdown time at time, t.

The above equation can be derived from the Moore and Cross equations (see Table 2.2.1B). A derivation of Equation 6.1.3 is given in Appendix 4.

A relatively good fit for all the curves from the experimental results was obtained using the above equation.

Figure 6.1.3g: Curve fitting of shear rate jump experiments on Sn15%Pb alloys (Fs=0.36, Rest time=0.05 hrs) from 0 to 100 s^{-1} using equation 6.1.3

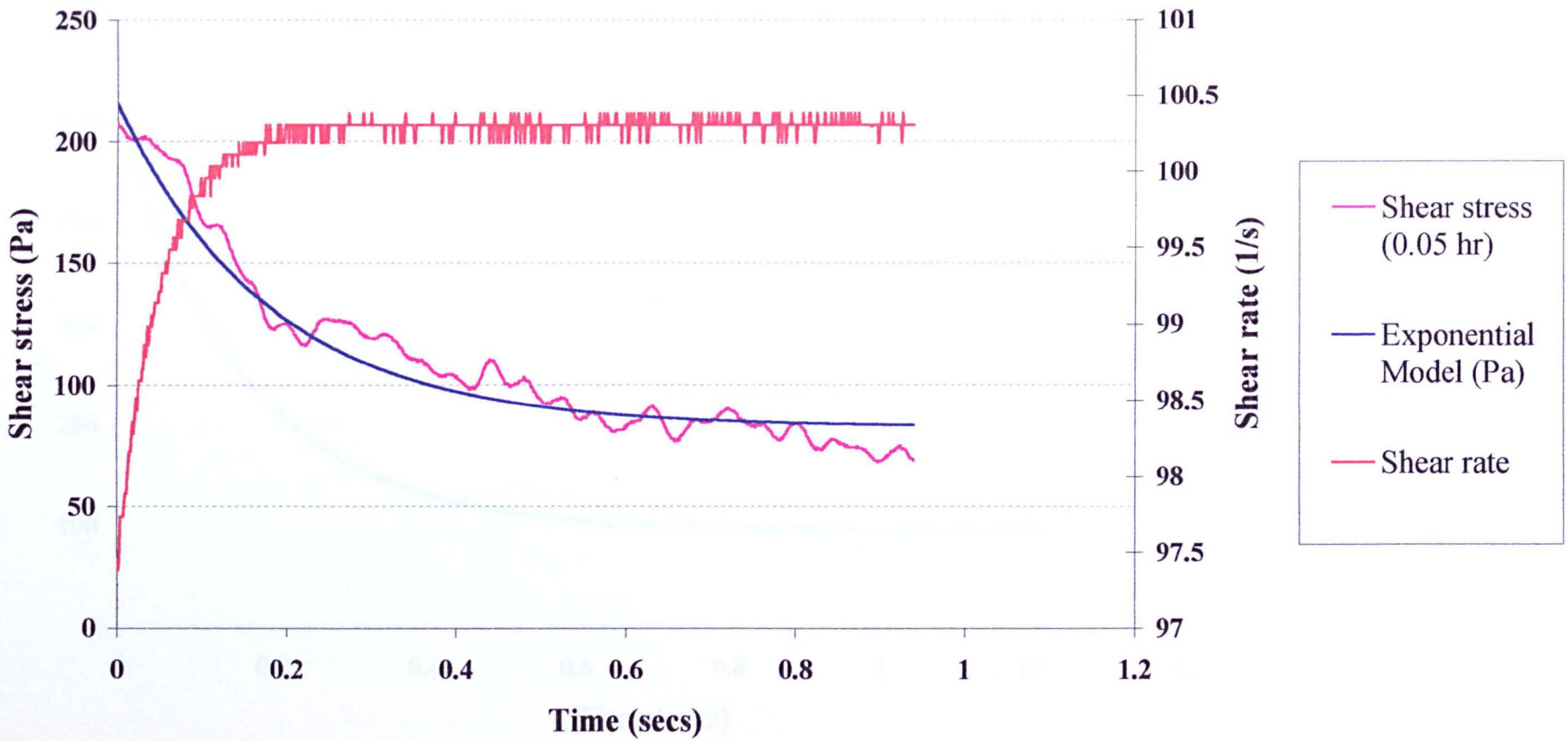

Figure 6.1.3h: Curve fitting of shear rate jump experiments on Sn15%Pb alloys (Fs=0.36, Rest time=1 hr) from 0 to 100 s^{-1} using equation 6.1.3

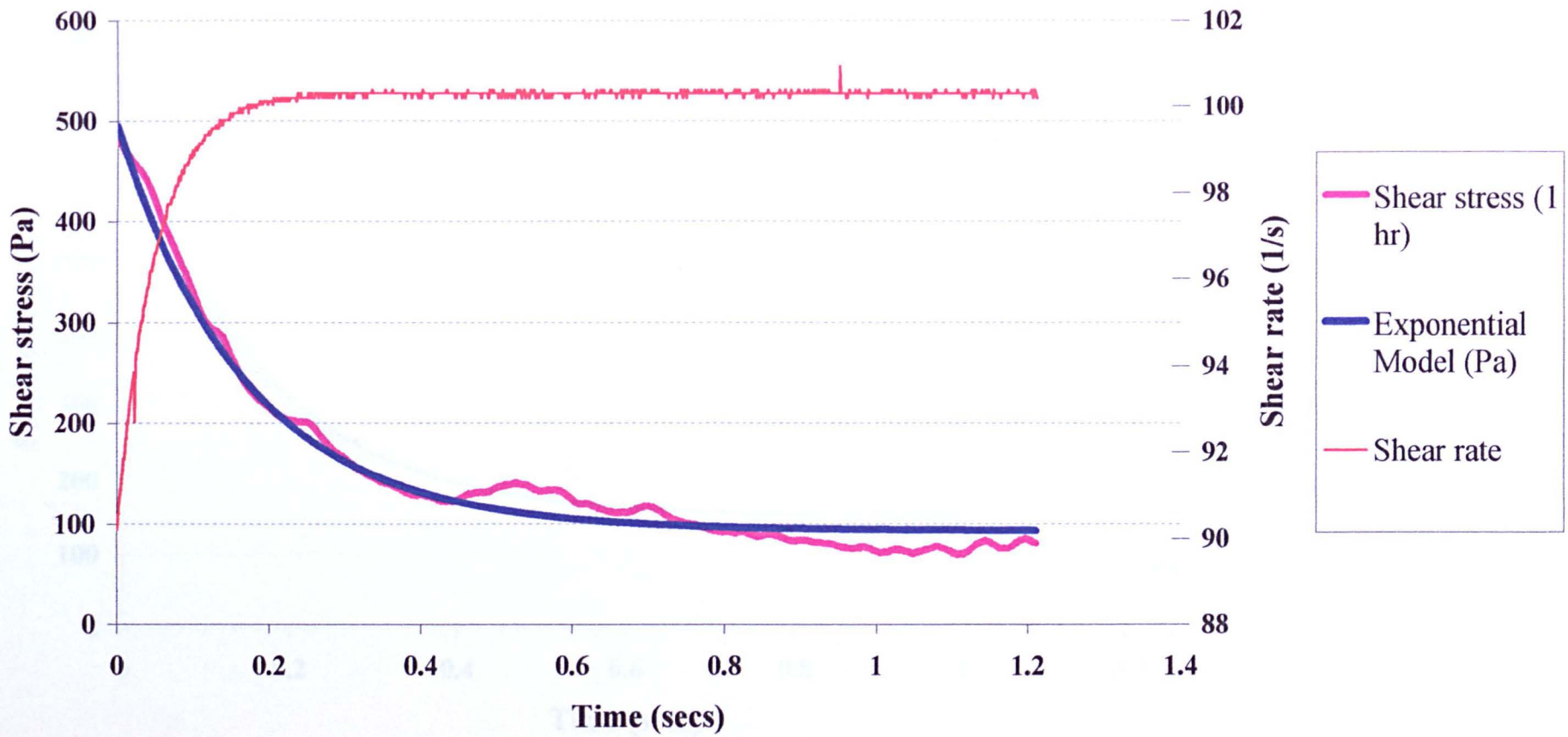

Figure 6.1.3i: Curve fitting of shear rate jump experiments on Sn15%Pb alloys (Fs=0.36, Rest time=2 hrs) from 0 to 100 s^{-1} using equation 6.1.3

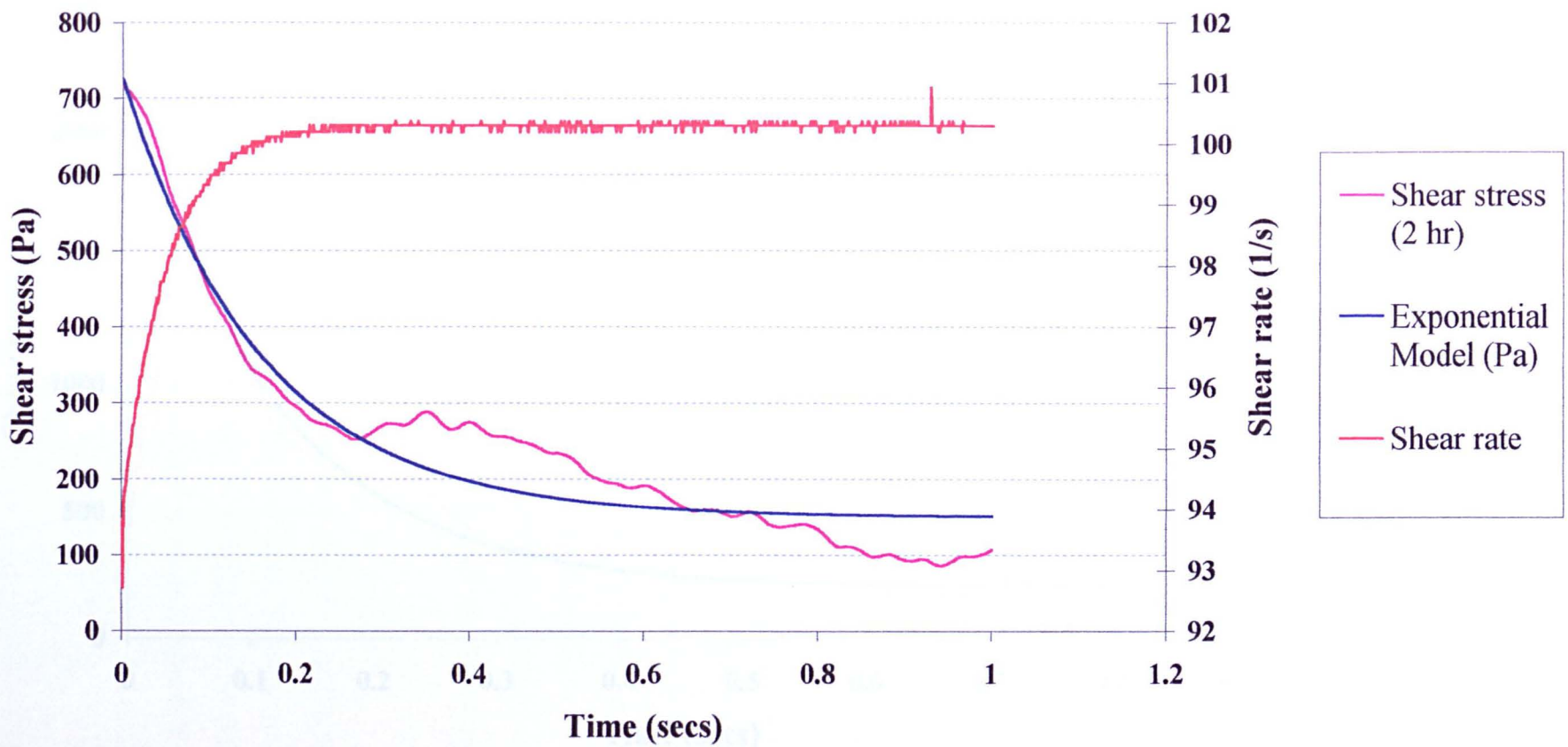

Figure 6.1.3j: Curve fitting of shear rate jump experiments on Sn15%Pb alloys (Fs=0.36, Rest time=5 hrs) from 0 to 100 s^{-1} using equation 6.1.3

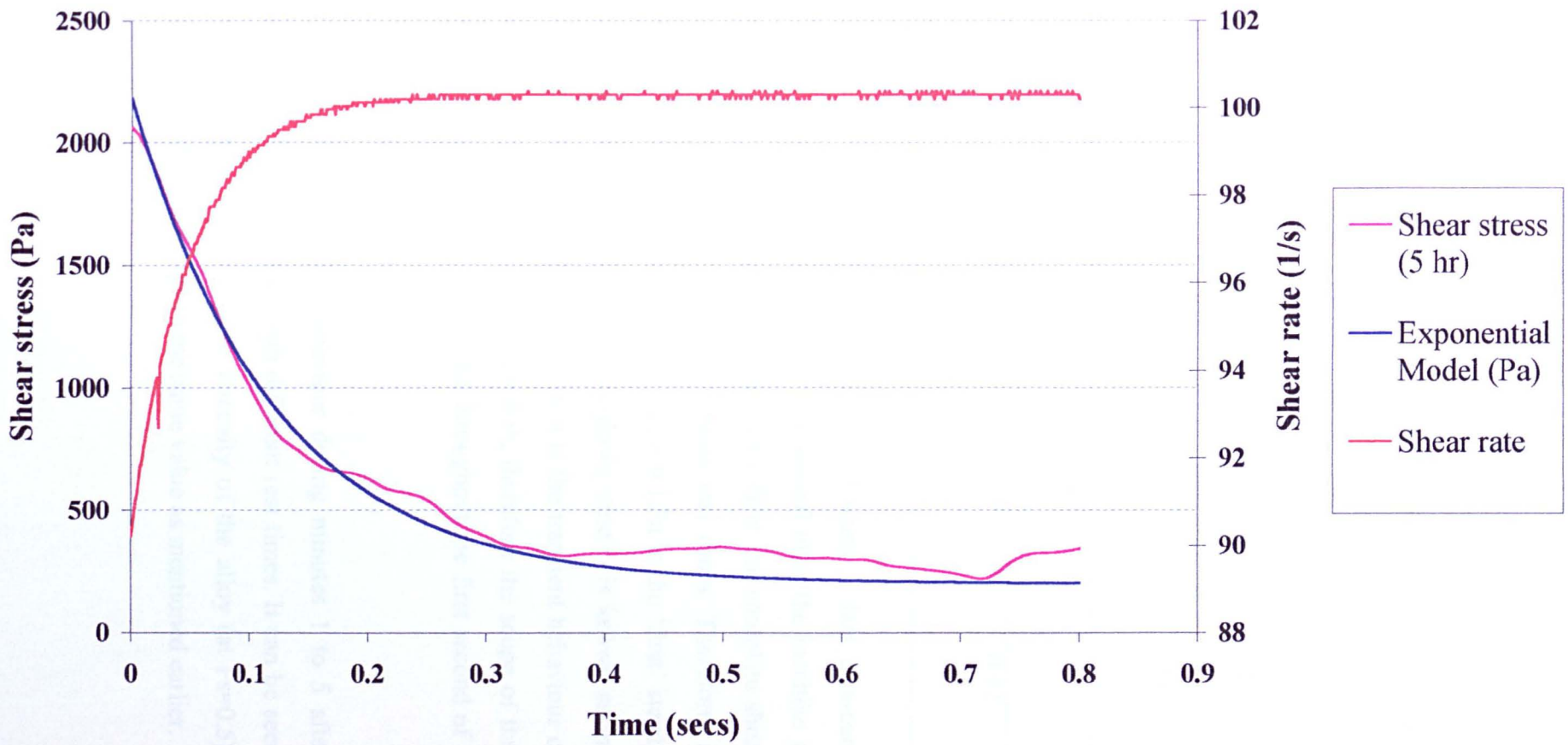

The parameters calculated from the fits to the curves in Figures 6.1.3g to 6.1.3j are shown in Table 6.1.3a. The initial viscosity, η_o, is shown to increase with rest times while the breakdown time, τ, sees to decrease with increasing rest times.

Table 6.1.3a. Tabulation of parameters obtained from shear rate jump experiments on Sn15%Pb alloys (at Fs= 0.36) under different rest times.

Shear rate Jumps (s^{-1})	**0-100**			
Rest times (hrs)	**0**	**1**	**2**	**5**
η_o (Pas)	2.13	5.4	8	23
$\eta_{s.s}$ (Pas)	0.8	0.8	1.23	2
τ (s)	0.18	0.16	0.15	0.12

The above breakdown times shown are modelled using a fast data-card (~1 kHz). Data is being collected throughout the first second after the machine is instructed to make the shear rate change. This does not reflect the complete shear thinning behaviour of the Sn15%Pb alloy after various rest times. Therefore, it should be mentioned here that the value of $\eta_{s.s}$ in Table 6.1.3a is the 'first' steady state viscosity after a shear rate jump and the breakdown time,τ, is known as the 'first' breakdown time (c.f. Section 4.1.5). However, it is the transient behaviour of the semisolid slurries that is of interest in this research, therefore the scope of this work will concentrate on extracting the parameters throughout the first second of a shear rate change.

Figure 6.1.3k shows the viscosity behaviour during minutes 1 to 5 after changing the shear rate from 0 $s^{-1}$to 200 s^{-1} with different rest times. It can be seen that after 5 minutes of shearing at 200 s^{-1}, the viscosity of the alloy (at Fs=0.5), regardless of its rest time, tends to converge to the same value as mentioned earlier.

Figure 6.1.3k: Viscosity behaviour of Sn15%Pb alloy sheared at 200 s-1 after different rest times (Fs=0.5)

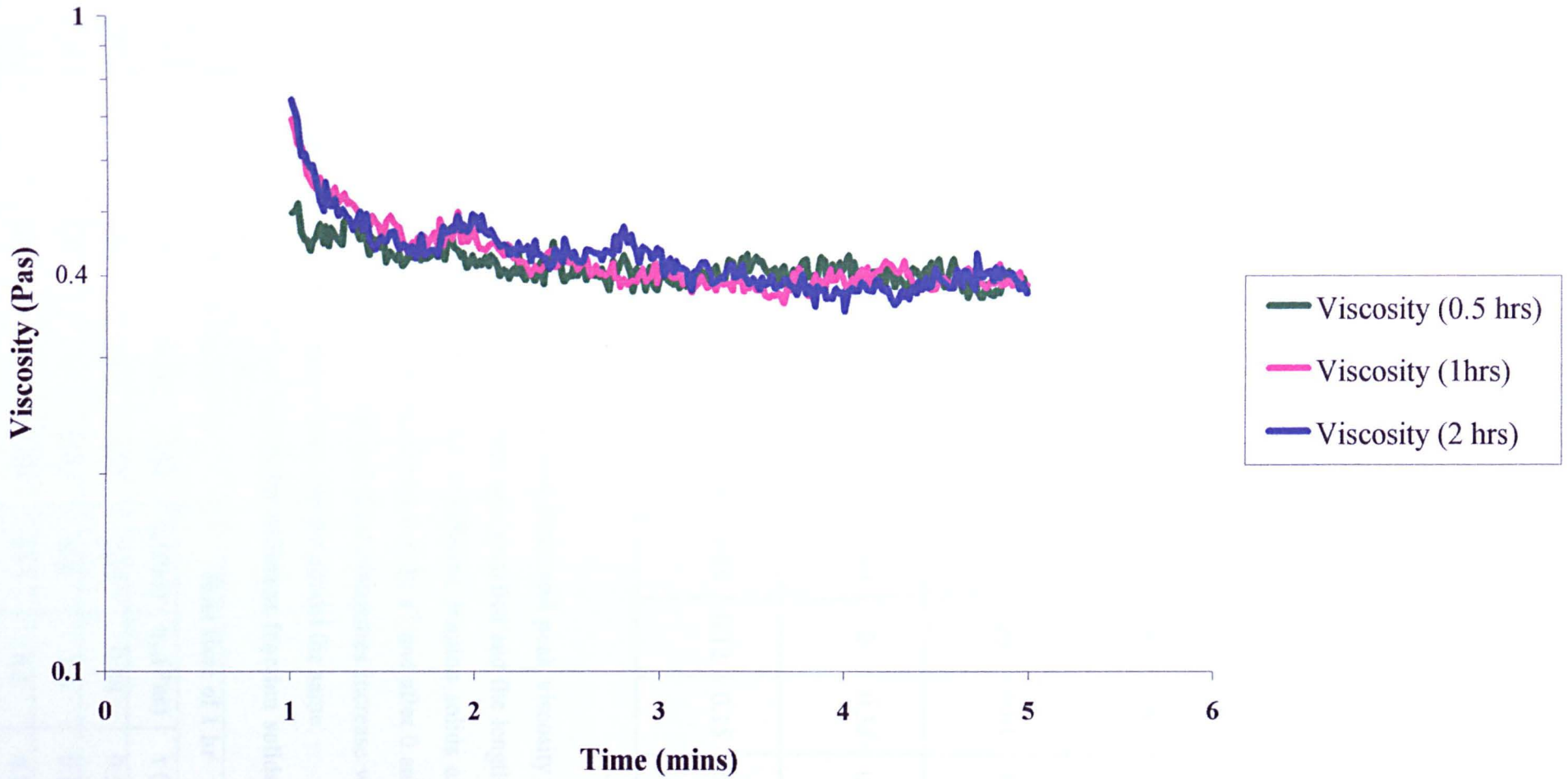

Table 6.1.3b shows the calculated parameters (initial, steady state viscosities and breakdown times) for Sn15%Pb alloys at different rest times for different final shear rates specified.

Table 6.1.3b Tabulation of parameters obtained from different shear rate jump experiments on Sn15%Pb alloys (at Fs= 0.36) under different rest times

Shear rate jumps (s^{-1})	**0-50**				**0-100**				**0-200**		
Rest times (hrs)	**0**	**1**	**2**	**5**	**0**	**1**	**2**	**5**	**0**	**1**	**2**
η_o (Pas)	3.6	8.8	13.3	37	2.13	5.4	8	23	0.61	1.59	3.38
$\eta_{s.s}$ (Pas)	1.9	1.8	2.1	3.6	0.8	0.8	1.23	2	0.35	0.68	0.98
τ (s)	0.20	0.18	0.18	0.14	0.18	0.16	0.15	0.12	0.15	0.13	0.13

The errors are within 95% confidence limit

It is clear from the results that the breakdown times and peak viscosity (or shear stresses) are influenced both by the final shear rate specified and the length of the rest times. Table 6.1.3c shows the results for 3 different fraction solids after similar shear rate jumps and rest times (shear rate from 0 to 50 s^{-1} and after 0 and 1 hours of rest time respectively). Both the initial and final viscosities increase with increasing fraction solids while the breakdown times remain almost the same.

Table 6.1.3c Tabulation of parameters obtained for different fraction solids of Sn15%Pb alloys to a final shear rate of 50 s^{-1}

Shear rate (0-50 s^{-1})	**Rest time of 0 hr**			**Rest time of 1 hr**		
Fraction Solid (Fs):	**η_o(Pas)**	**$\eta_{s.s}$(Pas)**	**τ (s)**	**η_o(Pas)**	**$\eta_{s.s}$(Pas)**	**τ (s)**
0.20	1.86	0.66	0.11	2.13	0.88	0.19
0.36	3.6	1.9	0.20	8.8	1.8	0.18
0.50	16.8	5.1	0.14	43.1	6.5	0.18

6.1.4 Viscosity behaviour during a shear rate step change experiment

In the preceding section (6.1.3), all experiments started off from an initial shear rate of 0 s^{-1}. In the shear rate step change experiments, the semisolid alloy slurries are first sheared at a pre-determined initial shear rate ($\dot{\gamma}_i$), achieving a constant viscosity state, before step changing to the final shear rate ($\dot{\gamma}_f$). A steady state is attained when the viscosity has become constant after the step change in shear rate.

Figures 6.1.4a and 6.1.4b show examples of shear rate jumps for 2 different initial shear rates to the same final shear rate. Both figures show good repeatability and some anomalies in the results. During the rapid change in shear rate, there is an apparent 'dip' in the shear rate. This resulted in a corresponding 'dip' in the shear stress curve. By plotting the viscosity curves on the same graphs, it can be seen that a shear thinning behaviour is present during a shear rate jump (i.e. viscosity decreases with increasing shear rate). Repeatability of the viscosity values is also shown to be quite consistent.

The cause of this 'dip' effect was attributed to the electronic switching system from the viscometer's controller. The 'dip' in the shear rate and shear stress curve was reproduced as shown in Figure 6.1.4c when the experiment was conducted in air. Experiments were then conducted on a Newtonian fluid (Silicone oil (SiOil) at 1Pas) and the same effect was shown again. Figure 6.1.4d shows the shear stress and viscosity behaviour of the SiOil during a step change in shear rate from 10 to 100 s^{-1}. It can be seen that the shear stress increases with increasing shear rate while the viscosity remains constant after the jump. Again the 'dip' in the shear rate during the shear rate jump has an effect on the recorded shear stress and viscosity. Henceforth, curve fitting of all shear rate jumps are done after the shear rate has reached ~90% of its specified $\dot{\gamma}_f$. Since the purpose of this experiment is to understand the transient behaviour of the semisolid alloy during a step change, all results are collected using the fast data card (1 kHz). Therefore results are shown during the first second of the shear rate jump, a considerably faster collection rate than other workers investigating transient behaviour on semisolid alloy slurries (Qua 96b: ~9Hz, Kum 94c: ~200Hz).

Figure 6.1.4a: Repeatability of shear rate jumps from 1 to 100 s^{-1} (for Sn15%Pb alloys at fs=0.36)

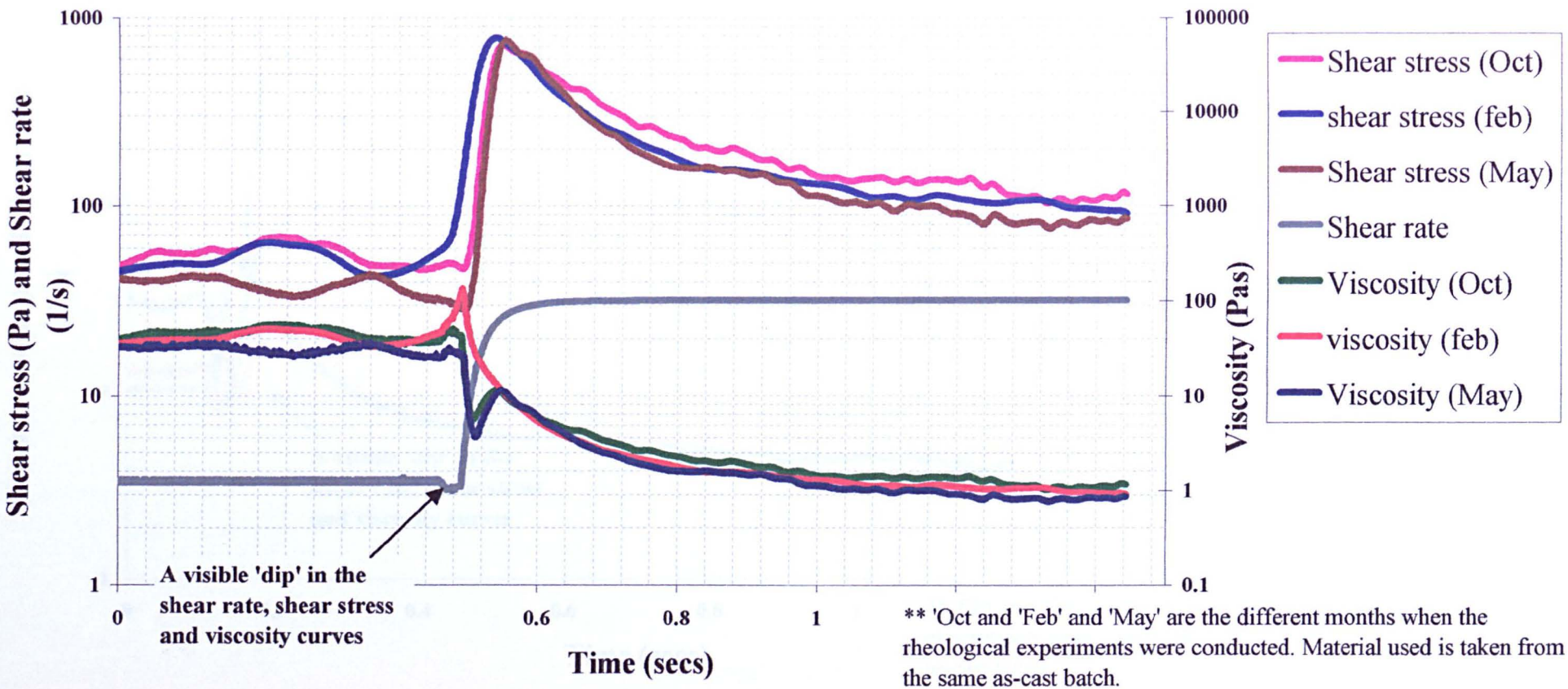

** 'Oct and 'Feb' and 'May' are the different months when the rheological experiments were conducted. Material used is taken from the same as-cast batch.

Figure 6.1.4b: Repeatability of shear rate jumps from 10 to 100 s^{-1} (for Sn15%Pn alloys at fs=0.36)

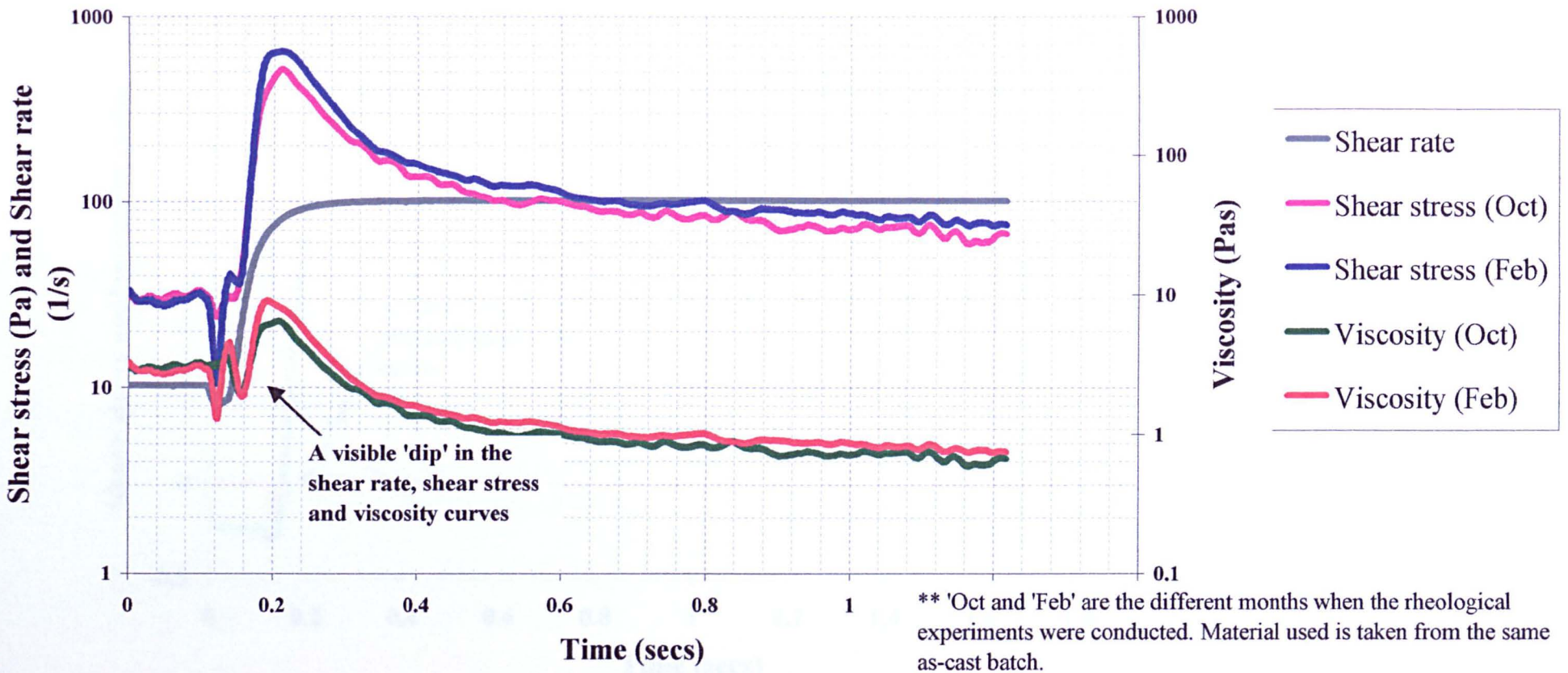

** 'Oct and 'Feb' are the different months when the rheological experiments were conducted. Material used is taken from the same as-cast batch.

Figure 6.1.4c: Shear rate jump in air (10 to 100 s^{-1})

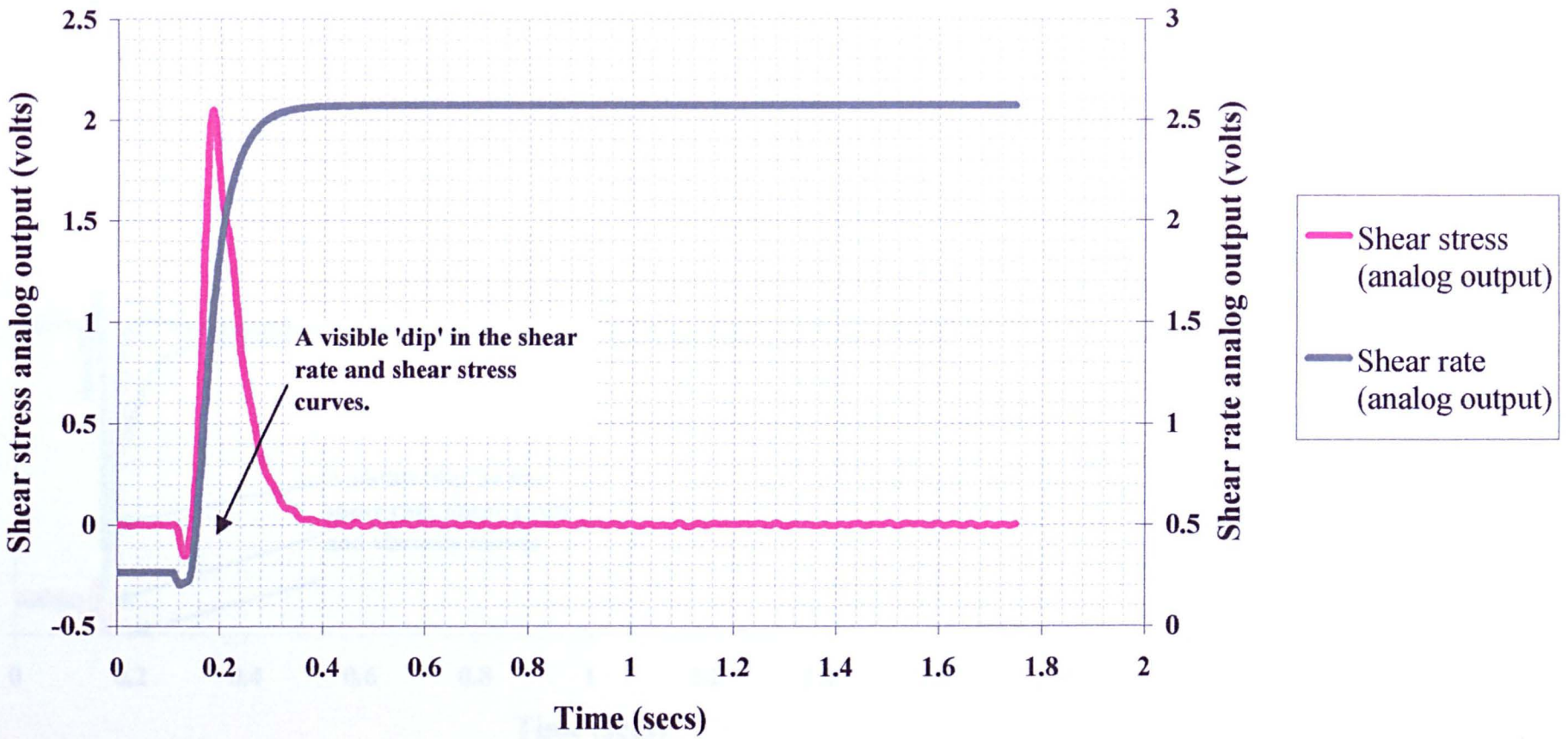

Figure 6.1.4d: Shear rate jump in 1 Pas silicone oil (10 to 100 s^{-1})

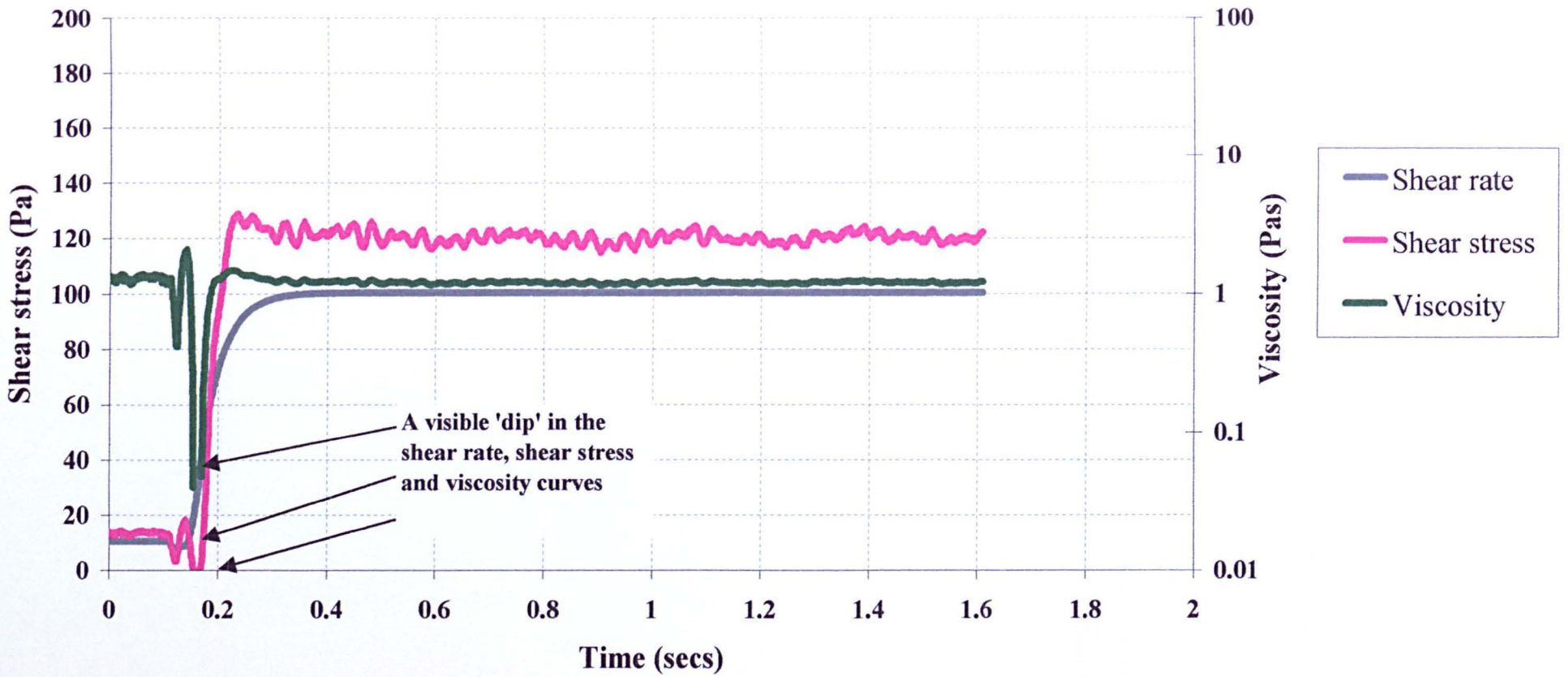

Figure 6.1.4e shows shear rate jumps (from 1 to 200 s^{-1}) for two different fraction solids (Fs =0.36 and 0.5). It can be seen that the peak stress and peak viscosity encountered increases with increasing fraction solid. The viscosity values for each fraction solid at 1 s^{-1} and 200 s^{-1}correspond to those found during the steady state experiments (see Figure 6.1.2a). This implies that the semisolid alloy has a constant structure (i.e. constant viscosity, see Figure 4.1.5a) before the shear rate jump.

Following the curve fitting procedure in the rest time experiments, the breakdown times for the step change experiments were obtained for a series of initial and final shear rates. Figures 6.1.4f and 6.1.4g shows 4 examples of the curve fitting attempts at different $\dot{\gamma}_i$ and $\dot{\gamma}_f$ respectively.

Figure 6.1.4e: Shear rate jumps (1 to 200 s^{-1}) for Sn15%Pb alloy at different fraction solids

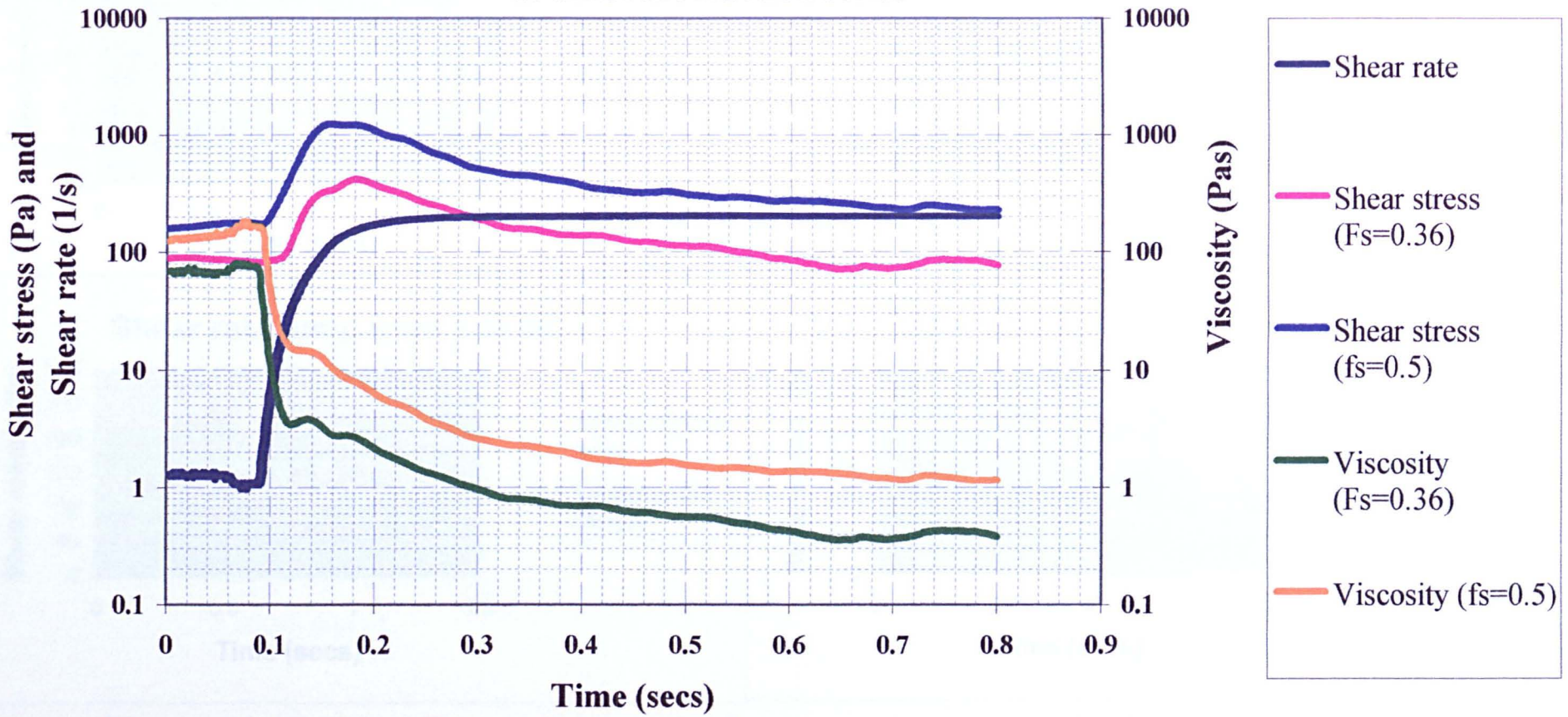

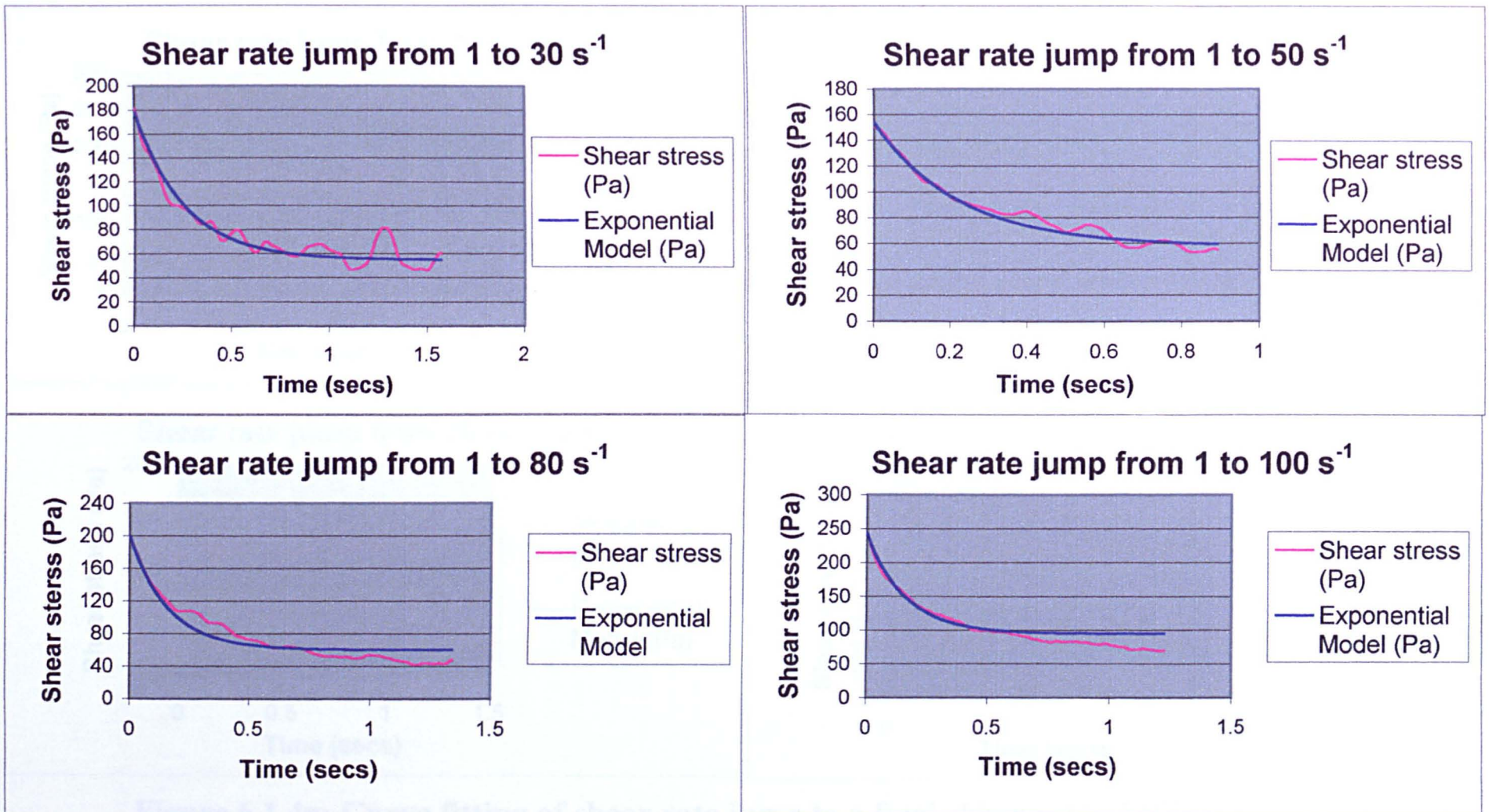

Figure 6.1.4f: Curve fitting of shear rate jump starting from an initial shear rate of 1 s^{-1}

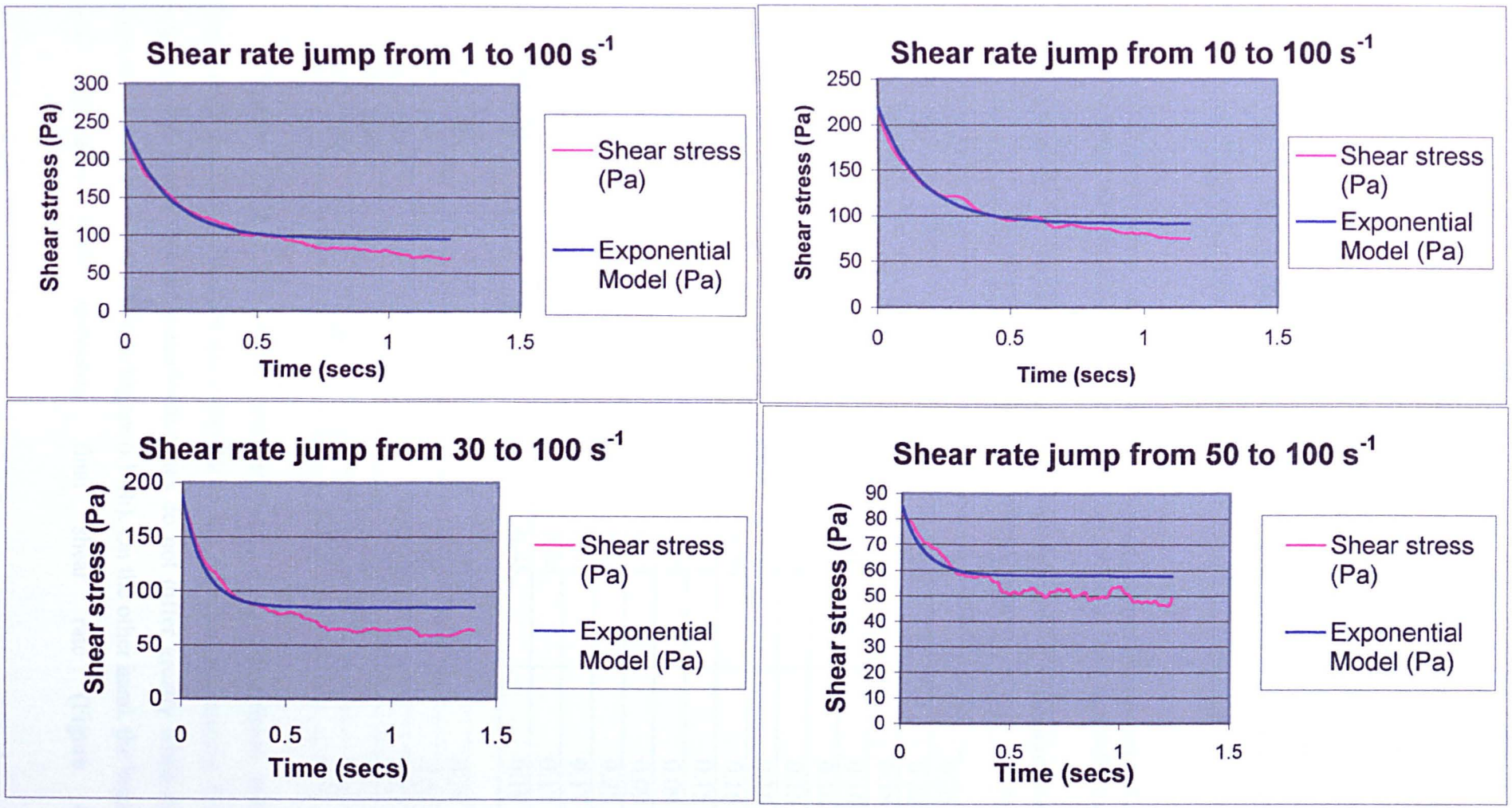

Figure 6.1.4g: Curve fitting of shear rate jump to a final shear rate of 100 s^{-1}

Table 6.1.4a lists the calculated parameters for the various shear rates for fraction solids at 0.36 and 0.5. From the table below, it can be seen that the peak or initial viscosity encountered during the step change decreases with increasing initial shear rate. This can be attributed to the slurry being more broken down before the step change and hence a lower viscosity value is recorded. By comparing the viscosity values for the same initial shear rate, it was found that the viscosity values differ slightly from each other. The viscosity and breakdown time values are found to be greater for fraction solid of 0.5, as expected from a more packed structure.

Table 6.1.4a. Parameters obtained from step change experiments using Equation 6.1.3. **(Material: Sn15%Pb alloy slurry, Fraction solid at 0.36 and 0.50 (*in italics*).)**

Shear rate range (s^{-1})	Initial or peak viscosity (Pas)	Steady state viscosity (Pas)	Breakdown times τ (s)
1 – 30	6.4	2.28	0.25
1 – 50	3.1	1.08	0.22
1 – 80	2.56	0.89	0.18
1 – 100	2.47	0.82	0.16
1 - 200	0.97	0.41	0.10
10 - 100	2.2	0.79	0.16
30 - 100	2.1	0.63	0.16
50 – 100	0.8	0.50	0.16
80 - 100	0.50	0.41	0.15
50 – 200	0.77	0.25	0.09
80 – 200	0.26	0.15	0.09
100 – 200	0.18	0.14	0.25
10 – 80	1.20	0.58	0.17
30 – 80	1.00	0.54	0.17
50 – 80	0.65	0.45	0.18
30 – 80	*8.3*	*1.5*	*0.19*
50 – 80	*7.1*	*1.91*	*0.20*
50 – 200	*2.30*	*1.21*	*0.12*
80 – 200	*1.36*	*0.70*	*0.12*
100 – 200	*0.68*	*0.43*	*0.11*

Figures 6.1.4h and 6.1.4i plot the parameters (breakdown times, initial and steady state viscosity) obtained from the fits to the experimental curves. From the graphs it was found that the breakdown times do not differ greatly when the final shear rate specified is constant (see Figure 6.1.4h). On the other hand, the breakdown time decreases with increasing final shear rate (Figure 6.1.4i).

Figure 6.1.4h: Plot of breakdown times, initial and steady state viscosity during a step change to a final shear rate of 100 s^{-1} (values obtained from Table 6.1.4a)

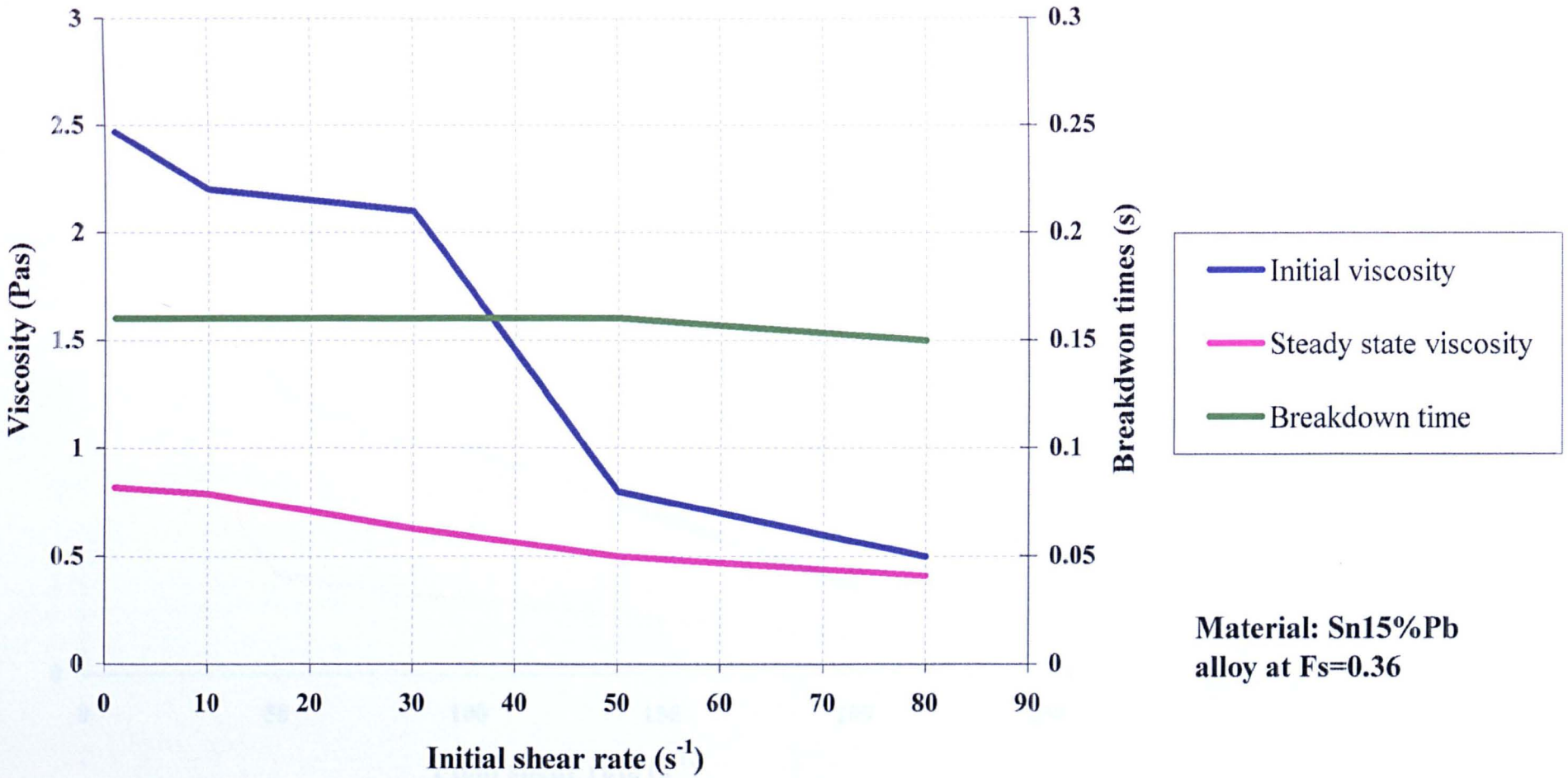

Figure 6.1.4i: Plot of breakdown times, initial and steady state viscosity during a step change from an initial shear rate of 1 s^{-1} (values obtained from Table 6.1.4a)

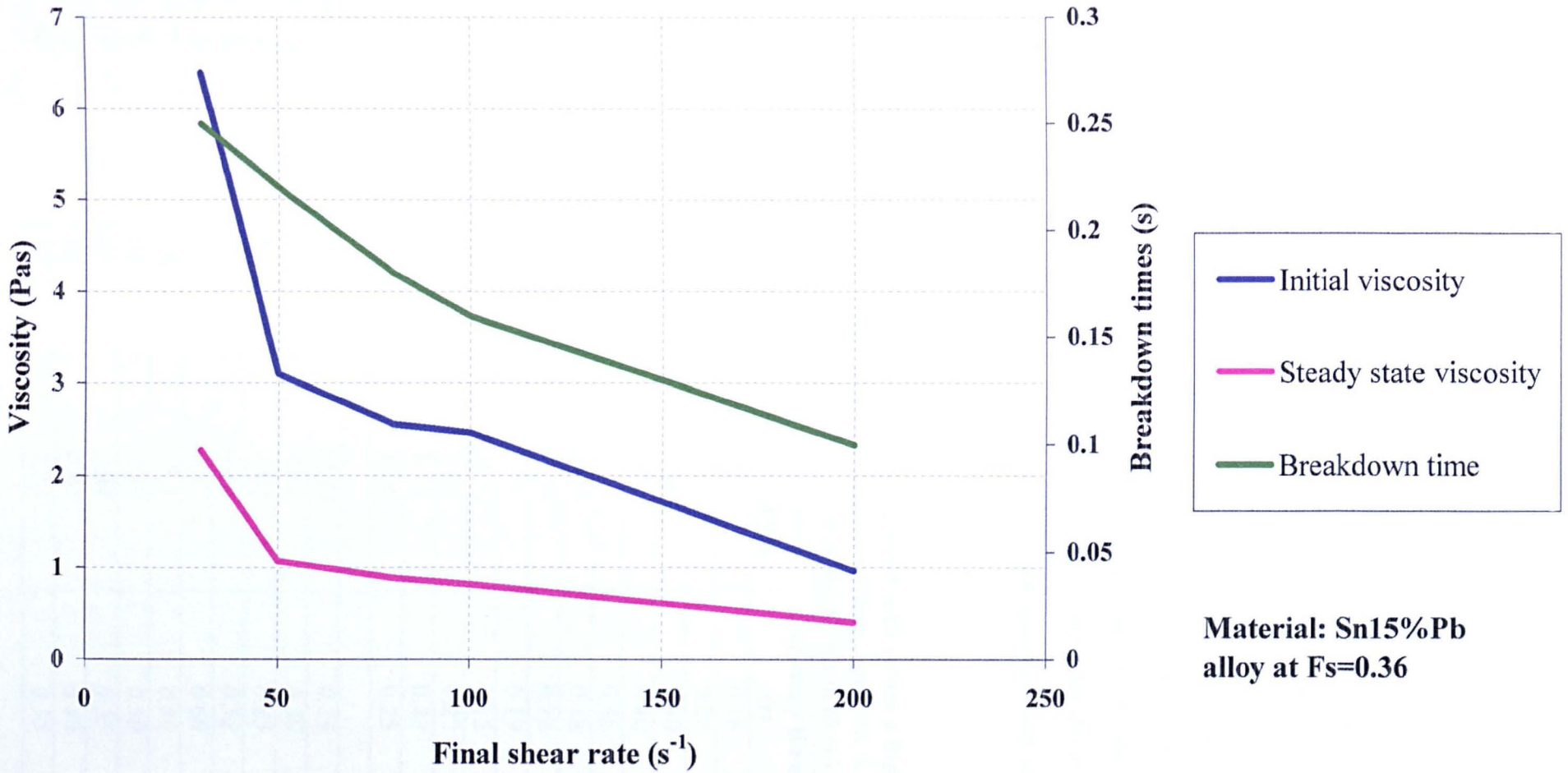

Experiments were also conducted on various step change jumps from a higher shear rate to a lower shear rate. Figure 6.1.4j shows the modelling part of the step change to a lower shear rate. In these experiments, the shear stress recorded decreases initially before increasing. It was noted that the time taken for the shear stress to achieve the value corresponding to its shear rate is longer compared to a step change to a higher shear rate where breakdown of the structure occurs more rapidly. On the step change to a lower shear rate, the time taken after the 'first' steady state value is reached is known as the recovery time. Table 6.1.4b shows the parameters obtained from the modelling of the shear stress curve with time. The results for the step change to a lower shear rate showed similar behaviour to the step change to a higher shear rate. The recovery time is dependent on the final shear rate specified while the initial or peak viscosity decreases with increasing initial shear rate.

Table 6.1.4b. Parameters obtained from step change downwards (from a higher initial shear rate to a lower final shear rate) experiments using Equation 6.1.3. **(Material: Sn15%Pb alloy slurry, Fraction solid at 0.36 and 0.50 (*in italics*).)**

Shear rate range (s^{-1})	Initial or peak viscosity (Pas)	Steady state viscosity (Pas)	Recovery times τ (s)
100 - 1	2.51	6.15	0.18
100 - 10	0.93	1.45	0.20
100 - 30	0.54	0.66	0.30
100 - 50	0.44	0.52	0.40
100 - 80	0.30	0.44	0.45
10 - 1	14.89	26.66	0.18
30 - 1	7.98	14.14	0.18
50 - 1	3.4	7.95	0.19
200 - 1	0.86	18.74	0.15
50 - 10	1.27	2.05	0.22
80 - 50	0.51	0.74	0.42
30 - 10	1.76	3.24	0.25
100 - 1	*4.22*	*12.23*	*0.25*
100 - 10	*1.11*	*2.13*	*0.50*
100 - 30	*0.55*	*1.02*	*0.45*
100 - 50	*0.52*	*0.87*	*0.52*
100 - 80	*0.55*	*0.67*	*0.60*
10 - 1	*15.00*	*35.1*	*0.30*
50 - 10	*2.04*	*3.50*	*0.50*
50 - 30	*1.09*	*2.04*	*0.35*
200 - 30	*0.18*	*0.44*	*0.40*
80 - 50	*0.75*	*1.13*	*0.55*

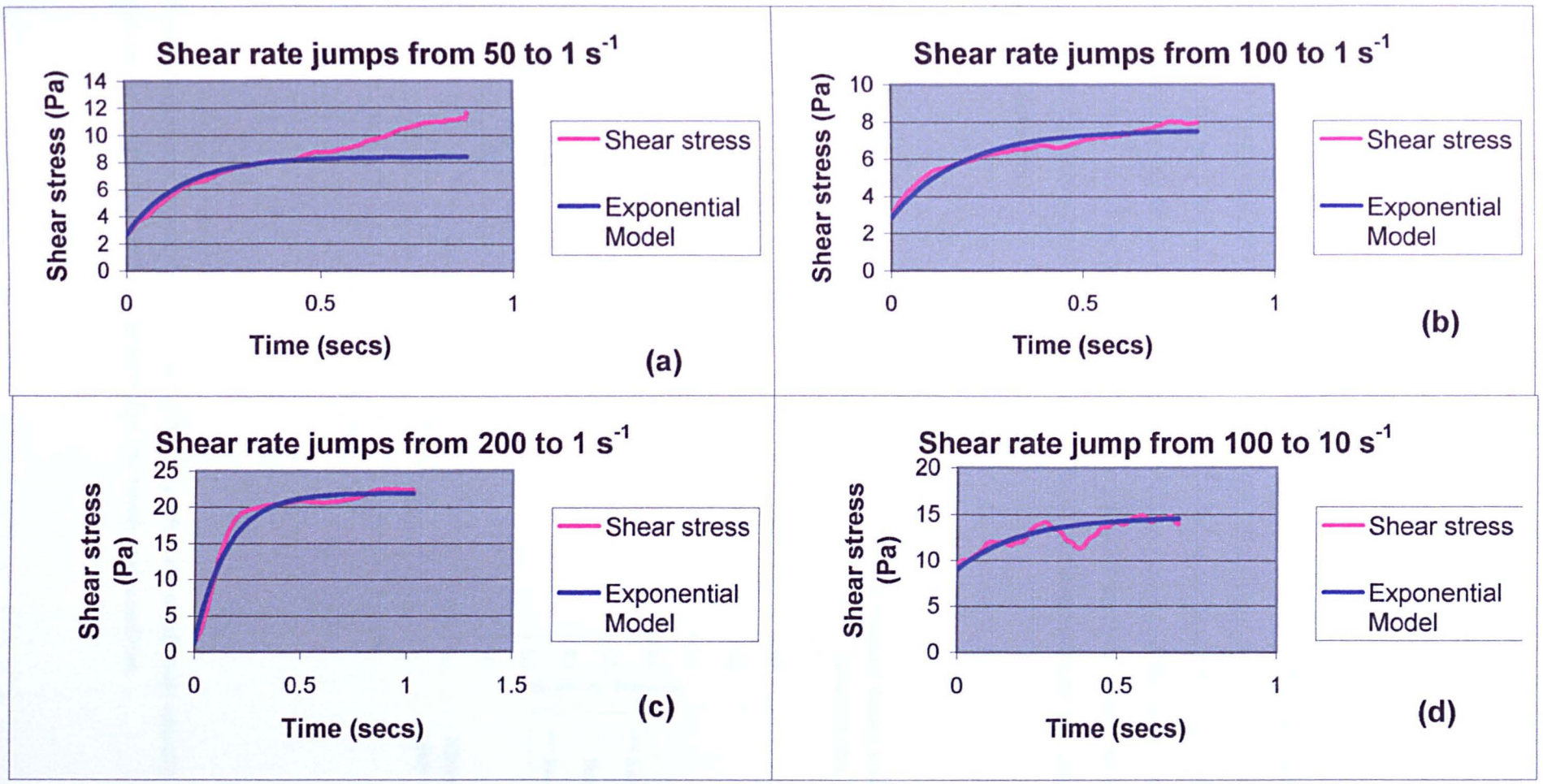

Figure 6.14j: Curve fitting of shear rate downward jumps. (a), (b) and (c) have the same final shear rat of 1 s^{-1} while (b) and (d) start from the same intial shear rate of 100 s^{-1}

Figure 6.1.4k and Figure 6.1.4l plot the parameters obtained from the fits to the shear stress curve for the step change down to a lower shear rate. From Figure 6.1.4k, the recovery time remains almost constant if the final shear rate is constant, regardless of the initial shear rate prior to the step change. Figure 6.1.4l shows that the recovery time increases with increasing final shear rate.

The result for the step change from 200 s^{-1} to 1 s^{-1} deviates greatly from the trend for other shear rate change. It is not clear why the recorded 'first' steady state viscosity has such a high value. However, the initial or peak viscosity encountered fits the decreasing trend of lower viscosity with increasing initial shear rate. This is expected since at a high initial shear rate, the particles are very much broken down, hence the viscosity recorded on the onset of the step change should correspond to the specified shear rate.

Figure 6.1.4k: Plot of recovery times, initial and steady state viscosity during a step change to a final shear rate of 1 s^{-1} (values obtained from Table 6.1.4b)

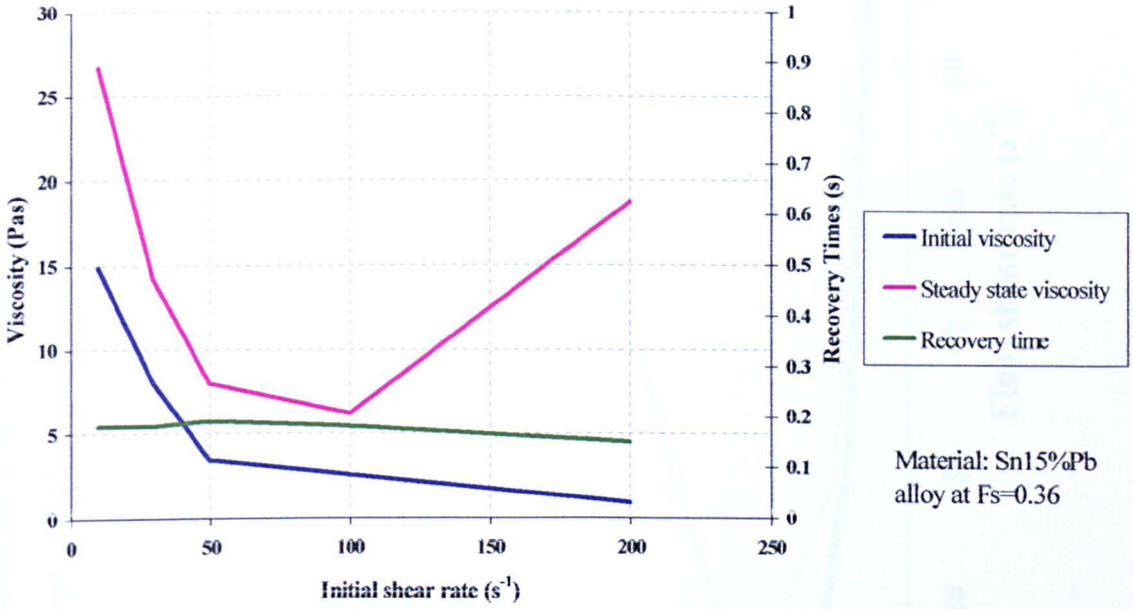

*** Initial viscosity is recorded on the onset of the jump while the steady state viscosity is recorded after the jump when the material has achieved its first steady state condition.*

Figure 6.1.4l: Recovery times, initial and steady state viscosity during a step change from an initial shear rate of 100 s^{-1} (values obtained from Table 6.1.4b)

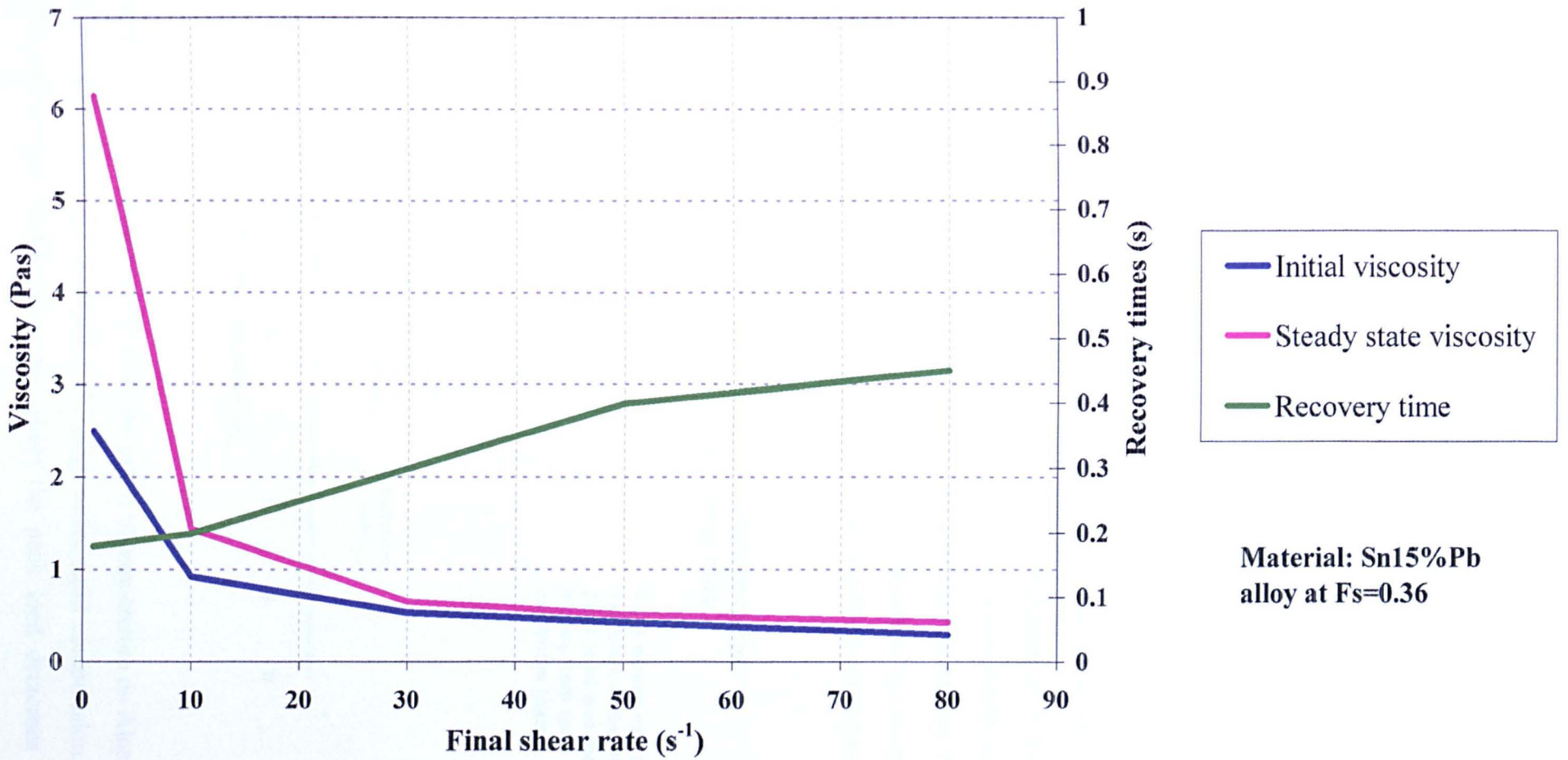

6.2 Rapid Compression Experiments

The rapid compression experiments were conducted to obtain the rheological behaviour of semisolid alloy slurries at a higher fraction solid and for aluminium (Al) alloys that are used industrially. Four different types of aluminium alloys were tested (see Table 5.2b). Experiments were also conducted on Sn15%Pb alloy to correlate with any rheological behaviour obtained from the viscometry experiments.

6.2.1 Rapid compression on Al alloys under different temperatures

Figure 6.2.1a shows a typical load signal response from the rapid compression experiments. The graph is plotted against the displacement of the slug from its initial height to its final height when the experiment is completed. A peak load (L_1) is encountered when the slug first touches the sindanyo insert (see Figure 5.2b) in the die. This is followed by a drop in the load to a minimum (L_2) during the rapid compression of the slug. As the material fills the die, the force encountered by the load cell increases with increasing shear rate.

Figure 6.2.1a: Typical signal response to rapid compression of a semisolid alloy slug.

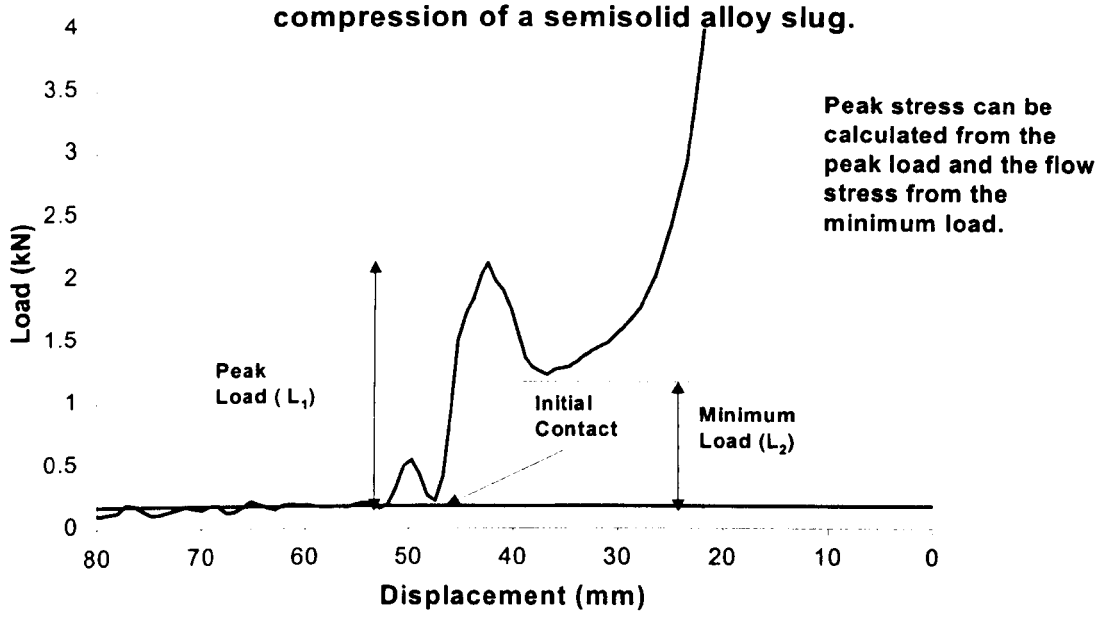

Figures 6.2.1b, 6.2.1c and 6.2.1d show the effect of temperature on Alusuisse A356, Northwest Al A319 and Sheffield A357 slugs under rapid compression. The three graphs all showed similar behaviour where the peak load decreases with

increasing temperature. With the highest temperature (see Figure 6.2.1b), it can be seen that the peak load has almost disappeared. This seemed to indicate that at that highest temperature, the slug would be in its optimised state for thixoforming.

The equivalent microstructures of the alloys after rapid compression experiments are shown together with their load signal behaviour in Figures 6.2.1b, 6.2.1c and 6.2.1d. The microstructures showed that with increasing temperature, the particles become more globular in shape and fraction liquid increases. This would account for the lower load signal encountered with increasing temperature as globular particles move more freely than non-globular particles. The fraction liquid acts as a lubricating medium for the particles to slide past each other hence a higher fraction liquid helps the particles to slide past each other more easily (c.f. Chapter 4).

Figure 6.2.1b: Load signals and microstructures at different temperatures for Alusuisse A356 Al alloy. Microstructres are taken from the Edge_Centre (see Figure 6.4a) of the slug after compression has been completed

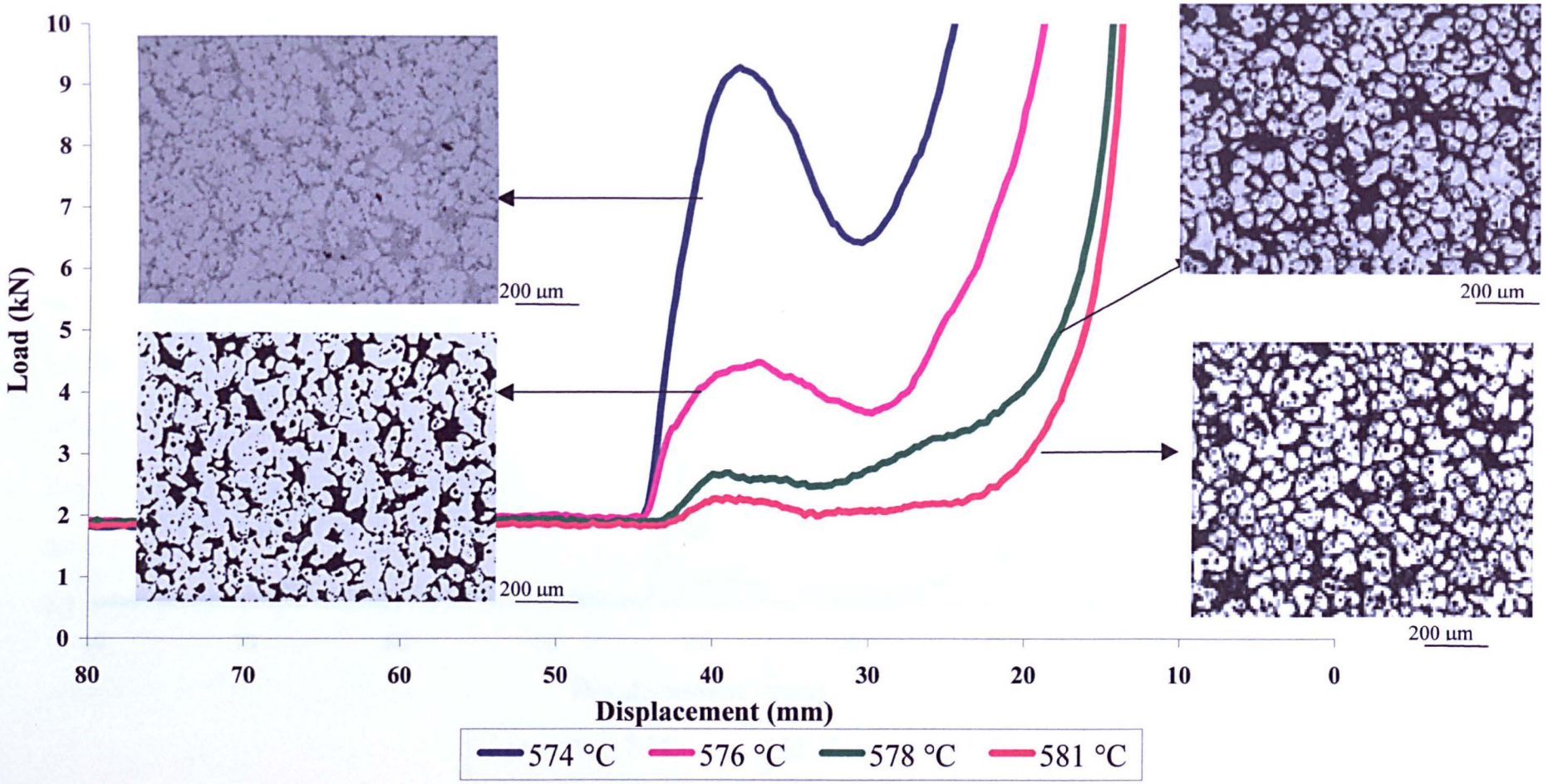

Figure 6.2.1c: Load signals and microstructures at different temperatures for NorthWest A319 Al alloy. Microstructres are taken from the Edge_Centre (see Figure 6.4a) of the slug after compression has been completed

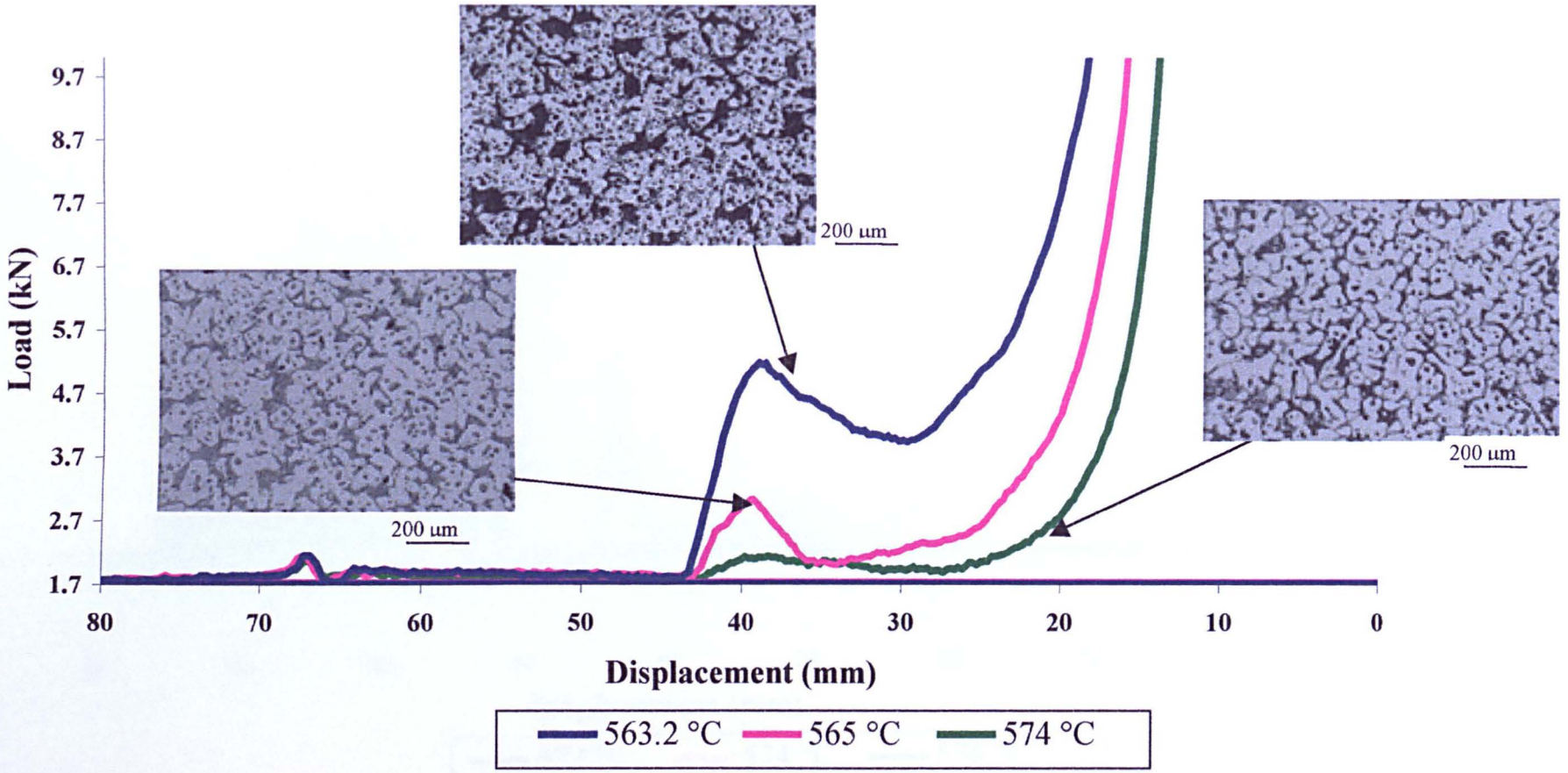

Figure 6.2.1d: Load signals and microstructures at different temperatures for Sheffield A357 Al alloy. Microstructres are taken from the Edge_Centre (see Figure 6.4a) of the slug after compression has been completed

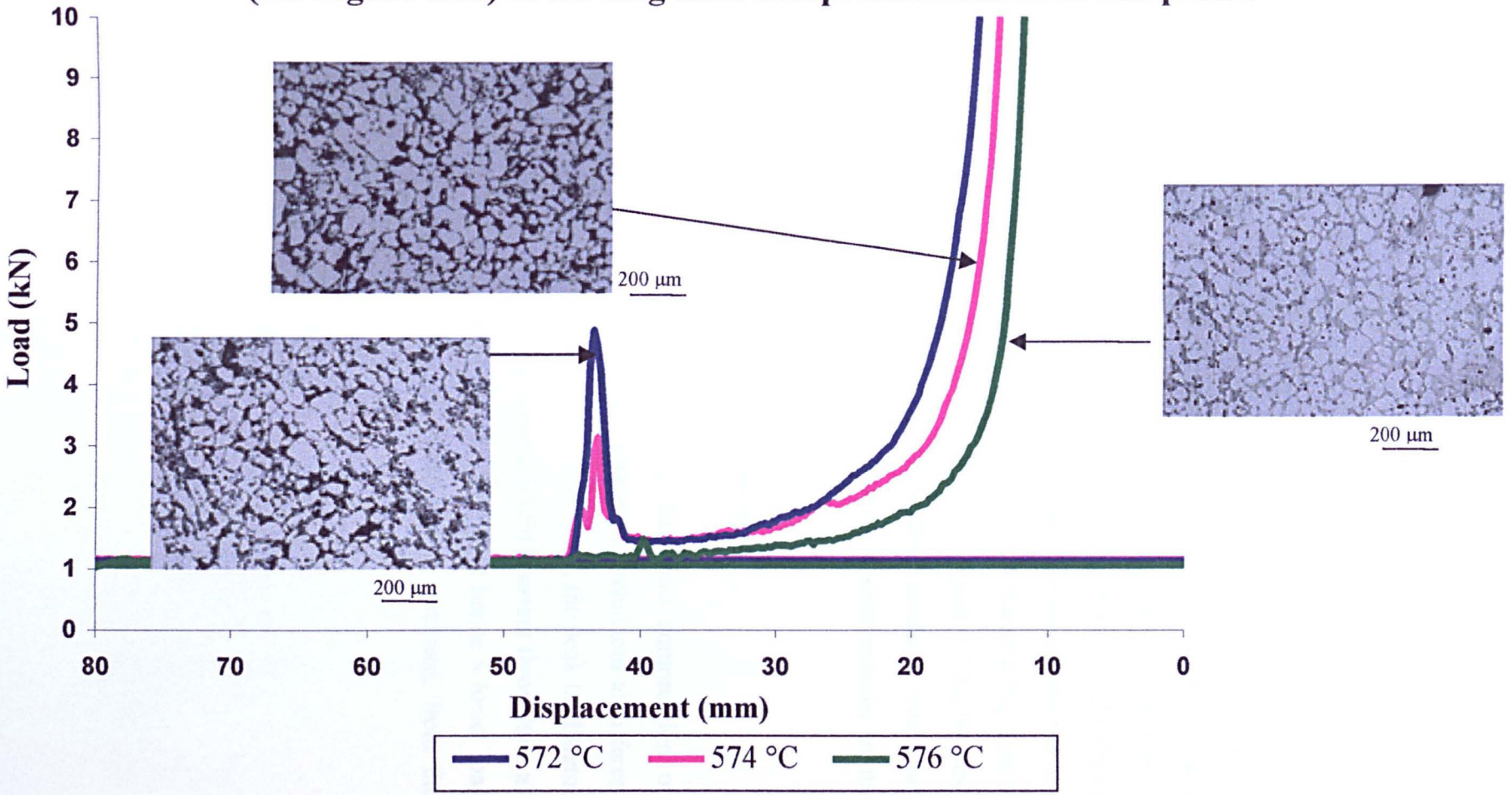

6.2.2 Rapid compression on Al alloys under different holding (soak) times

Figures 6.2.2a and Figure 6.2.2b show the effect of holding (soak) times on the rapid compression experiments. With increasing holding times at the same temperature, the peak load signal encountered during the experiments decreases,

The microstructures shown together with the graphs indicate a similar behaviour with that from the different temperature experiments in 6.2.1. With increasing holding times, the particles became more spheroidal resulting in the decrease in the load signal encountered. From the microstructures, it can also be seen that with increasing holding times, liquid entrapment in the solid particles decreases. Experiments were then conducted for the same alloy composition (for Alusuisse A356 Al alloys) at a lower temperature under different holding times (Figure 6.2.2c). As expected, the peak load encountered in Figure 6.2.2a is lower than the experiment that was conducted at a lower temperature (Figure 6.2.2c). In Figure 6.2.2c, the peak load signal decreases with increasing holding time and this correlates with more spheroidal solid particles as shown in the corresponding microstructures in the figure.

6.2.3 Rapid compression on Al alloys under different ram speed

Different ram speeds were employed during the rapid compression on Alusuisse A356 Al alloys. Figure 6.2.3a shows the load signal behaviour at different ram speeds. Figure 6.2.3a shows that with decreasing ram speed, the peak load signal decreases. Since both temperature and holding times are held constant throughout all these experiments, the viscosity of the slug should not change hence a lower load signal with a lower ram speed should be expected, and is obtained, from the experiment done shown in Figure 6.2.3a.

Figure 6.2.2a: Load signals and microstructures at different holding (soak) times for Alusuisse A356 Al alloys at 575 °C. Microstructures are taken from the Edge_Centre (see Figure 6.4a) of the slug after compression has been completed

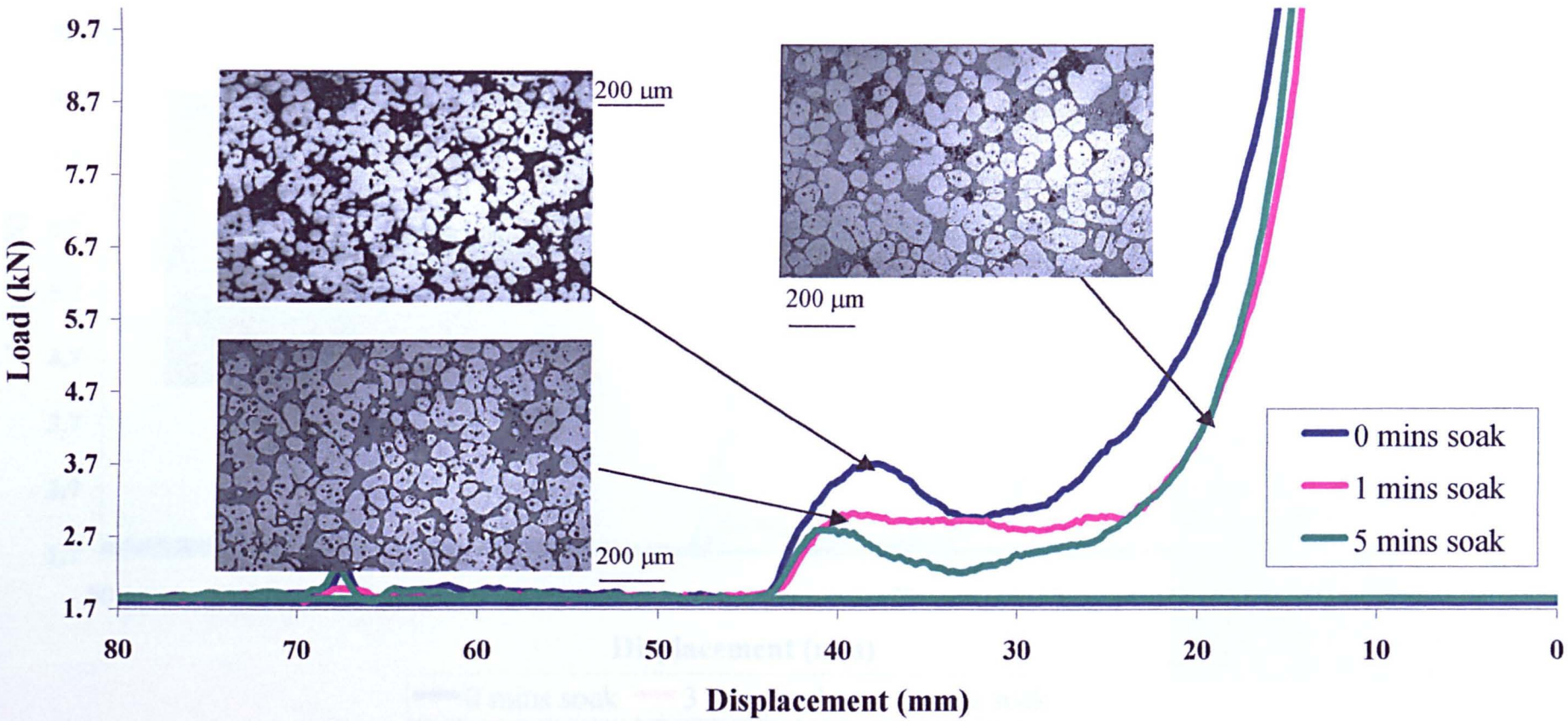

Figure 6.2.2b: Load signals and microstructures at different holding (soak) times for NorthWest A357 Al alloy. Microstructures are taken from the Edge_Centre (see Figure 6.4a) of the slug after compression has been completed

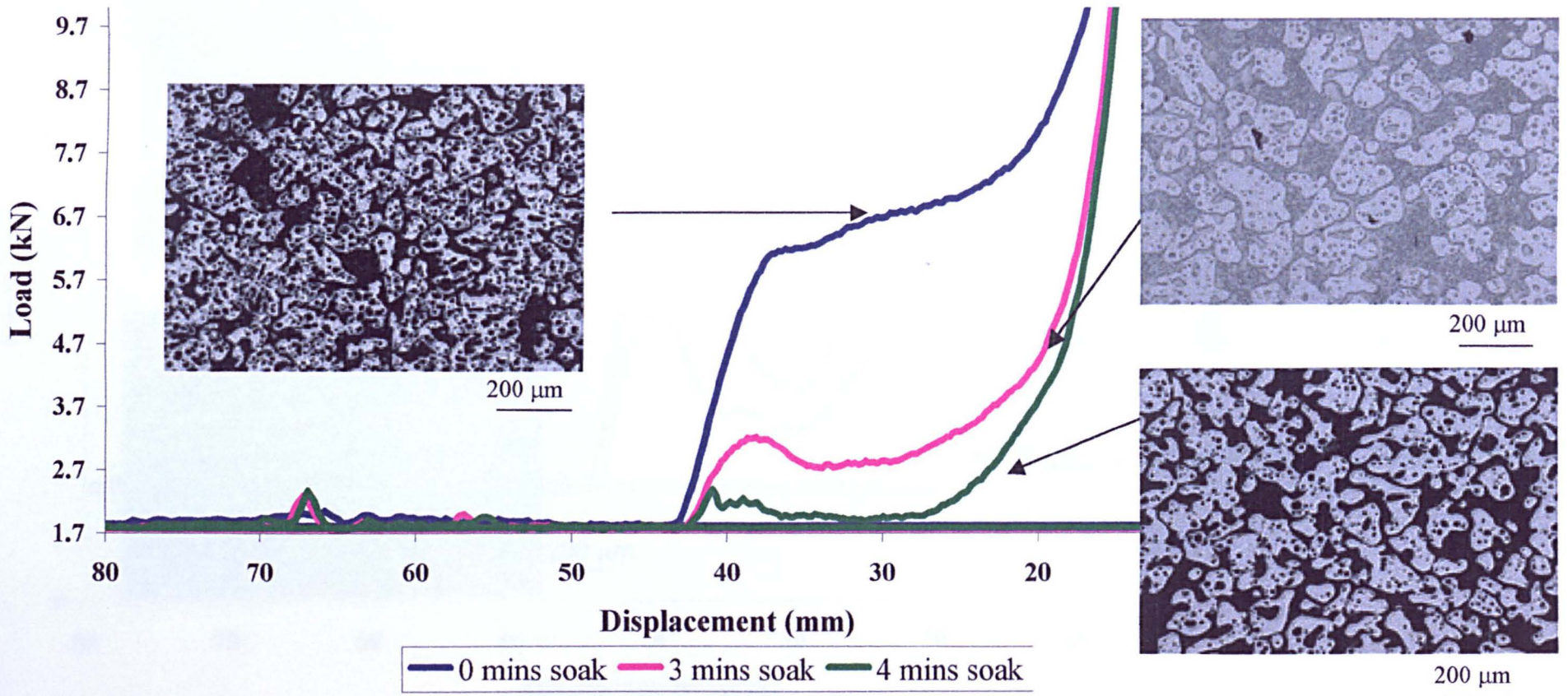

Figure 6.2.2c: Load signals and microstructures at different holding (soak) times for Alusuisse A356 Al alloys at 574 °C. Microstructures are taken from the Edge_Centre (see Figure 6.4a) of the slug after compression has been completed

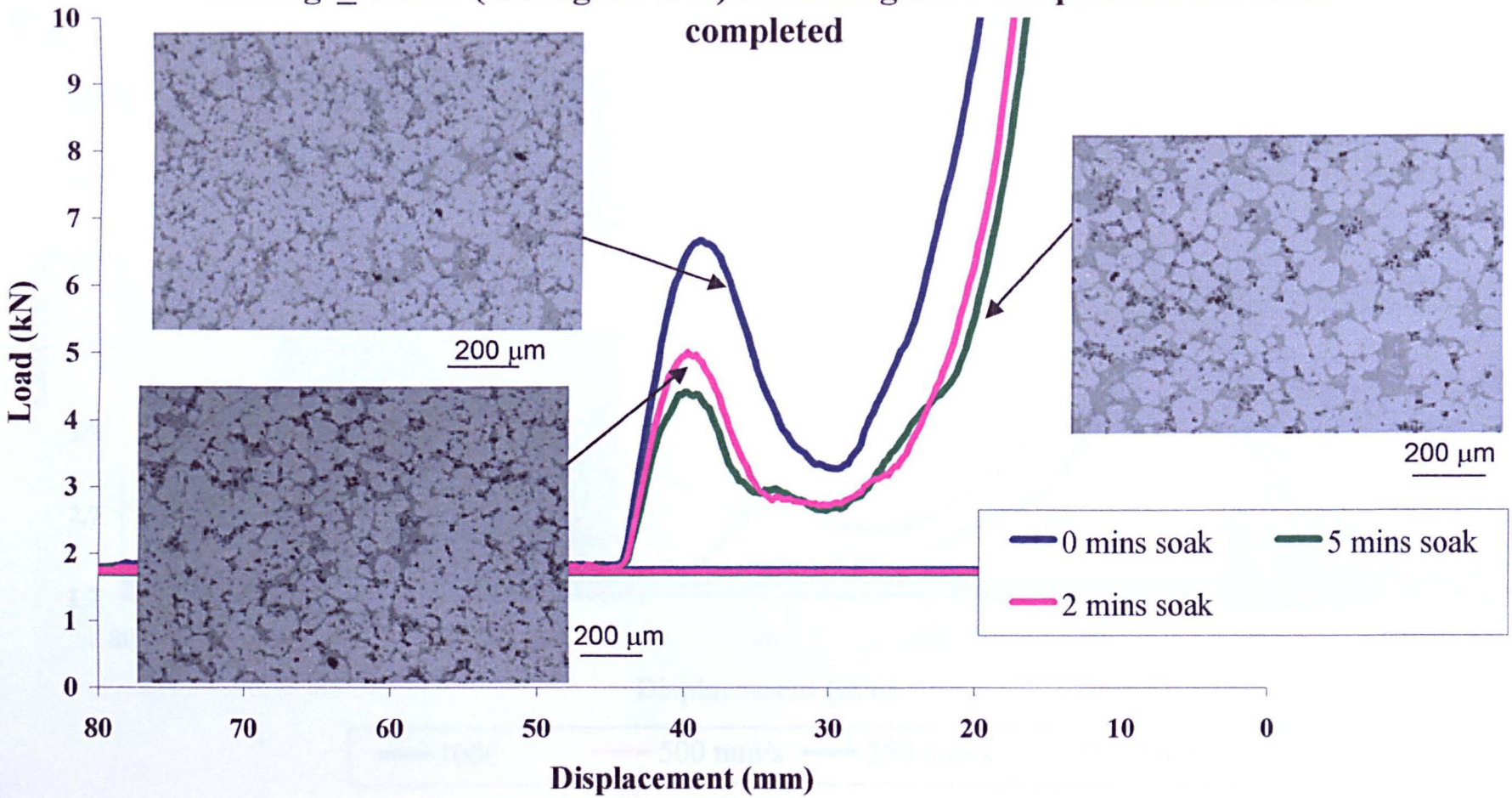

Figure 6.2.3a: Load signals and microstructres at different ram speeds for Alususise A356 Al alloys. Microstructures are taken from the Edge_Centre (see Figure 6.4a) of the slug after compression has been completed

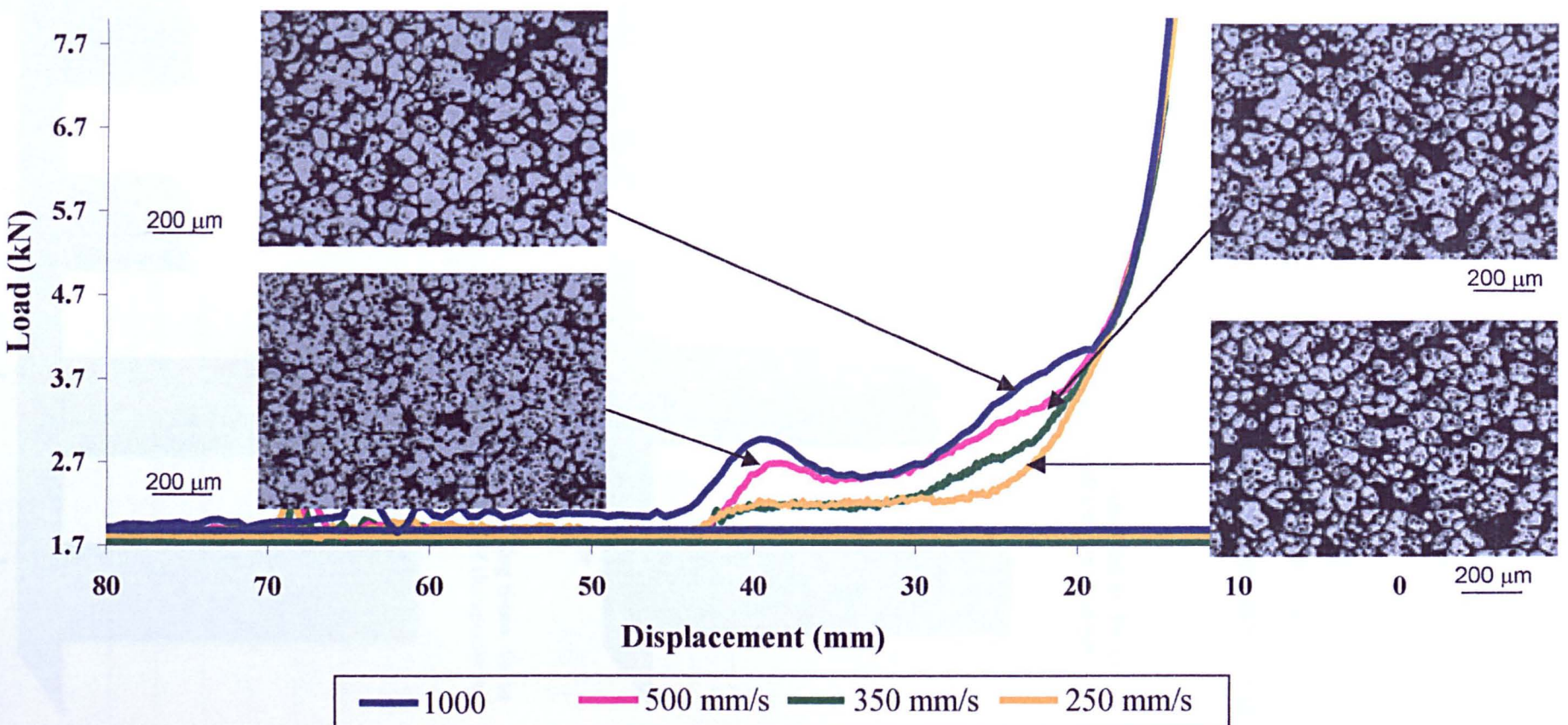

6.2.4 Form factor calculations

The microstructures of the alloys from the experiments were re-examined and the spheroidicity in ters of form factors calculated using equation 5.3a. Figures 6.2.4a, 6.2.4b, 6.2.4c, 6.2.4d and Figure 6.2.4e show the calculated form factors for Alusuisse A356, NorthWest A357 and A319 and Sheffield A357 Al alloys under different temperatures and holding times. All the figures validate the results obtained from the load signal behaviour, i.e. that with increasing temperature or holding time, the solid particles becomes more spheroidal hence the calculated form factor tends to a value of 1.

Figure 6.2.4a: Form factor of Alusuisse A356 at different temperatures. Form Factor measured on the final microstructure at Edge_Centre of the specimen (see Figure 6.4a) after rapid compression

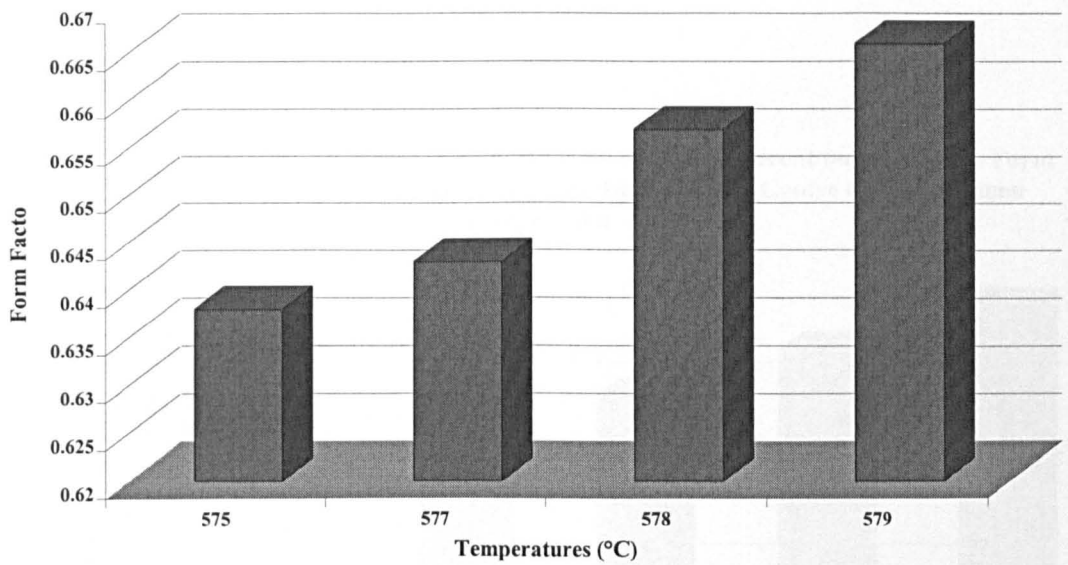

Figure 6.2.4b: Form factor of Alusuisse A356 at different soaking times. Form Factor measured on the final microstructure at Edge_Centre of the specimen (see Figure 6.4a) after rapid compression

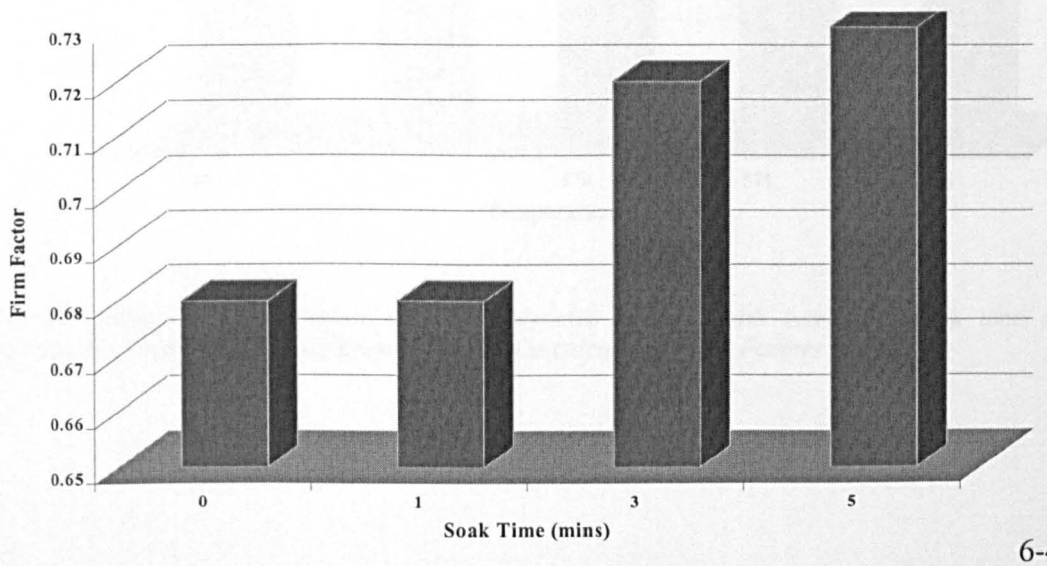

Figure 6.2.4c: Form factor of NorthWest A357 at different soak times. Form Factor measured on the final microstructure at Edge_Centre of the specimen (see Figure 6.4a) after rapid compression

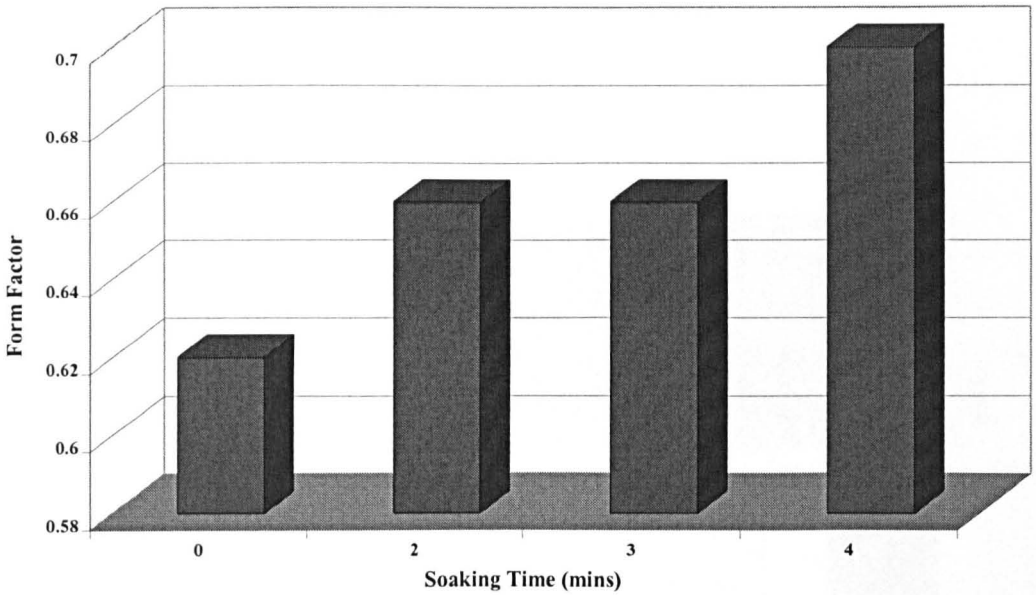

Figure 6.2.4d: Form factor of NorthWest A319 at different temperatures. Form Factor measured on the final microstructure at Edge_Centre of the specimen (see Figure 6.4a) after rapid compression

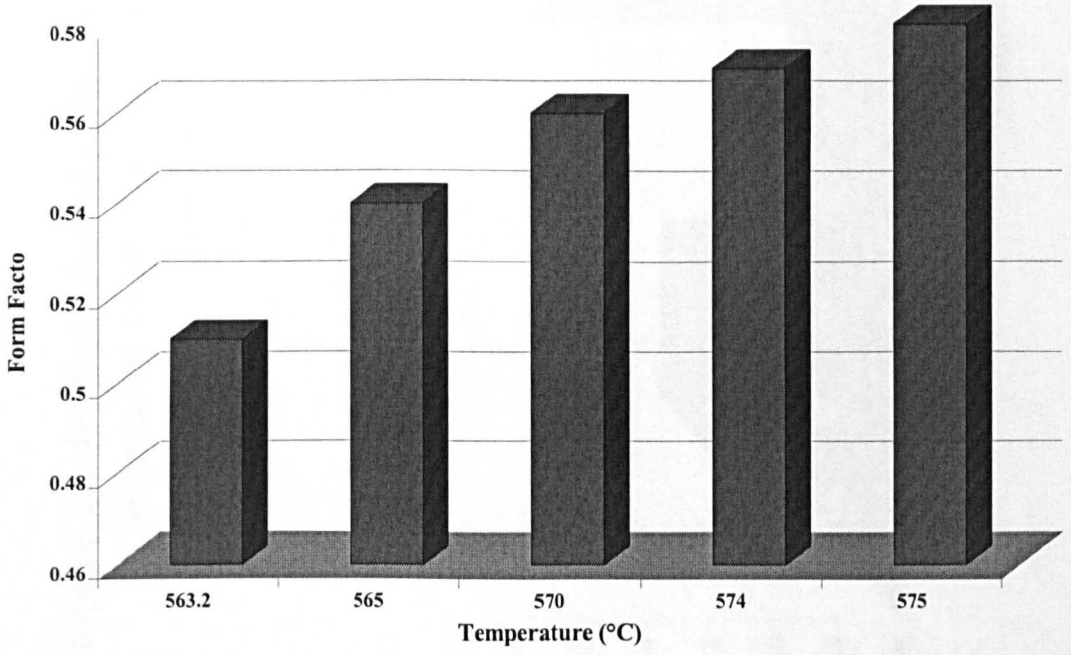

** *Calculations of Form Factors showed a definite increase with increasing soak time and temperatures even though the difference between the calculated From Factors is small.*

Figure 6.2.4e: Form factor of Sheffield A357 at different temperatures. Form Factor measured on the final microstructure at Edge_Centre of the specimen (see Figure 6.4a) after rapid compression

6.2.5 Viscosity behaviour evaluation

An analytical formula following the work of Laxmanan and Flemings [Lax 80] was used to derive the viscosity of the slug as a function of the average shear rate. A derivation of the formula is showed in Appendix 6. Figures 6.2.5a, 6.2.5b and 6.2.5c show the effect of varying the temperatures, holding times and ram speeds on the viscosity behaviour for Alusuisse A356 Al alloys. Figure 6.2.5a shows a 'kink' (or a hump) in the viscosity curves before decreasing to a near constant value. This 'kink' is present in all the temperatures except at T = 578 °C. This effect can be attributed to the material not reaching its desired state for thixoforming process. It sees highly possible that at the lower temperatures, the particles are still not well spheroidised (c.f. Figure 6.2.1b) hence the solid particles are not able to slide past each other as easily as in those experiments which are carried out at higher temperatures. Nevertheless, all the above figures showed a clear shear-thinning behaviour with increasing shear rate. Viscosity values dropped rapidly initially before tending to a near constant value with increasing shear rate.

Another set of experiments on the A356 alloys was done at a temperature of 581 °C. This was thought to be the temperature (or the thixoforming temperature) at which complete die-filling is achieved. Figure 6.2.5d shows viscosity under different temperatures. At the temperature of 581 °C, the figure shows a near constant viscosity value regardless of the shear rate, indicating a Newtonian behaviour in the slug/billet during the experiment.

Figure 6.2.5e shows the viscosity under different temperatures at various shear rates. At the lowest temperature (575 °C), the difference in viscosity values is clearly seen between the different shear rates. With increasing temperature (> 577 °C), this difference reduces and becomes nearly equal for shear rates at 30, 40, 60 and 80 s^{-1}. However, there is still a marked difference when comparing the lowest shear rate (at $10s^{-1}$) with the other shear rates.

Figure 6.2.5f plots the viscosity under different temperatures at various shear rates for the Sheffield A357 alloys. The result shows a similar trend to that obtained in Alusuisse A356 alloys (Figure 6.2.5e).

Figure 6.2.5a: Effect of temperature on viscosity under rapid compression of Alusuisse A356 Al alloys. Average shear rate and viscosity are calculated using the approach of Laxmanan and Flemings [Lax 80]

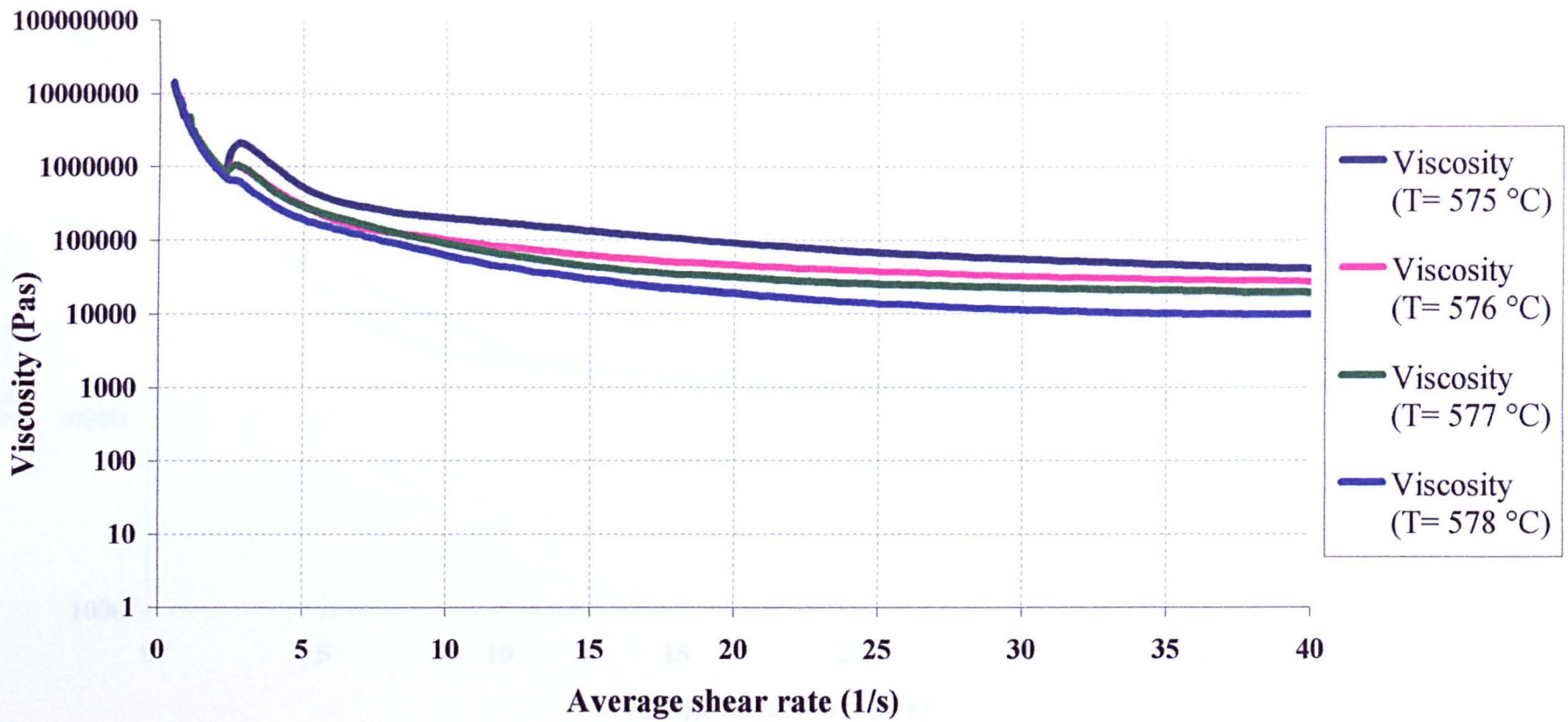

Figure 6.2.5b: Effect of soaking times on viscosity under rapid compression of Alusuisse A356. Average shear rate and viscosity are calculated using the approach of Laxmanan and Flemings [Lax 80]

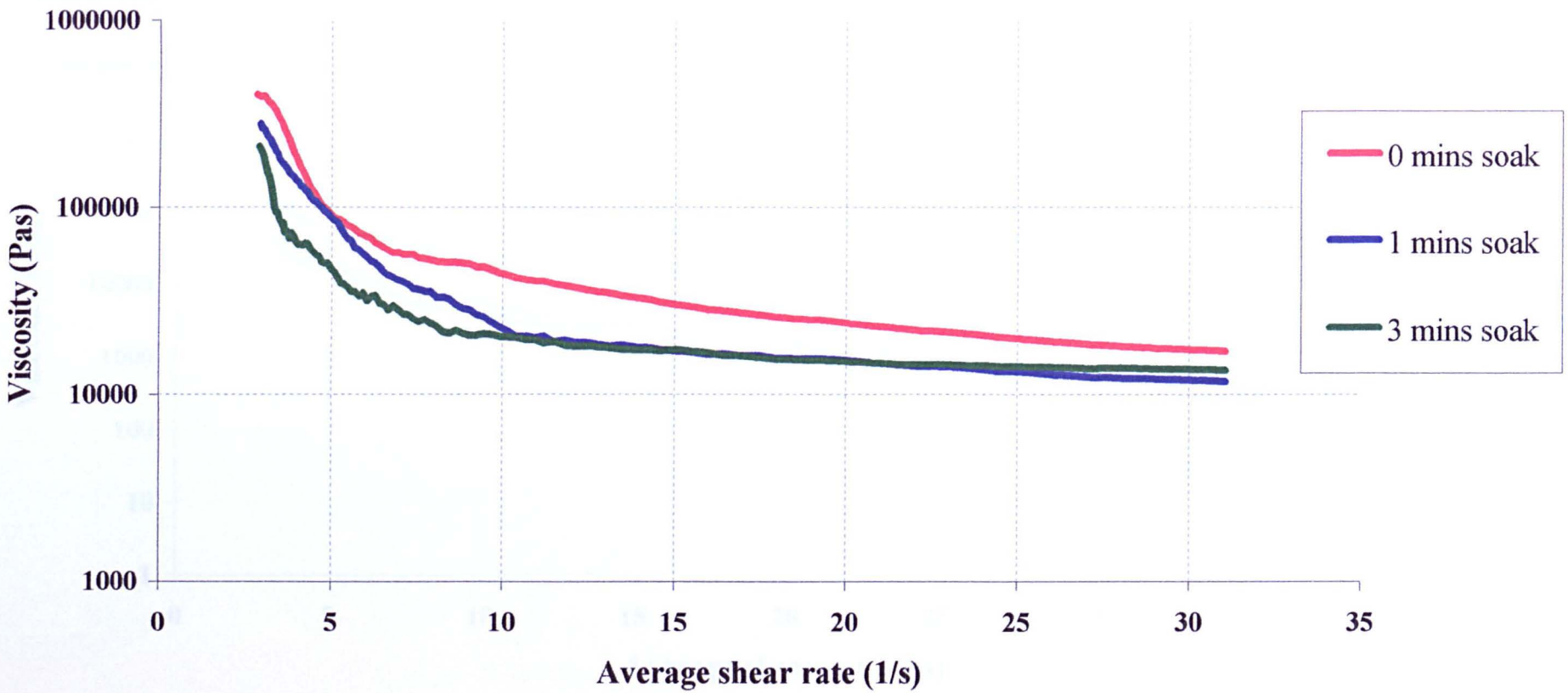

Figure 6.2.5c: Effect of different ram speeds on viscosity under rapid compression of Alusuisse A356 Al alloys. Average shear rate and viscosity are calculated using the approach of Laxmanan and Flemings [Lax 80]

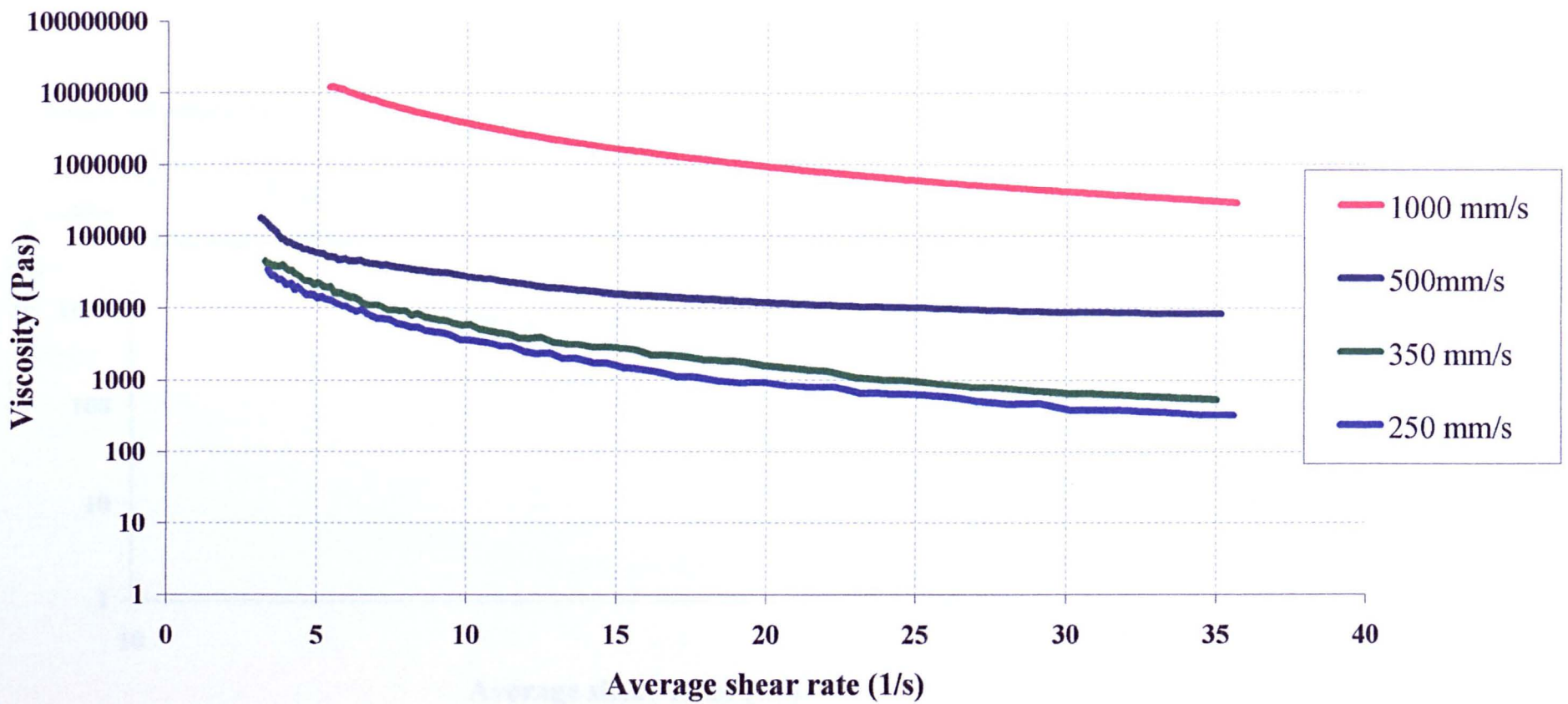

Figure 6.2.5d: Effect of viscosity under different temperatures for Alusuisse A356 Al alloy. Average shear rate and viscosity are calculated using the approach of Laxmanan and Flemings [Lax 80]

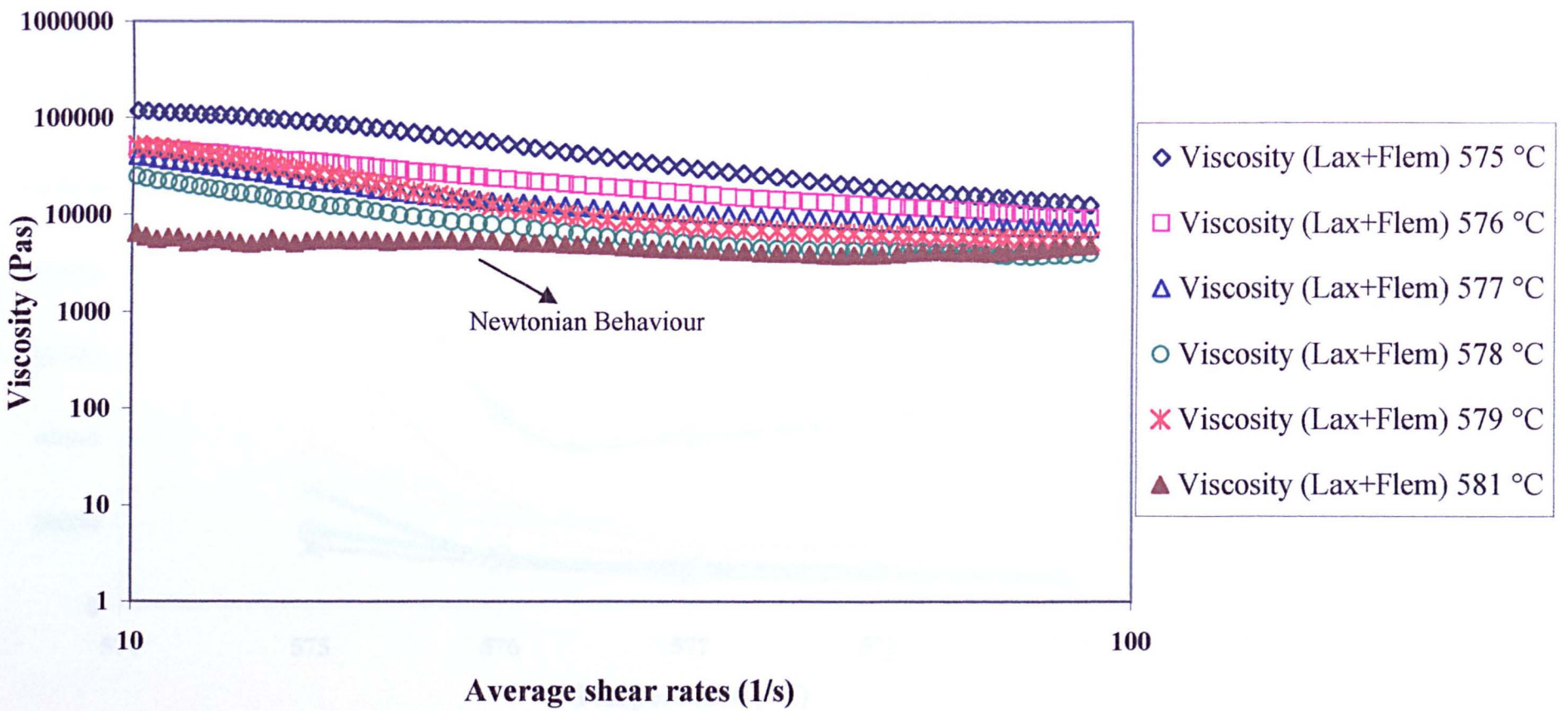

Figure 6.2.5e: Effect of viscosity at different shear rates under different temperatures for Alusuisse A356 Al alloys. Shear rate specified in the legend is the average shear rate calculated using the approach of Laxmanan and Flemings

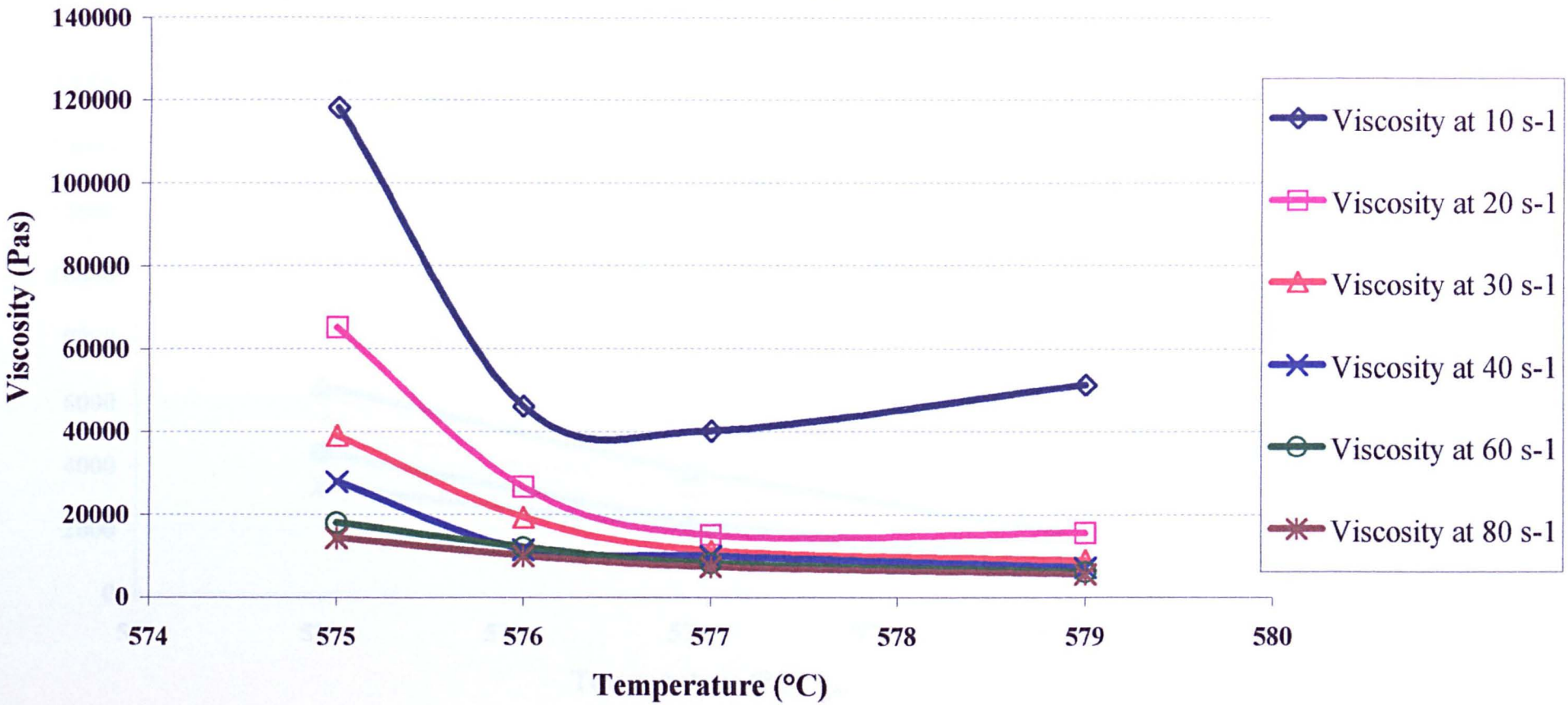

Figure 6.2.5f: Effect of viscosity at different shear rates under different temperatures for Sheffield A357 Al alloys. Shear rate specified in the legend is the average shear rate calculated using the approach of Laxmanan & Flemings

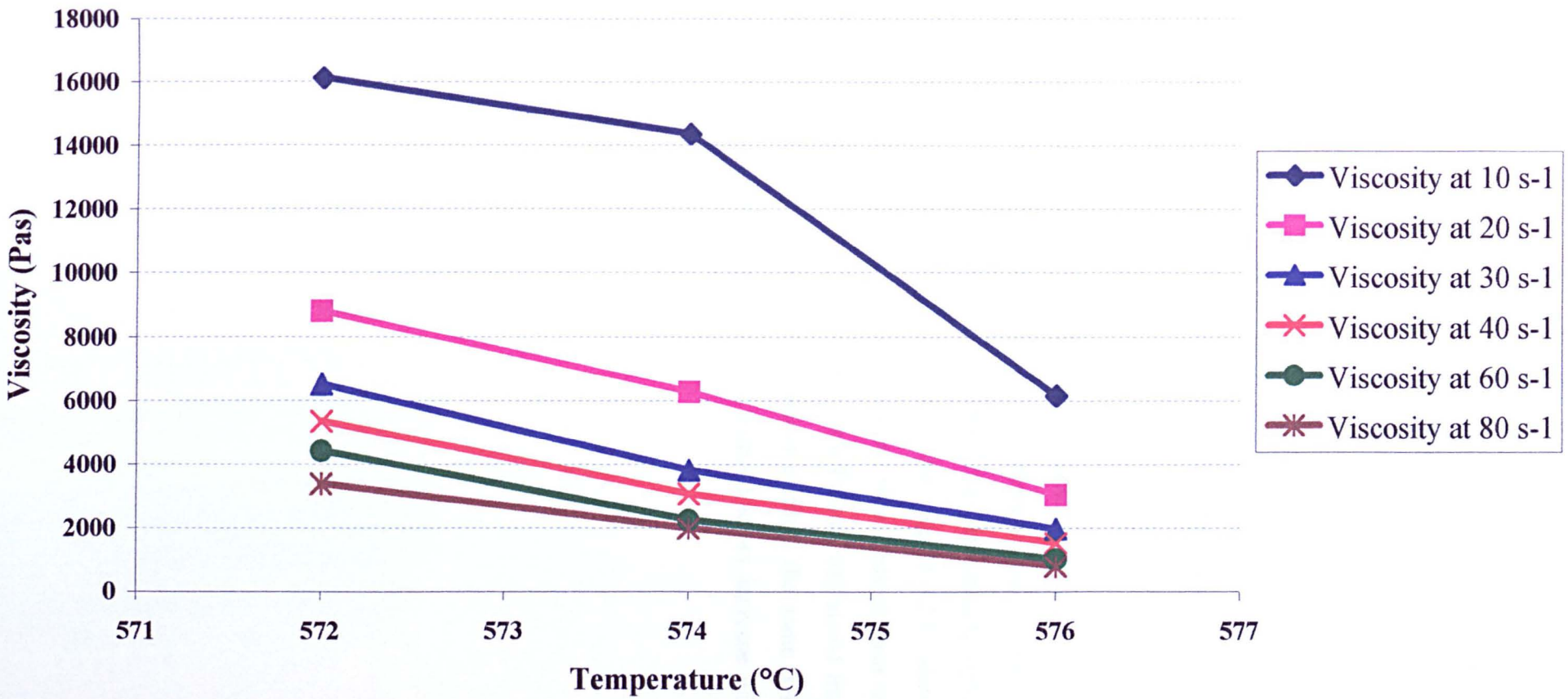

6.2.6 Rapid compression experiments on Sn15%Pb alloys.

Experiments on Sn15%Pb alloys were conducted under different temperatures. The alloys used in the rapid compression differ from those used in the rheological experiments. All Sn15%Pb alloys used in the rapid compression are extruded before the experiment. Figure 6.2.6a shows the load signal behaviour at different temperatures during the experiment. The results showed similar behaviour to the experiments on aluminium alloys. The load signal encountered decreases with increasing temperature. Microstructures of the alloy are presented together with their load signal.

The result in Figure 6.2.6a was analysed using the Laxmanan and Flemings approach [Lax 80]. The viscosity behaviour under different temperatures is presented in Figure 6.2.6b. From the figure, the viscosity dropped rapidly initially before approaching a near constant value with increasing shear rate. Figure 6.2.6c shows that the Sn15%Pb alloy exhibits a near Newtonian behaviour regardless of shear rate at a temperature of 193 °C. Figure 6.2.6d shows the Form Factors calculated from the microstructures of the Sn15%Pb alloy. The behaviour exhibits the same trend with previous experiments on aluminium alloys, i.e. Form Factors increase with increasing temperatures.

Figure 6.2.6a: Load signal and microstructures at different temperatures for Sn15%Pb (extruded) alloys.

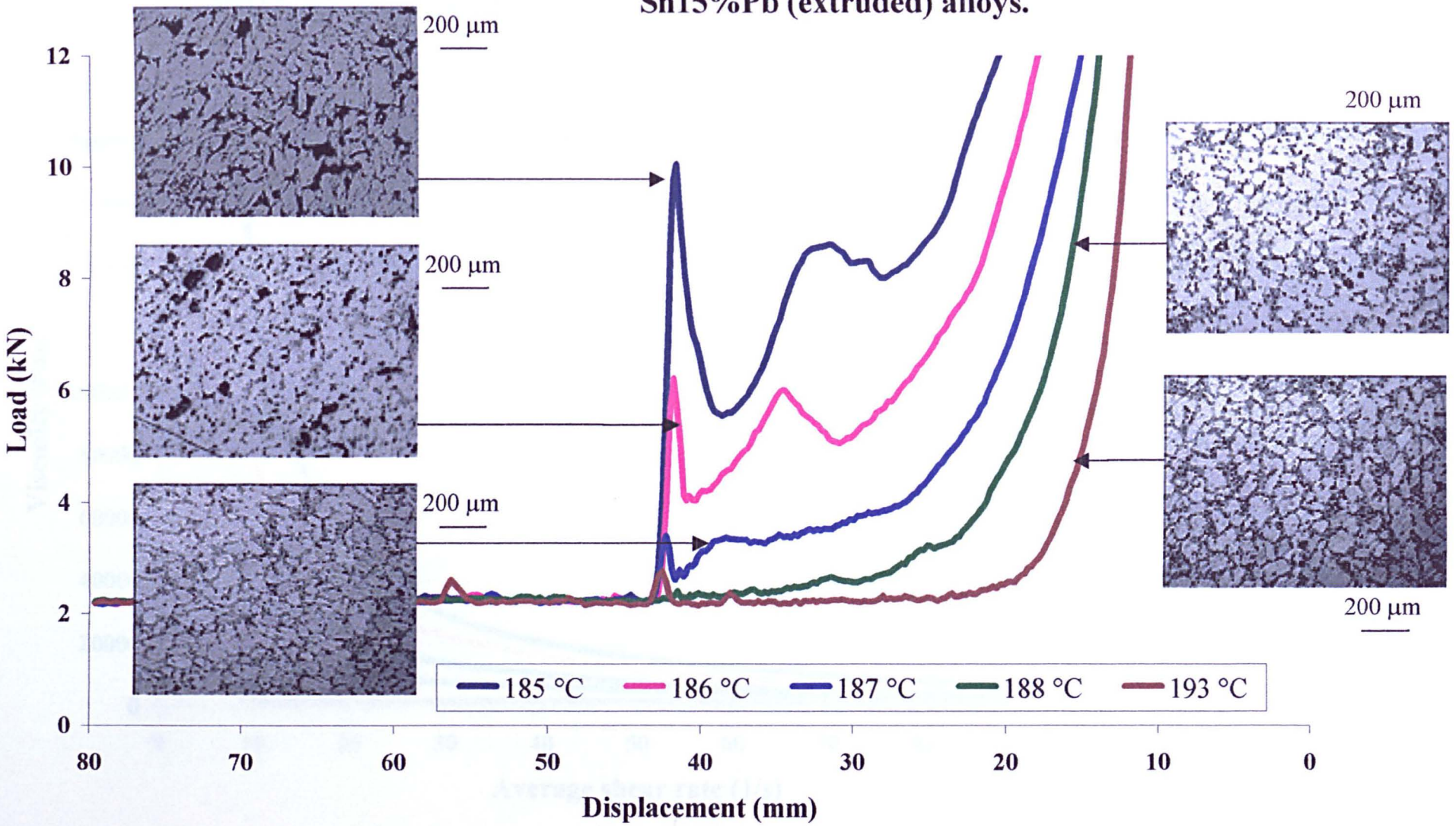

Figure 6.2.6b: Effect of viscosity at different temperatures for Sn15%Pb (extruded) alloys. Average shear rate and viscosity are calculated using the approach of Laxmanan and Flemings [Lax 80]

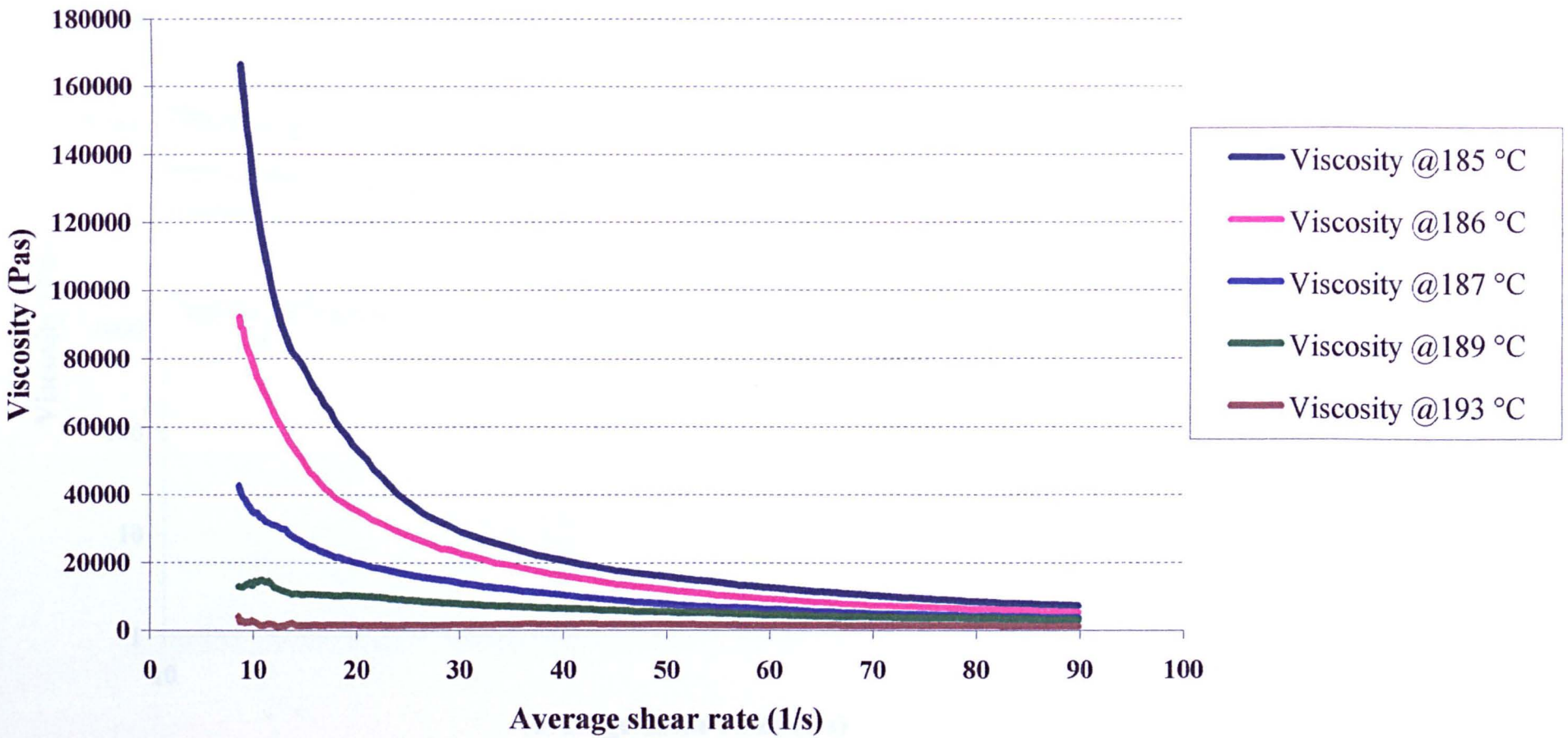

Fiugre 6.2.6c: Effect of viscosity with respect to shear rates of Sn15%Pb alloy. Average shear rate and viscosity are calculated using the approach of Laxmanan and Flemings [Lax 80]

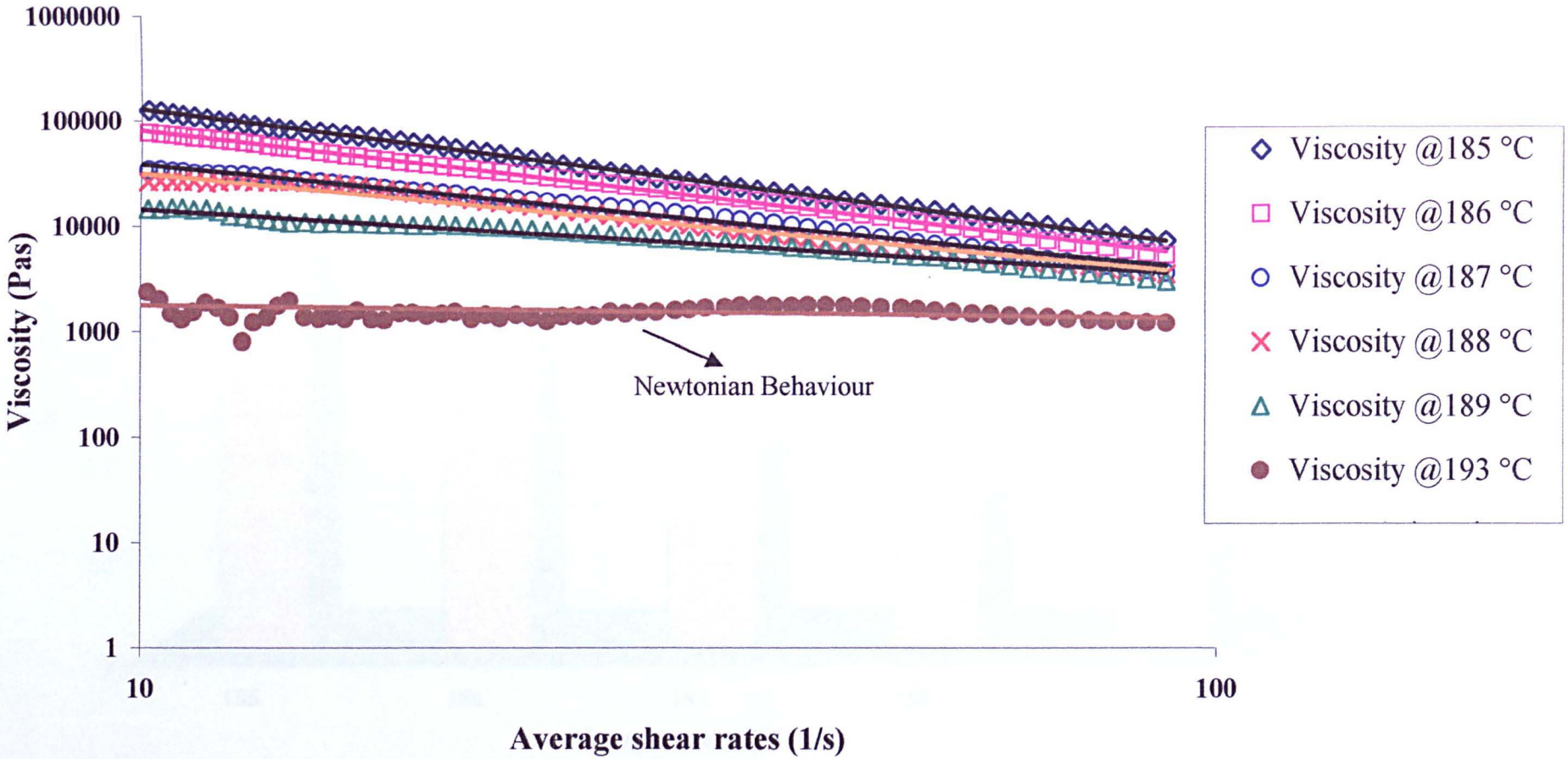

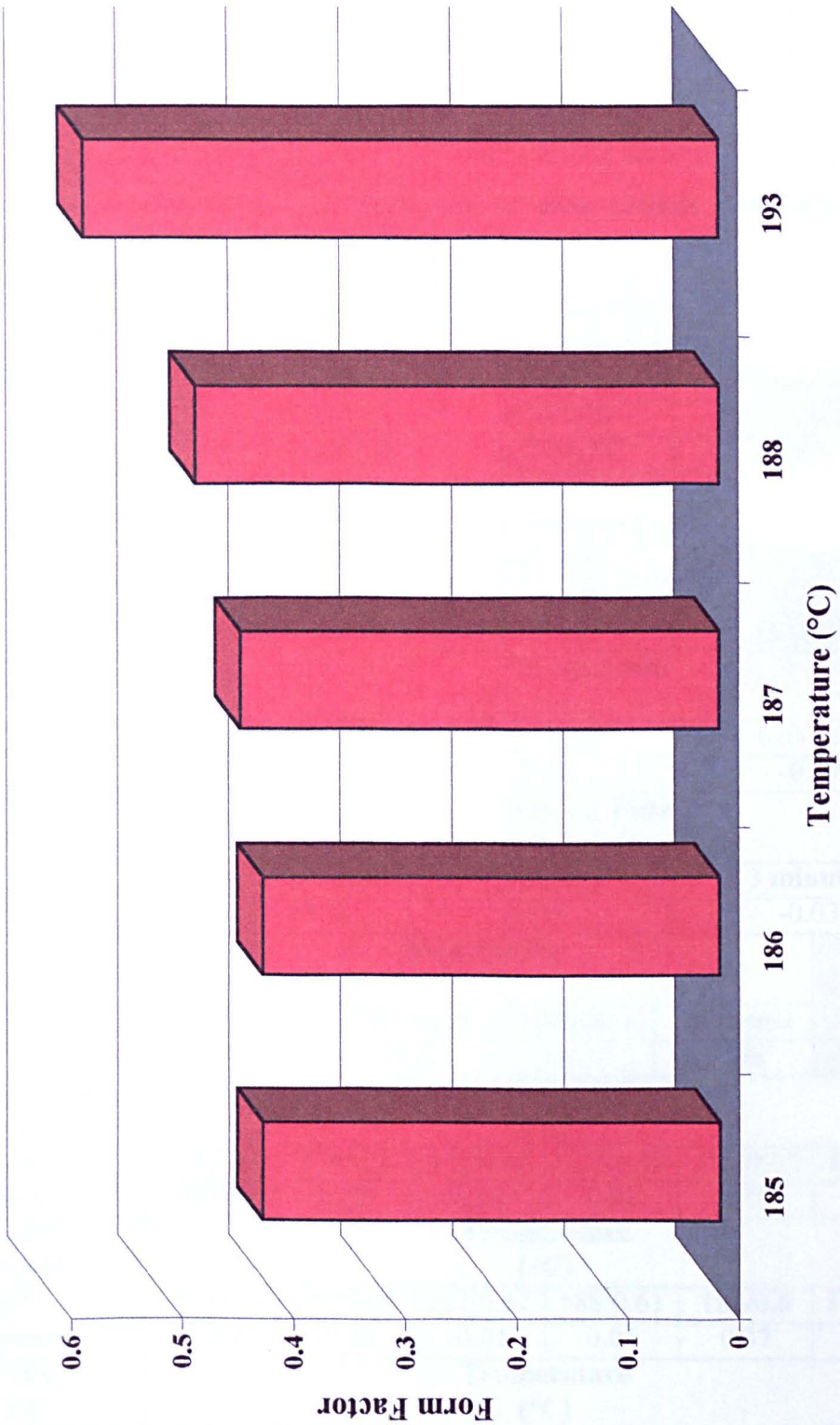

Figure 6.2.6d: Form Factor of Sn15%Pb alloys at different temperatures

6.2.7 Determination of the power law indices

The results obtained from Figures 6.2.5a, 6.2.5b, 6.2.5c and 6.2.6b are re-plotted on a log-log scale and fitted to the power law equation, Equation 4.2.c. Figures 6.2.7a, 6.2.7b, 6.2.7c and 6.2.7d show that the power law indices (of n-1) obtained are less than 1 in both A356 Al alloys and Sn15%Pb alloys. This indicates shear thinning behaviour as expected. The 'n' values for the various thixoforming conditions are tabulated in Table 6.2.7a. Included in the table are values reported by Hogg [Hog 01b] for sprayformed alloys and Chayong [Cha 02] for wrought alloys.

Table 6.2.7a: Variation of shear rate exponent 'n' with various thixoforming conditions for different alloys.

(Fraction solid for high silicon alloys varies with soaking times [Hog01b])

Al30%Si5%Cu [Hog 01b]	**Soaking Times 'n' exponent / Fs**					
T (°C)	**0 minutes**		**2 minutes**		**5 minutes**	
558	-0.31/0.92		0.02/0.91		-0.1/0.89	
560	-0.35/0.95		-0.14/0.95		-0.08/0.94	
Al30%Si5%Cu2%Mg [Hog 01b]	**Soaking Times 'n' exponent / Fs**					
T (°C)	**0 minutes**		**2 minutes**		**5 minutes**	
552	-0.26/0.9		-0.01/0.9		-0.17/0.89	
555	-0.16/0.91		-0.19/0.89		-0.37/0.88	
Al5.3%Zn2.3%Mg1.5%Cu [Cha 02]	**'n' exponent**					
T (°C) / Fs	605/0.80		615/0.68		620/0.58	
	0.2		-0.29		-0.89	
Al7%Si0.3%Mg [This Work]	**Soaking Times**					
T (°C)/Fs	**0 minutes**		**1 minutes**		**3 minutes**	
575/0.50	-0.32		-0.41		-0.03	
Al7%Si0.3%Mg [This Work]	**Ram Speeds**					
T (°C)	**1000 mm/s**	**500 mm/s**	**350mm/s**	**250mm/s**		
576/0.51	-0.99	-0.23	-0.91	-0.98		
Al7%Si0.3%Mg [This Work]	**Temperature (°C)**					
T(°C)/F_s	575/0.51	576/0.5	577/0.49	578/0.48	579/0.47	581/0.46
'n' exponent	-0.06	0.28	0.19	0.06	0.18	0.77
Sn15%Pb [This Work]	**Temperature (°C)**					
T(°C)/Fs	185/0.64	186/0.63	187/0.62	188/0.61	189/0.6	193/0.54
'n' exponent	-0.31	-0.20	-0.01	0.05	0.37	0.88
Sn15%Pb [Lax 80]	**Temperature (°C)**					
T (°C)	189/0.6	192/0.55	195/0.5	201/0.4	204/0.3	207/0.2
'n' exponent	0.70	0.58	0.49	0.32	0.22	0.19

Figure 6.2.7a: Calculated viscosity vs shear rates based on Laxmanan and Flemings [Lax 80] approach re-plotted in log form for Alusuisse A356 alloys under different temperatures. The curves are fitted to the power law equtation (shown below).

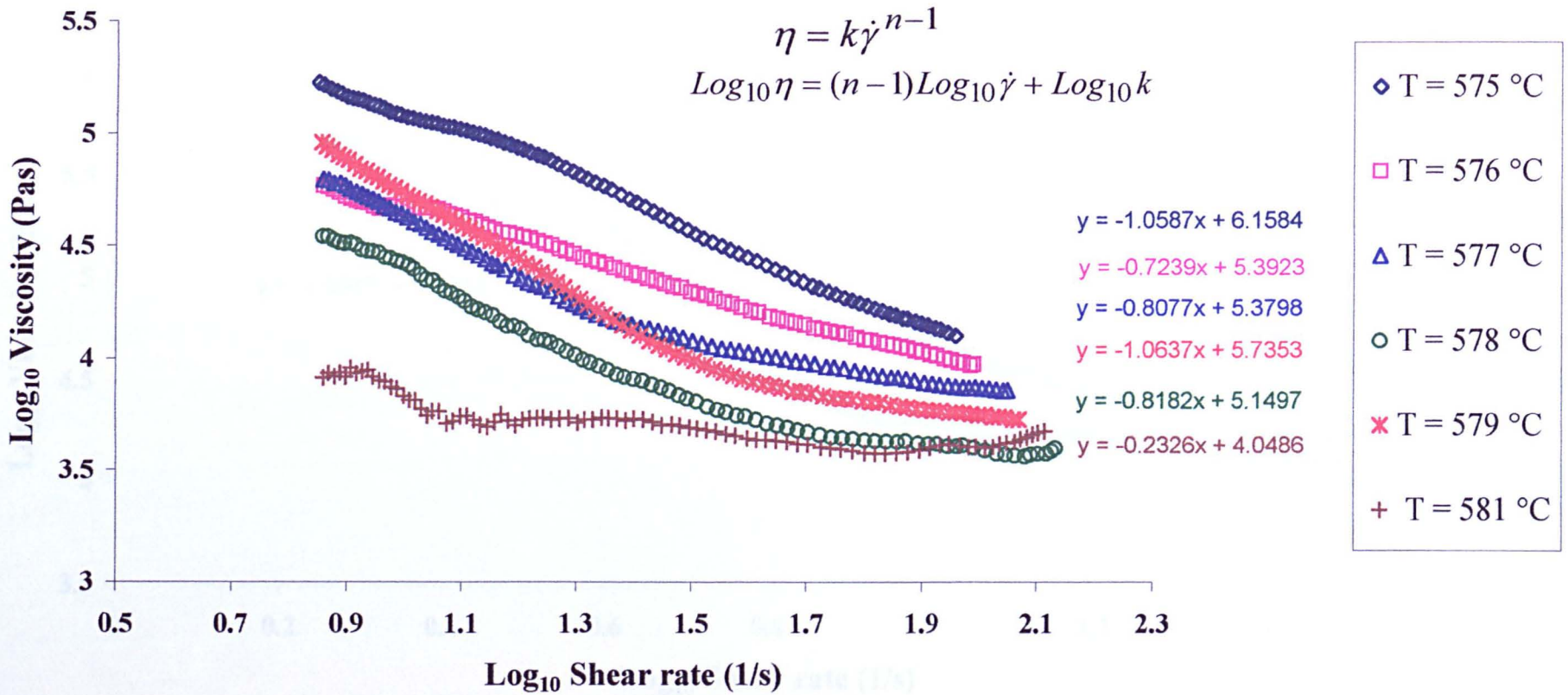

Figure 6.2.7b:Calculated viscosity vs shear rates based on Laxmanan and Flemings [Lax 80] approach re-plotted in log form for Alusuisse A356 alloys (T = 575°C) under different soaking times. The curves are fitted to the power law equtation (shown below).

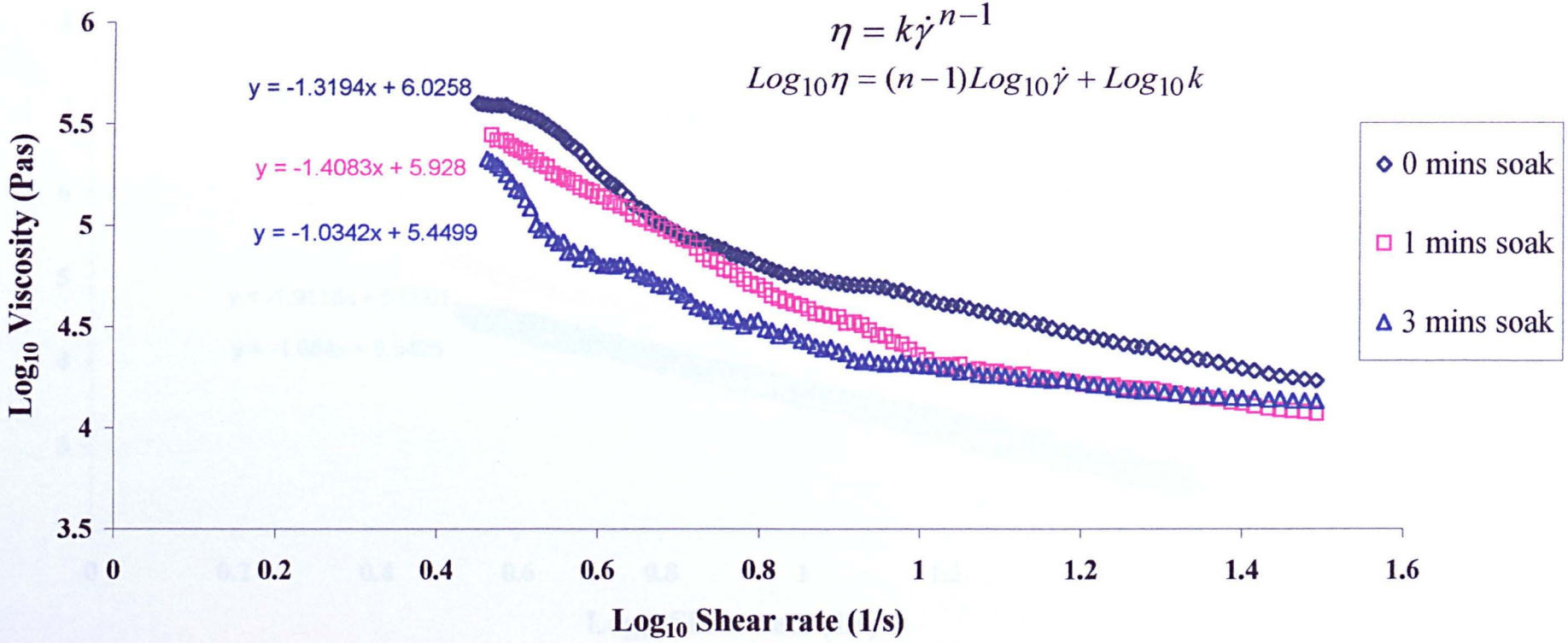

Figure 6.2.7c: Calculated viscosity vs shear rates based on Laxmanan and Flemings [Lax 80] approach re-plotted in log form for Alusuisse A356 alloys (T = 576 °C) under different ram speeds. The curves are fitted to the power law equtation (shown below).

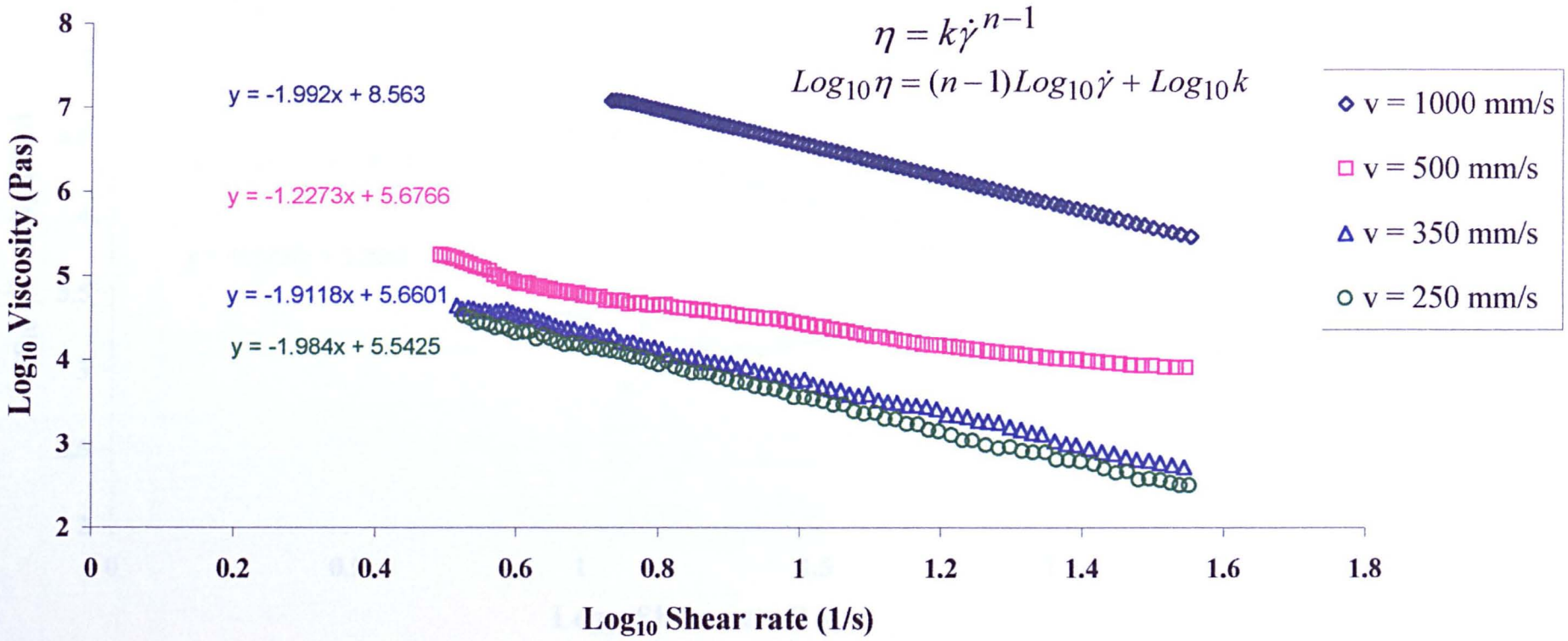

Figure 6.2.7d: Calculated viscosity vs shear rates based on Laxmanan and Flemings [Lax 80] approach re-plotted in log form for Sn15%Pb alloys under different temperatures. The curves are fitted to the power law equtation (shown below).

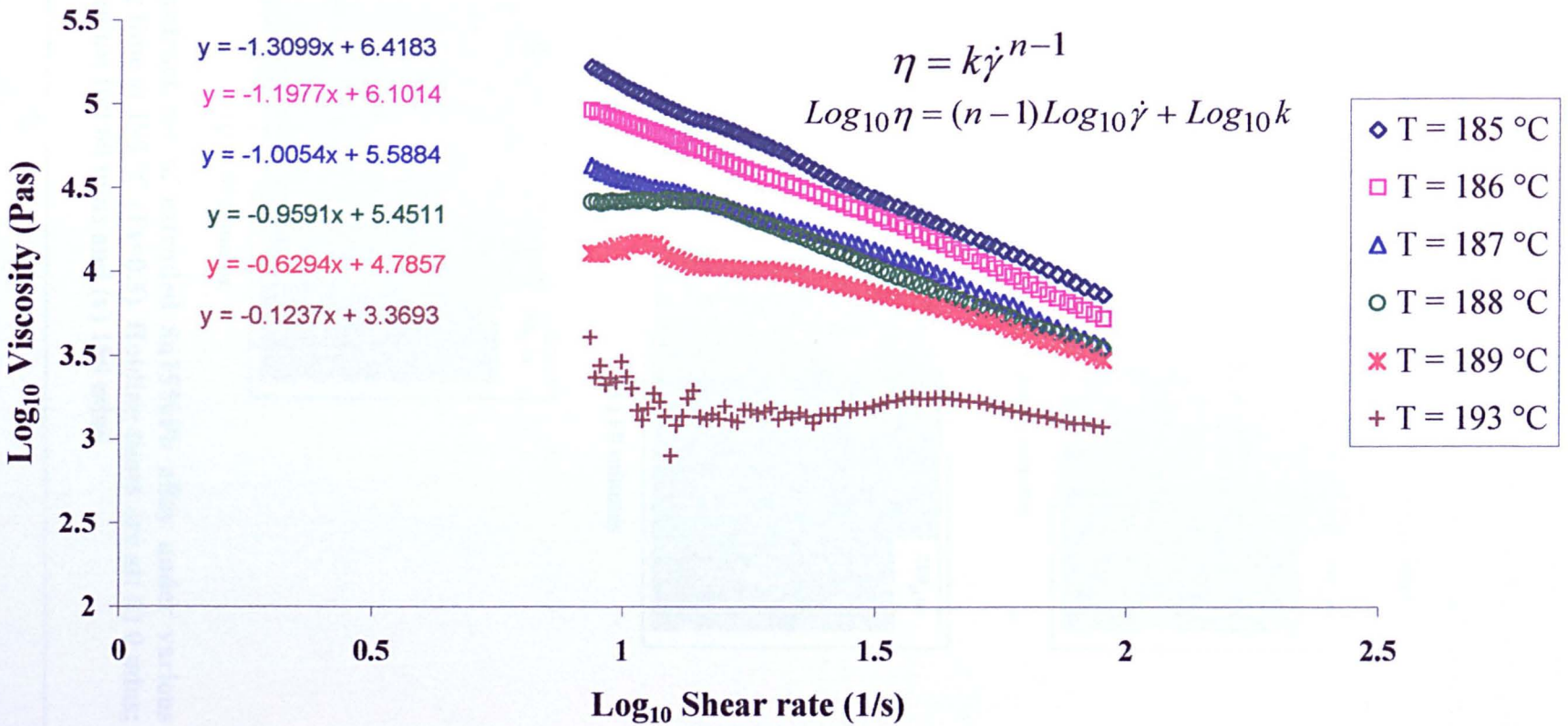

6.3 Isothermal holding experiments in the induction heater.

Isothermal holding experiments were conducted in the induction heater for various holding times at 195 °C (Fs=0.5). Figure 6.3a below shows the microstructures of the Sn15%Pb extruded alloy at (i) 0 minutes; (ii) 5 minutes; (iii) 30 minutes; (iv) 60 minutes and (v) 180 minutes. It can be seen quite clearly that with increasing holding time, the particles became larger and more spheroidal.

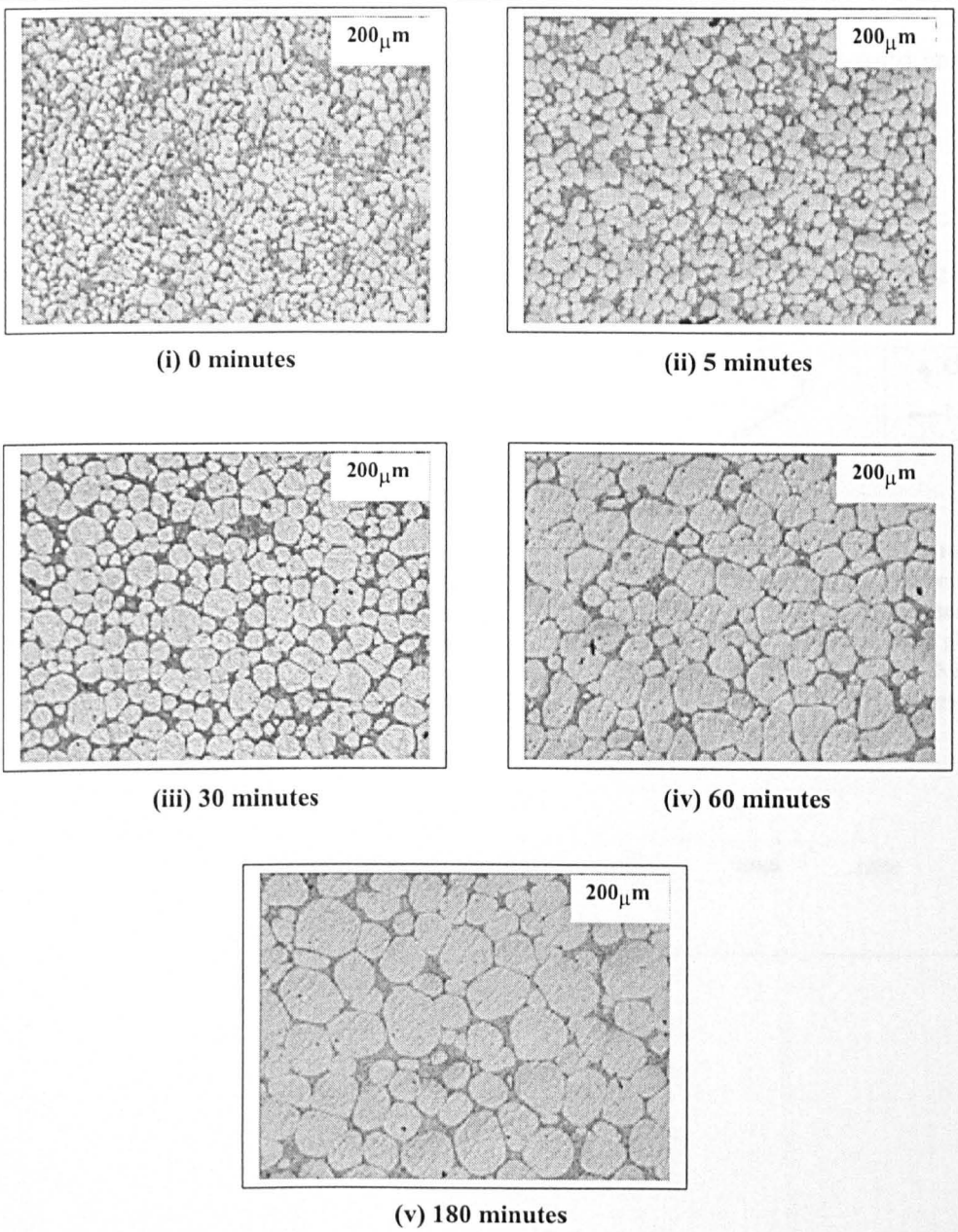

(i) 0 minutes

(ii) 5 minutes

(iii) 30 minutes

(iv) 60 minutes

(v) 180 minutes

Figure 6.3a. Microstructures of extruded Sn15%Pb alloy under various isothermal holding time at 195 °C (Fs=0.5). Holding times are at: (i) 0 mins; (ii) 5 mins; (iii) 30 mins; (iv) 60 mins and (v) 180 mins.

The grain growth behaviour of the Sn15%Pb alloy subjected to isothermal holding at 195 °C was analysed using image analysis. The results were then plotted assuming cubic (or diffusion controlled) coarsening kinetics (i.e. n=3, from Equation 3.4.1A), which is a reasonable assumption for solid/liquid coarsening at high volume fraction liquid [Ann 95]. The coarsening rate constant was calculated to be 172 x 10^{-18} m^3/s (see Figure 6.3b below). This value was approximately 2 times higher than the coarsening rate (of 100 x 10^{-18} m^3/s) for a sprayformed nickel super-alloy (IN 718) [Whi 99] at a similar fraction solid of 0.5. Sprayformed materials have been shown to exhibit inhibited coarsening [Ann 95] which would account for the higher value obtained in this work.

Figure 6.3b: Average grain size of Sn15%Pb alloy versus isothermal holding times at a fraction solid of 0.5.

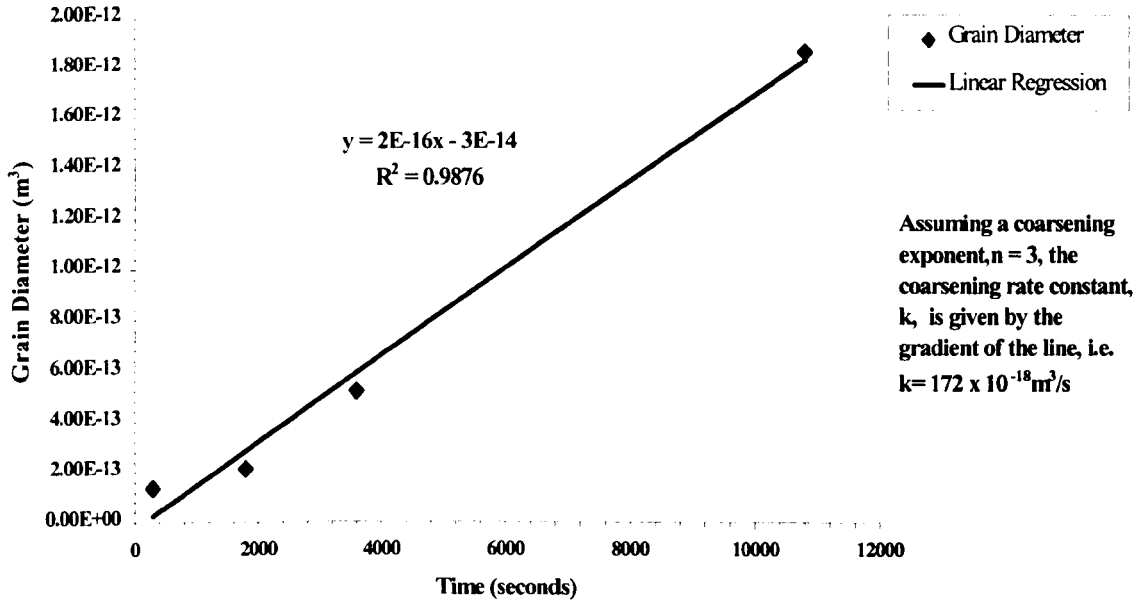

6.4 Liquid Segregation in the thixoformed sample

The thixoformed sample was cut and the microstructure examined across the whole area. Figure 6.4.a shows a schematic diagram of the sample. Only a quarter of the sample was examined as it is assumed to be symmetrical for a circular disc.

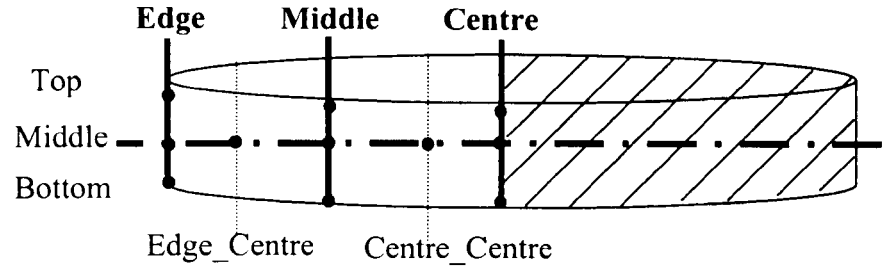

• are points of examinations of the microstructures.

Figure 6.4.a: Schematic diagram of microstructural examination of a typical thixoformed sample

Microstructural examination showed liquid segregation as the points of examination moved towards the edge of the sample. Figure 6.4.b shows the microstructures taken from Alusuisse A356 alloys at 575 °C with a soak time of 1 minute. It can be seen that there is less liquid in the centre of the sample compared to the edge of the sample. Liquid is being pushed towards the edge as the sample is filling the die. Figure 6.4.c shows the microstructures examined from the top towards the bottom of the sample. Liquid segregation can also be seen at the middle part of the sample. Both figures showed that the liquid is being pushed outwards during the thixoforming process. Liquid segregation was also thought to be influenced by the ram speed, soaking time and temperature. Appendix 5 shows a series of micrographs on Alusuisse A356 alloys for different temperatures, soaking times and ram speed. From the micrographs, it can be seen clearly that more liquid can be seen at the edges of the sample than at the centre of the sample.

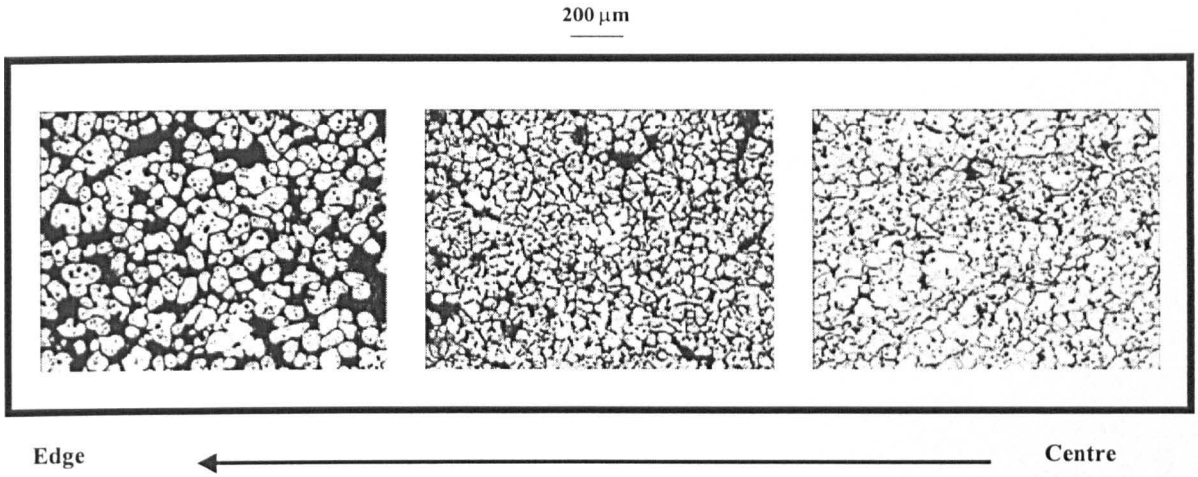

Figure 6.4b: Microstructures along a thixoformed sample. Liquid segregation is seen as the examination moves towards the edge of the sample

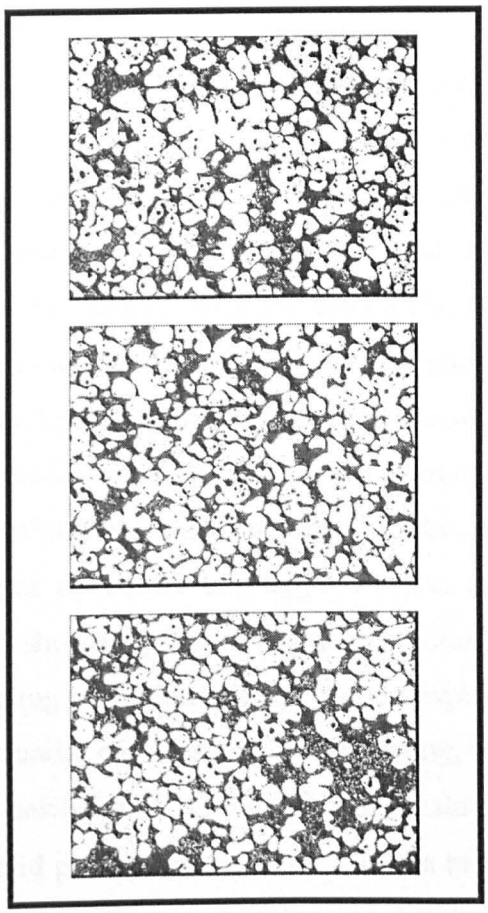

Figure 6.4.c: Microstructures along a thixoformed sample taken from the top surface to the bottom surface showing more liquid at the top and bottom and less liquid in the centre of the sample. Liquid is being pushed outwards during the thixoforming process.

CHAPTER 7

Discussion

Results given in the previous chapter (Chapter 6) will be discussed beginning with the experimental results from (1) viscometry experiments, followed by (2) rapid compression experiments.

7.1 Viscometry Experiments

7.1.1 Continuous cooling on Sn15%Pb alloys.

During continuous cooling, solidification takes place (mainly), resulting in an increase in the viscosity values. From Figure 6.1.1a, it was shown that with increasing shear rate, the viscosity encountered for the same fraction solid decreases. Due to the limitations of the instrument, the effect of cooling rate on the viscosity behaviour was not investigated. A quantitative comparison of the results in Figure 6.1.1a could not be done as the experiments from Joly et al (see Figure 4.1.1c(a) and Figure 4.1.1D(a)) were carried out at different cooling rates and at higher shear rates. The trend where the viscosity curve shifts towards a higher fraction solid with increasing shear rate during the solidification process is similar to the work of [Jol 76], [Wan 90a, Wan 90b] and [Mod 99]. Microstructural examination showed a smaller and more spheroidal particle with increasing shear rate. Figure 6.1.1b showed that the solid particles are not as broken down as Figure 6.1.1c. At low shearing rate, solid particles that are broken down may agglomerate where Ostwald ripening and coarsening of the particles are more likely to happen than at higher shearing rate where a high shear rate may inhibit the agglomeration of the solid particles by constantly breaking the particles up before any agglomeration may occur [Wan 90b]. Figures 6.1.1d and 6.1.1e showed the solid particles becoming smaller and less clustered. This reduced clustering of particles can be used to explain the results in Figure 6.1.1a. With smaller and rounder particles and less clustering, the particles are able to move/slide past each other easily hence a lower viscosity value is encountered. The high shear rate causes the solid particles to break up and as a result, smaller particles that are formed during the breaking up may dissolve and disappear into the liquid medium while some may

combine with a larger particle. The presence of high shear rate may also inhibit the particles from combining with each other. Therefore it is highly possible that this explanation is valid in describing the microstructural evolution with shear rate in a continuously cooled experiment.

7.1.2 Isothermal holding steady state experiment.

The steady state experiment is also the conditioning stage for the step change experiments. The steady state experiments condition the primary phase particles until they are more or less spheroidal and have achieved a steady state structure. This is reflected in their viscosity values that are (nearly) constant over time. This viscosity is usually referred to as the apparent viscosity. The result from Figure 6.1.2a showed the decrease in the apparent viscosity values with increasing shear rate and decreasing fraction solid. All the experiments were conditioned at 50 s^{-1} and cooled at 1 °C/min. The curves in Figure 6.1.2a have been fitted with a power law equation (Table 2.2.1B) and the indices were comparable to the results from Mclelland [Mcl 93]. Figures 7.1.2a and 7.1.2b shows the result of applying the Cross equation (Table 2.2.1B) to this study and results from other workers. A good description was obtained whereby a near Newtonian behaviour (i.e. constant viscosity) can be seen at the very low and very high shear rate regions. Figure 7.1.2b showed the decreasing trend in viscosity values with decreasing fraction solid. It was found that by using a nominal value of – 1.3 for the power law index, a good fit to the results from this work and other works can be obtained. Furthermore, using the same value for the results on Figure 7.1.2b, the slope of the curve varies little with the fraction solid while still obtaining a good fit to the curves but the material constant, k, increases with increasing fraction solid. Although the results on Figure 7.1.2c could not be adequately described by the Cross equation due to insufficient data on the very low shear rate region for aluminium alloys, a comparison could still be done. Figure 7.1.2c shows similar behaviour with Figure 7.1.2b where the viscosity values decrease with increasing shear rate. It should be noted that in Figure 7.1.2c, the viscosities are more dependent on the fraction solid than the composition, i.e. the results can be compared directly. However, this may not be the case for any alloy compositions. Surprisingly, the power law index used is the same as that for Figure 7.1.2b (on Sn15%Pb alloys) and yet, a good fit to the intermediate shear rate region can still be obtained.

Figure 7.1.2a: Apparent viscosities at different shear rates fitted to the Cross Model for Sn15%Pb alloys (Fs=0.36)

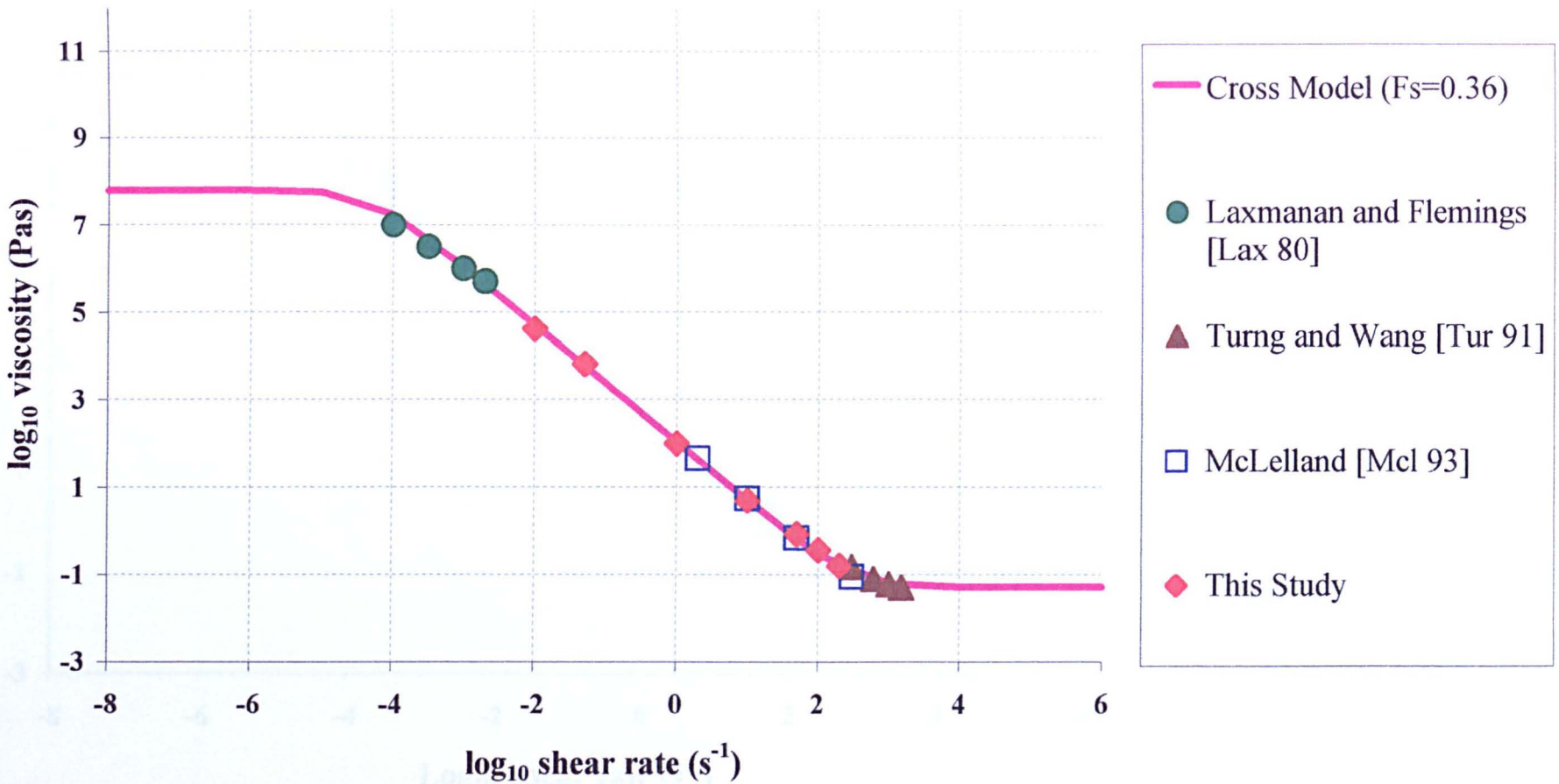

Figure 7.1.2b: Cross Model fitted to apparent viscosities obtained from various works on Sn15%Pb alloys.

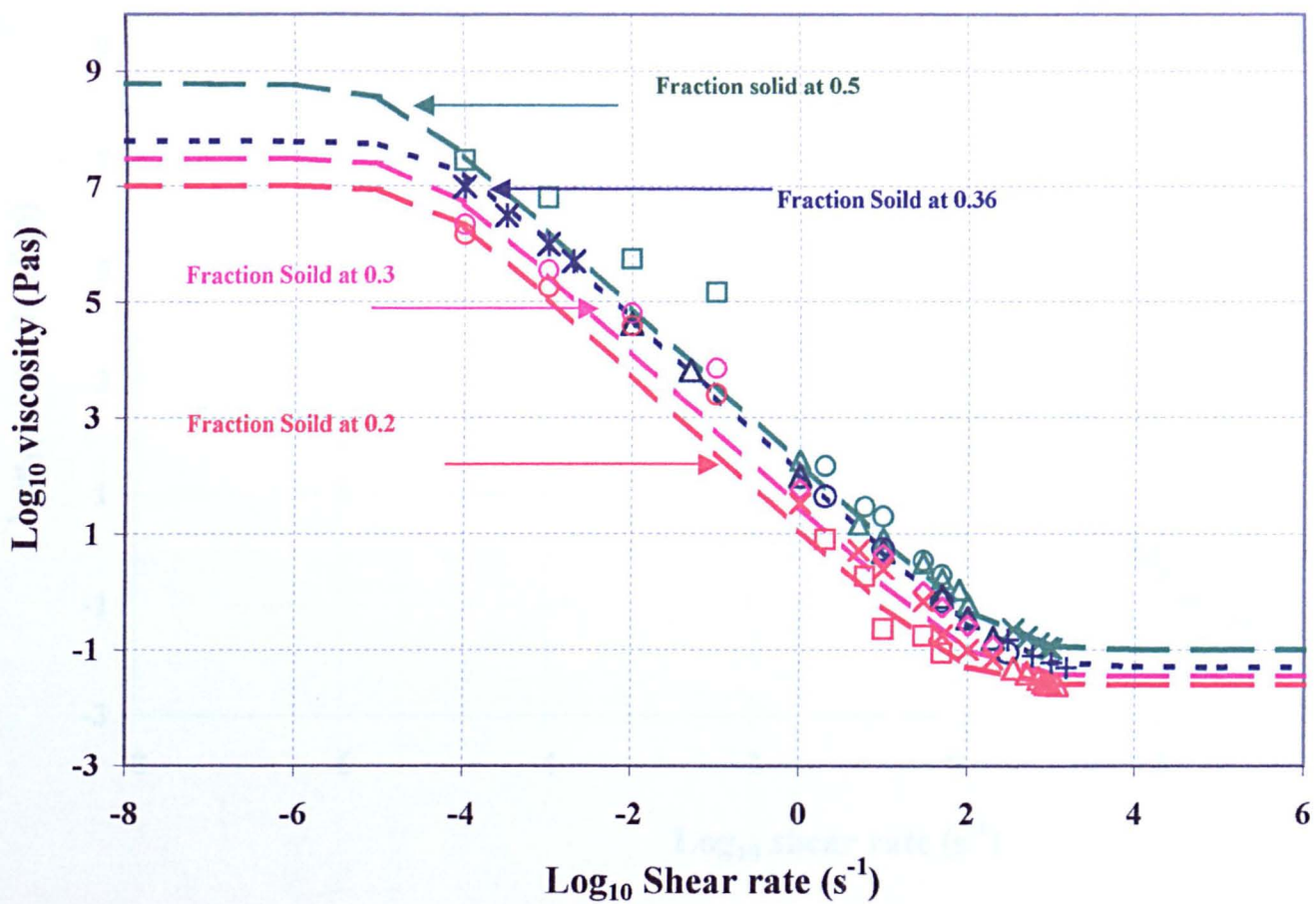

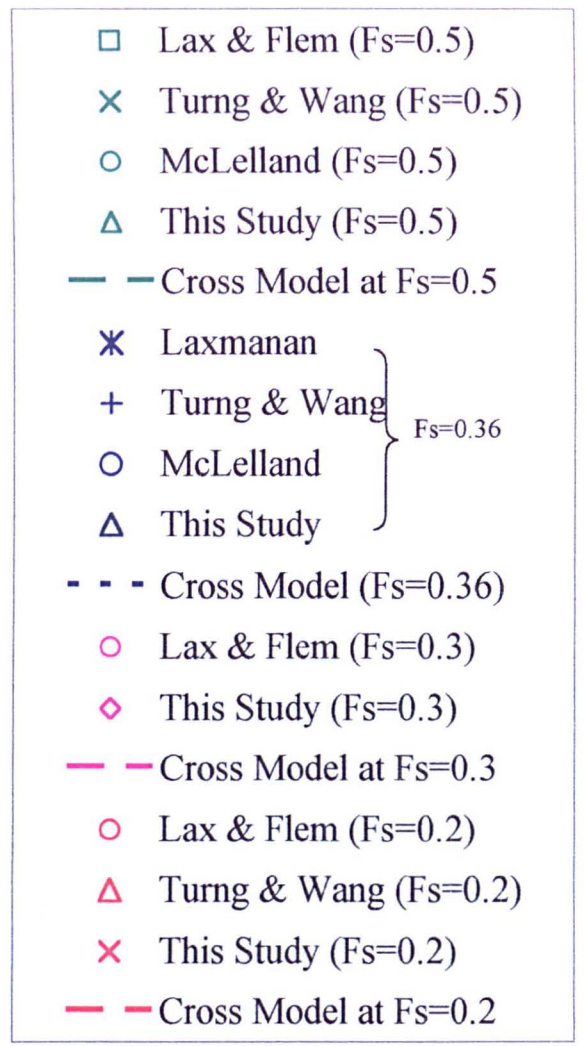

Figure 7.1.2c: Apparent viscosities at different shear rates and fraction solids fitted to the Cross Model for aluminium alloys

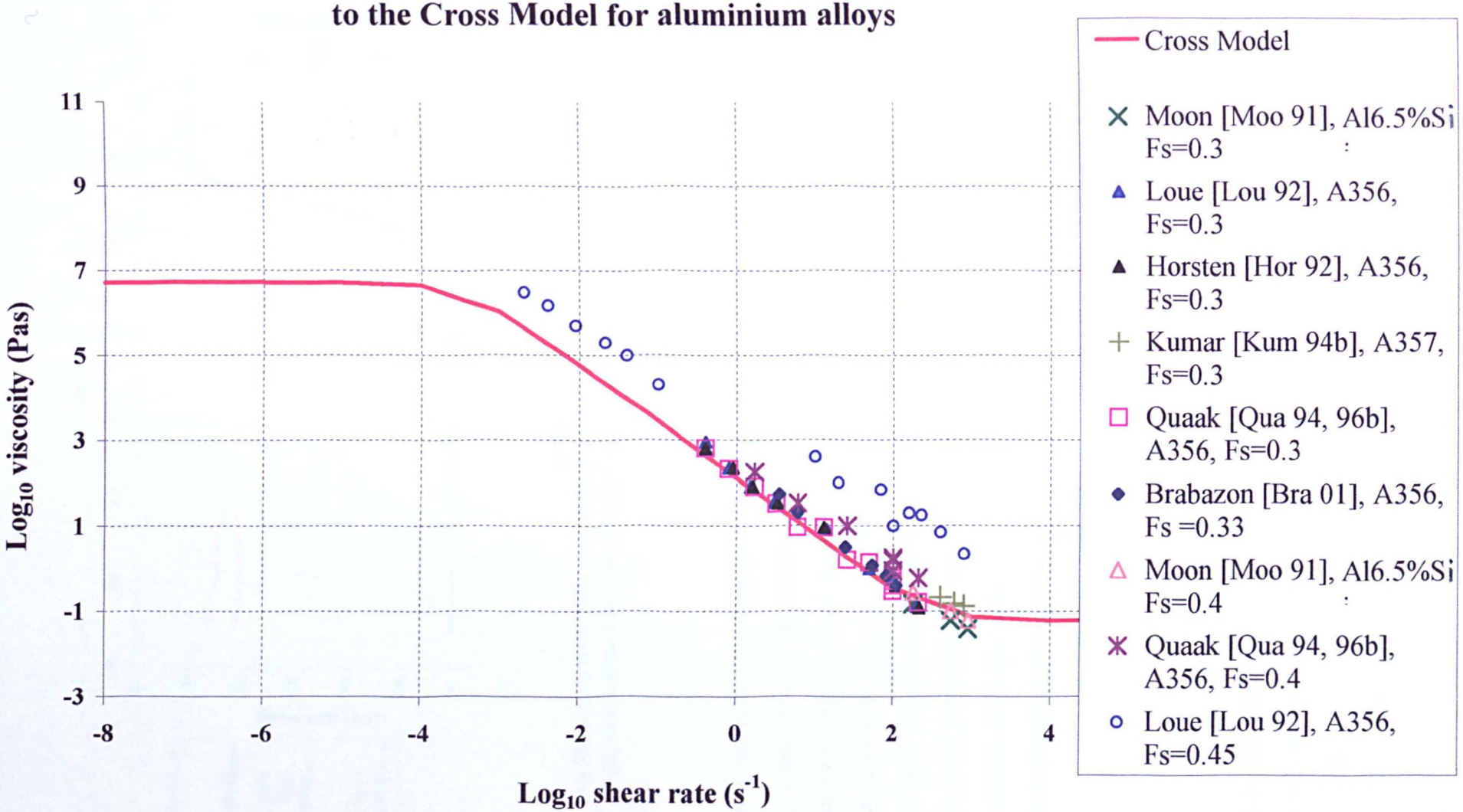

Microstructural examination at the various fraction solids on Sn15%Pb alloys, after the steady state condition has been achieved, showed particle agglomeration and coarsening with increasing fraction solid. Figures 6.1.2b and 6.1.2e showed this marked effect between fraction solids of 0.2 and 0.5. Figure 6.1.2b showed less solid spheroidal particles to Figure 6.1.2e. At high fraction solid, particles were able to agglomerate more easily which effectively increases the particle size.

7.1.3 Effect of rest times.

The sample is left to rest for various rest times before a sudden change in shear rate is introduced. The results in Figures 6.1.3a to 6.1.3c show the shear stress value recorded during the first second of the change in shear rate from rest (i.e. shear rate is 0 s^{-1} at rest). All three figures show the same behaviour whereby the peak stress encountered increases with increasing rest times. Figure 7.1.3a shows a comparison for two different fractions solid of Sn15%Pb alloys. Both samples have been left to rest for the same time period before carrying out identical shear rate jumps (0 to 100 s^{-1}). The shear stress recorded was observed to increase with increasing fraction solid.

Figure 7.1.3a: Comparison of shear stresses under a shear rate change of 0 to 100 s^{-1} for Sn15%Pb alloys at two different fraction solids after resting (i.e. no stirring) for 5 hours.

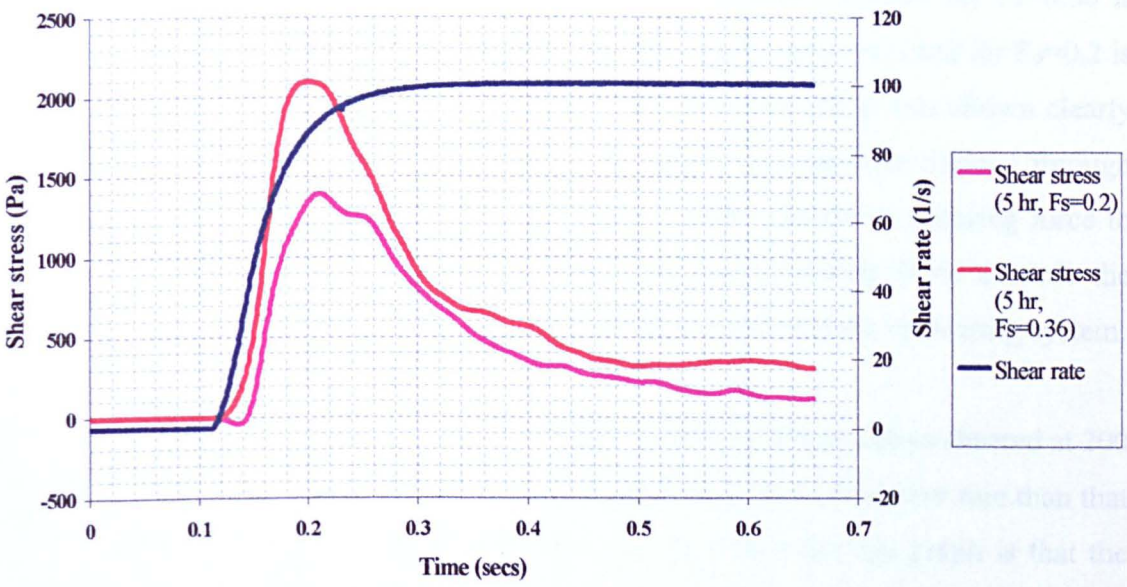

During the rest time, particle agglomeration and coarsening are more pronounced than when the sample is continuously sheared for the same amount of time. In Chapter 3.4, it was mentioned that at steady state condition during stirring, a dynamic equilibrium exists in a steady state condition where the agglomeration and de-agglomeration processes both co-exist. Figures 6.1.3e and 6.1.3f show the microstructures of Sn15%Pb alloys under different rest times. By comparing Figure 6.1.3e(ii) with Figure 6.1.2f(ii) for the same fraction solid of 0.36, it can be seen that after achieving its steady state condition and allowing the sample to rest (i.e. by stopping the stirring), the primary solid particles become more spheroidal in shape. In Figures 6.1.3e and 6.1.3f microstructural examination shows that increasing the rest times increases the solid particle sizes. This increase would impede the movement of the particles upon an imposition of a shear stress/rate. The ease with which the particles are able to move past each other depends on the liquid medium present and the size of the particles. This relates to the shear stress recorded during a sudden imposition of shear rate.

Therefore, from Figure 6.1.3e and 6.1.3f, it can be seen that at longer rest times, the solid particles are larger and more clustered giving a higher value of peak stress with increasing rest times. The peak stress encountered is also highly dependent on the fraction solid. For the same length of rest time (e.g. 5 hrs), the peak stress recorded for the same shear rate change (0 to 100 s^{-1}) is very much higher for Fs=0.36 compared to a Fs of 0.2 (c.f. 6.13a and 6.1.3b). The value recorded for Fs=0.36 is about 2100 Pa after a rest time of 5 hours while the peak stress recorded for Fs=0.2 is only about 1400 Pa. The cut-off effect from the viscometer head was shown clearly for Fs=0.5 after about 2 hrs of rest time. The very large particles formed through agglomeration and coarsening with time require a large amount of shearing force to slide these large particles past one another. This large shearing force exceeds the capability of the machine hence causing an automatic cut-off to the measuring system.

Figure 6.1.3k shows the viscosity behaviour of Sn15%Pb alloys sheared at 200 s^{-1} after different rest times. The data collected here is at a much slower rate than that from Figures 6.13a to 6.13c. An important point to note from this graph is that the viscosity tends to the same value with time regardless of its initial rest times. Although, different initial rest times may give different lengths of time before

achieving the same viscosity values, it was found that given enough time, the viscosity values will tend to have the same final apparent viscosity value corresponding to the shear rate specified. Figure 6.1.3k also shows that the peak viscosity follows the same behaviour as before (i.e. increases with increasing rest times). However, because of the slow data collection rate, the transient behaviour during the first second of the jump cannot be recorded. This would mean that the peak viscosity value might not be the true value. To investigate the transient behaviour of the alloy slurries during a sudden change in shear rate, the results were analysed using the fast data collection card (~ 1kHz).

Figures 6.1.3g to 6.1.3j shows the best fit to the shear stress versus time graph by using equation 6.1.3 for the various rest times. The accuracy of these fits is subjective. In Table 6.1.3a, the breakdown times obtained for the various rest times are shown. All the breakdown times are in the order of seconds. It is quite difficult to discern whether any of the breakdown times is applicable to all the results. Figure 7.1.3b shows an example of fitting the breakdown curve using different breakdown times. Values of 0.16-0.20 can be fitted quite adequately to the stress decay curve while clearly a value of 0.15 does not give such a good fit. In Figure 7.1.3c, the breakdown curve is again modelled using the whole range of breakdown times found for the various rest times. In this figure, a breakdown time of 0.15 and 0.16 seconds gives the best fit. A breakdown time of 0.15 would give an equally good fit to an experimental condition with a rest time of 2 hrs (Figure 7.1.3d) but not at a rest time of 0.05 hrs (Figure 7.1.3b). Therefore, the general behaviour of decreasing breakdown time with increasing rest time is still valid.

The initial viscosities for the various rest times were compared and found to increase with increasing rest times. The amount of rest times would allow the solid particles to agglomerate and coarsen forming stronger welds between the particles. This would translate into higher stresses needed to overcome these welds in order for the particles to slide past each other. As a result, the shear stress increases with increasing rest time. The 'first' steady state viscosity shown in Table 6.1.3a did not vary greatly between the different rest times.

Figure 7.1.3b: Curve fitting of shear rate jump on Sn15%Pb alloys from 0 to 100 s^{-1} (Fs=0.36, Rest times= 0.05 hrs) using various breakdown times (from Table 6.1.3b)

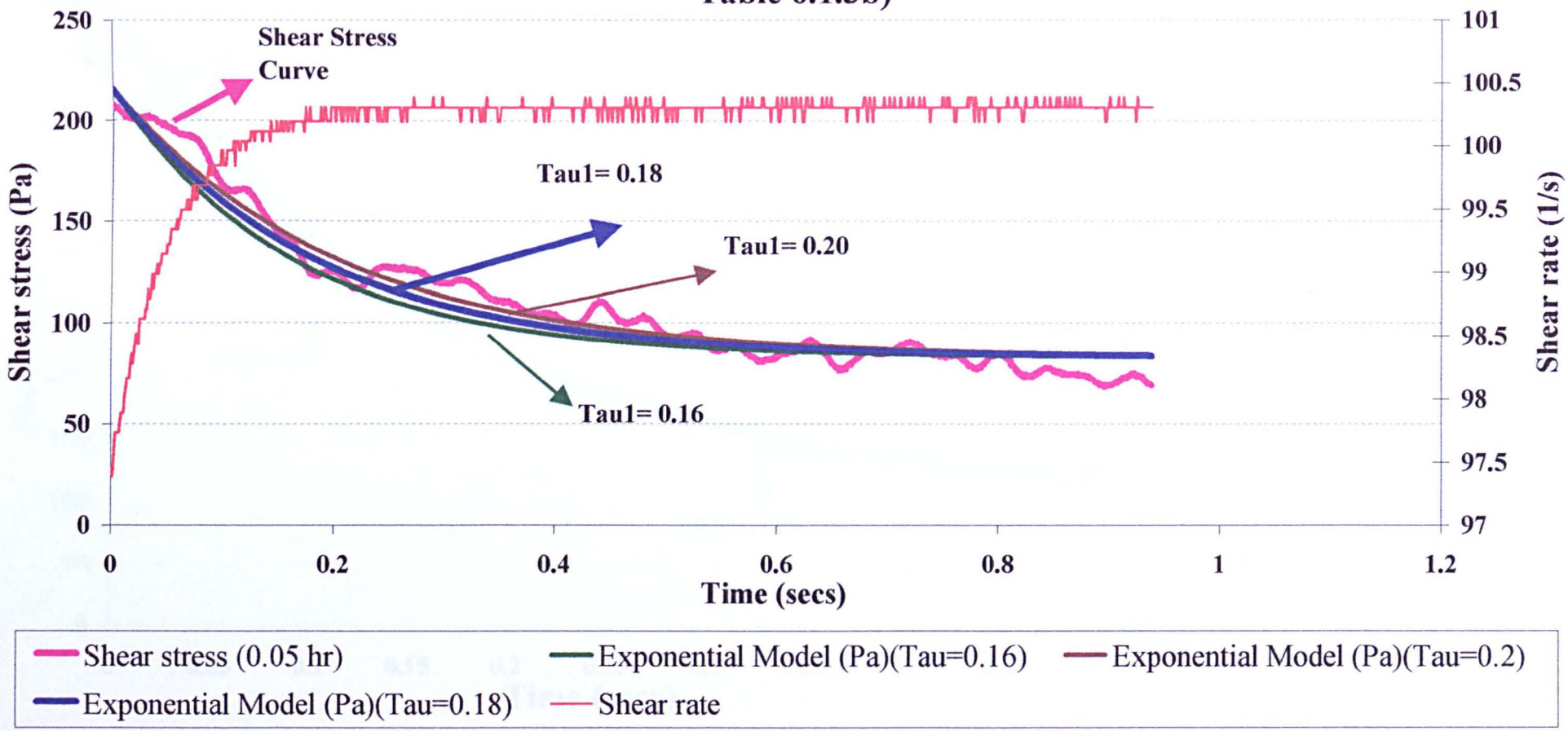

Figure 7.1.3c: Curve fitting of shear rate jump on Sn15%Pb alloys from 0 to 100 s^{-1} (Fs=0.36, Rest times=1 hr) using various breakdown times (from Table 6.1.3b)

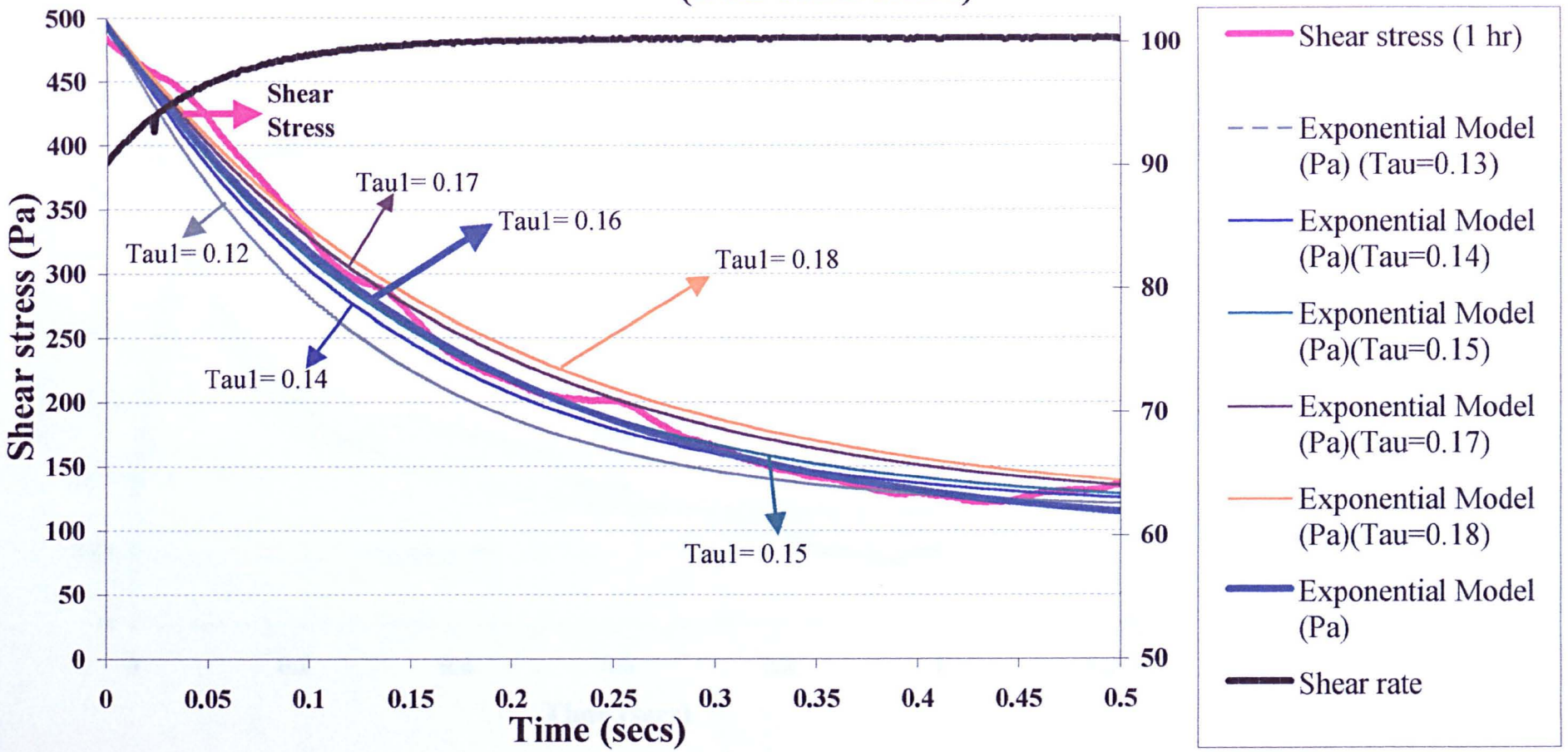

Figure 7.1.3d: Curve fitting of shear rate jump on Sn15%Pb alloys from 0 to 100 s^{-1} (Fs=0.36, Rest times= 2 hrs) using various breakdown times (from Table 6.1.3b)

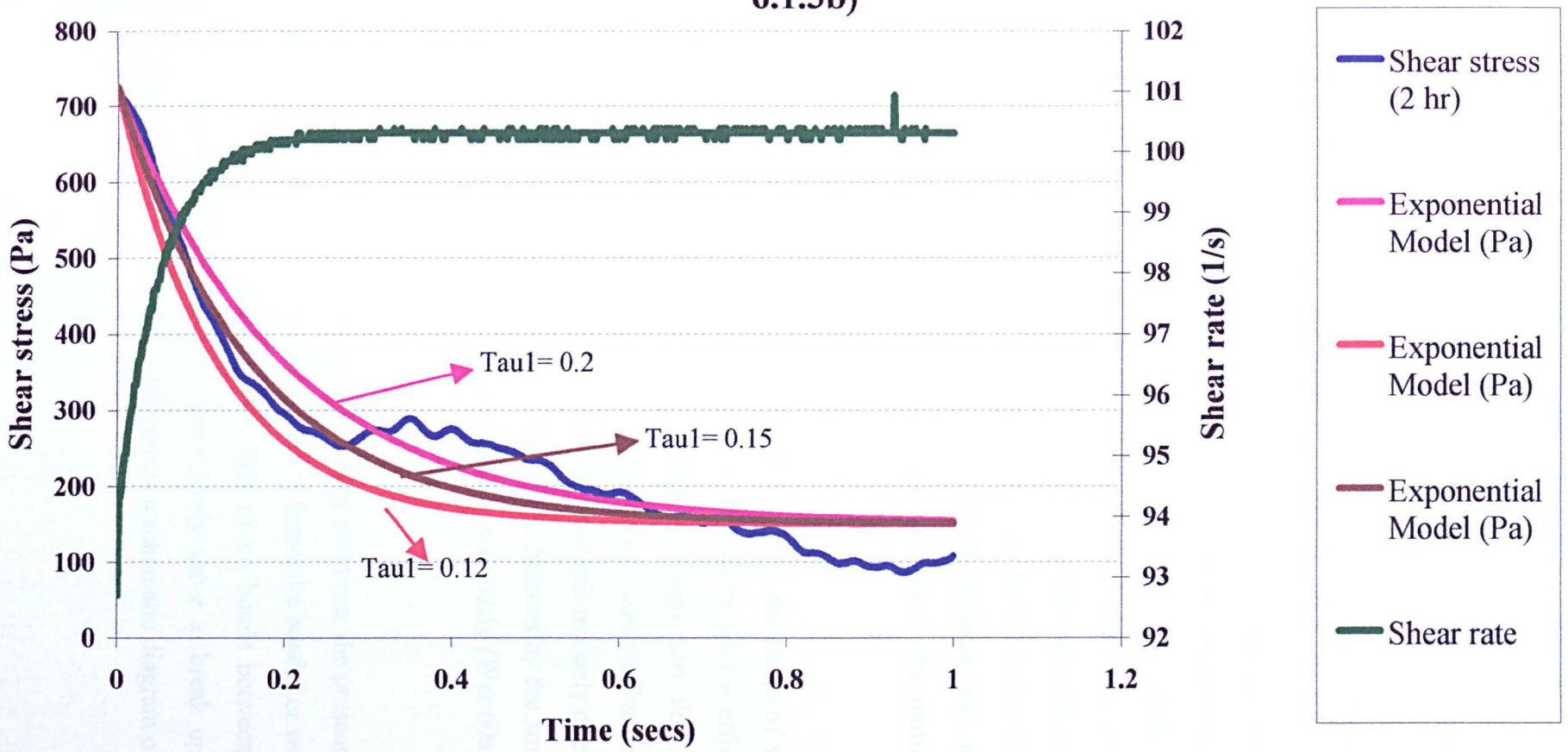

The effect of shear rate was investigated. Three different final shear rates were applied: (i) 50 s^{-1}, (ii) 100 s^{-1} and (iii) 200 s^{-1} from an initial shear rate of 0 s-1 under different rest times. Table 6.1.3b tabulates the results on the initial, steady state viscosity and the breakdown times for a Sn15%Pb alloy (Fs=0.36). Figure 7.1.3e plots the parameters obtained for two different rest times (at 0 hours and 2 hours). The initial viscosity decreases sharply at rest time of 2 hours with increasing shear rate compared to a rest time of 0 hours where the decrease is more gradual. This effect can be attributed to the solid particles not having enough time (i.e. at 0 hours rest time) to form welds and where particle agglomeration is not as marked as the experiment that has a rest time of 2 hours (compare Figure 6.1.3f(i) and 6.1.3f(ii)). The steady state viscosity value varies slightly between the two different rest times. This can be attributed to the behaviour of the slurry where the breakdown of the particles occurs very rapidly such that during the shear rate change, the solid particles are already broken down quite considerably. With enough time, further breakdown will occur, decreasing the viscosity until the apparent viscosity corresponding to that particular shear rate is reached (see Figure 6.1.3k).

Unfortunately, the capability of the viscometer restricted the range of shear rates investigated to equal and below 200 s^{-1}. Figure 7.1.3e also shows the effect of breakdown time with rest times and shear rates. With a longer rest time, the breakdown time decreases (i.e. particles are more rapidly broken down). Comparing the breakdown times for the different shear rates, it can be seen that not only does the breakdown time depend on the final shear rate, it is largely influenced by the amount of rest times. These results have been reported in work done previously [War 00a, Kir 00 and Liu 00a].

Since particle agglomeration takes place after a long rest time, the presence of welds between the particles means that it is much easier to break the bonds (or welds) than in a sample that is not left to rest (i.e. with little or no bonds between the particles) where the imposition of stress would most likely serve to break up the agglomerates into smaller particles. Figure 7.1.3f below is a schematic diagram of the theory put forward.

Figure 7.1.3e: Parameters obtained from curve fitting using Equation 6.1.3 on Sn15%Pb alloys (Fs=0.36) under different shear rates

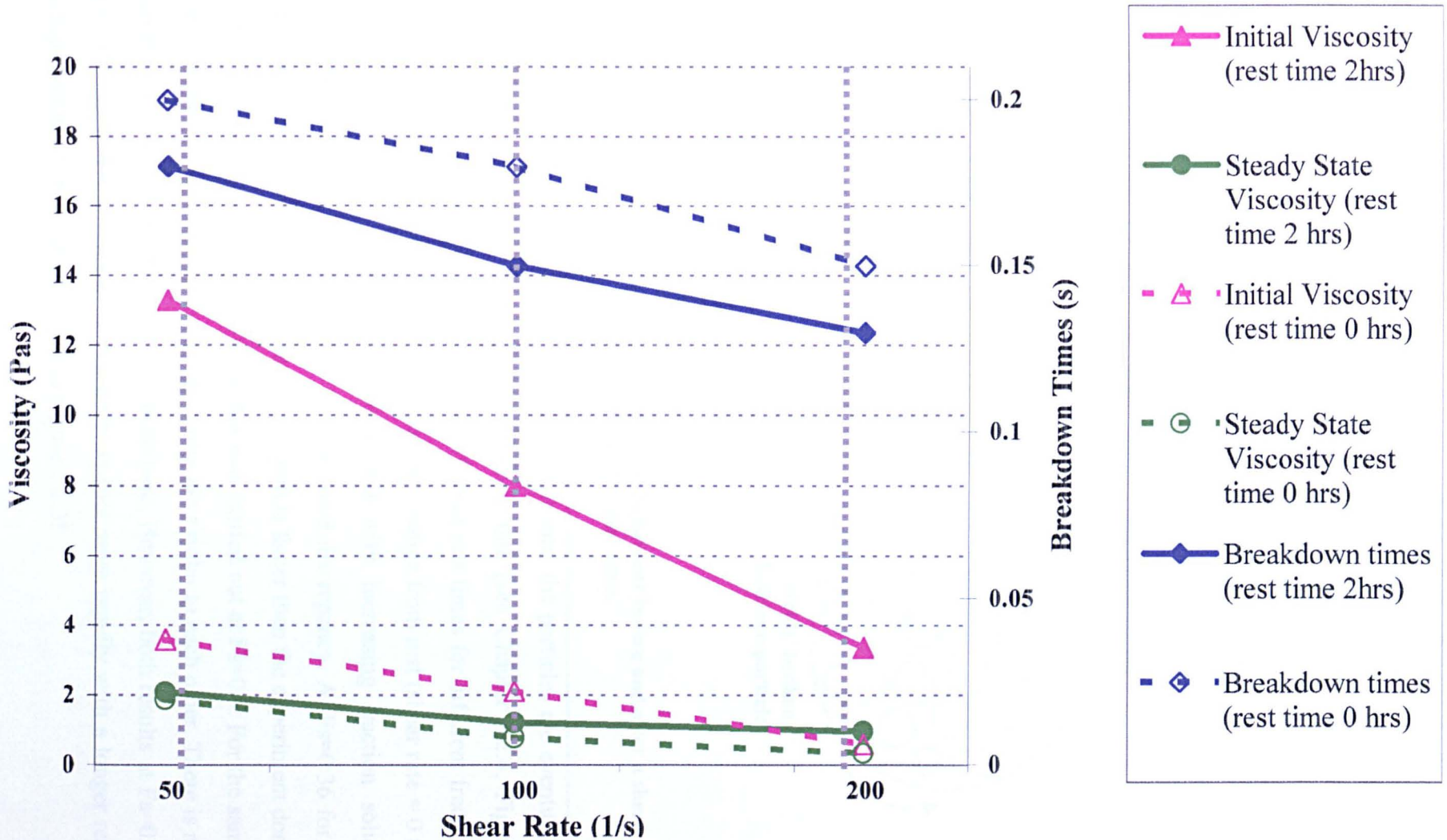

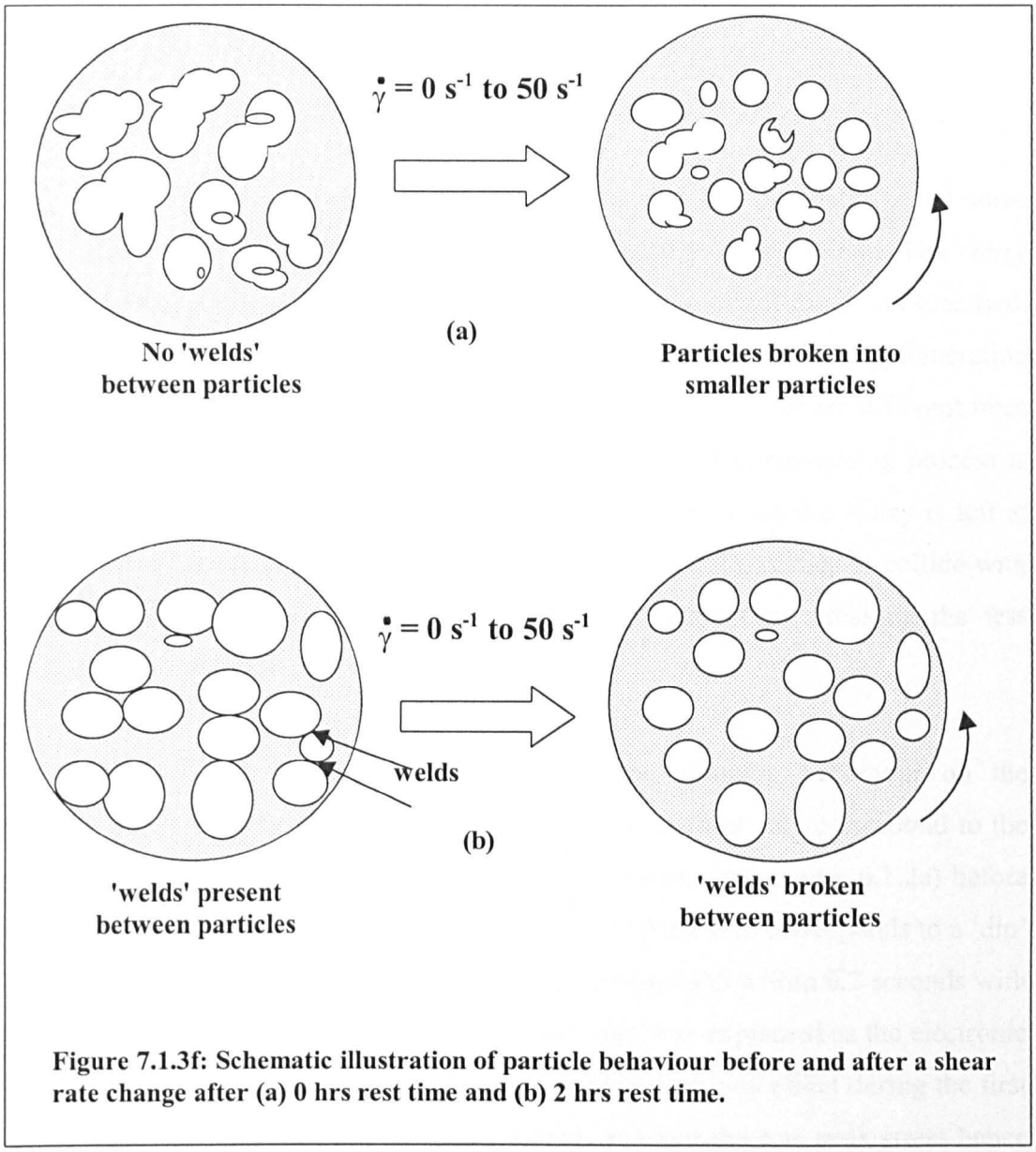

Figure 7.1.3f: Schematic illustration of particle behaviour before and after a shear rate change after (a) 0 hrs rest time and (b) 2 hrs rest time.

With increasing time at that particular shear rate, the particles are eventually broken up into a size corresponding to that shear rate (see Chapter 2.2.4, Figure 2.2.4D). Table 6.1.3c compares the result of different rest times for different fraction solids of Sn15%Pb alloy under the same shear rate change from rest (shear rate = 0 to 50 s^{-1}). Clearly, the viscosity values increased with increasing fraction solid. However, the breakdown times seemed to have some discrepancy. At Fs=0.36 for a rest time of 0 hours, the breakdown time calculated is faster than the experiment done at Fs=0.2 but slower than the experiment that was carried out at Fs=0.5. For the same test at a rest time of 1 hour, the breakdown times are similar to each other. There is no apparent trend that can be seen from the result here. However, both results at Fs=0.2 and Fs=0.5 showed that the breakdown times occurs more rapidly with a longer rest time supporting the theory put forward in Figure 7.1.3f.

7.1.4 Step change from an initial shear rate (Shear rate jumps up)

All the step change experiments are conditioned at a particular initial shear rate for a period of time (> 30 minutes) before changing the shear rate. The slurry would achieve a steady state structure corresponding to the initial shear rate specified. There exists a dynamic equilibrium between the agglomeration and de-agglomeration processes during the conditioning. Therefore, the particle structures are different from the step change experiments that are left to rest initially. The coarsening process is dominant through the agglomeration between the particles when the slurry is left at rest. The steady constant shearing of the particles causes the particles to collide with each other, forming bonds (or welds) whilst at the same time breaking the less strongly bonded particles.

Figures 6.1.4a and 6.1.4b show clear shear thinning behaviour on the Sn15%Pb alloys slurries. Both viscosities at their initial shear rate correspond to the apparent viscosity found from the isothermal experiments (see Figure 6.1.2a) before the change in shear rate. In both figures, a 'dip' in the shear rate corresponds to a 'dip' in the shear stress, The step change in shear rate is completed within 0.2 seconds with the 'dip' occurring in the first 0.05 seconds. This 'dip' was explained as the electronic switching system in the viscometer in Chapter 5. Therefore, any effect during the first 0.05 seconds was ignored. The 'dip' has probably masked the true peak stress hence the peak stress shown in this work may not be the actual true stress. However, the collection rate (~ 1 kHz) is much faster than any other works in the literature therefore the results presented in this work gives a more detailed insight than previously achieved into the transient behaviour of semisolid alloy slurries in a step change condition. Experiments on step change were carried out on two different fraction solids (Fs=0.35 and Fs=0.5). A higher viscosity is expected for higher fraction solid and is shown in Figure 6.1.4e. Figures 6.1.4f and 6.1.4g show the attempt at modelling these step change experiments. From figure 6.1.4f, the peak stress increases with increasing final shear rate. However, comparing the step change from 1 to 30 s^{-1} and 1 to 50 s^{-1}, the peak stress recorded is slightly higher for the former. In view of the 'dip' effect, this was not considered as a major inaccuracy. Furthermore, experimental scatter would suggest that at shear rates of 30 s^{-1} and 50 s^{-1}, the

difference between these two shear rates is not great therefore the stress recorded may be quite close to each other. Still, the general trend of increasing peak stress with final shear rate is seen clearly. From the peak stress curve in Figure 6.1.4f, with increasing shear rate, the stress curve became less 'bumpy' (i.e. smoother). This effect can be attributed to the particle structures. With increasing shear rate, the particles are more broken down hence a more uniform structure giving a smoother curve. At a low shear rate, the agglomerate particles are not as broken down, therefore, bigger agglomerates/clusters may still be present resulting in a less uniform flow (i.e. 'bumpy' curves). Figure 7.1.4a below shows an example of the microstructure for two different shear rates. A rounder and smaller particle size is obtained at the higher shear rate for the same fraction solid (Fs=0.5)

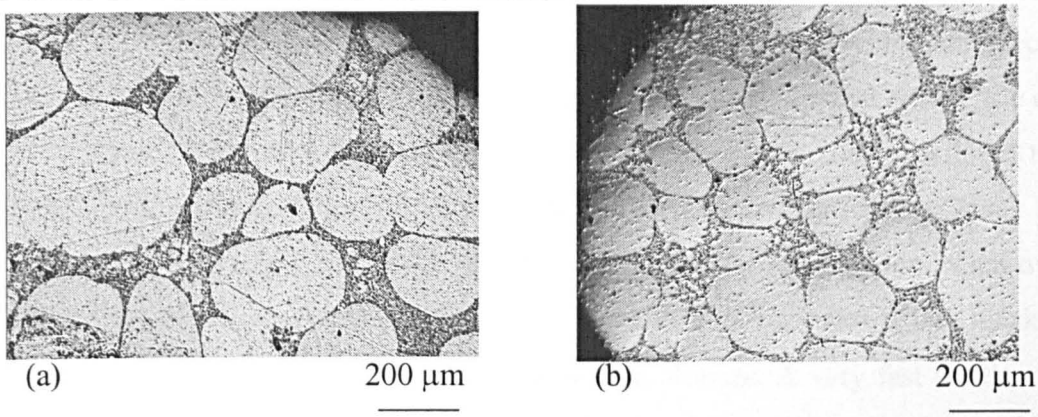

Figure 7.1.4a: Microstructures of Sn15%Pb alloy at two different shear rates: (a) 10 s^{-1} and (b) 50 s^{-1}

In Figure 6.1.4g, the peak stress recorded increases with decreasing initial shear rate. The results agree well with works from other authors [Qua 96b, Kok 99]. At the low initial shear rate, the structure is more built-up therefore a higher peak stress is recorded. [Kir 94] suggested that at the high initial shear rate, the degree of de-agglomeration is higher than that at the low initial shear rate. The result from Figure 6.1.4g agrees well with Quaak [Qua 96b] who observed that a higher initial shear rate shows a lower viscosity compare to one done on a lower initial shear rate after a step change to the same final shear rate. Table 6.1.4a tabulates the parameters obtained for various step change experiments. Figures 6.1.4h and 6.1.4i showed a decreasing trend in the viscosity values for a step change to the same final shear rate and from the same initial shear rate respectively.

In view of the experimental scatter in Figure 6.1.2a, it is reasonable to state that the viscosities do not vary greatly between each other. The results obtained agree with works by other workers [Mad 96a, 96b, Qua 96a, 96b, Azz 00 and Bra 01] who put forward the term 'iso-structure' viscosity for the viscosity during the onset of a shear rate jump (i.e. the structure remains the same as the previous steady state structure before decreasing or increasing with increasing or decreasing shear rates respectively). The steady state viscosity in Table 6.1.4a is also known as the 'pseudo-viscosity' or the 'first steady state viscosity' after a step change in shear rate. With increasing time at the constant shear rate, this viscosity will decrease or increase until it attains the final steady state viscosity corresponding to that shear rate. The breakdown times from the step change experiments from an initial shear rate are affected by the final shear rate specified. Comparing Figure 6.1.4d and 6.1.4i, it can be seen clearly that regardless of its initial shear rate, for the same final specified shear rate (Figure 6.1.4h), the breakdown times remain almost constant. On the other hand (Figure 6.1.4i), starting from the same initial shear rate, the breakdown times decrease with increasing final shear rate. This effect was also shown by Quaak [Qua 96b] and Koke [Kok 99]. However, the results obtained by Koke are collected over a long period of time (~ 10 data points in 480 seconds). It was shown by Quaak that there exist two breakdown behaviours in semisolid slurries. A very fast (of the order of a few seconds) initial breakdown followed by a slower process (of the order of hundreds of seconds). Results from this work have shown that the first breakdown process occurs within a second and in this time the metal slurry will have achieved its first steady state condition. This is then followed by a second and longer breakdown (~ 5 minutes of constant shearing) before the material achieves its steady state condition corresponding to the specified shear rate. Koke's results are shown over a period of 480 seconds and this can be regarded as the long term behaviour of the metal slurry after a change in shear rate. Figure 6.1.4i also shows that the breakdown times decrease more rapidly in the lower final shear rate region than in the higher shear rate region.

7.1.5 Step change from an initial shear rate (Shear rate jump down)

To compare the recovery times with the breakdown times from the preceding section, step change experiments to a lower shear rate from an initial high shear rate

were conducted. Figure 6.1.4j shows the results for a step change to a final shear rate of 1 s^{-1} from three different initial shear rates. Initial viscosity for the three different initial shear rates showed similar results (again in view of the experimental scatter) with that obtained from the steady state experiments. The recovery times obtained from the fits to the stress decay curves are shown to have similar behaviour to the step change experiments to a higher shear rate. The recovery time is shown to increase with increasing final shear rate whilst remaining largely unaffected by the initial shear rate specified. This behaviour is counter-intuitive since one would expect a shorter (or decrease in) recovery time with increasing final shear rate (i.e. the structure will need a longer period of time to build-up its structure at lower shear rate than at a higher shear rate). One possible explanation is that during a shear rate jump down, with increasing final shear rate, the rate of deceleration is slower, so that the agglomerates are brought into contact with each other relatively slowly and therefore it is easier for them to 'capture' each other, i.e. the recovery time is short. Nonetheless, it is the change in shear rate from a lower value to a higher value that has more significance in industrial thixoforming (i.e. increase in shear rate upon hitting the die). One important finding in this experiment is that the recovery times obtained are slower than the breakdown times obtained in the previous section. For a step change to a lower shear rate, the structure consists of a more de-agglomerated structure during shearing at the high initial shear rate. By reducing the shear rate, the time needed for the structure to agglomerate would be longer than that needed to break a well structured state to a less structured state. Quaak [Qua 96a, 96b] observed that the 'breakdown' and 'recovery' times are independent of the shear rate jump magnitude.

The results from section 7.1.4 and 7.1.5 show that these times are affected by the final shear rate specified regardless of the initial shear rate. The results here agree with the behaviour observed from Quaak [Qua 96b]. Works from Mada [Mad 96a, 96b], Modigell [Mod 99] and Azzi [Azz 00] also support the behaviour of the slurry during a step change as observed in this work. A quantitative comparison of the breakdown times could not be carried out as all the works from the various authors are collected at a different collection rate and the shear rate jumps are done differently.

7.2 Rapid Compression Experiments

7.2.1 Rapid compression of Al alloys under different temperatures

Results on the force load signal versus the displacement of the slug on all the aluminium alloys under different temperatures showed similar behaviour where the force signal decreases with increasing temperature (Figure 6.2.1b). At the lowest temperature for all three alloys, a sharp peak was observed when the slug first hit the die. This was followed by a rapid decrease in the load signal which was attributed to the structure breaking down as the slug starts to fill the die. At the highest temperature however, the force load signal remains almost constant during the first contact with the die. The high temperature would correspond to an increase in the fraction liquid in the slug. Furthermore, the particles became more spheroidal with increasing temperature. This increase in fraction liquid and spheroidicity contributes to the decrease in load signal observed. The Form Factors calculated in Chapter 6.2.4 support the results obtained. Viscosity calculation in Chapter 6.2.5 showed a near constant behaviour for Alusuisse A356 alloys at a temperature of 581 °C (see Figure 6.2.5d). Figure 6.2.5e shows the viscosity behaviour against temperature of Alusuisse A356 alloys at different shear rates. The figure shows that with increasing shear rate, the viscosity values differ slightly from each other. It also shows that at a temperature above 577 °C, the viscosity curves are almost identical in shape (for shear rates above 20 s^{-1}, independent of the temperature). Referring back to Figure 6.2.1b, it can be seen that the force load signal curves for 578 °C and 581 °C are almost identical to each other. This shows that the viscosity values would be identical to each other as shown in Figure 6.2.5d. From the above discussion, it can be concluded that at temperatures above 578 °C, the slug is within the thixoforming range for good filling of the slug into the die. Using MTDATA Thermodynamic modelling [Hog 01a], Figure 7.2.1a indicates the equilibrium temperature (lever rule calculation) to be about 580 °C for a fraction liquid of 50%. This temperature corresponds to the temperature above which the viscosity shows an almost Newtonian behaviour and the force load signal recorded by the load cell is almost negligible (Figure 6.2.1b).

Figure 7.2.1a: Fraction Liquid versus Temperature for A356 Al alloys (Using MTDATA Thermodynamics Predictions)

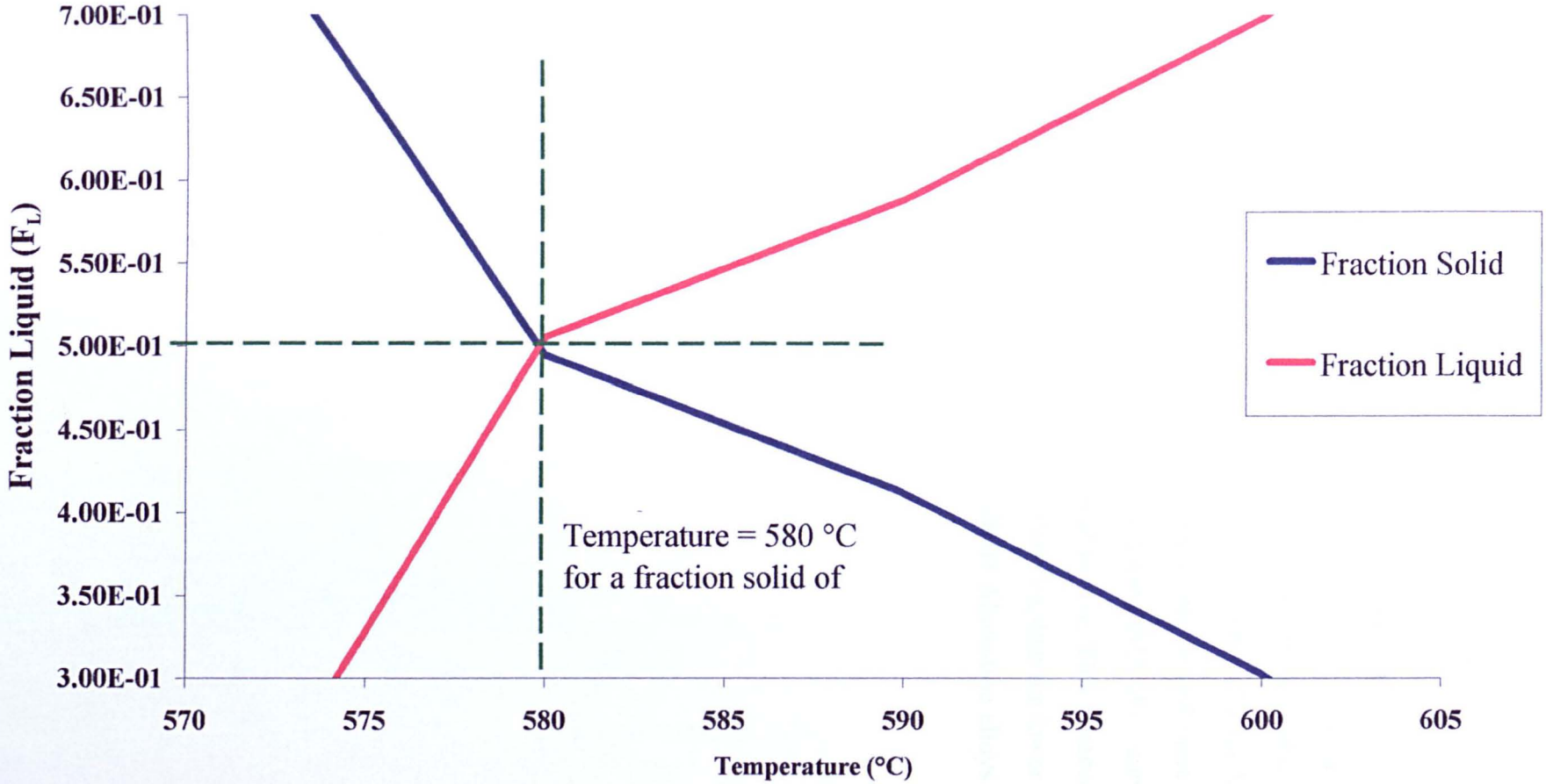

Comparing the results for Alussuisse A356 alloys, NorthWest A357 and A319 alloys and Sheffield A357 alloys, Figure 7.2.1b shows that under the same conditions (i.e. temperatures, soak times and ram speed), the Sheffield A357 alloys gives the lowest force load signal and has a better microstructure (i.e. more spheroidal). The work of Tzimas and Zavaliangos [Tzi 00c] observed the effects of temperature and soaking time on the grain size of an A357 alloy (produced through MHD process, similar to the production of the feedstock Alusuisse alloy used in this work) and an Al7.2%Si alloy (produced through SIMA route, similar to the RAP Sheffield A357 alloy used in this work). The authors also observed [Tzi 00b, Tzi 00c] that for MHD cast alloys in the semisolid state, the grains were irregular in shape and there was segregation of the liquid and solid phases. On the other hand, the SIMA alloy consists of regular shaped grains, dispersed uniformly in the liquid matrix. This observation corresponds to the results obtained in this work and would also explain the lower load detected for the Sheffield RAP alloys compared to the MHD Alussuisse alloys (c.f. Figure 7.2.1b)

Figure 7.2.1b: Load signals and microstructures for different feedstock routes

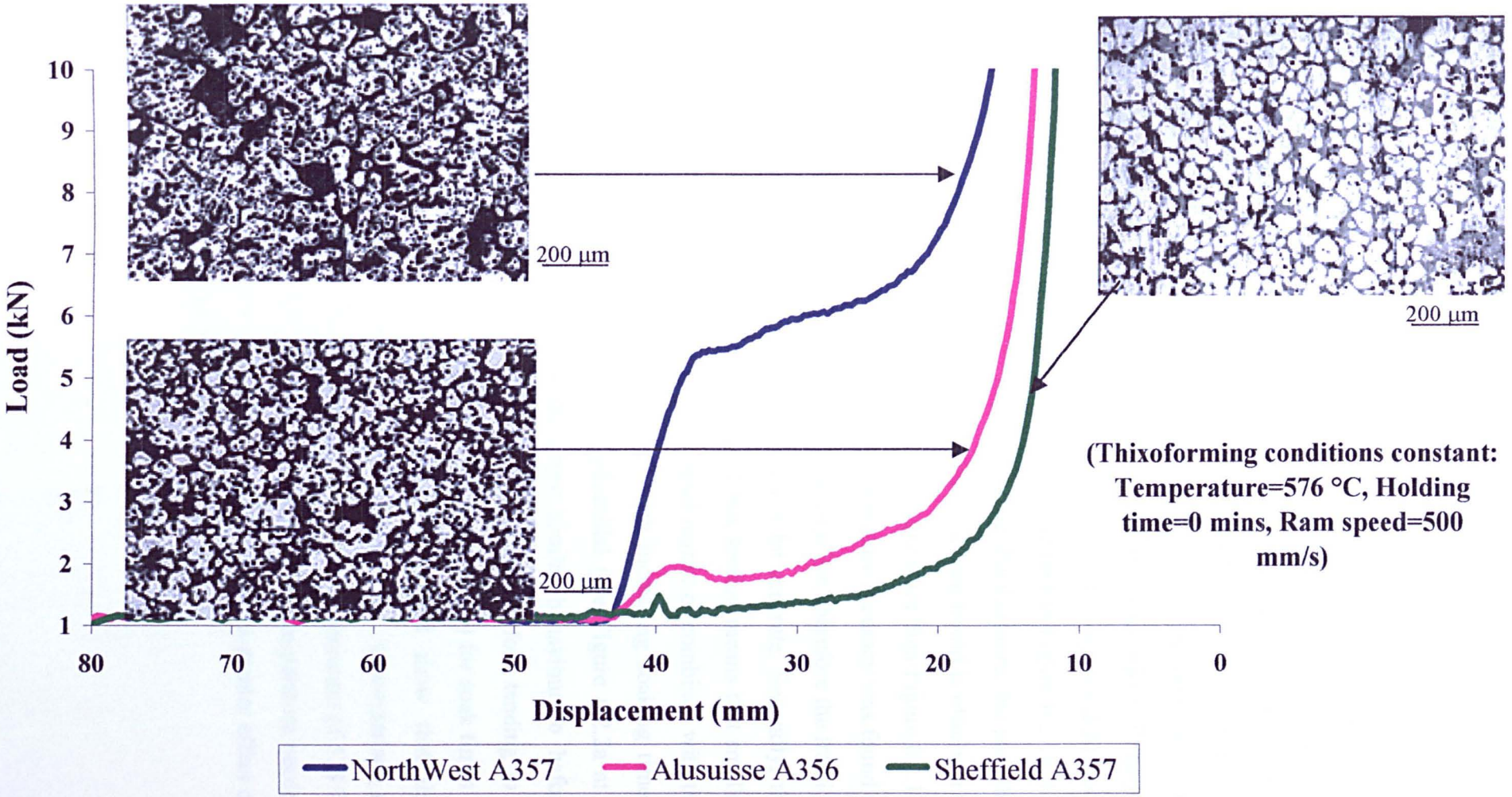

7.2.2 Rapid compression of Al alloys under different soaking times

Similar behaviour is also shown when the slug is subjected to different soaking times (Figure 6.2.2a). An increase in the soak time showed a decrease in the force load encountered. Particles are more spheroidal and larger as the soak time increases. Soaking times allow the particles to agglomerate and grains with lower surface energy (i.e. larger particles) will grow larger whilst the smaller particles dissolve into the liquid matrix. The more spheroidal shape will allow the particles to slide past each other more easily than for less spheroidal particles. Comparing Figures 6.2.1b and 6.2.2a, it can be seen that at a temperature of 575 °C, Figure 6.2.2c has a lower load signal after soaking the slug for 1 minute compared to Figure 6.2.1b that was done at a temperature of 576 °C with no soaking time. Furthermore, the particles are more spheroidal when a soaking time is introduced. Fraction liquid is observed to be higher in Figure 6.2.2a, which was held at a lower temperature than Figure 6.2.1b. Two probable causes were considered. Firstly, the temperature accuracy was found to be ± 1 °C. Since both temperatures are quite close to each other, therefore the fraction liquid difference between the two experiments may not be accurate. Secondly, the effect of soak time as mentioned in the beginning of this section means that smaller particles that were present have dissolved into the liquid matrix or combined with the larger particles leaving only these larger particles. With increasing soaking times, these particles will grow even larger and more spheroidal (see Figure 6.2.2a at 5 minutes soaking time). Viscosity calculations show similar behaviour to before (Section 7.2.1) where the viscosity decreases rapidly initially before tending to a similar constant viscosity with increasing shear rates (Figure 6.2.5b) for soak times at 1 and 3 minutes. Consequently, the Form Factors calculated show that this spheroidicity of particles increases with increasing soaking times. A comparison of Figures 6.2.1b and 6.2.2a shows that to obtain a load of 3 kN, a temperature of 578 °C is required while if a soaking time of 1 minute is employed, the temperature needed can be reduced to 575 °C. This shows that the soaking times have a greater effect on the load signal and spheroidicity of the particles than temperature.

7.2.3 Rapid compression of Al alloys under different ram speed

Results on the effect of ram speed show that for the same thixoforming conditions, the alloy slurries exhibit almost identical behaviour. Figure 6.2.5a shows the microstructures of the alloys to be identical. The viscosity under different ram speeds shows a gentler decrease in viscosity compared to the experiments done under different soaking times and temperatures. The results in Figure 6.2.5c show a gradual decrease in viscosity with increasing shear rate.

Figure 7.2.3a shows four micrographs (micrographs are extracted from Appendix 5) for the different ram speeds used in this experiment. At a ramp speed of 250 mm/s and 350 mm/s, the particles sizes are almost similar to each other. However, with increasing ram speed (at 500mm/s and 1000 mm/s), the particles are found to be less spheroidal than those found at the lower speeds when the microstructures at the middle of the samples were examined. The more spheroidal particles at the lower speed seem to correspond to the lower force load signal obtained in Figure 6.2.5a. This effect can be attributed to the particles being forced more rapidly towards the edge of the die with increasing ram speed. However, examination of the microstructures at the edge of the sample revealed a different picture (Figure 7.2.3b).

With increasing ram speed, the particles become more spheroidal in size. A probable reason for this is that the increase in ram speed causes the particles to flow 'more'. This increase in shear rate causes the particles to become more spheroidal (i.e. particles are more susceptible to abrasion or friction against each other, see Section 3.3 and Figure 3.3B). . The above effect can also be used to explain the difference in the microstructures seen in various positions of the thixoformed sample mentioned in Section 6.4.

Figure 7.2.3a: Microstructures of Alusuisse A356 Al alloys under different ramp speeds. Particles are more spheroidal with decreasing ramp speeds at the middle of the sample.

Figure 7.2.3b: Microstructures of Alusuisse A356 Al alloys under different ramp speeds. Particles are more spheroidal with increasing ramp speeds towards the edge of the sample.

Zavaliangos and Martin [Zav 00] has proposed that at high shear rates, shear localisation in the semisolid alloys causes inhomogeneous flow during the forming process. The authors also suggested that thermal softening in the material due to temperature variations (non uniform heating) causes this localisation. This will result in layering of the flow front. Figure 7.2.3c shows a schematic diagram of uniform flow and flow with shear localisation. The layer in the flow field may thus provide an explanation for the segregation effects seen in Figure 6.4.b.

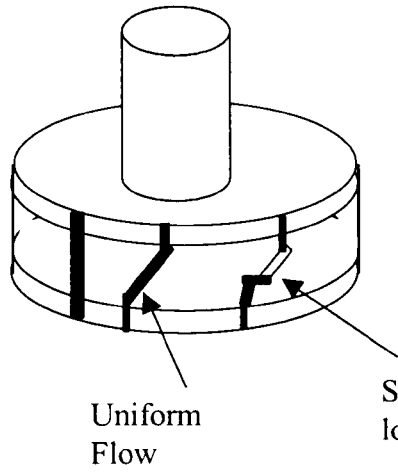

Figure 7.2.3c. Schematic diagram showing both uniform flow and shear localisation.

7.2.4 Power law indices

The 'n' values in Table 6.2.7a for aluminium alloys vary quite erratically with soaking time and temperatures. In the Al30%Si5%Cu alloys, the 'n' values increase with increasing soaking time and temperature (or decreasing fraction solid) while in the Al30%Si5%Cu2%Mg alloys, the 'n' values decrease with increasing soaking times. Results from this work on A356 alloys show an increase in 'n' (tending towards Newtonian behaviour) with increasing soaking times and temperatures. A comparison of Sn15%Pb alloys from this work and that of Laxmanan and Flemings [Lax 80] showed opposite behaviour. The work of Laxmanan and Flemings showed an increase in 'n' value with increasing fraction solid while this work shows an increase in 'n' value with decreasing fraction solid. This behaviour was observed in the recent work done by S. Chayong [Cha 02]. The work of McLelland et al [Mcl 97] observed that the 'n' value did not vary much with fraction solid.

7.3 Isothermal Holding Experiments

The coarsening exponent, n, used in Figure 6.3b assumes cubic coarsening (or diffusion controlled) kinetics. For Ostwald Ripening theory [Lif 61, Wag 61] to be applicable, an infinitesimal volume fraction of the coarsening phase is assumed (i.e. the particles are assumed to be so far from each other that they don't interact with each other hence the diffusion fields do not overlap). Voorhees and Schaefer [Voo 87] have shown experimentally that as little as approximately 3% solid will result in the diffusion fields overlapping. Therefore an exponent of n equals 3 may not be a valid assumption in determining the best fit to the experimental results in Figure 6.3b. Using a regression analysis, the R^2 value is found to be 0.9876 (using n=3). A separate analysis was carried out using a value of n=2 and the R^2 value was found to be 0.9952. This value is closer to 1 which would indicate a perfect fit to the experimental data. However, experimental data can often be fitted with exponents ranging from 2 to 4 [Boe 87, Whi 99]. Nevertheless, semisolid coarsening is generally considered to be diffusion controlled, and therefore an exponent of 3 is normally applied [Ann 95]

Figure 6.3b shows that the y-intercept does not pass through a positive value on the graph on the y-axis. This indicates a negative grain size at zero isothermal holding time, which is impossible. However, this is probably due to the fact that only a small data set (< 200 grains) was used to plot the results. Clearly, a wider data set is required to obtain more statistically sound results. No experiments were carried out at a lower fraction solid as the material starts to slump whilst a higher fraction experiment was not conducted since the work here investigated up to a fraction solid of 0.5 for Sn15%Pb alloys.

The Form Factors (FF) from the isothermal holding experiments were calculated and are shown in Figure 7.3a. With increasing holding time, the FF increases. This effect corresponds to the solid particles coarsening as shown in Figures 6.3a and 6.3b where the particles became larger and fewer and more spheroidal.

Figure 7.3a: Form Facotrs calculated from the isothermal holding experiments on Sn15%Pb alloy. Solid particles coarsened and spheroidise with holding times

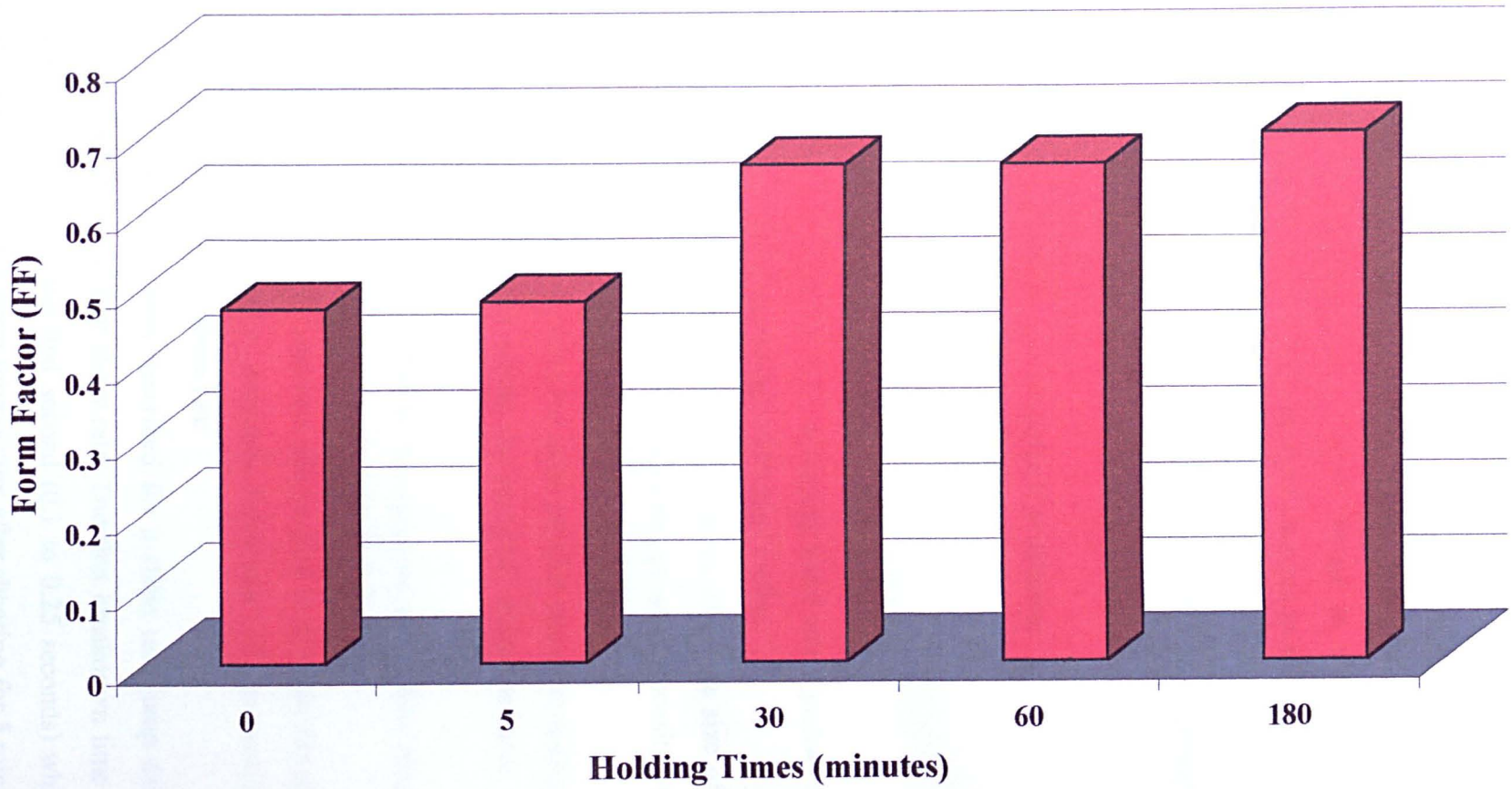

CHAPTER 8

Conclusions

The objectives of this work were to gain a better understanding to the flow and behaviour of semisolid alloy slurries during a rapid change in shear rate. The viscometry experiments were used to conduct fast rapid changes in shear rate (for a limited range of 0 s^{-1} to 200 s^{-1}) whilst the rapid compression experiments were used to test higher fraction solids of alloys (shear rate of 1 to 100 s^{-1}). It should be emphasized that the conclusions are only valid for these shear rate ranges.

The main findings from this work are summarised as follows:

8.1 Viscometry Experiments

(1) Apparent viscosity decreases with increasing shear rate. Qualitatively, the results showed good agreement with other works.

(2) The variations in shear rate and fraction solid affect the size of the solid phase particles and in turn influence the apparent viscosity of the semisolid alloy slurries.

(3) The size of the primary particles becomes smaller and more spheroidal with increasing shear rates whilst the particles' sizes increases with increasing shear rates.

(4) Power law indices can be fitted to the apparent viscosities obtained over a range of shear rates. A value of –1.2 was obtained.

(5) A single exponential decay equation can be used to describe the initial transient breakdown and/or recovery behaviour of the semisolid slurries during a change in shear rate

(6) Two breakdown times were described for a shear rate jump from a lower shear rate to a higher shear rate. The first breakdown time was found to occur within the first second (0.1 to 0.25 seconds) while a longer and slower breakdown time occurs after shearing for 5 minutes. This behaviour was also seen in the recovery times for a shear rate

jump from a higher to a lower shear rate. The first recovery time was found to be longer than the breakdown times (0.18 to 0.45 seconds).

(7) Rest times were found to affect the initial peak viscosity. A longer rest time corresponds to a higher initial viscosity value recorded.

(8) The first breakdown time was found to be largely unaffected by the amount of rest time.

(9) Breakdown or recovery times were found to be dependent on the final shear rate specified. A higher final shear rate resulted in a faster breakdown time while a higher final shear rate resulted in a longer recovery time.

8.2 Rapid Compression Experiments

(1) Load signal is dependent on the feedstock alloys and the temperature and soaking times before the forming process. Results obtained show that the load encountered for a RAP feedstock alloy is about 5 times lower than a SSTT feedstock alloy.

(2) The form factor equation calculates the spheroidicity of the solid phase particles. The higher the form factor (i.e. increasing spheroidicity), the lower is the load signal (i.e. stresses).

(3) An analytical formula applied to investigate the viscosity behaviour showed a rapid decrease initially (corresponding to a rapid breakdown in the structure) followed by a steady decrease to a near constant value with increasing shear rate.

(4) A near Newtonian behaviour (power law index → 1) is observed at the thixoforming temperature (T = 581 °C for MHD A356 Al alloys and T = 193 °C for Sn15%Pb alloys. These temperatures correspond to a fraction solid of 0.5)

8.3 Isothermal Experiments

(1) Coarsening and spheroidisation of solid phase particles occur with increasing soaking times.

(2) The coarsening rate constant ($k = 172 \times 10^{-18}$ m^3/s) for an Sn15%Pb alloy is shown to be comparable to a spray-formed alloy ($k = 100 \times 10^{-18}$ m^3/s).

8.4 Liquid Segregation

(1) Liquid segregation is observed in the thixoformed samples.

(2) Microstructural examination shows a high fraction of liquid at the edge (or perimeter) of the sample. Solid phase particles are more spheroidal at the edge than the centre of the sample.

(3) Segregation was attributed to non-uniform heating and friction during the forming process.

Chapter 9

Future Work

The following chapter describes certain considerations into some probable work that should be carried out in the future.

9.1 Viscometry experiments

Based on the experimental results obtained in this work, a new viscometer is imperative if a more thorough understanding to the rheological behaviour of semisolid alloys is to be achieved. The following are some points that have to be taken into account for a new viscometer:

1) The viscometer should be capable of performing experiments at the very low shear rates regime. The current viscometer is capable of performing shear rates at 0.01 s^{-1}. In the literature, there have been no experimental results carried out at lower shear rates. A viscometer capable of doing such low shear rates will provide additional information on the rheological behaviour of semisolid alloy slurries and will provide evidence supporting the steady state viscosity using the Cross Equation.
2) The new viscometer should also be capable of performing viscometry experiments on higher fraction solid alloy slurries and on alloys that would be of commercial interest to the manufacturing industry.
3) Inertia effects reported in this work should be minimised in the new viscometer. Currently, results can only be taken after the shear rate has achieved about 90% of its shear rate jump and after the inertia effects have been subtracted. Eliminating the inertia effect by means of subtraction means that important information during the jump may have been lost. In recent years, there have been strong inclinations towards the use of air bearings as opposed to the standard 'O' rings used in the current viscometer. The use of air

bearings would minimise inertia effects from the driving system since the bearing and the driving shaft remains contactless and therefore frictionless.

4) The current motor employed in the viscometer is an electrically commutated motor (also known as a Direct Current, DC motor). In this type of motor, permanent magnets are placed within the rotor. This imposes a large amount of inertia and as a result, limits the transient response during a sudden change in shear rate. The use of an inductive motor, which dispenses with the use of magnets in the rotor, would provide a faster transient response to a sudden change in shear rate.
5) Although the data card currently used in this work has a very high collection rate, it is only able to obtain the response change in about 1.5 seconds at the highest collection rate. A data card capable of obtaining as many data points as the current one but over a longer time period would be desirable.
6) In this work, the results from the rapid change in shear rate are fitted to a single exponential term for the decaying part of the shear stress curve. It would be appropriate if a mathematical model can be used to fit the shear stress response before and after the shear rate jump. This will describe the whole rheological response of the semisolid slurry under a rapid change in shear rate.
7) Based on the new viscometer, a range of shear rate up and down-jumps should be carried out to support the experimental evidence from this work that show: (i) the breakdown times are affected largely by the final shear rate, (ii) an up-jump exhibits a different characteristic time (breakdown), to a down-jump characteristic time (build-up) and (iii) establish whether there is a definite trend in the peak viscosity, the steady state viscosity and breakdown/build-up time with respect to shear rate, time and fraction solid.

This will provide invaluable information when comparing the behaviour of the slurry to that of the actual thixoforming process. The breakdown behaviour would mimic how the material will respond when entering a die while the build-up time will be akin to the slurry meeting an obstacle in the die.

9.2 Rapid compression experiments

The rapid compression experiments have provided an alternative for investigating alloys at higher fraction solids and alloys of commercial interest. However, the non-uniform temperature/heating and ramp velocity have limited the capability of correlating the viscometry results with the results from the rapid compression testing. Therefore the following improvements are proposed:

1) The microstructures showed liquid segregation in the thixoformed samples. It was also shown that particles are less spheroidal in the centre of the sample compared to the edge. Therefore, better control in heating the material is required in order to obtain more uniform microstructures prior to compression tests.
2) Improved control in the ram velocity. Currently, the ram velocity is calculated with respect to the displacement of the ram in a given time. An actual measurement of the ram velocity would be more appropriate.
3) The size of the slug used in the rapid compression experiments is quite large. In order to achieve a much higher shear rate in the slurry, the sample should be made as thin as possible. In the Laxmanan and Flemings calculations [Lax 80], the viscosity is proportional to the reciprocal fifth power of the height of the sample, hence it is important to be able to measure the sample height very accurately from the ram displacement in the thixoforming press.
4) Results on Sn15%Pb alloys showed slumping of the slug during the heating stages, especially at the lower fraction solids. As a result, the slug would not be at its nominal height when it is entering the die. This will induce a large error in the calculation of its viscosity. One method would be to design a holder, which would contain the sample at the low fraction solid but without the holder interfering with the flow of the alloy slurry during the filling process.

The rheological parameters extracted from both the viscometry and rapid compression experiments can be used to develop a sound mathematical thixotropic model to be used in Computational Fluids Dynamics (CFD) software. This will enable a better insight into the characteristic flow behaviour of the slurry.

Die filling during the thixoforming process is of extreme importance to the industry. Filming of the metal slurry's flow during the filling process can provide valuable information to the flow path of the metal slurry. Captured images of the flow path of the slurry can then be used to validate the rheological model used in the CFD software.

The successful integration of CFD modelling will improve the efficiency of both die design and die filling.

10 References

References from works by various authors are listed alphabetically according to their last names. The only exceptions are works quoted from the biennial semisolid processing international conferences, denoted as SSP 1 to SSP 6 in order of the year held. For example, 1st International Conference on Semi-Solid Processing of Alloys and Composites, 1990, Sophia-Antipolis, France is referenced as SSP 1. Works taken from these conferences will be denoted with the author's names and year together with the above annotations.

SSP

[SSP 1] 1st International Conference on Semi-Solid Processing of Alloys and Composites, Sophia-Antipolis, France, 1990.

[SSP 2] 2nd International Conference on Semi-Solid Processing of Alloys and Composites, Cambridge, Massachusetts, U.S.A, Editors: S.B. Brown and M.C. Flemings, 1992.

[SSP 3] 3rd International Conference on Semi-Solid Processing of Alloys and Composites, Tokyo, Japan, Editor: M. Kiuchi, 1994.

[SSP 4] 4th International Conference on Semi-Solid Processing of Alloys and Composites, Sheffield, U.K, Editors: D.H. Kirkwood and P. Kapranos, 1996.

[SSP 5] 5th International Conference on Semi-Solid Processing of Alloys and Composites, Colorado, U.S.A, Editors: A.K. Bhasin, J.J. Moore, K.P. Young and S. Midson, 1998.

[SSP 6] 6th International Conference on Semi-Solid Processing of Alloys and Composites, Turin, Italy, Editors: G.L. Chiarmetta and M. Rosso, 2000.

A

[Aka 91] N. Akaiwa, S.C. Hardy and P.W. Voorhees. Acta Metall. Mater., 1991, Vol. 39, p2931, 'The Effects Of Convection On Ostwald Ripening In Solid-Liquid Mixtures'.

[Ale 00] A.N. Alexandrou, G. R. Burgos and V.M. Entov. In SSP 6, p 161, 'Rheology Of Semisolid Suspensions: Current Understanding And Future Challenges'.

[Ann 95] S. Annavarpu and R.D. Doherty. Acta Metall. Mater., 1995, Vol. 43, p3207, 'Inhibited Coarsening Of Solid-Liquid Microstructures In Spray Casting At High Volume Fractions Of Solid'.

[Azz 00] L. Azzi, F. Ajersch and T.F. Stephenson. In SSP 6, 2000, 'Rheological Characteristics Of Semisolid Grani® Composite Alloy'.

B

[Bar 85] H.A. Barnes and K. Walters. Rheol. Acta, 1985, Vol. 24, p323, 'The Yield Stress Myth?'.

[Bar 89a] H.A. Barnes, J.F. Hutton and K. Walters. Rheology Series, Elsevier, Amsterdam, The Netherlands, 1989, Vol. 3, 'An Introduction To Rheology'.

[Bar 89b] H.A. Barnes. J. Of Rheo., 1989, Vol. 33, p329, 'Review Of Shear Thickening Of Suspensions'.

[Bar 95] H.A. Barnes. J. Non-Newtonian Fluid Mech., 1995, Vol. 56, p221, 'A Review Of The Slip (Wall Depletion) Of Polymer Solutions, Emulsions And Particle Suspensions In Viscometers: Its Cause, Character And Cure'.

[Bar 97] H.A. Barnes. J. Non-Newtonian Fluid Mech., 1997, Vol. 70, p1, 'Thixotropy - A Review'.

[Bar 99] H.A. Barnes. J. Non-Newtonian Fluid Mech., 1999, Vol. 81, p 133, 'The Yield Stress - A Review Or 'παντα ρει' - Everything Flows ?'.

[Bar 00] M. Barraco, M.A. Adria, R. Torres and P. Suria. In XIIIth Int'l Congress On Rheology, Cambridge, U.K, 2000, Vol. 4, p410, 'Thixotropical Behaviour Of Gelling Agents (Carbopol Gels) For Therapeutical Applications'.

[Bra 98] D. Brabazon, D.J. Browne. A.J. Carr and J.C. Healy. In SSP 5, 1998, p21, 'Design, Construction And Operation Of A Cobined Rheocaster/Rheometer'.

[Bra 01] D. Brabazon. PhD Thesis, University College Dublin, Ireland, U.K, 2001, 'Processing And Properties Of Rheocast Alloys'.

[Boe 87] W.J. Boettinger, P.W. Voorhees, R.C. Dobbyn and H.E. Burdette. Metall. Trans. A, 1987, Vol. 18, p487, 'A Study of the Coarsening of Liquid--Solid Mixtures Using Synchrotron Radiation Microradiography'.

C

[Car 72] P.J. Carreau. Trans. Soc. Rheo., 1972, p99. 'Rheological Equations From Molecular Network Theories'.

[Cas 59] N. Casson. Pergamon Press, editor: C.C. Mill, 1959, p84, 'Rheology Of Disperse System', reference taken from [Who 92]

[Cha 86] J.M. Chaix, N. Eustathopoulos and C.H. Allibert. Acta Metall., 1986, Vol. 34, p1589, ''Ostwald Ripening Growth Rate for Non-Ideal Systems With Significant Mutual Solubility – 1. Binary Systems'.

[Cha 02] S. Chayong, PhD Thesis, University of Sheffield, U.K, 2002, 'Thixoforming Of Aluminium 7075 Alloys'.

[Che 85] D.C.-H. Cheng. Private Communications, 'Yield Stress: A Time Dependent Property And How To Measure It'.

[Che 87] D.C.-H. Cheng. Int'l. J. Cosmetic Sci., 1987, Vol. 9, p151. 'Thixotropy'.

[Che 97] D.C. -H Cheng. Private Communications. 'Characterisation Of Thixotropy Revisited'.

[Cro 65] M.M. Cross. J. Colloidal Sci., 1965, Vol. 20, p117, 'Rheology Of Non-Newtonian Fluids: A New Flow Equation For Pseudoplastic Systems'.

D

[Dav 80] C.K.L. Davies, P. Nash and R.N. Stevens. Acta Metall., 1980, Vol. 28, p179, 'The Effect Of Volume Fraction Of Precipitate On Ostwald Ripening'

[Die 46] G.J. Dienes and H.F. Klemm, J. Appl. Phys., 1946, Vol. 17, p458, 'Theory And Application Of The Parallel Plate Plastometer'

[Die 96] I. Diewwanit and M.C. Flemings, in SSP 4, 1996, p30, 'Semisolid Forming Of Hypereutectic Al-Si Alloys'.

[Doh 84] R.D. Doherty, H.I. Lee and E.A. Feest. Mater. Sci. Engrg., 1984, Vol. 65, p181, 'Microstructure Of Stir-Cast Alloys'.

F

[Fan 02] Z. Fan. International Materials Review. 2002, in press

[Fer 91] F. Ferguson and Z. Kemblowski. Applied Science, Elsevier, London, U.K, 1991, 'Applied Fluid Rheology'.

[Fer 98] M. Ferrante, E. Freitas, M. Bonilha and V. Sinka. In SSP 5, 1998, p35, 'Rheological Properties And Microstructural Evolution Of Semisolid Aluminium Alloys Inoculated With Mischmetal And With Titanium'.

[Fig 00] A.M. Figuerdo, A. Kato and M.C Flemings. In SSP 6, 2000, p477, 'Viscosity Of Semisolid A357 Alloy In The Transient High Shear Rate Regime'.

[Fin 00] S. Finke, M. Suéry, C.L. Martin and W. Wei. In SSP 6, 2000, p169 'Microstructural And Rheological Aspects Of The Extrusion And Deposition Of A Partially Remelted Pb-Sn Alloy During Solid Freeform Fabrication'.

[Fle 74] M.C. Flemings. McGraw and Hill, New York, U.S.A., 1974, 'Solidification Processing'.

[Fle 76] M.C. Flemings, R.G. Riek and K.P. Young. Mater. Sci. Engrg., 1976, Vol. 25, p103, 'Rheocasting'.

[Fle 91] M.C. Flemings. Metall. Trans. A, 1991, Vol. 22, p957, 'Behaviour Of Metal Alloys In The Semisolid State'.

[Fle 92] M.C. Flemings, S.F. Chen, I. Diewwanit and J.A. Cornie. In SSP 2, 1992, p202, 'Rheology And Structure Of Some Aluminium Base Composites'

[Fro 83] H.J. Frost and M.F. Ashby. Pergamon, Oxford, 1983, 'Deformation Mechanism Maps'.

G

[Gar 00] M. Garat, L. Maenner and Ch. Sztur. In SSP 6, 2000, p187, 'State Of The Art Of Thixocasting'.

[Gho 94] D. Ghosh, R. Fan and C. VanSchilt. In SSP 3, 1994, p85, 'Thixotropic Properties Of Semisolid Magnesium Alloys AZ91D And AM50'.

[Guo 92] G. Chai, T. Rolland, L. Arnberg and L. Backerud. In SSP 2, 1992, p193, 'Studies Of Dendritic Coherency In Solidifying Aluminium Alloy Melts By Rheological Measurements'.

H

[Hag 00] T. Haga and S. Suzuki. In SSP 6, 2000, p735, 'Production Of Aluminium Alloy Ingots For Thixoforming By The Semisolid Casting Using A Cooling Slope'.

[Hak 91] HAAKE, Carl Stuart Ltd, Leek-Staffordshire, U.K, 1991, 'Haake Instruction Manual For Rotovisco RV20 Measuring System'.

[Hal 00] K. Hall, H. Kaufmann and A. Mundl. In SSP 6, 2000, p23, 'Detailed Processing And Cost Processing And Cost Considerations For New Rheocasting Of Light Metal Alloys'.

[Han 98] D.S. Han, G. Durrant and B. Cantor. In SSP 5, 1998, p43, 'Semisolid Deformation Of 2014 Al Alloys'.

[Har 88] S.C. Hardy and P.W. Voorhees. Metall. Trans. A, 1988, Vol. 19, p2713, 'Ostwald Ripening In A System With A High Volume Fraction Of Coarsening Phase'.

[Hir 93] M. Hirai, K. Takebayashi and Y. Yoshikawa. ISIJ Int'l., 1993, Vol. 33, No. 11, p1182, 'Effect Of Chemical Composition On Apparent Viscosity Of Semisolid Alloys'.

[Hel 96] A. Hellawell. In SSP 4, 1996, p60, 'Grain Evolution In Conventional And Rheo-Castings'.

[Hen 92] N.G. Henderson, A.R.A. McLelland, H.V. Atkinson and D.H. Kirkwood. In SSP 2, 1992, p349, 'High Temperature Rheology Of Novel Metal Matrix Composites Based On Aluminium/High Silicon Alloys'.

[Hen 93] N.G. Henderson. PhD Thesis, Sheffield University, U.K.,1993, 'The Rheology Of Semisolid Alloy Slurries'.

[Hog 01a] S.C. Hogg. Private Communications, 2001.

[Hog 01b] S.C. Hogg. PhD Thesis, University of Sheffield, U.K, 2001, 'Silicon Networks In Sprayformed Aluminium/High Silicon Alloys And Their Affect On Semisolid Processing'.

[Hor 92] M.G. Horsten, C.J. Quaak and W.H. kool. In SSP 2, 1992, p359, 'Pseudoplastic And Thixotropic Behavior Of Al/SiC Composites In The Semisolid State'.

I

[Ito 92] Y. Ito, M.C. Flemings and J.A. Cornie. Proc. Symp. Nature and Properties of Semisolid Materials, TMS, Warrendale, U.S.A, Editors: J.A. Sekhar and J.A. Dantzig, 1992, p1, 'Rheological Behaviour And Microstructure Of Al-6.5wt%Si Alloy'.

J

[Jab 92] S. Jabrane, B. Clément and F. Ajersch. In SSP 2, 1992, p223, 'Evolution Of Primary Particle Morphology During Rheoprocessing Of Al-5.2%Si Alloy'.

[Jay 89] C.S. Jayanth and P. Nash. J. Mater. Sci., 1989, Vol. 24, p3041, 'Factors Affecting Particle-Coarsening Kinetics and Size Distribution'

[Ji 01] S. Ji, Z. Fan and M.J. Bevis. Mater. Sci. Engrg. A, 2001, p210, 'Semisolid Processing Of Engineering Alloys By A Twin-Screw Rheomoulding Process'.

[Jol 74] P.A. Joly. PhD Thesis, MIT, U.S.A, 1974, 'Rheological Properties And Structure Of A Semisolid Tin-Lead Alloy'.

[Jol 76] P.A. Joly and R. Mehrabian. J. Mater. Sci., 1976, Vol. 11, p1393, 'The Rheology Of A Partially Solid Alloy'.

[Jou 00] C. Journeau, M. Ramacciotti and G. Cognet. In SSP 6, 2000, p143, 'Rheology And Microstructure Of Continuously Cooled Semisolid Materials'.

K

[Kan 82] S.S. Kang and D.N. Yoon. Metall. Trans. A, 1982, Vol. 13, p1405, 'Kinetics Of Grain Coarsening During Sintering Of Co-Cu and Fe-Cu Alloys With Low Liquid Contents'.

[Kap 98] P. Kapranos, D.H. Kirkwood and M.R. Barkhudarov. In SSP 5, 1998, p11, 'Modelling Of Structural Breakdown During Rapid Compression Of Semisolid Alloy Slugs'.

[Kap 00] P. Kapranos, H.V. Atkinson and D.H. Kirkwood. Mater. Sci. Forum, Vol. 329, p552, 'Rapid Compression Testing Of Semisolid Alloy Slugs'.

[Kap 01] P. Kapranos, T.Y. Liu, H.V. Atkinson and D.H. Kirkwood. J. Mater. Processing Tech., 2001, Vol. 111, p31, 'Investigation Into The Rapid Compression Of Semisolid Alloy Slugs'.

[Kat 91] T.Z. Kattamis and T.J. Piccone. Mater. Sci. Engrg. A, 1991, Vol. 131, p265, 'Rheology Of Semisolid Al-4.5Cu-1.5Mg Alloy'.

[Kat 92a] T.Z. Kattamis and T.J. Piccone. Proc. Symp. Nature and Properties of Semisolid Materials, TMS, Warrendale, U.S.A, Editors: J.A. Sekhar and J.A. Dantzig, 1992, p69, 'Rheological Behavior Of A Semisolid Al-Cu-Mg Alloy'.

[Kat 92b] T.Z. Kattamis and A.I. Nakhla. In SSP 2, 1992, p237, 'Rheological, Microstructural And Constitutional Studies Of Semisolid Al-4.5%Cu-1.5%Mg Alloy'.

[Ken 88] M.P. Kenney, J.A. Courtois, R.D. Evans, G.M. Farrior, C.P. Kyonka, A.A. Koch and K.P. Young. Metals Handbook, 9th Edition, Editor: B.P. Bardes, 1988, Vol. 15, p327, 'Semisolid Metal Casting And Forging'.

[Kir 89] D.H. Kirkwood and P. Kapranos. Met. Mater., 1989, Vol. 5, p16, 'Semisolid Processing Of Alloys'.

[Kir 94] D.H. Kirkwood. International Materials Review. 1994, Vol. 39, p173, 'Semisolid Metal Processing'

[Kir 00] D.H. Kirkwood D.H. Kirkwood, P.J. Ward, M. Barkhudarov, S.B. Chin, H.V. Atkinson and T.Y. Liu. In SSP 6, 2000, p545, 'An Initial Assessment Of The Flow-3D Thixotropic Model'.

[Kiu 92] M. Kiuchi and S. Sugiyama. In SSP 2, 1992, p47, 'Anew Process To Manufacture Semisolid Metals'.

[Kiu 94] M. Kiuchi and S. Sugiyama. In SSP 3, 1994, p245, 'Mashy State Extrusion, Rolling And Forging'.

[Kok 99] J. Koke and M. Modigell. Proc. Of AFDM'99, Haeundae-Pusan, Korea, 1999, p101,'Rheological Modelling On Semisolid Metal Alloys And Simulation Of Thixocasting Processes'.

[Kok 00] J. Koke, M. Hufschmidt, M. Modigell, C. Heine, S. Han, S. Srapf and J. Petera. In SSP 6, 2000, p623, 'Segregation And Wall Slip In Semisolid Alloys: Measurement, Modelling And Simulation'.

[Kri 96] P.G. Kristensen, C.T.B. Jensen and Q.D. Nguyen. XIIth Int'l Congress on Rheology, Quebec City, Canada, 1996, p779.

[Kum 93] P. Kumar, C.L. Martin and S.B. Brown. Metall. Trans. A, 1993, Vol. 24, p1107, 'Shear Rate Thickening Flow Behaviour Of Semisolid Slurries'.

[Kum 94a] P. Kumar, C.L. Martin and S.B. Brown. Acta Metall. Mater., Vol. 42, p3595, 'Constitutive Modeling And Characterization Of The Flow Behavior Of Semisolid Metal Alloy Slurries: Part 1, The Flow Response'.

[Kum 94b] P. Kumar, C.L. Martin and S.B. Brown. In SSP 3, 1994, p37, Predicting The Constitutive Flow Behaviour Of Semisolid Metal Alloy Slurries'.

[Kum 94c] P. Kumar. PhD Thesis, MIT, USA, 1994, ' Constitutive Modeling And Characterization Of The Flow Behavior Of Semisolid Metal Alloy Slurries'.

[Kur 92] W. Kurz and D.J. Fisher. Trans Tech. Publications, Aedermannsdorf, Switzerland, 1992, 3rd Edition, 'Fundamentals Of Solidification'.

L

[Lax 80] V. Laxmanan and M.C. Flemings. Metall. Trans. A, 1980, Vol. 11, p1927, 'Deformation Of Semisolid Sn-15%Pb Alloy'.

[Lev 90] C. Levaillant. In SSP 1. Session D: Rheology, 1990, p1, 'Rheological Aspects Of Semisolid Processing'.

[Lif 61] I.M. Liftshitz and V.V. Slyozov. J. Phys. Chem. Solids, 1961, Vol. 19, p35, 'The Kinetics Of Precipitation From Supersaturated Solid Solutions'.

[Liu 98] J.M. Liu and Z.G. Liu. Solid State Comms., 1998, Vol. 105, Issue 8, p517, 'Phase Precipitation On Grain Boundaries In Binary Alloys: A Monte-Carlo Approach'.

[Liu 00a] T.Y. Liu, P.J. Ward, D.H. Kirkwood and H.V. Atkinson, In XIIIth Int'l Congress on Rheology, Cambridge, U.K, 2000, Vol. 4, p61, 'A Study Of The Transient Rheological Behaviour Of Semisolid Sn15%Pb Alloy'.

[Liu 00b] T.Y. Liu, P. Kapranos and H.V. Atkinson, In SSP 6, 2000, p747, 'Assessing Thixoformability By Rapid Compression Testing'.

[Lop 92] D.E. Loper. Proc. Symp. Nature and Properties of Semisolid Materials, TMS, Warrendale, U.S.A, Editors: J.A. Sekhar and J.A. Dantzig, 1992, p91, 'Dynamical Processes In Slurries And Mushes'.

[Lou 92] W.R. Loué, S. Landkroon and W.H. Kool. Mater. Sci. Engrg A, 1992, Vol. 9, p241, 'Rheology Of Partially Solidified AlSi7Mg0.3 And The Influence Of SiC Additions'.

M

[Mad 96a] M. Mada and F. Ajersch. Mater. Sci Engrg. A, 1996, Vol. 212, p157, 'Rheological Model Of Semisolid A356 - SiC Composite Alloys Part I: Dissociation Of Agglomerate Structures During Shear'.

[Mad 96b] M. Mada and F. Ajersch. Mater. Sci Engrg. A, 1996, Vol. 212, p171, 'Rheological Model Of Semisolid A356 - SiC Composite Alloys Part II: Reconstitution Of Agglomerate Structures At Rest'.

[Mcl 92] A.R.A McLelland, N.G. Henderson, H.V. Atkinson and D.H. Kirkwood. In SSP 2, 1992, p349, 'The Evaluation Of Rheological Measurements On Semisolid Metal Slurries'.

[Mcl 93] A.R.A. McLelland. PhD Thesis, Sheffield University, U.K, 1993, 'Rheology And Thixoforging Of Aluminium Alloy/Silicon Carbide Metal Matrix Composites'.

[Mcl 97] A.R.A McLelland, N.G. Henderson, H.V. Atkinson and D.H. Kirkwood. Mater. Sci Engrg. A, 1997, Vol. 232, p110, 'Anomalous Rheological Behaviour Of Semisolid Alloy Slurries At Low Shear Rates'.

[Met 70] S.A. Metz and M.C. Flemings. AFS Trans., 1970, Vol. 78, p453, 'Fundamental Study Of Hot Tearing'.

[Mew 79] J. Mewis. J. Non-Newtonian Fluid Mechs., 1979, Vol. 6, p1, 'Thixotropy - A General Review'.

[Mew 96] J. Mewis and J. Schryvers. Int'l Fine Particle Research Ins. Report, 1996, reference taken from [Bar 97].

[Mit 96] Mitsuru et al., European Patent 0 745 694 A1, UBE Industries Ltd, 1996, 'A Method For Shaping Semisolid Materials'.

[Mod 98] M. Modigell, J. Koke and J. Petera. In SSP 5, 1998, p317, 'Two-Phase Model For Metal Alloys In The Semisolid State'.

[Mod 99] M. Modigell and J. Koke. Mechs. Time Dependent Mater., 1999, Vol. 3, p15, 'Time Dependent Rheological Properties Of Semisolid Metal Alloys'.

[Mod 00] M. Modigell, J. Koke, R. Kopp, D. Neudenberger, P.R. ahm and O. Klaassen. In SSP 6, p605, 'Comparison Of Rheological Measurement Methods For Semisolid Alloys'.

[Mol 87] J.M.M. Molenaar, W.H. Kool and R.J. Smeulders. J. Mater. Sci., 1987, Vol. 22, p1057, 'Coarsening During Stir-Casting'.

[Moo 59] F. Moore. Trans. British Ceramic Soc., 1959, Vol. 58, p470, 'The Rheology Of Ceramic Slips And Bodies'.

[Moo 90] H.K. Moon, PhD Thesis, MIT, U.S.A, 1990, 'Rheological Behavior And Microstructure Of Ceramic Particulate/Aluminium Alloy Composites'.

[Moo 91] H.K. Moon, J.A. Cornie and M.C. Flemings. Mater. Sci. Engrg. A, 1991, Vol. 144, p253, Rheological Behaviour Of SiC Particulate Composite Slurries At Temperature Above The Liquidus And Within The Liquid + Solid Region Of The Matrix'.

N

[Nab 96] S.M. Nabulsi, T.A. Steinberg, C.J. Davidson and N.W. Page. In SSP 4, 1996, p47, 'The Shear Strength Of Semisolid Alloys'.

[Ngy 92] L. Ngyuen and M. Suéry. In SSP 2, 1992, p427, 'Compression Behavior Of Partially Remelted SiC Reinforced Al-Cu Alloys'.

[Nir 00] B. Niroumand, K. Xia. Mater. Sci Engrg. A, 2000, Vol. 283, p70, '3D Study Of The Structure Of Primary Crystals In A Rheocast Al-Cu Alloy'.

O

[Old 56] J.G. Oldroyd. Rheology, Theory and Aplications (ed. F.R. Eirich), Academic Press, New York, U.S.A, 1956, p653, 'Non-Newtonian Flow Of Liquids And Solids'.

P

[Par 68] W. Parzonka and J. Vocadlo. Rheol. Acta, 1968, Vol. 7, p260, reference taken from [Who 92].

[Pas 92] L. Pasternak, R. Carnahan, R. Decker and R. Kilbert. In SSP 2, 1992, p159, 'Semisolid Production Processing Of Magnesium Alloys By Thxiomolding'.

[Pin 84] D.A. Pinsky, p.O. Charreyron and M.C. Flemings. Metall. Trans. B, 1984, Vol. 15, p173, 'Compression Of Semisolid Dendritic Sn-Pb Alloys At Low Strain Rates'.

[Pen 94] H. Peng, S.P. Wang, N. Wang and K.K. Wang. In SSP 3, 1994, p191, 'Rheomolding – Injection Molding Of Semisolid Metals'.

[Pen 96] H. Peng and K.K. Wang. In SSP 4, 1996, p2, 'Steady State And Transient Rheological Behaviour Of A Semisolid Tin-Lead Alloy In Simple Shear Flow'.

[Pen 00] H. Peng and W.M. Hsu. In SSP 6, 2000, p313, 'Development On Rheomolding Of Magnesium Parts'.

Q

[Qua 94] C.J. Quaak, M.G. Horsten and W.H. Kool. Mater. Sci. Engrg. A, 1994, p247, 'Rheological Behaviour Of Partially Solidified Aluminium Matrix Composites'.

[Qua 96a] C.J. Quaak. PhD Thesis, Technische Univesiteit Delf, The Netherlands, 1996, 'Rheology Of Partially Solidified Aluminium Alloys And Composites'.

[Qua 96b] C.J. Quaak, L. Katgerman and W.H. Kool. In SSP 4, 1996, p35, 'Visocisty Evolution Of Partially Solidified Aluminium Slurries After A Shear Rate Jump'.

R

[Ram 78] S.D.E. Ramati, G.J. Abbashian and R. Mehrabian. Metall. Trans. B, 1978, Vol. 9, p241, 'The Structure Of A Partially Solid Alloy'.

[Ryo 96] Y.H. Ryoo, I.J. Kim and D.H. Kim. In SSP 4, 1996, p66, 'Microstructural Characteristics Of Semisolid State Processed Hypereutectic Al-Si Alloys'.

S

[Sal 94] L. Salvo, W.R. Loué and M. Suéry. In SSP 3, 1994, p261, 'Influence Of Thermomechanical History On The Structure And Rheological Behaviour Of Semisolid Al-Alloys'.

[Sal 96] L. Slavo, M. Suéry, Y.D. Charentenay and W. Loué. In SSP 4, 1996, p10, 'Microstructural Evolution And Rheological Behaviour In The Semisolid State Of A New Al-Si Based Alloy'.

[San 94a] S. Sannes, H. Gjestland, L. Arnberg and J.K. Solberg. In SSP 3, 1994, p75, 'Microstructural Coarsening Of Semisolid Mg Alloys'.

[San 94b] S. Sannes, H. Gjestland, L. Arnberg and J.K. Solberg. In SSP 3, 1994, p271, 'Yield Point Behaviour Of Semisolid Mg Alloys'.

[Sec 84] J.F. Secondé and M. Suéry. J. Mater. Sci., 1984, Vol. 19, p3995, 'Effect Of Solidification Conditions On Deformation Behaviour Of Semisolid Sn-Pb Alloys'.

[Sis 58] A.W. Sisko. Ind. Engrg. Chem., 1958, p1789, 'The Flow Of Lubricating Greases', reference taken from [Bar 89].

[Spe 71] D.B. Spencer. Sc.D., MIT, U.S.A, 1971, 'Rheology Of Liquid-Solid Mixtures Of Lead-Tin'.

[Spe 72] D.B. Spencer, R. Mehrabian and M.C. Flemings. Metall. Trans., 1972, Vol. 3, p1925, 'Rheological Behaviour Of Sn-15%Pb In The Crystallization Range'.

[Str 89] Strawberry Tree Incorporated. Application and Development Software For IBM® PC ™ and Compatible Computers, 1989, 'Analog Connection PC Software ™ And Development System ™'.

[Sué 82] M. Suéry and M.C. Flemings. Metall. Trans. A, 1982, Vol. 13, p1809, 'Effect Of Strain Rate On Deformation Behaviour Of Semisolid Dendritic Alloys'.

[Sué 96] M. Suéry, C.L. Martin and L. Salvo. In SSP 4, 1996, p21, 'Overview Of The Rheological Behaviour Of Globular And Dendritic Slurries'.

[Sué 00] M. Suéry and A. Zavaliangos. In SSP 6, 2000, p129, 'Key Problems In Rheology Of Semisolid Alloys'.

T

[Tak 84] S. Takajo, W.A. Kaysser and G. Petzow. Acta Metall., 1984, Vol. 32, p107, 'Analysis Of Particle Growth By Coalescence During Liquid Phase Sintering'.

[Tho 65] D.G. Thomas. J. Colloidal Sci., 1965, Vol. 20, p267, 'Transport Characteristics Of Suspension: VII. A Note On The Viscosity Of Newtonian Suspensions Of Uniform Spherical Particles'.

[Tur 91] L.S. Turng and K.K. Wang. J. Mater. Sci., 1991, Vol. 26, p2173, 'Rheological Behaviour And Modelling Of Semisolid Sn-15%Pb Alloy'.

[Tzi 00a] E. Tzimas and A. Zavaliangos. J. Mater. Sci., 2000, Vol. 35, p5319, 'Evaluation Of Volume Fraction Of Solid In Alloys Formed By Semisolid Processing'.

[Tzi 00b] E. Tzimas and A. Zavaliangos. Mater. Sci. Engrg. A, 2000, Vol. 289, p217, 'A Comparative Characterization Of Near-Equiaxed Microstructures As Produced By Spray Casting, Magnetohydrodynamic Casting And The Stress Induced Melt Activated Process'.

[Tzi 00c] E. Tzimas and A. Zavaliangos. Mater. Sci. Engrg. A, 2000, Vol. 289, p228, 'Evolution Of Non-Equiaxed Microstructure In The Semisolid State'.

V

[Val 98] J. Valer, F.S-.Antonin, P. Meneses and M. Suéry. In SSP 5, 1998, p3, 'Influence Of Processing On Microstructure And Semisolid Behavior Of Al-Ge Alloys'.

[Voo 84] P.W. Voorhees and M.E. Glicksman. Metall Trans. A, 1984, Vol. 15, p1081, 'Ostwald Ripening During Liquid Phase Sintering - Effect Of Volume Fraction On Coarsening Kinetics'.

[Voo 87] P.W. Voorhees and R.J. Schaefer, Acta Metall., 1987, Vol. 35, p327, 'In Situ Observation Of Particle Motion And Diffusion Interactions During Coarsening'.

W

[Wag 61] C. Wagner. Z.Elektrochem, 1961, Vol. 65, p581, 'Theorie der Alterung von Niederschlägen durch Umlösen (Ostwakd-Reifung)'.

[Wah 00] A. Wahlen. In SSP 6, 2000, p565, 'Modeling The Thixotropic Flow Behavior Of Semisolid Aluminium Alloys'.

[Wan 90a] N. Wang, G.J. Shu and H.G. Yang, Mater. Trans., JIM, 1990, Vol. 31, p715, 'Rheological Study Of Partially Solidified Tin-Lead And Aluminium-Zinc Alloys For Stir-Casting'.

[Wan 90b] N. Wang, G.J. Shu and H.G. Yang. J. Mater. Sci, 1990, Vol. 25, p2185, 'Formation And Growth Of Solid Particles In Shear Flow'.

[Wan 90c] G. Wan and P.R. Sahm. Acta. Metall. Mater., 1990, Vol. 38, p967, 'Ostwald Ripening In The Isothermal Rheocasting Process'.

[Wan 92a] G. Wan and P.R. Sahm. In SSP 2, 1992, p328, 'Particle Characteristics And Coarsening Mechanisms In Semisolid Processing'.

[Wan 92b] S.P. Wang. K.K Wang and L.S. Turng. In SSP 2, 1992, 'Die-Casting Of Semisolid Metals'.

[War 00a] P.J. Ward, H.V. Atkinson, D.H. Kirkwood, T.Y. Liu and S.B. Chin. Conf. Of Metallurgists, Ottawa-Ontario, Canada, 2000, (On CD) 'Issues In The Validation Of CFD Modelling Of Semisolid Metal Forming'.

[War 00b] P.J. Ward, H.V. Atkinson, D.H. Kirkwood, S.B. Chin, T.Y. Liu and M.R. Barkhudarov. MCWASP IX, Aachen, Germany, 2000, p397, 'Thixotropic Property Measurement And Flow Modelling In Semisolid Metal Alloy Slurries'.

[Who 92] R.W. Whorlow. Physics and its applications in Ellis Horwood, 2nd Edition, New York, U.S.A, 1992, 'Rheological Techniques'.

[Whi 99] E.M. Whitton. PhD Thesis, University of Oxford, U.K, 1999,'Microstructral Evolution Of Spray Formed Nickel-Based Super Alloys'.

[Wit 98] T. Witulski, U. Morjan, I. Niedick and G. Hirt. In SSP 5, 1998, p353, 'The Thixoformability Of Aluminium Alloys'.

[Wor 64] W.E. Worrall and S. Tuliani. Trans. British Ceramic Soc., 1964, Vol. 63, p167, reference taken from [che87].

Y

[Yan 92] S.C. Yang, G.T. Higgins and P. Nash. Mater. Sci Tech., 1992, Vol. 8, p10, 'Coarsening Kinetics Of Solid And Liquid Silver Particles In Nickel'

[Yan 97] Y.S. Yang and C.-Y.A. Tsao. J. Mater. Sci., 1997, Vol. 32, p2087, 'Viscosity And Structure Variations Of Al-Si Alloy In The Semisolid State'.

[You 92] K.P. Young. Proc. Symp. Nature and Properties of Semisolid Materials, TMS, Warrendale, U.S.A, Editors: J.A. Sekhar and J.A. Dantzig, 1992, p245, 'Semisolid Metal Forming Alloys And Composites'.

[You 94] K.P. Young and R. Fitze. In SSP 3, 1994, p155, 'Semisolid Metal Cast Aluminium Automotive Components'.

[You 00] K.P. Young and P. Eisen. In SSP 6, 2000, p97, 'SSM (Semisolid Metal) Technological Alternatives For Different Applications'.

Z

[Zav 00] A. Zavaliangos and C.L. Martin. In SSP 6, 2000, p385, 'Strain Localization In Semisolid Alloys'.

Appendix 1

The Cross model [Cro 65] is based upon the assumption that shear thinning (or pseudoplastic flow) is associated with the formation and rupture of structural linkages.

The effective rate constant for rupture (or breakdown) involves the n^{th} power of the shear rate, D, and is given as: $k_0 + k_1 (D^n)$

The effective rate constant for buildup is simply k_2 and does not involve any shear rate.

For an average chain of molecules having L, linkages, the rate of change in the linkages would be: $\frac{dL}{dt} = k_2 P - \left(k_0 + k_1 D^n\right) L$ [AP 1.1]

where P is the total number of single particles per unit volume. Equation AP 1.1 is the rate equation.

At equilibrium conditions, dL/dt = 0, therefore $L = \frac{k_2 P}{k_0 + k_1 D^n}$

At D = 0, L = L_0, therefore $L_0 = \frac{k_2 P}{k_0}$

Hence, $\frac{L}{L_0} = \frac{k_0}{k_0 + k_1 D^n}$ [AP 1.2]

and (÷by k_0) gives $\frac{L}{L_0} = \frac{1}{1 + \left(\frac{k_1}{k_0} D^n\right)} = \frac{1}{1 + \alpha D^n}$ [AP 1.3]

where $\alpha = k_1 / k_0$

Assuming that the viscosity, η, is proportional to the number of segments per chain in a molecule, at equilibrium, $\eta = \eta_\infty + BL$

where B is a constant. [AP 1.4]

Equation AP 1.4 is the state equation.

When L = L_0, $\eta = \eta_0$, therefore $\eta_0 - \eta_\infty = BL_0$ [AP 1.5]

Relating Equations AP .4 and AP 1.5 by division,

$$\frac{\eta - \eta_\infty}{\eta_0 - \eta_\infty} = \frac{L}{L_0}$$ [AP 1.6]

Combining Equations AP 1.3 and AP 1.6,

$$\frac{\eta - \eta_\infty}{\eta_0 - \eta_\infty} = \frac{1}{1 + \alpha D^n}$$ [AP 1.7]

where $\alpha = k_1 / k_0$. Equation AP 1.7 is the Cross model at equilibrium conditions.

Appendix 2

To derive the fundamental equations for Couette system, certain assumptions are made. The formulae derived apply equally for a Searle-type system provided that the angular velocity is taken relative to the cylinders only. The assumptions are:

(1) The liquid is incompressible and the flow is steady and laminar.

(2) Inertial effects are neglected

(3) End and edge effects are ignored.

(4) The system is isothermal

(5) No slippages between the surface of the cylinders

In a Searle system, the inner cylinder of radius R_1 rotates with a constant angular velocity, Ω, while the outer cylinder is stationary with radius, R_2 (Figure AP 2.1).

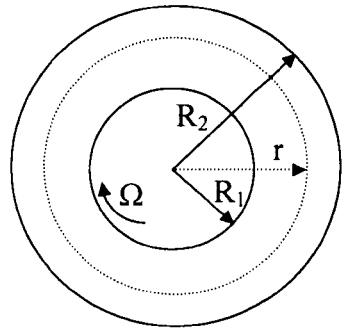

Figure AP 2.1: Schematic diagram of a Searle viscometer.

In steady flow, the shear stress at any radius, r, is:

$$\sigma = \frac{T}{2\pi r^2} \qquad \text{[AP 2.1]}$$

Consider now a fluid element in the annulus gap (Figure AP 2.2). Assuming that the fluid elements moves in circles about the common axis of the cylinder with an angular velocity, ω, which is a function of radius r only.

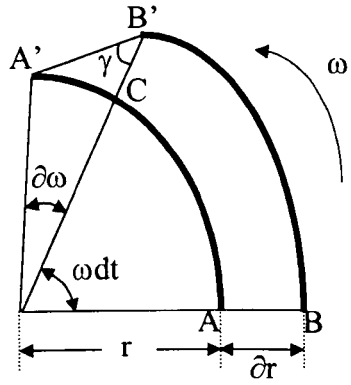

Figure AP 2.2: Schematic diagram of the deformation of a fluid element in the system.

The shear strain,γ, is given by:

$$\gamma = \frac{B'C}{CA'} = \frac{(r + \partial r)\partial\omega\partial t}{\partial r}$$

$$\partial r \rightarrow 0,\ \dot{\gamma} = r\left(\frac{d\omega}{dr}\right) \qquad \text{[AP 2.2]}$$

At any radius, r, in the gap,

$$\dot{\gamma} = r\frac{d\omega}{dr} = r\frac{d\omega}{d\sigma}\cdot\frac{d\sigma}{dr} \qquad \text{[AP 2.3]}$$

Differentiating Equation AP 2.1,

$$\frac{d\sigma}{dr} = \frac{T}{2\pi}(r^{-2}) = \frac{-2T}{2\pi}(r^{-3})$$

$$\frac{d\sigma}{dr} = \frac{-T}{\pi r^3} \qquad \text{[AP 2.4]}$$

Substituting AP 2.4 into AP 2.3,

$$\dot{\gamma} = r\frac{d\omega}{dr}\left(\frac{-T}{\pi r^3}\right) = \frac{d\omega}{d\sigma}\cdot\left(\frac{-T}{\pi r^2}\right) \qquad \text{[AP 2.5]}$$

Substituting AP 2.1 into AP 2.5 gives:

$$\dot{\gamma} = -2\sigma\left(\frac{d\omega}{d\sigma}\right)$$

$$d\omega = \frac{\dot{\gamma}}{-2\sigma}d\sigma \qquad \text{[AP 2.6]}$$

$$\int_{\omega_{R_2}}^{\omega} d\omega = \int_{\sigma_{R_2}}^{\sigma} \frac{\dot{\gamma}}{-2\sigma}d\sigma \qquad \text{[AP 2.7]}$$

For a Newtonian fluid, $\dot{\gamma} = \left(\frac{\sigma}{\eta}\right)$. From AP 2.1 and AP 2.2

$$r\frac{d\omega}{dr} = \frac{T}{2\pi\eta r^2}$$

At r = R_1, w = 0 and at r = R_2, w = Ω

$$\int_0^{\Omega} d\omega = \int_{R_1}^{R_2} \frac{T}{2\pi\eta r^3}dr = \frac{T}{2\pi\eta}\int_{R_1}^{R_2} \frac{1}{r^3}dr$$

$$\Omega = \frac{T}{2\pi\eta}\left[\frac{r^{-3+1}}{-3+1}\right]_{R_1}^{R_2}$$

$$\Omega = \frac{T}{4\pi\eta}\left[\frac{1}{R_1^2} - \frac{1}{R_2^2}\right] \qquad \text{[AP 2.8]}$$

The shear rates at the inner cylinder can be derived using Equation AP 2.1 and AP 2.8. For a Newtonian fluid of viscosity,η, $\dot{\gamma} = \sigma/\eta$

At r = R_1 for a Searle Visocmeter,

$$\dot{\gamma} = \frac{T/2\pi R_1^2}{\frac{T}{4\pi\Omega}\left(\frac{R_2^2 - R_1^2}{R_1^2 R_2^2}\right)}$$

$$\dot{\gamma} = \frac{2\Omega R_2^2}{R_2^2 - R_1^2} \qquad \text{[AP 2.9]}$$

If the flow curve is described by a power law relationship, the viscosity and shear rate are determined by:

$$\eta = C\dot{\gamma}^m \qquad \text{[AP 2.10]}$$

Since $\eta = \frac{\sigma}{\dot{\gamma}} = \sigma\dot{\gamma}^{-1}$ [AP 2.11]

Comparing AP 2.10 and AP 2.11 and rearranging gives:

$$\dot{\gamma} = \sigma^{\frac{1}{m+1}} C^{\frac{-1}{m+1}}$$

$$\dot{\gamma} = K\sigma^N \qquad \text{[AP 2.12]}$$

Using Equation AP 2.1, AP 2.2 and AP 2.12 and equating them gives:

$$r\frac{d\omega}{dr} = K\sigma^N$$

$$r\frac{d\omega}{dr} = K\left(\frac{T}{2\pi r^2}\right)^N \qquad \text{[AP 2.13]}$$

Boundary conditions are: at $r = R_1$, $\omega = 0$ and at $r = R_2$, $\omega = \Omega$

$$\int_0^{\Omega} d\omega = \int_{R_1}^{R_2} \frac{K}{r}\left(\frac{T}{2\pi r^2}\right)^N dr$$

$$\Omega = K\left(\frac{T}{2\pi}\right)^N \int_{R_1}^{R_2} \left(r^{-1}\right)\left(r^{-2N}\right) dr \qquad \text{[AP 2.14]}$$

By substitution method (u = 1 + 2N), and integrating AP 2.14 gives:

$$\Omega = \frac{K}{2N}\left(\frac{T}{2\pi}\right)^N \left[R_1^{-2N} - R_2^{-2N}\right] \qquad \text{[AP 2.15]}$$

Rearranging AP 2.13 gives:

$$\left(\frac{T}{2\pi}\right)^N = \frac{r}{Kr^{-2N}}\left(\frac{d\omega}{dr}\right)$$

and from AP 2.2, substitute $d\omega/dr$ gives:

$$\left(\frac{T}{2\pi}\right)^N = \frac{r}{Kr^{-2N}} \qquad \text{[AP 2.16]}$$

Substitute AP 2.16 into AP 2.15 gives the calculation of shear rate for a power law fluid across the annulus gap:

$$\dot{\gamma} = \frac{2N\Omega(r^{-2N})}{R_1^{-2N} - R_2^{-2N}} \qquad \text{[AP 2.17]}$$

A Newtonian and power law fluid shear rate distribution normalised to angular velocity at the rotor wall for the current viscometer system is shown for various position throughout the annulus gap (Figure AP 2.3). It can be seen from the graph that only at one point is the shear rate for the Newtonian model equal to the shear rate for the power law model. The cross over point occurs at 7.6Ω for the present viscometer system. This factor was observed not to vary much for different m indices used in the power law equation. Figure AP 2.4 shows the cross over point to be at 7.5Ω for the power law index of m= -1.24 of Sn15%Pb alloys (at Fs=0.36) found in this work. The factor used is different for each geometry system. Quaak [Qua 96b]

used 4.2Ω while Brabazon [Bra 01] used 6.3Ω in his system. The figures showed that the shear rate decreases from the rotating surface to the stationary wall.

Figure AP 2.3: Shear rate distribution in the viscometerused in this work for Newtonian fluid and Power law fluid

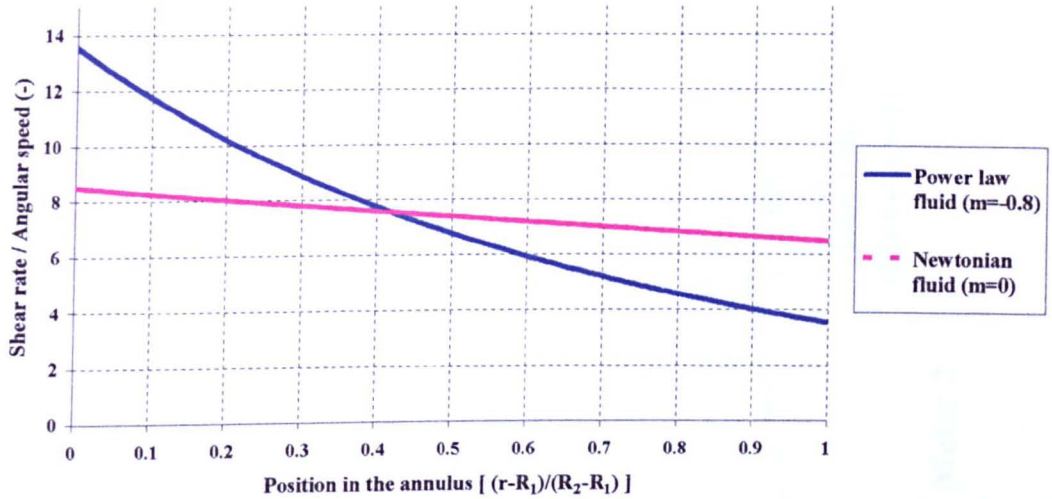

Figure AP 2.4: Shear rate distribution in the viscometerused in this work for Newtonian fluid and Power law fluid

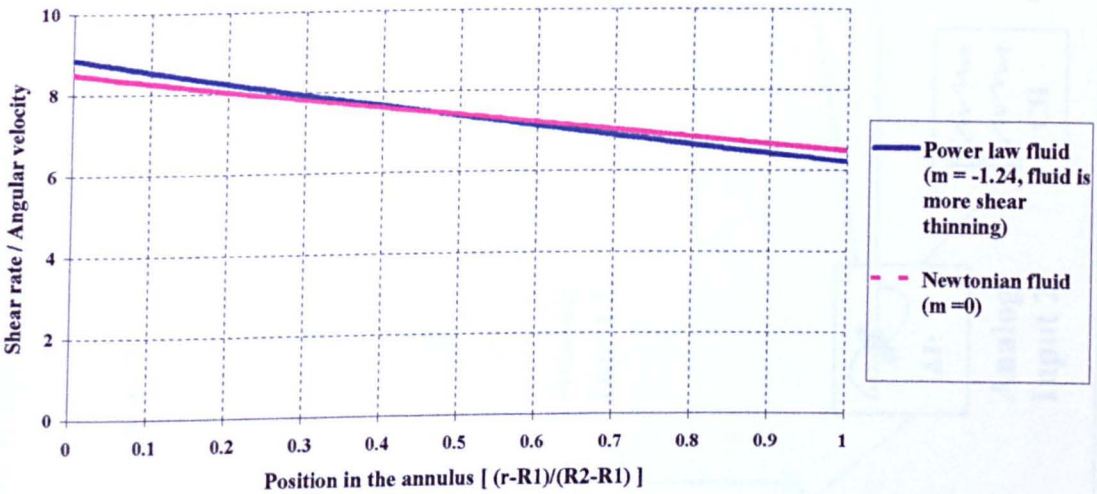

Appendix 3 Schematic diagram of program used in data card for analog capture in viscometry experiments.

Analog output from the RV20 is saved in the Log File after the Set Point is triggered (just before the shear rate change). AI: 1 and AI: 2 record the shear rate and shear stress voltages respectively whilst TI:1 records real time in seconds.

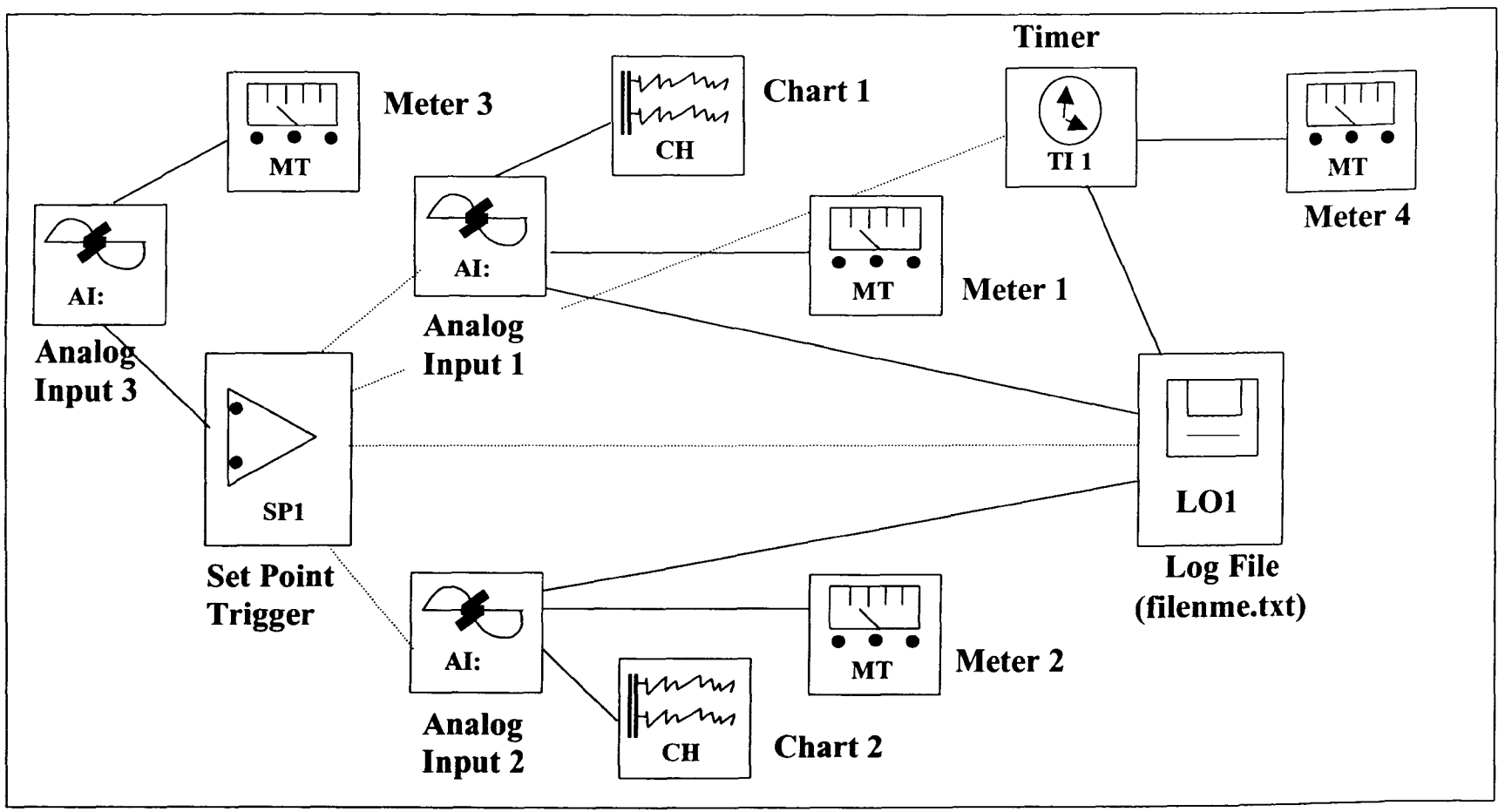

Appendix 4

The Cross model for a Non-Newtonian fluid is given by (1) a state equation and (2) a rate equation.

State equation: $\eta = (\eta_\infty + c\lambda)$ [AP 4.1]

Rate equation: $d\lambda / dt = a(1-\lambda) - b \dot{\gamma}^m \lambda$ [AP 4.2]

where $\dot{\gamma}$ is the shear rate, η is the viscosity (subscript ∞ indicates at infinite shear rate, i.e. equilibrium viscosity) and λ is the structure parameter. 'a', 'b' and 'm' are material constants.

The Moore model is equivalent to the Cross model except that the shear rate for the Moore model is not described by a power law relationship.

To describe the breakdown of structure,λ, from its initial state, equation AP 4.2 can be integrated (assuming that the shear rate is constant):

$$\int \frac{d\lambda}{a - a\lambda - b\lambda\dot{\gamma}^m} = \int dt$$

$$\int \frac{d\lambda}{a - \lambda(a + b\dot{\gamma}^m)} = \int dt$$

Assuming that at $t = 0$, $\lambda = \lambda_o$ and at $t = t$, $\lambda = \lambda$

$$\int_{\lambda_o}^{\lambda} \frac{d\lambda}{a - \lambda(a + b\dot{\gamma}^m)} = \int_0^t dt$$

$$\left(- \frac{1}{a + b\dot{\gamma}^m} \right) \left[- \ln \left(a - \lambda (a + b\dot{\gamma}^m) \right) \right]_{\lambda_o}^{\lambda} = [t]_0^t$$

$$\left[- \ln(a - \lambda(a + b\lambda\dot{\gamma}^m)) \right]_{\lambda_o}^{\lambda} = -(a + b\dot{\gamma}^m)[t - 0]$$

$$\ln \left[\frac{a - \lambda (a + b\dot{\gamma}^m)}{a - \lambda_o (a + b\lambda\dot{\gamma}^m)} \right] = (a + b\lambda\dot{\gamma}^m)t$$

$$\frac{a - \lambda(a + b\lambda\dot{\gamma}^m)}{a - \lambda_o(a + b\lambda\dot{\gamma}^m)} = \exp(a + b\dot{\gamma}^m)t$$

$$\frac{\dfrac{a}{a + b\dot{\gamma}^{m}} - \lambda}{\dfrac{a}{a + b\dot{\gamma}^{m}} - \lambda_o} = \exp(\ a + b\dot{\gamma}^{m}\ )t$$

At steady state, $\dfrac{d\lambda}{dt} = 0$, $\lambda_{s.s} = \dfrac{a}{a + b\dot{\gamma}^{m}}$

$$\therefore \quad \frac{\lambda_{s.s} - \lambda}{\lambda_{s.s} - \lambda_o} = \exp(a + b\dot{\gamma}^{m})t$$

$$\frac{\lambda - \lambda_{s.s}}{\lambda_o - \lambda_{s.s}} = \exp-(a + b\dot{\gamma}^{m})t \qquad \text{[AP 4.3]}$$

From Equation [AP 4.1]

$$\eta = (\ \eta_\infty + c\lambda\ )$$

$$c\lambda = \eta - \eta_\infty \text{ or } \lambda = (\eta - \eta_\infty) / c$$

For a fully built up structure, $\lambda = 1$, therefore:

$$c = \eta_o - \eta_\infty$$

Hence,

$$\lambda = \frac{\eta - \eta_\infty}{\eta_o - \eta_\infty} \qquad \text{[AP 4.4]}$$

Substitute Equation AP 4.4 into Equation AP 4.3,

$$\frac{\left(\dfrac{\eta - \eta_\infty}{\eta_o - \eta_\infty}\right) - \left(\dfrac{\eta_{s.s} - \eta_\infty}{\eta_o - \eta_\infty}\right)}{\left(\dfrac{\eta_o - \eta_\infty}{\eta_o - \eta_\infty}\right) - \left(\dfrac{\eta_{s.s} - \eta_\infty}{\eta_o - \eta_\infty}\right)} = \exp-(a + b\dot{\gamma}^{m})t$$

$$\frac{\eta - \eta_{s.s}}{\eta_o - \eta_{s.s}} = \exp-(a + b\dot{\gamma}^{m})t$$

For a constant $\dot{\gamma}$, $\eta \propto \sigma$

Therefore, $\dfrac{\eta - \eta_{s.s}}{\eta_o - \eta_{s.s}} = \dfrac{\sigma - \sigma_{s.s}}{\sigma_o - \sigma_{s.s}} = \exp\left(-\,t/\tau\right)$ [AP 4.5]

where the breakdown time, $\tau = \dfrac{1}{a + b\dot{\gamma}^{m}}$ [AP 4.6]

Equation AP 4.5 describes an exponential term and is valid for any stress decay exhibiting an exponential curve (i.e. at $t = \tau$, $\exp(-1) = 1/\exp$).

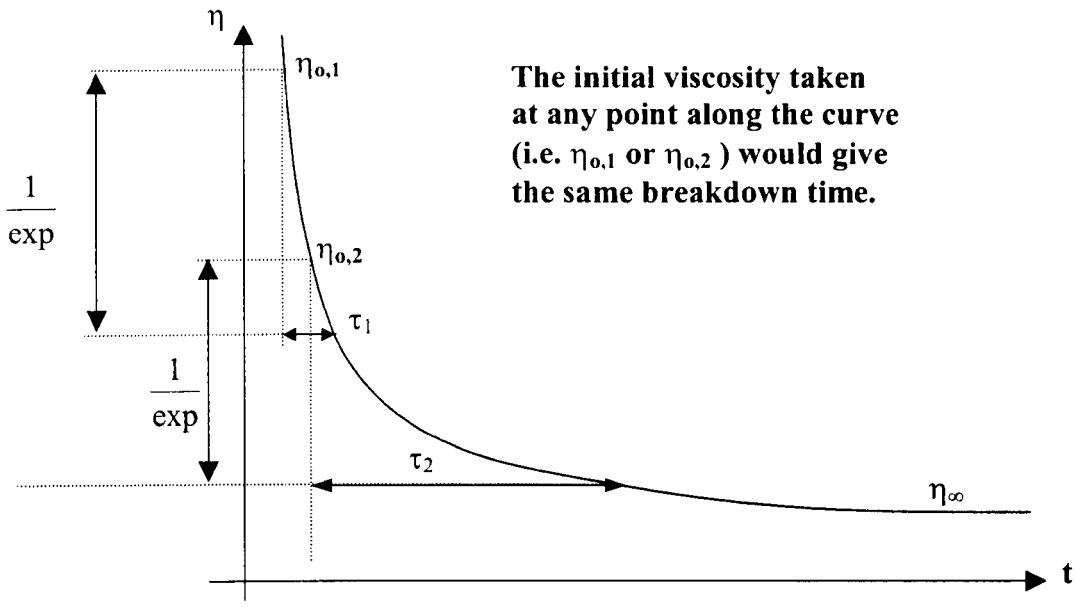

Appendix 5

The following figures in this Appendix show the microstructures of Alusuisse A356 alloys thixoformed under different ram speeds. Starting from the lowest ramp speed (of 250 mm/s), the microstructures are shown from the centre to the edge of the sample and the corresponding microstructures from the same position but examined from the top to the bottom. An example of how the microstructures are examined is given on Page 6-66

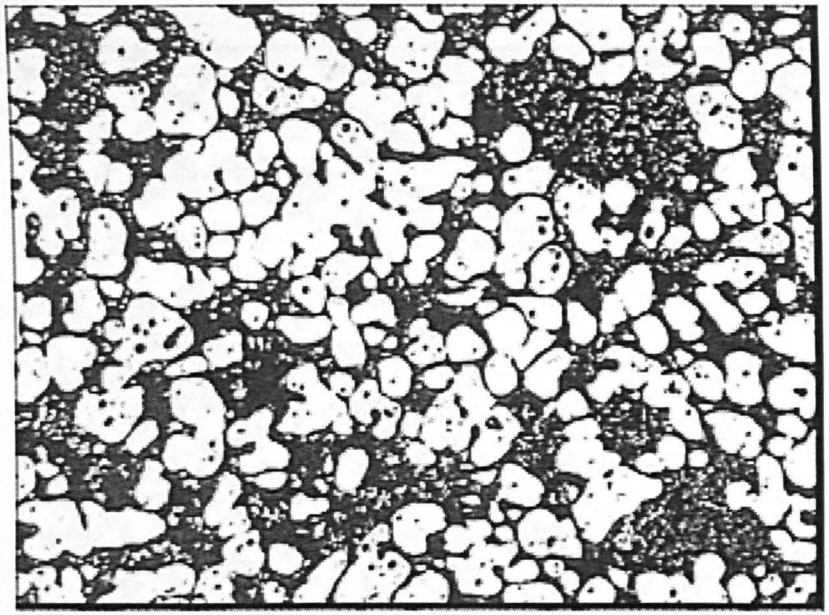

Top_Edge

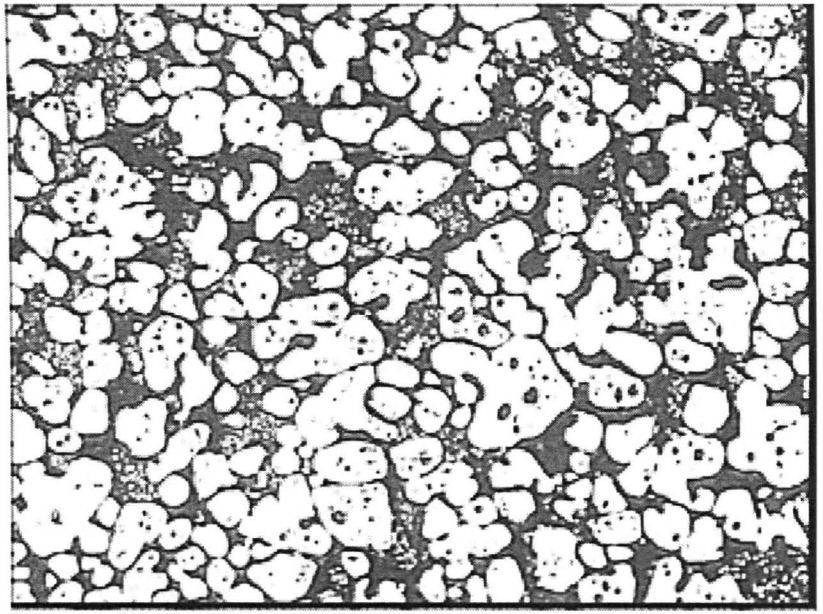

Middle_Edge

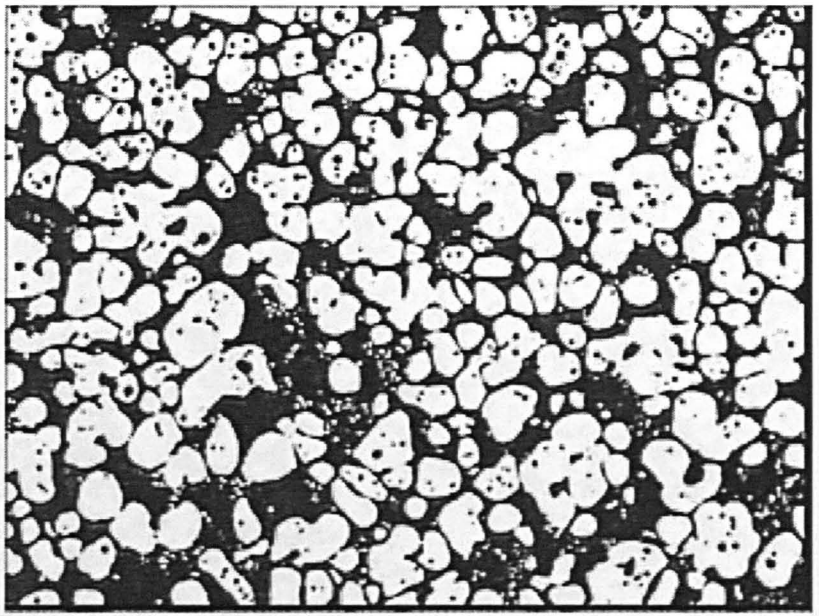

Bottom_Edge

Alusuisse A356

Temperature: 577 °C

Ram Speed: 250 mm/s

Soak Time: 0 mins

AP 5-1

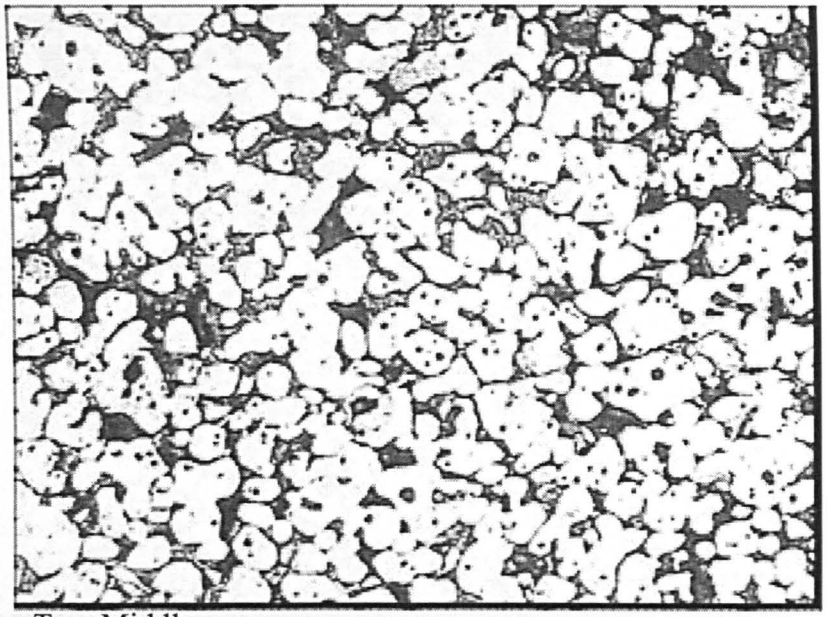

Top_Middle

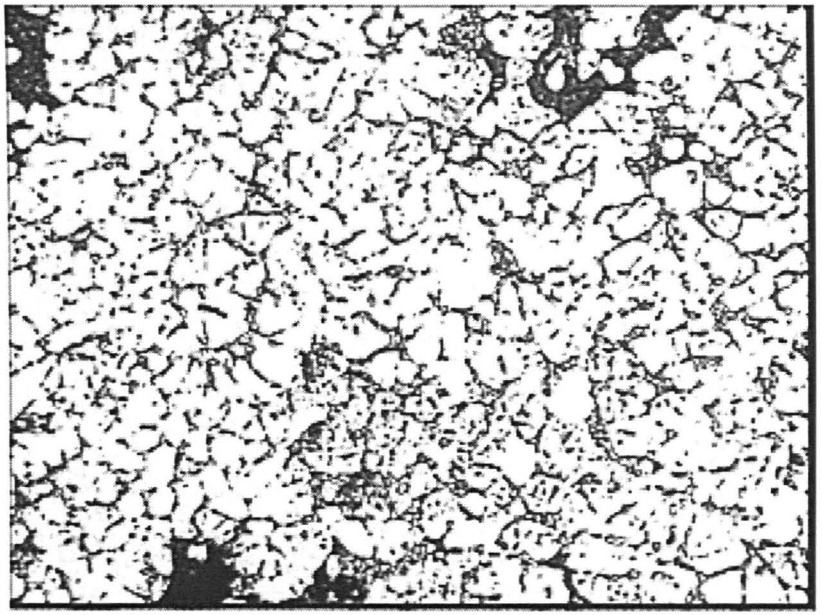

Middle_Middle

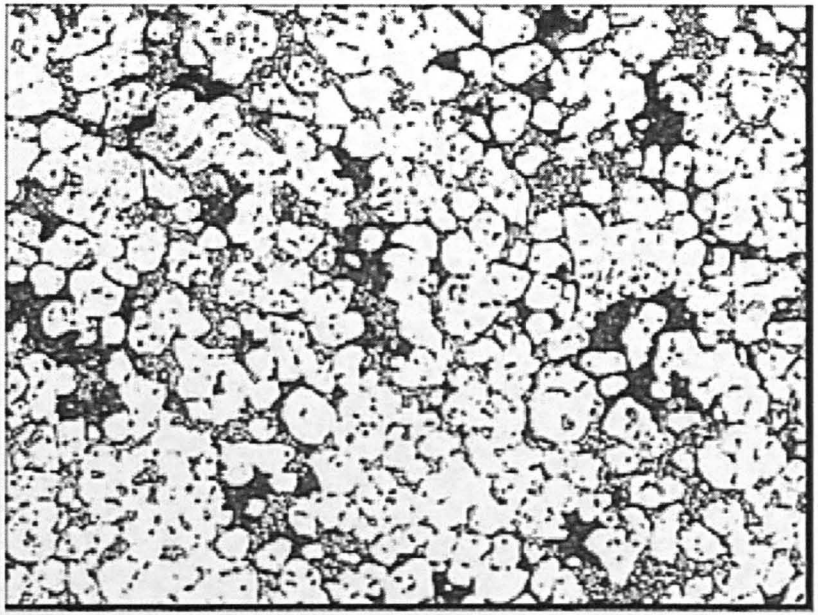

Bottom_Middle

Alusuisse A356

Temperature: 577 °C

Ram Speed: 250 mm/s

Soak Time: 0 mins

AP 5-2

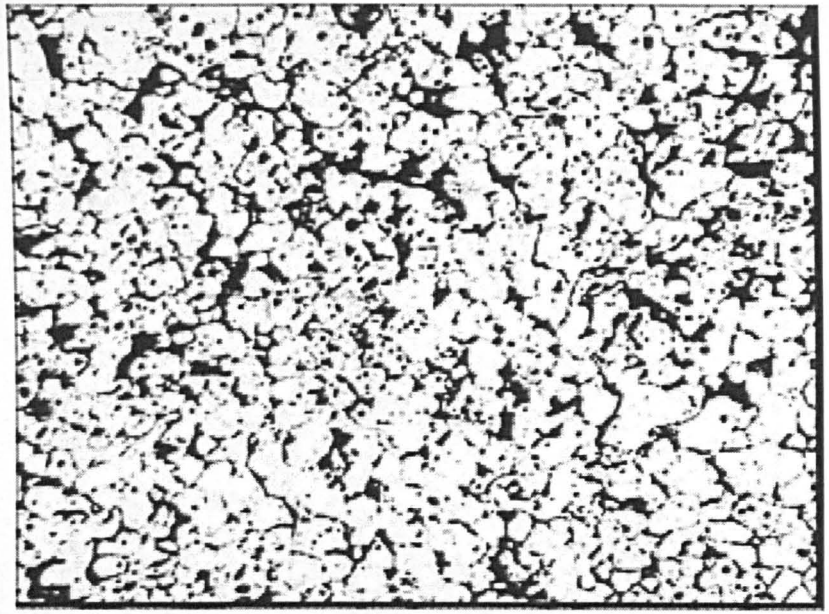

Top_Centre

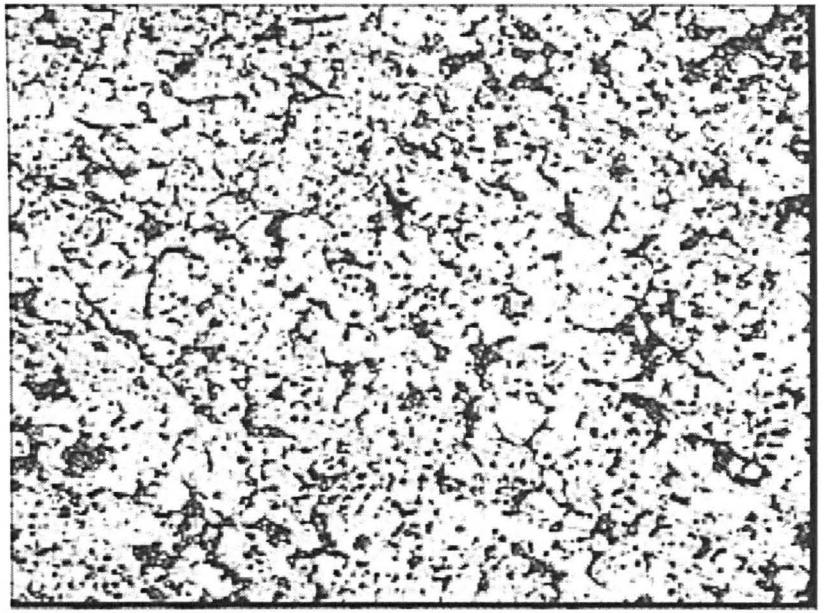

Middle_Centre

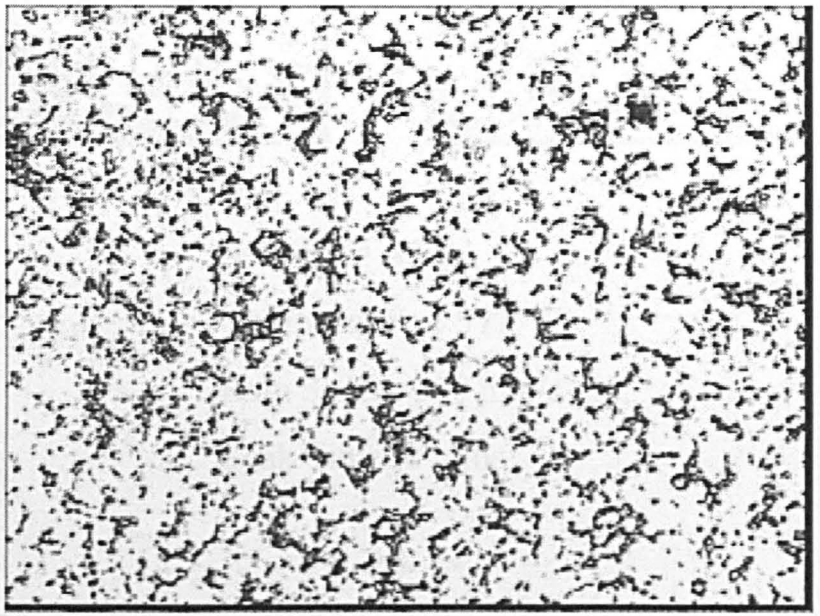

Bottom_Centre

Alusuisse A356

Temperature: 577 °C

Ram Speed: 250 mm/s

Soak Time: 0 mins

AP 5-3

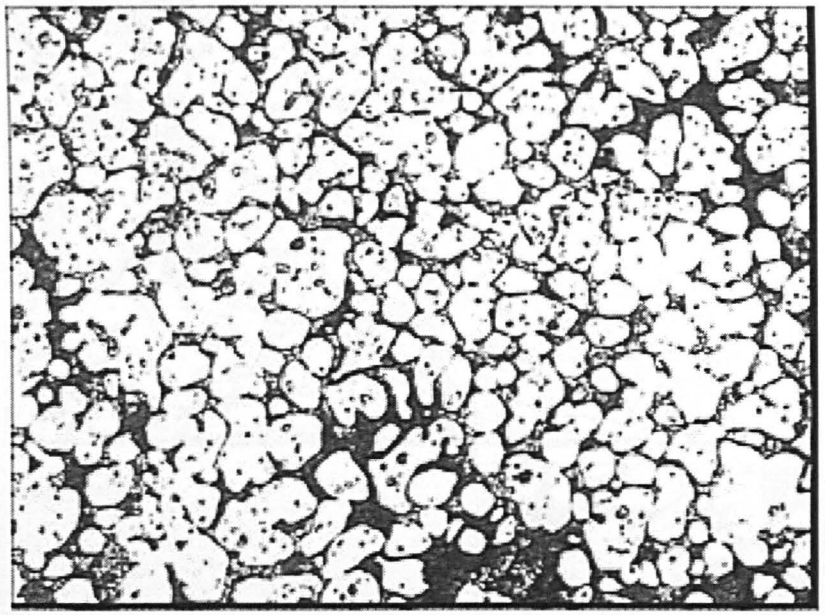

Centre_Edge

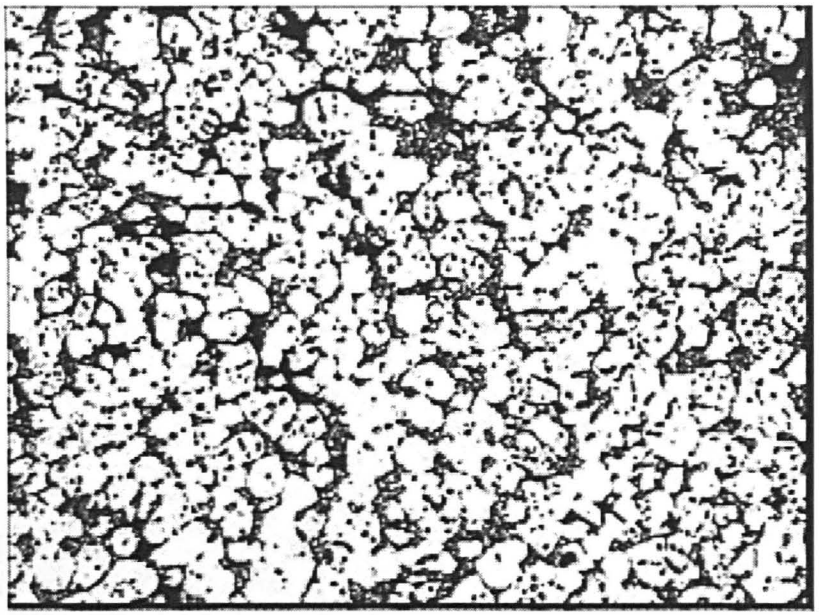

Centre_Centre

Alusuisse A356

Temperature: 577 °C

Ram Speed: 250 mm/s

Soak Time: 0 mins

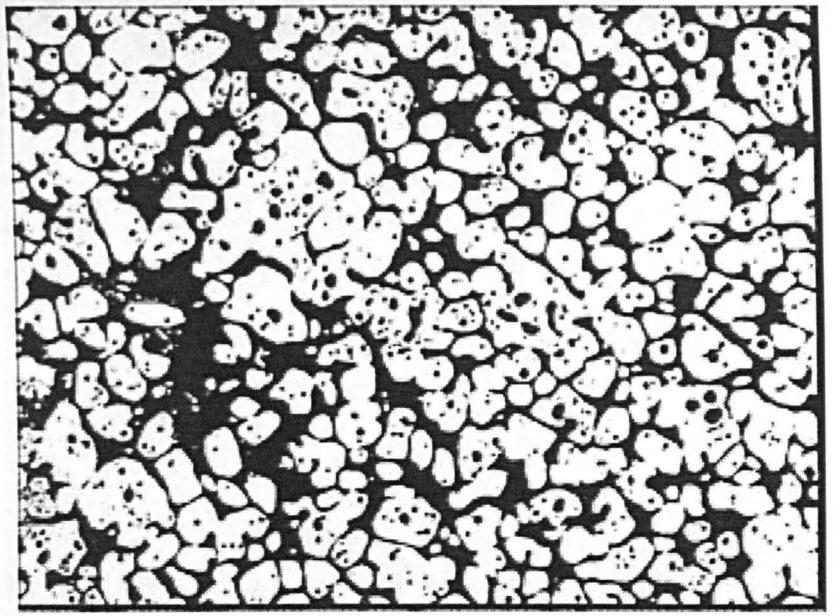

Top_Edge

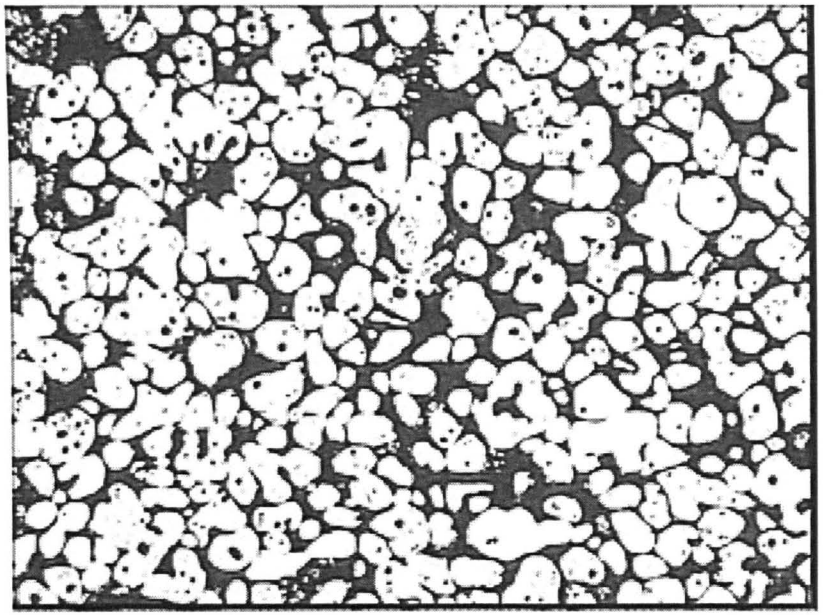

Middle_Edge

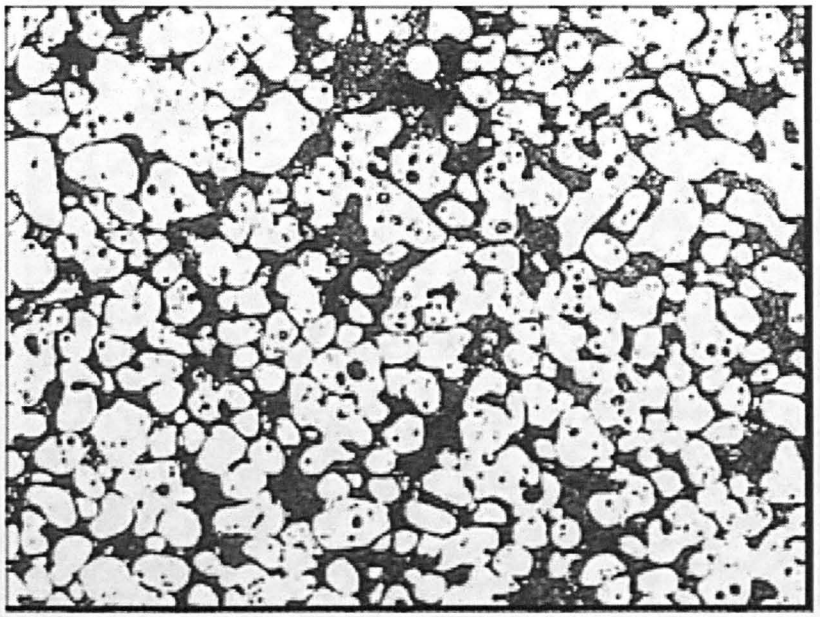

Bottom_Edge

Alusuisse A356

Temperature: 577 °C

Ram Speed: 350 mm/s

Soak Time: 0 mins

AP 5-5

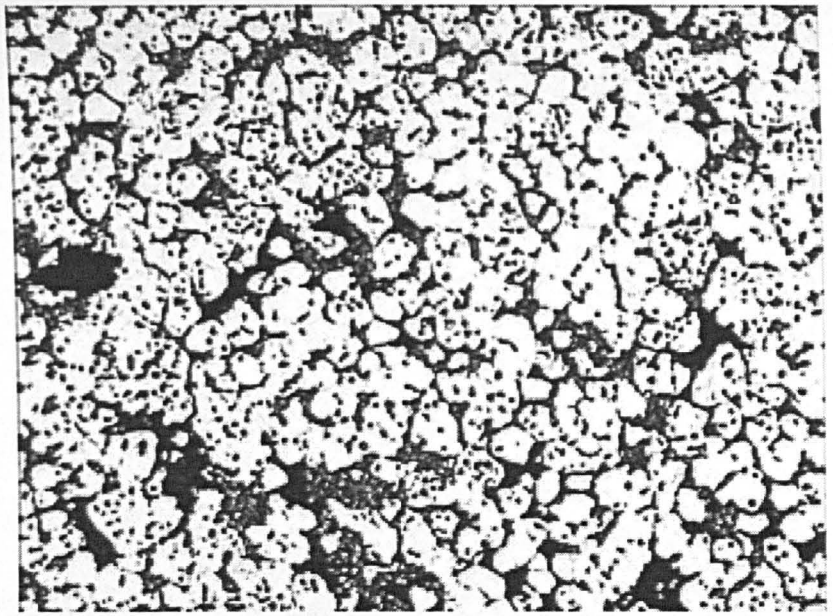

Top_Middle

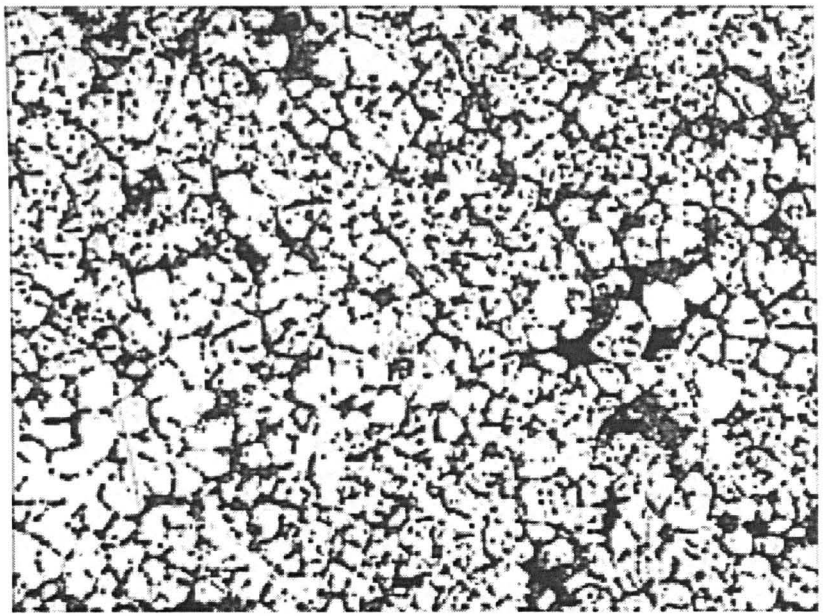

Middle_Middle

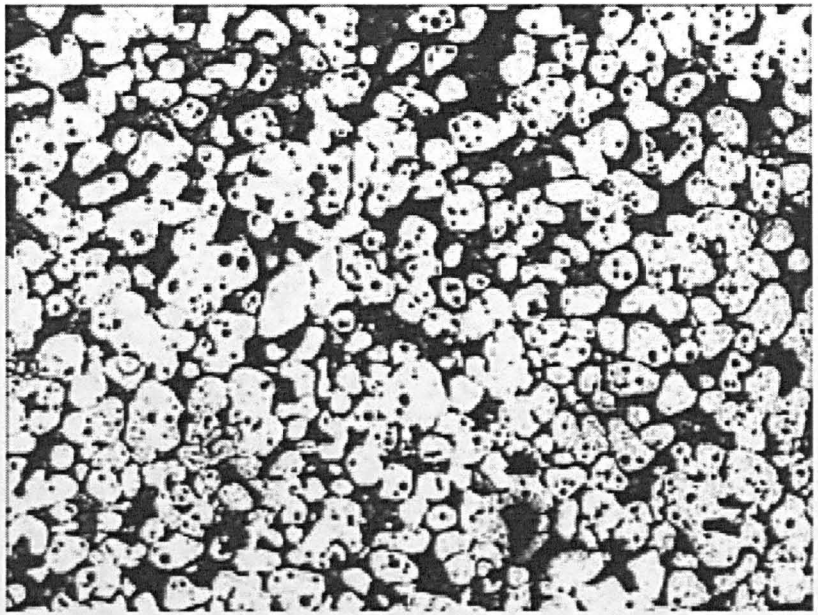

Bottom_Middle

Alusuisse A356

Temperature: 577 °C

Ram Speed: 350 mm/s

Soak Time: 0 mins

AP 5-6

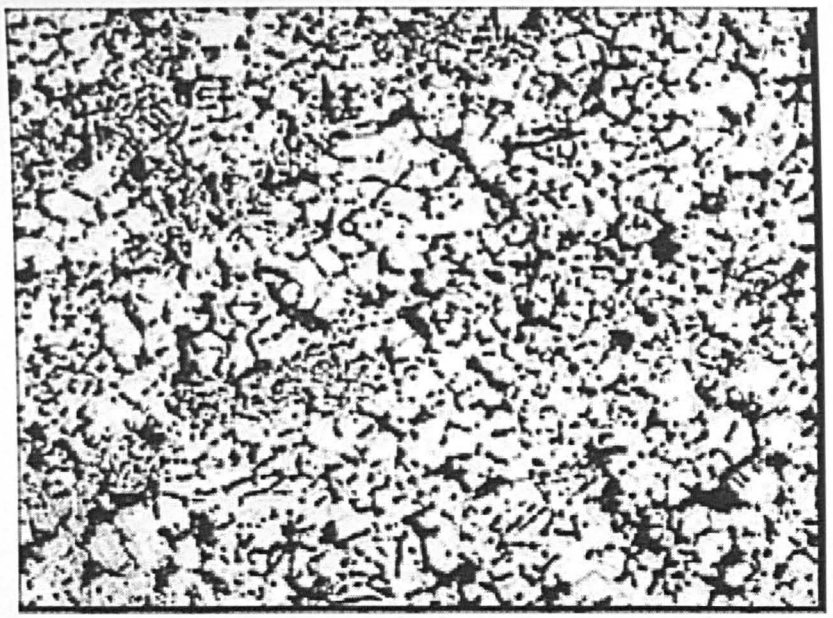

Top_Centre

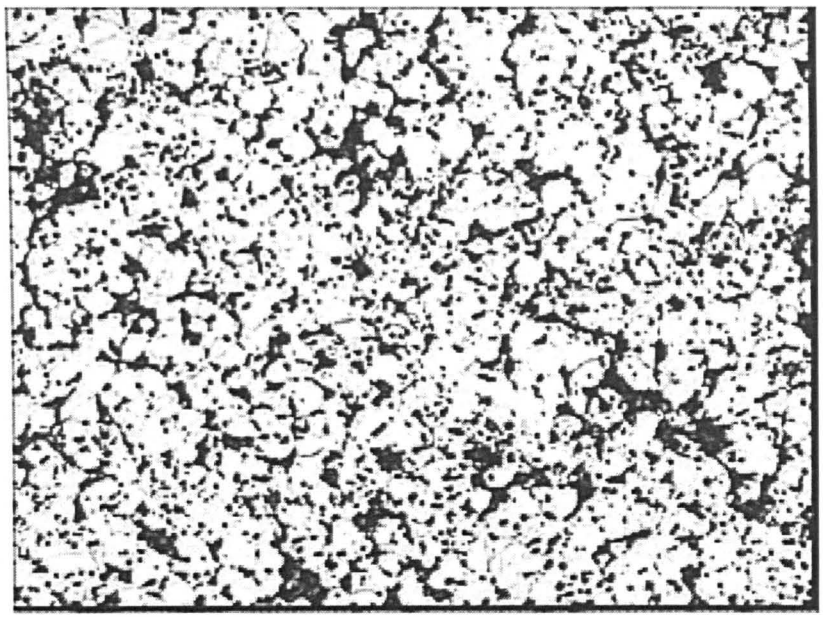

Middle_Centre

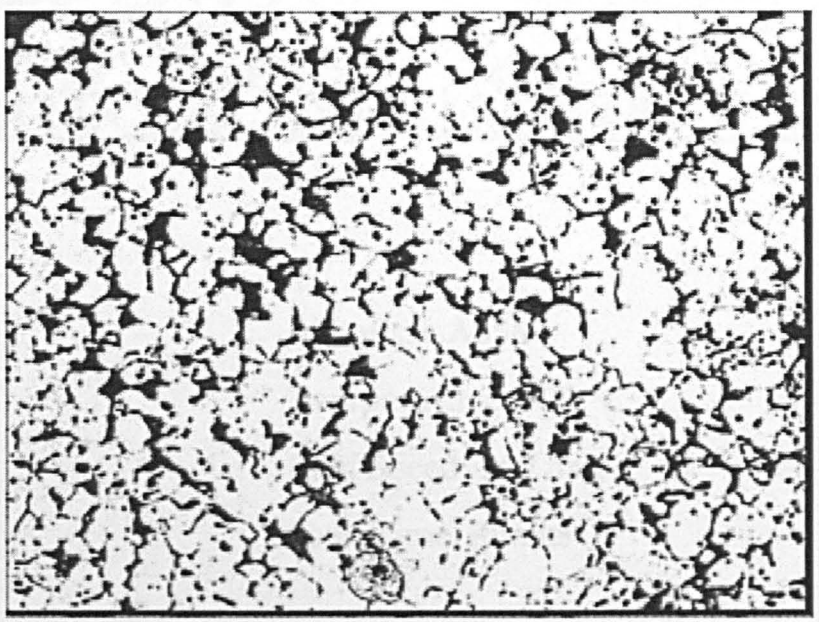

Bottom_Centre

Alusuisse A356

Temperature: 577 °C

Ram Speed: 350 mm/s

Soak Time: 0 mins

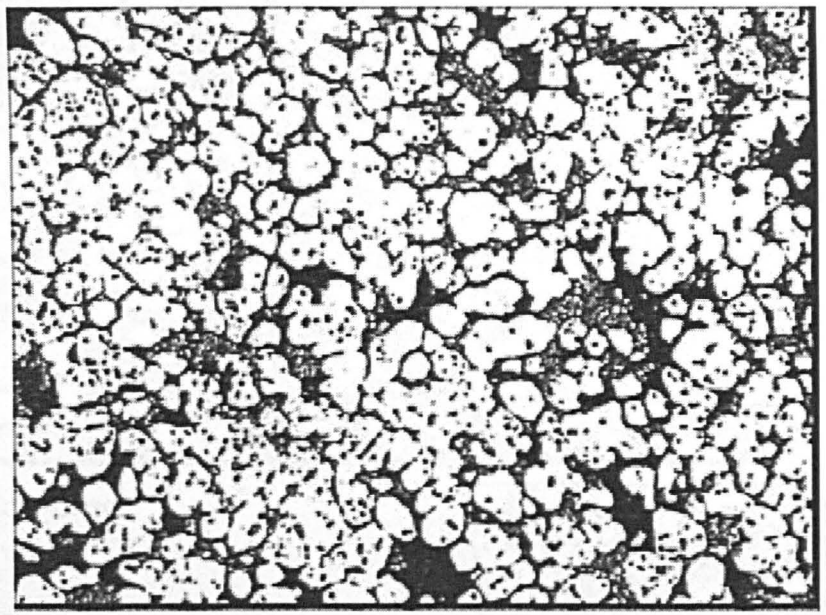

Centre_Edge

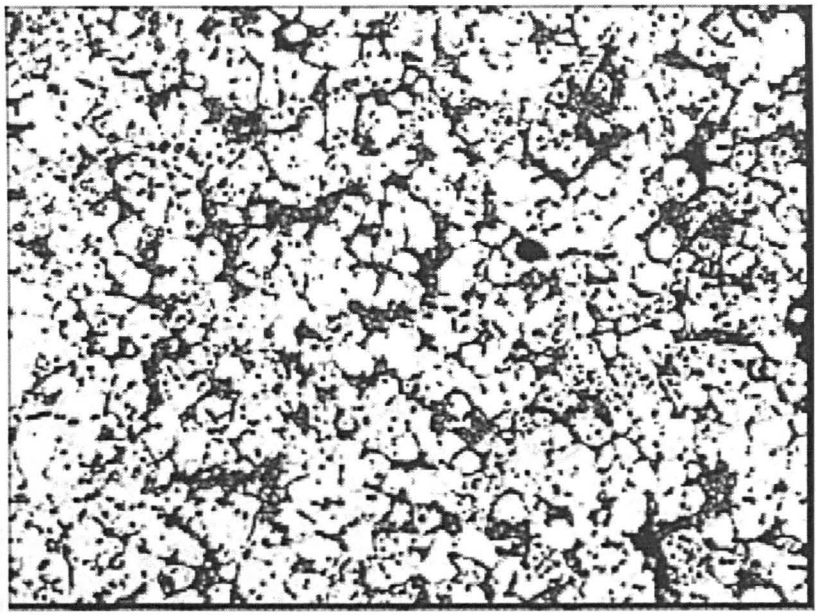

Centre_Centre

Alusuisse A356

Temperature: 577 °C

Ram Speed: 350 mm/s

Soak Time: 0 mins

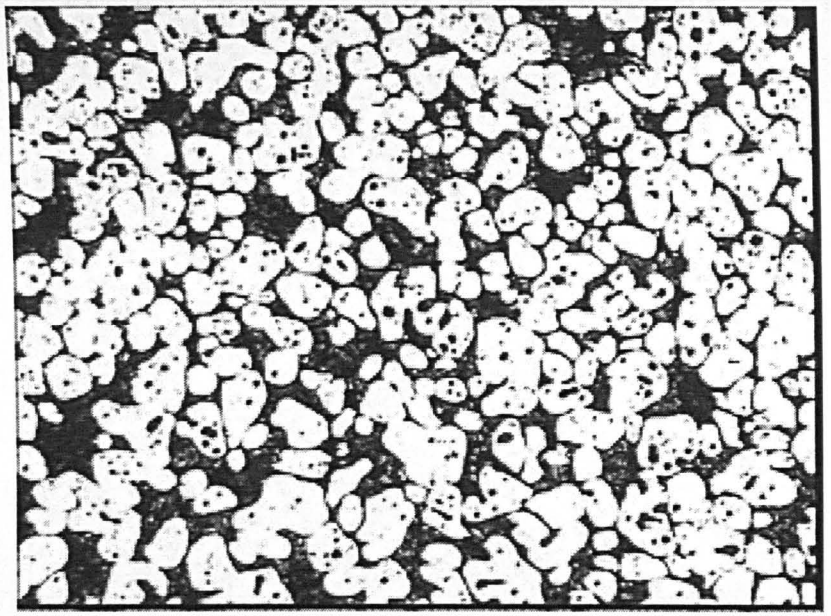

Top_Edge

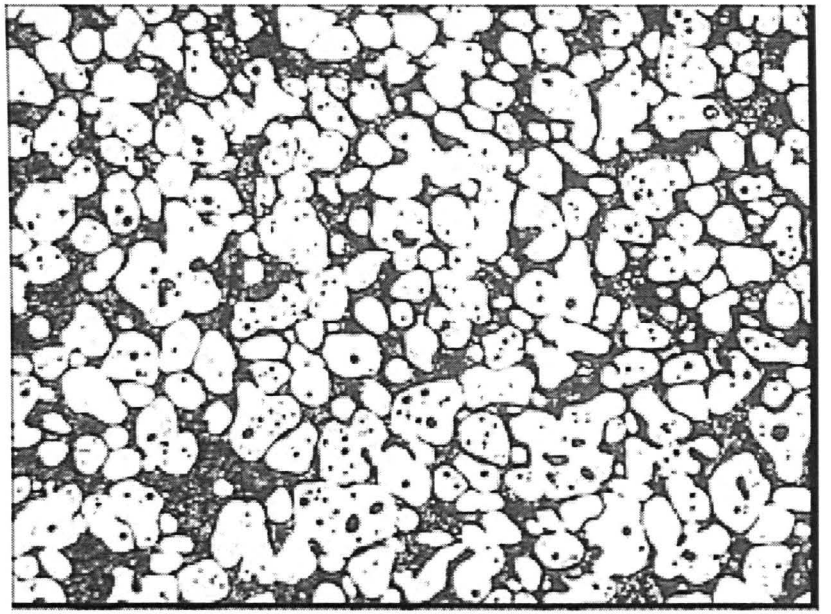

Middle_Edge

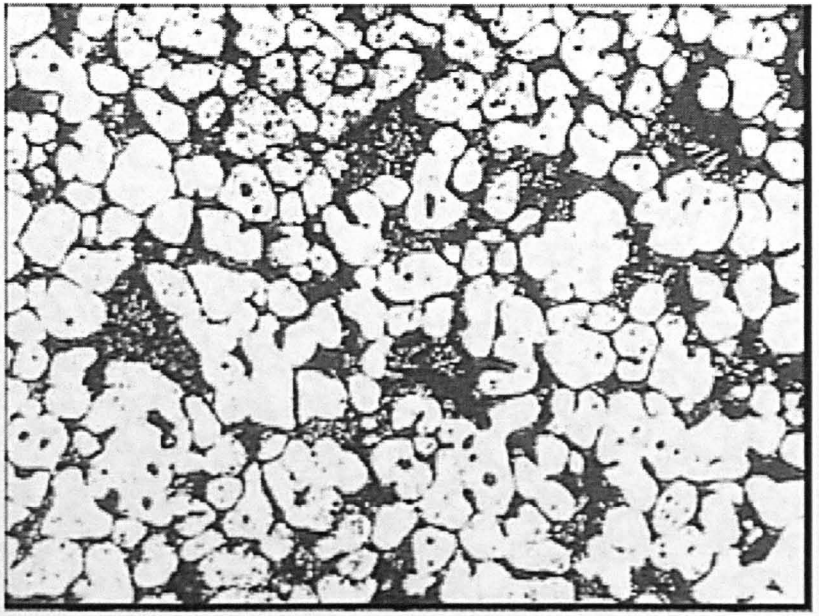

Bottom_Edge

Alusuisse A356

Temperature: 577 °C

Ram Speed: 500 mm/s

Soak Time: 0 mins

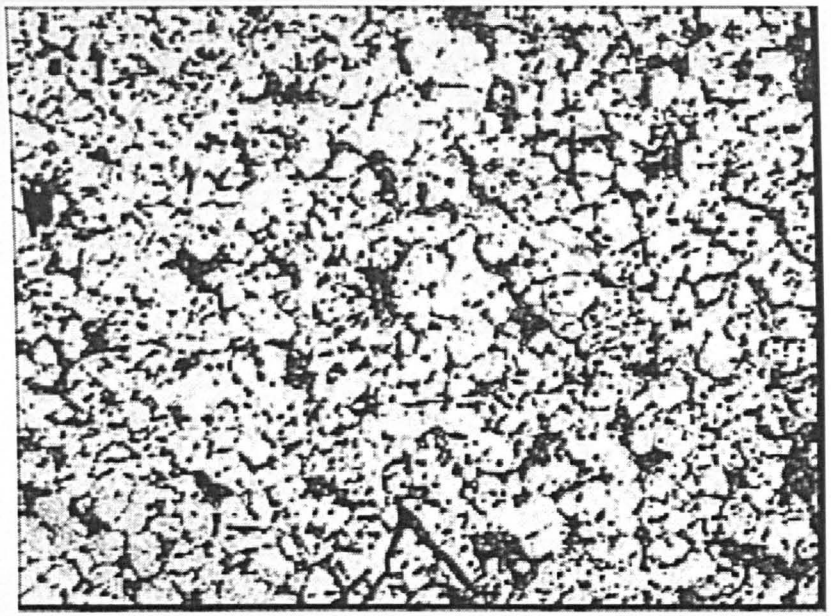

Top_Middle

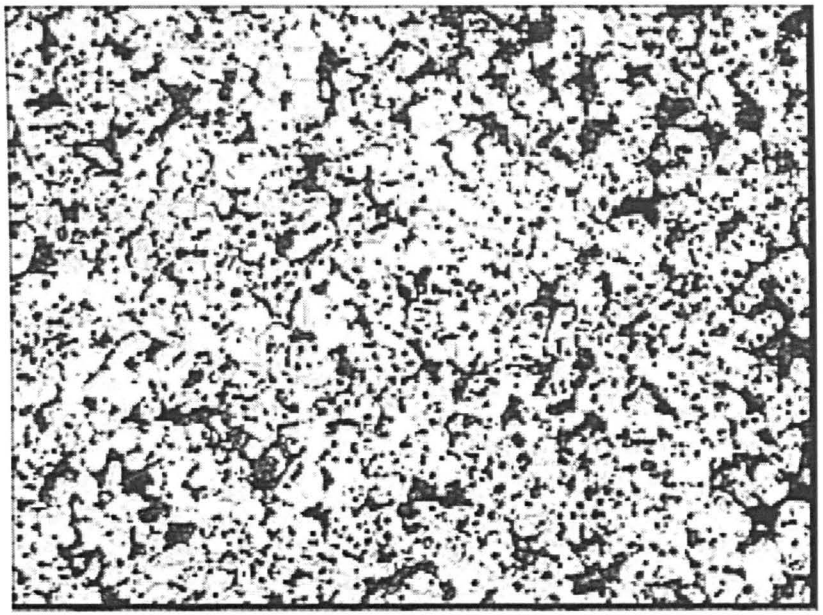

Middle_Middle

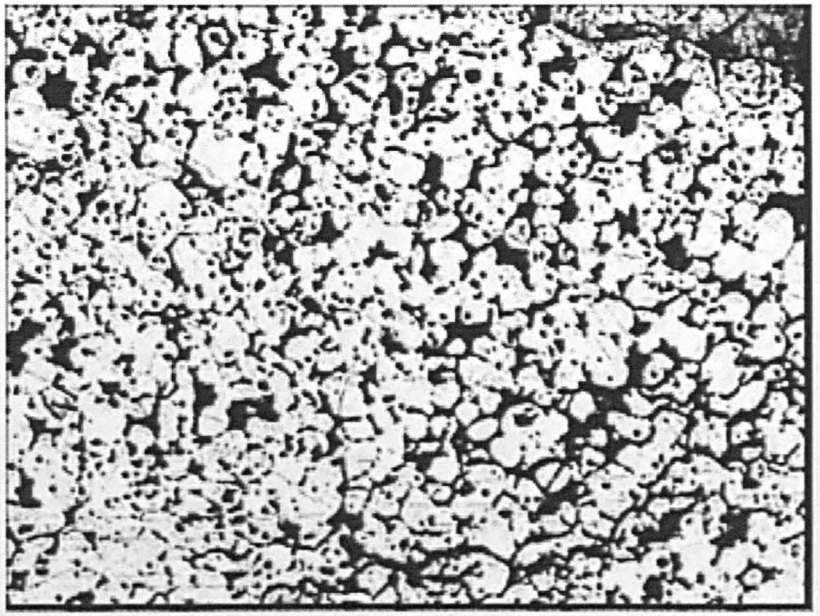

Bottom_Middle

Alusuisse A356

Temperature: 577 °C

Ram Speed: 500 mm/s

Soak Time: 0 mins

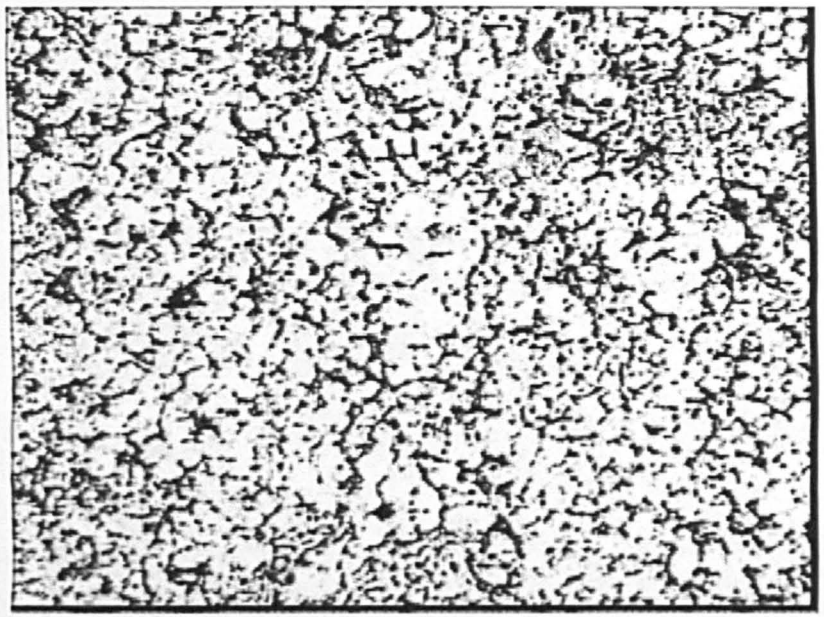

Top_Centre

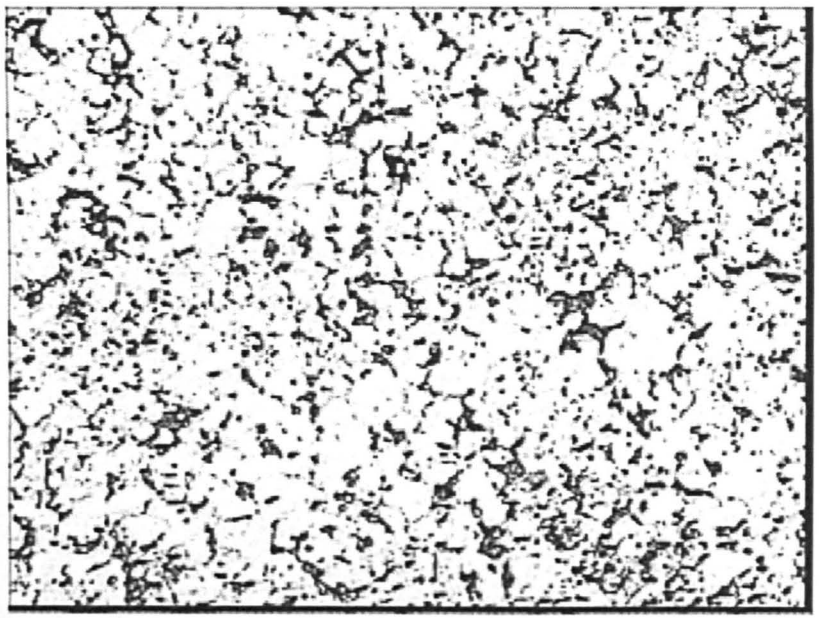

Middle_Centre

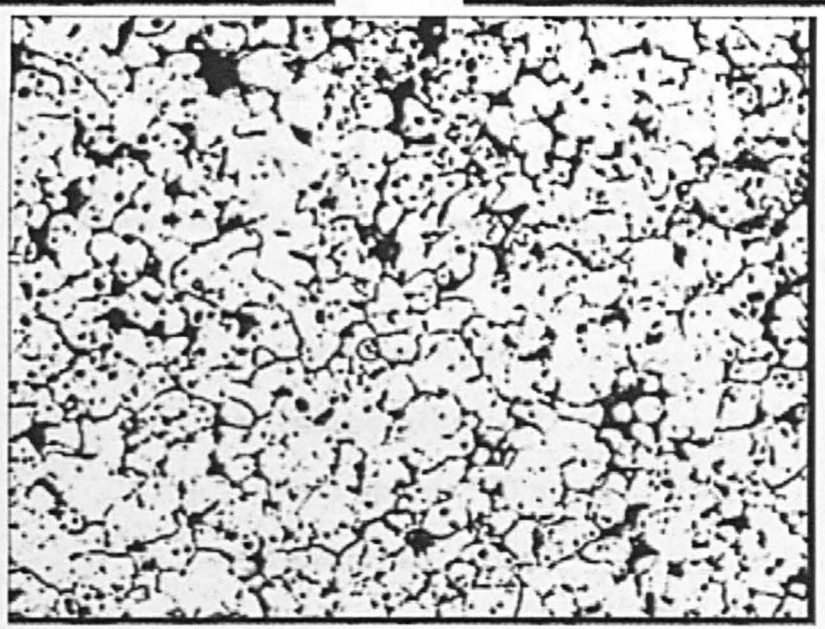

Bottom_Centre

Alusuisse A356

Temperature: 577 °C

Ram Speed: 500 mm/s

Soak Time: 0 mins

AP 5-11

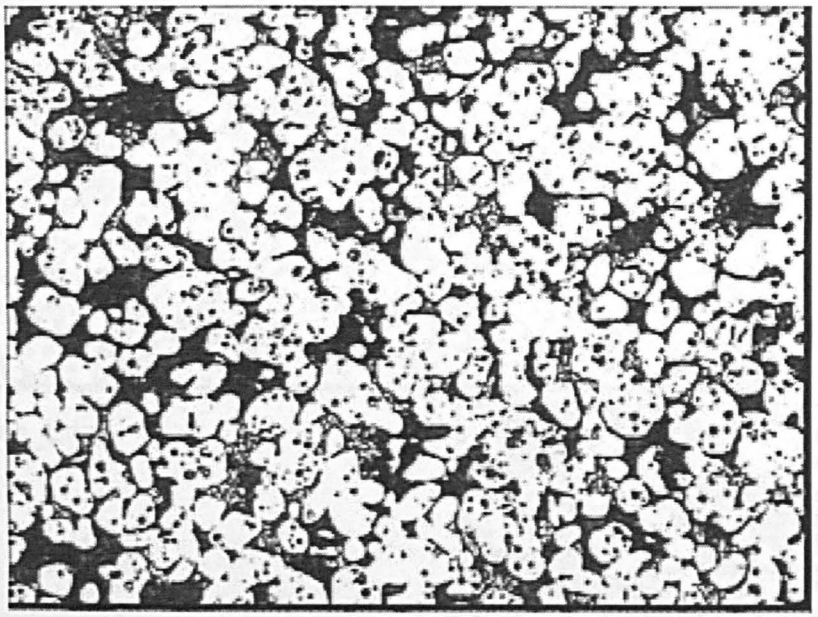

Centre_Edge

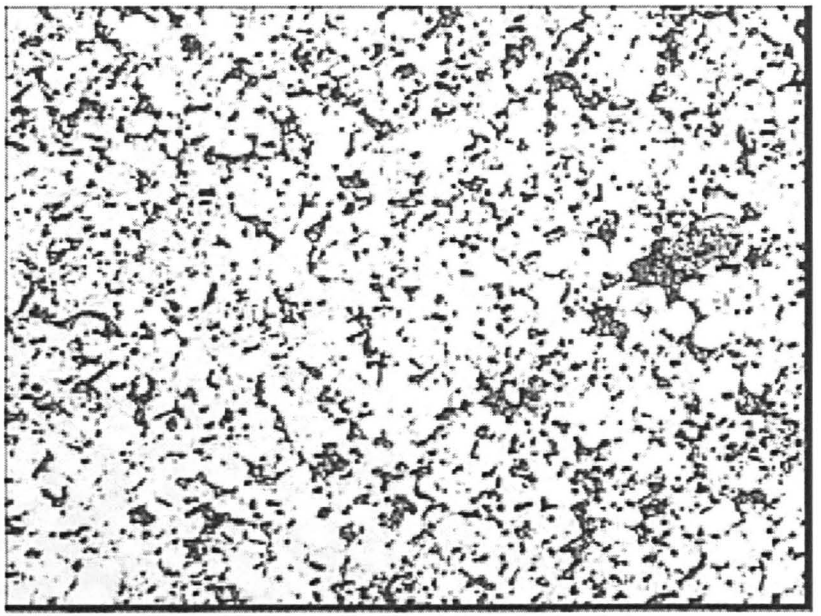

Centre_Centre

Alusuisse A356

Temperature: 577 °C

Ram Speed: 500 mm/s

Soak Time: 0 mins

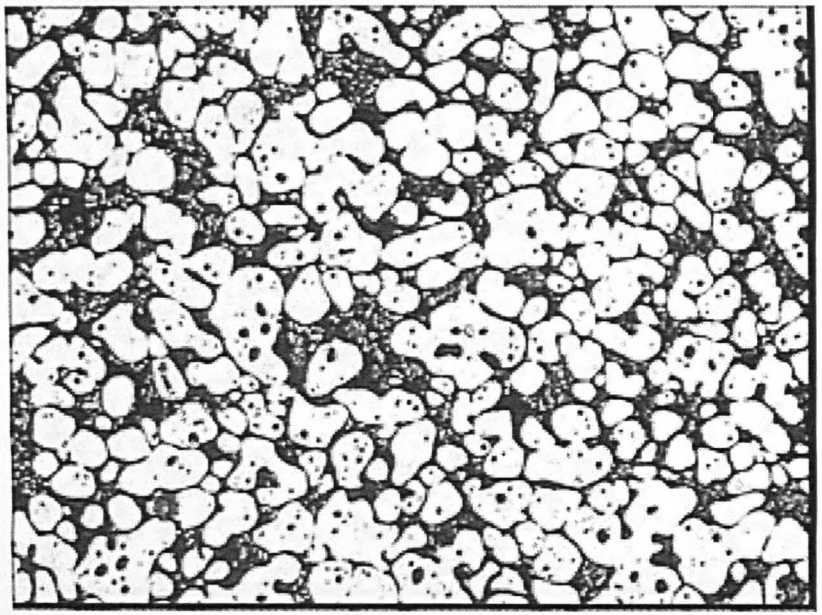

Top_Edge

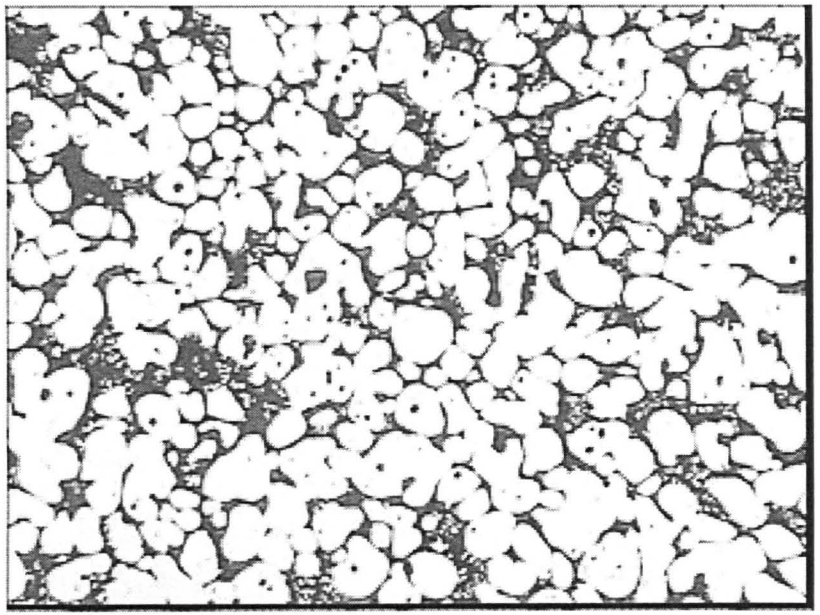

Middle_Edge

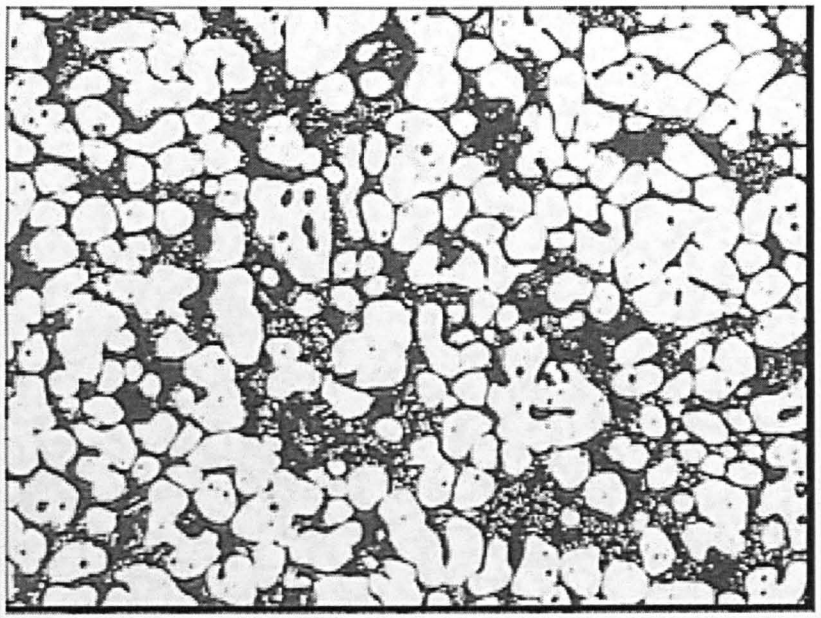

Bottom_Edge

Alusuisse A356

Temperature: 577 °C

Ram Speed: 1000 mm/s

Soak Time: 0 mins

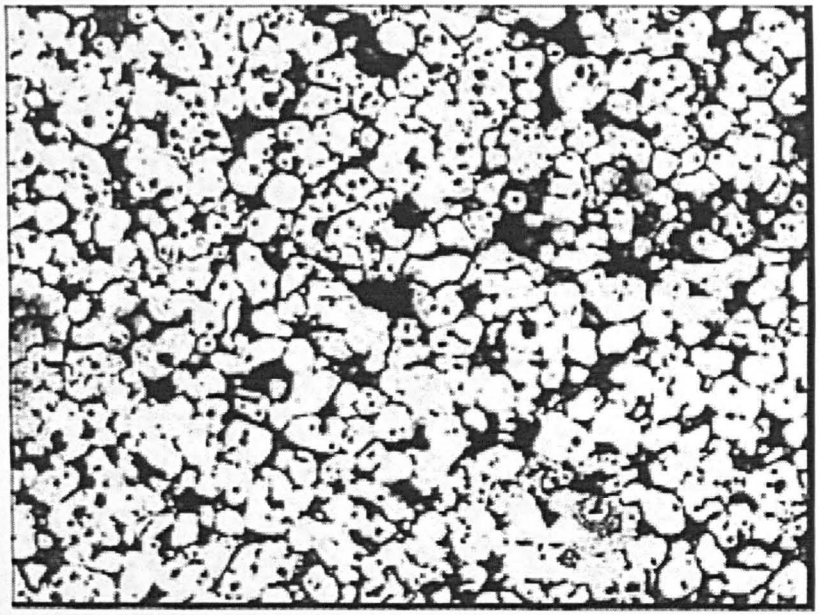

Top_Middle

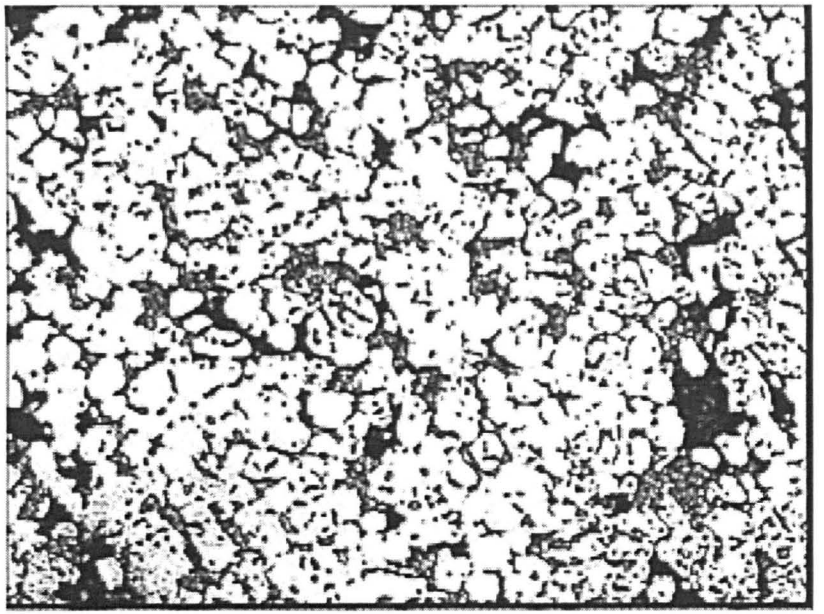

Middle_Middle

Bottom_Middle

Alusuisse A356

Temperature: 577 °C

Ram Speed: 1000 mm/s

Soak Time: 0 mins

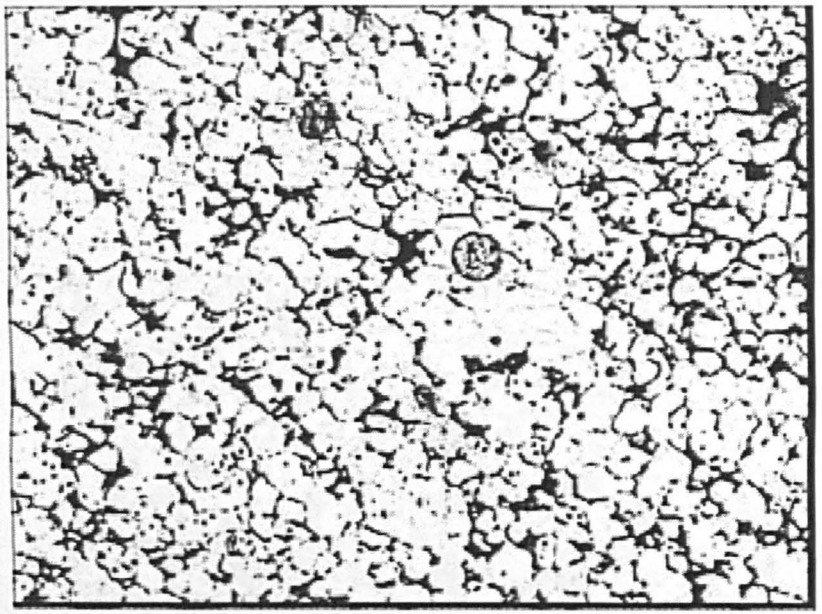

Top_Centre

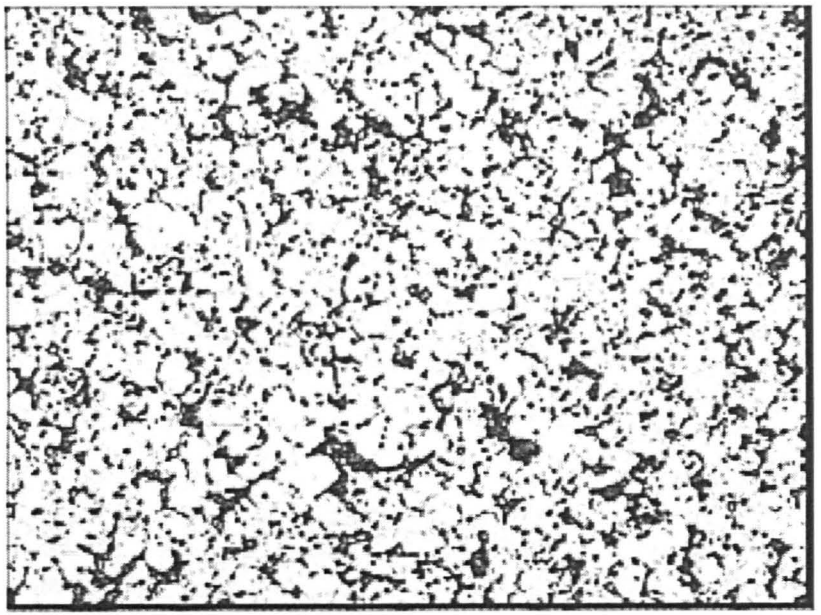

Middle_Centre

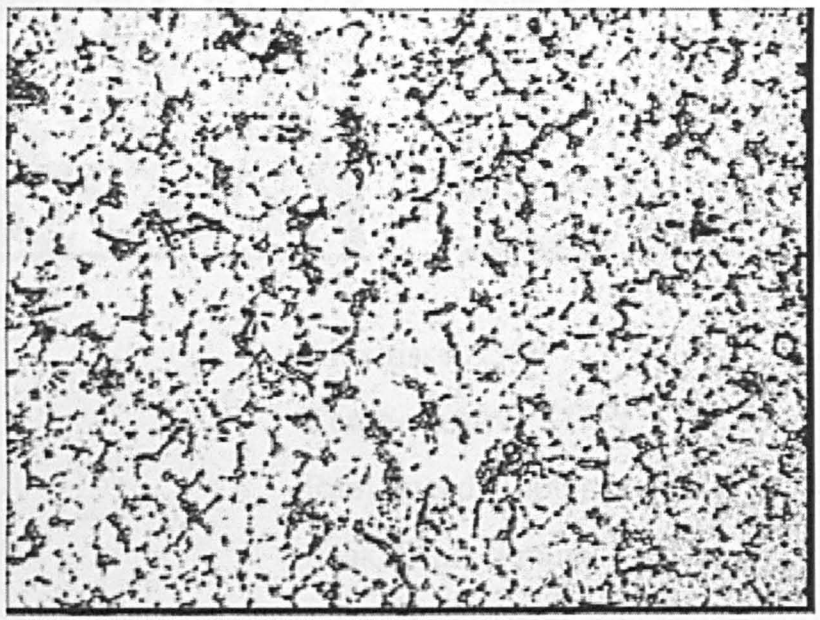

Bottom_Centre

Alusuisse A356

Temperature: 577 °C

Ram Speed: 1000 mm/s

Soak Time: 0 mins

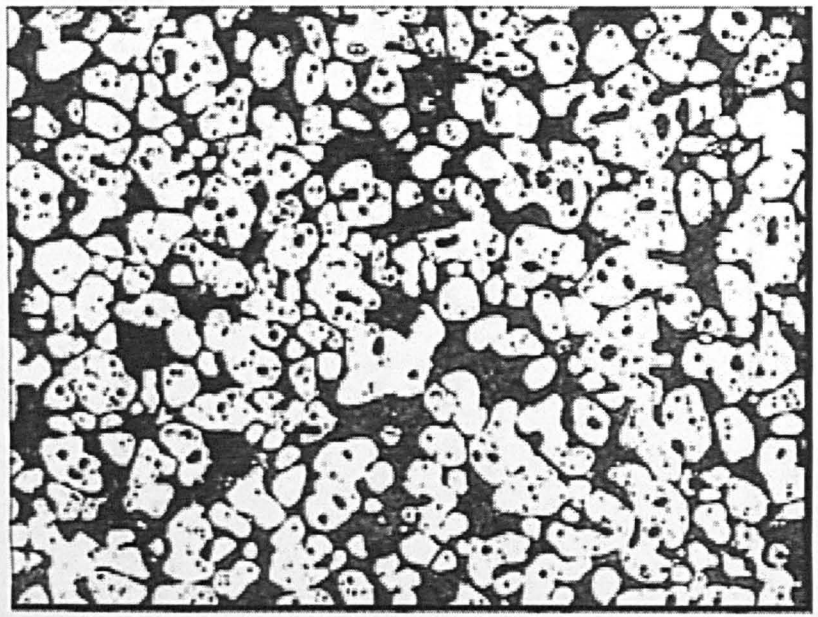

Centre_Edge

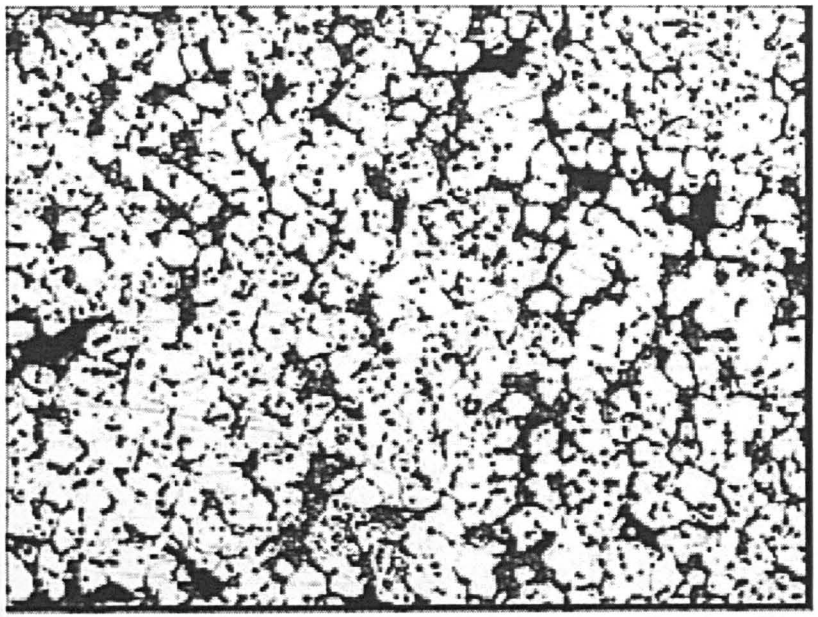

Centre_Centre

Alusuisse A356

Temperature: 577 °C

Ram Speed: 1000 mm/s

Soak Time: 0 mins

Appendix 6

For parallel plate compression (Figure AP 6.1), assuming that the semisolid slug behaves like a Newtonian fluid during compression, the shear rates do not vary greatly (see Figure 5.3b) and that the volume is constant throughout the compression, at time, $t \leq 0$, the slug has a radius R_o and height h_o. When a constant force, F is applied to the plate, h changes with time (Figure AP 6.2).

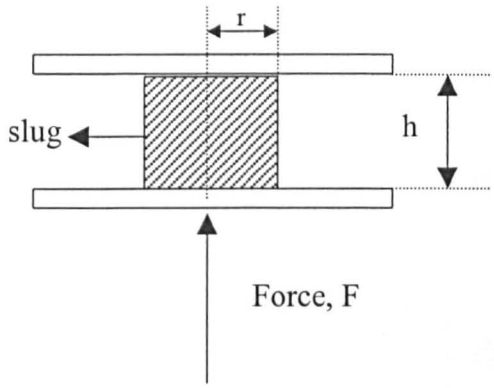

Figure AP 6.1

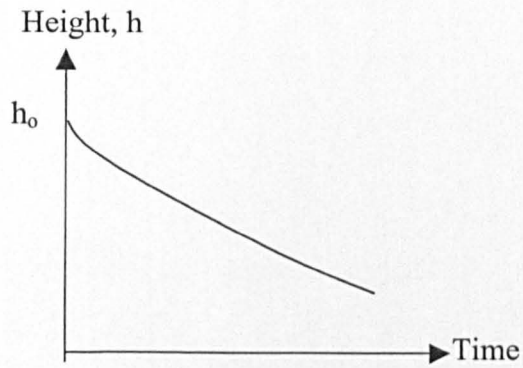

Figure AP 6.2

Using the Stefan* derivation for plate separation equation for a Newtonian fluid, Laxmanan and Flemings calculated the viscosity of the slug under compression from:

$$F = -\frac{3\eta v^2}{2\pi h^5}\left(\frac{dh}{dt}\right) \qquad \text{[AP 6.1]}$$

where η is the viscosity
v is the volume of the slug
h is the instantaneous height of the sample
dh/dt is the change in height with time, t.

For a Newtonian fluid, the shear rate at any instant during compression is given by:

$$\dot{\gamma} = -\frac{6rz}{h^3}\left(\frac{dh}{dt}\right) \qquad \text{[AP 6.2]}$$

where r is the radial distance from the centre of the slug
z is the vertical distance from the centreline of the slug height (i.e. h/2)

* The derivation of Stefan's equation will be shown later.

Integrating throughout the volume, the average shear rate can be obtained:

$$\dot{\gamma}_{avg} = \frac{2\pi}{v}\int_0^R \int_0^{h/2} \dot{\gamma} r dr dz \qquad \text{[AP 6.3]}$$

where R is the radius of the specimen at time, t.

Combining Equation AP 6.2 and AP 6.3 and integrating for a unit volume in an element gives:

$$\dot{\gamma}_{avg} = \frac{2\pi}{v}\int_0^R \int_0^{h/2} -\frac{6rz}{h^3} r dr \frac{dh}{dt} dz$$

Integrating by parts gives:

$$\dot{\gamma}_{avg} = \frac{2\pi}{v}\int_0^R \left[\frac{-6rz^2}{2h^3}\frac{dh}{dt} r.dr\right]_0^{h/2}$$

$$\dot{\gamma}_{avg} = \left[-\frac{2\pi}{v}\int_0^R \left(\frac{6rh^2}{4.2.h^3}\right) r.dr \frac{dh}{dt}\right]$$

$$\dot{\gamma}_{avg} = \left[-\frac{2\pi}{v}\left(\frac{6h^2}{8h^3}\right)\int_0^R r^2.dr \frac{dh}{dt}\right]$$

$$\dot{\gamma}_{avg} = -\frac{3\pi}{2vh}\frac{dh}{dt}\left[\frac{r^3}{3}\right]_0^R$$

$$\dot{\gamma}_{avg} = -\frac{\pi R^3}{2vh}\frac{dh}{dt}$$

Since $\pi r^2 h$ = volume, v,

$$\dot{\gamma}_{avg} = -\frac{\pi R^3}{2\pi R^2 h^2}\frac{dh}{dt}$$

$$\dot{\gamma}_{avg} = -\frac{R}{2h^2}\frac{dh}{dt} \qquad \text{[AP 6.4]}$$

Using Equations AP 6.1 and AP 6.4, a plot of viscosity against shear rates can be used to analyse the results on the rapid compression experiments.

Stefan Equation

Dienes and Klemm [Die 46] derived the original Stefan's equation for Newtonian fluid between two parallel planes:

The general equation of motion of a Newtonian fluid of viscosity, η, is given by the vector equation of:

$$\rho\frac{\partial \boldsymbol{v}}{\partial t}+\rho \boldsymbol{v}.\nabla \boldsymbol{v}=-\nabla \boldsymbol{P}+\eta\nabla^2\boldsymbol{v}+\frac{1}{3}\eta\nabla\nabla.\boldsymbol{v} \qquad \text{[AP 6.5]}$$

where ρ = density of fluid, v = velocity vector, and P = fluid pressure. Assuming incompressible fluid, ∇.v = 0 and that the velocity of the fluid elements is small. Therefore:

$$\rho\frac{\partial \boldsymbol{v}}{\partial t}=-\nabla \boldsymbol{P}+\eta\nabla^2\boldsymbol{v} \qquad \text{[AP 6.6]}$$

For a cylindrical geometry (Figure AP 6.3), Equation AP 6.6 can be written in scalar form as:

$$\begin{aligned}
&-\rho\frac{\partial \boldsymbol{P}}{\partial r}+\eta\nabla^2\boldsymbol{v}_r=\rho\frac{\partial \boldsymbol{v}_r}{\partial t}\\
&-\frac{1}{r}\frac{\partial \boldsymbol{P}}{\partial \theta}+\eta\nabla^2\boldsymbol{v}_\theta=\rho\frac{\partial \boldsymbol{v}_\theta}{\partial t} \qquad \text{[AP 6.7]}\\
&-\frac{\partial \boldsymbol{P}}{\partial z}+\eta\nabla^2\boldsymbol{v}_z=\rho\frac{\partial \boldsymbol{v}_z}{\partial t}
\end{aligned}$$

The boundary conditions for parallel planes are: z =0 and z = h. Since the assumption is for cylindrical geometry, v_θ is zero and v_z, the velocity normal to the plane is neglected in a 2-D flow field. Therefore, we only consider the radial velocity, v_r.

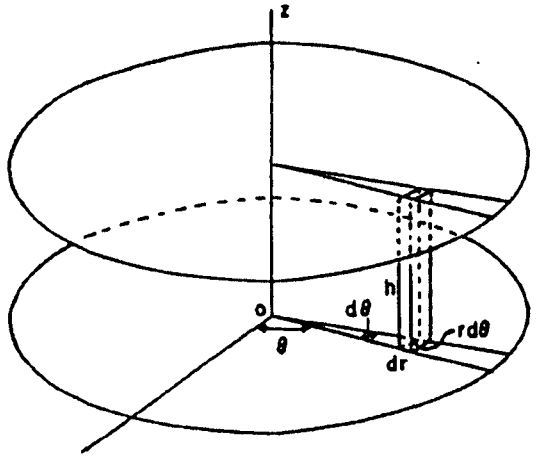

Figure AP 6.3: Schematic diagram of a parallel plate system illustrating the cylindrical co-ordinates system

Assuming no slippages at the planes,

$v_r = 0$ at $z = 0$ and at $z = h$

Simplifying Equation AP 6.7 using the above assumptions gives:

$$\frac{\partial P}{\partial r} = \eta \frac{\partial^2 v_r}{\partial z^2} \qquad \text{[AP 6.8]}$$

Integrating Equation AP 6.8 twice and inserting the boundary conditions at no slippage between the planes and that P is a function of r only:

$$\int \frac{1}{\eta}\frac{\partial P}{\partial r} = \int \frac{\partial^2 v_r}{\partial z^2}$$

$$\frac{\partial v_r}{\partial z} = \left(\frac{1}{\eta}\frac{\partial P}{\partial r}\right)(z) + C_1$$

For a parabolic equation, the gradient (i.e. $\partial v_r/\partial z$) is equal to zero at the centre (i.e. at z =h/2). Therefore:

$$C_1 = -\frac{1}{\eta}\frac{\partial P}{\partial r}\left(\frac{h}{2}\right)$$

Hence:

$$\frac{\partial v_r}{\partial z} = \left(\frac{1}{\eta}\frac{\partial P}{\partial r}\right)\left(z - \frac{h}{2}\right)$$

$$\int \frac{\partial v_r}{\partial z} = v_r = \frac{1}{\eta}\frac{\partial P}{\partial r}\int_0^h \left(z - \frac{h}{2}\right)$$

$$v_r = \frac{1}{\eta}\frac{\partial P}{\partial r}\left[\frac{z^2}{2} - \frac{hz}{2}\right]_0^h + C_2$$

Applying the boundary conditions for $v_r = 0$ at $z = 0$ and $z = h$,

$C_2 = 0$

$$v_r = \frac{1}{\eta}\frac{\partial P}{\partial r}\left[\frac{z^2}{2} - \frac{hz}{2}\right]$$

$$v_r = \frac{1}{2\eta}\frac{\partial P}{\partial r}(z - h)z \qquad \text{[AP 6.9]}$$

Considering a cylindrical element in Figure AP 6.3 contained between radii r and r + dr and between two radial planes parallel to z at an angle dθ apart, The flow

through a surface element $rd\theta dz$ is $rd\theta v_r dz$. The flow per unit arc length, U, between the planes at z = 0 and at z = h (in the direction of increasing r) is given as:

$$U = \int_0^h v_r \, dz$$

and substituting Equation AP 6.9 into the above equation gives:

$$U = \frac{1}{2\eta}\frac{\partial P}{\partial r}\int_0^h \left(z^2 - hz\right)dz = \frac{1}{2\eta}\frac{\partial P}{\partial r}\left[\frac{h^3}{3} - \frac{h\left(h^2\right)}{2}\right]$$

$$U = -\frac{h^3}{12\eta}\frac{\partial P}{\partial r} \qquad \text{[AP 6.10]}$$

Assuming that h moves only in the direction of z with velocity dh/dt, then the cylindrical element dr.r.dθ.h will change in volume at the rate of dr.r.dθ.dh/dt. For incompressible fluid, the rate of decrease of the volume element must be equal to the net rate of outward radial flow. Thus:

$$-dr.r.d\theta\left(\frac{dh}{dt}\right) = \frac{\partial}{\partial r}\left(r.d\theta.U\right)dr \qquad \text{[AP 6.11]}$$

Substituting Equation AP 6.10 into Equation AP 6.11 and simplifying gives:

$$\frac{12\eta}{h^3}\frac{dh}{dt}r = \frac{\partial}{\partial r}\left(r\frac{\partial P}{\partial r}\right) \qquad \text{[AP 6.12]}$$

Integrating the above equation twice with respect to r gives:

$$P = \frac{3\eta}{h^3}\frac{dh}{dt}r^2 + C'\ln r + C \qquad \text{[AP 6.13]}$$

At r = 0, P must be a finite number therefore C'lnr = 0.

At r = R, P must be in equilibrium with P_{atm} (atmospheric pressure). Therefore:

$$C = P_{atm} - \frac{3\eta}{h^3}\frac{dh}{dt}R^2 \qquad \text{[AP 6.14]}$$

Substituting AP 6.14 into AP 6.13 gives:

$$P = \frac{3\eta}{h^3}\frac{dh}{dt}\left(R^2 - r^2\right) + P_{atm} \qquad \text{[AP 6.15]}$$

The total force acting on the plane in the positive z direction is:

$$\int_0^R P\, 2\pi r dr \quad \text{(i.e. Force, F = Pressure, P / Area, A)} \qquad \text{[AP 6.16]}$$

(Area, A for a cylindrical geometry is $2\pi rdr$)

The total force acting on the plane in the opposite direction is:

$$F + \int_0^R P_{atm}\ 2\pi r dr \qquad \text{[AP 6.17]}$$

Therefore, equating the force (i.e. force balance) using Equations AP 6.15 to AP 6.17 gives:

$$F + \int_0^R P_{atm} 2\pi r dr = -\int_0^R \frac{3\eta}{h^3}\frac{dh}{dt}\left(R^2 - r^2\right)2\pi r dr + \int_0^R P_{atm} 2\pi r dr$$

$$F = -2\pi \frac{3\eta}{h^3}\frac{dh}{dt}\int_0^R \left(R^2 - r^2\right)(r dr) \qquad \text{[AP 6.18]}$$

The motion of the upper plate cause the radial distance, R, to change with time. Integrating from r = 0 to r = R and that the volume remains constant (for an incompressible fluid):

$$F = -2\pi \frac{3\eta}{h^3}\frac{dh}{dt}\left[\frac{R^2.r^2}{2} - \frac{r^4}{4}\right]_0^R$$

$$F = -2\pi \frac{3\eta}{h^3}\frac{dh}{dt}\left[\frac{R^4}{2} - \frac{R^4}{4}\right]$$

$$F \quad 2\pi \frac{3\eta}{h^3}\frac{dh}{dt}\frac{1}{4}\left(2R^4 \quad R^4\right)$$

$$F = -\frac{3\eta}{2h^3}.\pi R^4 \frac{dh}{dt} \qquad \text{[AP 6.19]}$$

Since volume for a cylindrical geometry is given as $v = \pi R^2 h$, Equation AP 6.19 can be re-written as:

$$F = -\frac{3\eta}{2h^3}.\frac{\pi R^2 h.\pi R^2 h}{\pi h^2}\left(\frac{dh}{dt}\right)$$

$$F = -\frac{3\eta v^2}{2\pi h^5}\frac{dh}{dt} \qquad \text{[AP 6.20]}$$

AP 6.20 is the same equation as AP 6.1 used in the work of Laxmanan and Flemings [Lax 80] to obtain a relationship between the viscosity and the average shear rate.

NOTES